

DYNAMICAL TIDES AND OSCILLATIONS IN STAR AND PLANETARY SYSTEMS

A Dissertation

Presented to the Faculty of the Graduate School

of Cornell University

in Partial Fulfillment of the Requirements for the Degree of

Doctor of Philosophy

by

Jim Fuller

August 2013

© 2013 Jim Fuller

ALL RIGHTS RESERVED

DYNAMICAL TIDES AND OSCILLATIONS IN STAR AND PLANETARY SYSTEMS

Jim Fuller, Ph.D.

Cornell University 2013

I investigate tidal interactions and global oscillations in various types of stellar and planetary systems, with a focus on dynamical tidal effects. Dynamical tides arise from the excitation of non-hydrostatic waves within the stellar components, with tidal dissipation resulting from the damping of the excited waves. The wave frequencies, characteristics, and dissipative qualities vary greatly in different types of stellar systems, as does the resultant tidally induced evolution.

The first few chapters of this thesis focus on the excitation and dissipation of gravity waves within white dwarfs (WDs) in compact binary systems. I find that gravity waves are excited at composition gradients within the WDs, and may reach non-linear amplitudes in the outer layers of the star. At sufficiently short orbital periods, the waves are strongly non-linear and will break in the envelope of the white dwarf, producing efficient tidal dissipation. I show that this tidal dissipation will cause WDs to be nearly synchronized upon gravitational radiation-driven orbital decay. Moreover, the dissipation will heat the envelope of the WD, substantially increasing its luminosity and potentially reigniting its hydrogen shell to create a tidally induced nova-like event.

I also study the tidal excitation of stellar oscillation modes in eccentric binary systems and in triple star systems, and I compare my theory with recent *Kepler* observations. In eccentric binary systems such as KOI-54, the tidal forcing excites stellar oscillation modes at discrete multiples of the orbital frequency. The resulting orbital and spin evolution produced by the damping of these modes may lead to resonance lock-

ing, in which a stellar oscillation mode remains nearly resonant with the tidal forcing, producing greatly enhanced tidal dissipation. In hierarchical triple star systems such as HD 181068, the orbital motion of the inner binary can excite pressure modes in a red giant tertiary component. No stable tidal equilibrium exists for these systems, and the dissipation of the modes can cause the orbit of the inner binary to decay.

Lastly, I examine the oscillation mode spectrum of giant planets with a solid core. The rigidity of the core allows for the existence of shear modes which are confined to the solid core. In a rotating planet, the Coriolis force may cause substantial mixing between core shear modes and fundamental or pressure modes that propagate in the fluid envelope. The gravitational perturbations produced by these mixed modes can excite visible disturbances within a planetary ring system, and I compare our theoretical expectations with recent *Cassini* observations of waves in Saturn's rings.

BIOGRAPHICAL SKETCH

Born in 1986, Jim Fuller grew up in Boulder, Colorado. He graduated Bixby Elementary school in 1997, Southern Hills Middle School in 2000, and Fairview High School in 2004. He then attended Whitman College (located in Walla Walla, WA), and graduated in 2004 as a Physics-Astronomy major. His career in astronomy began with an REU at the High Altitude Observatory in Boulder, CO, under the guidance of Dr. Sarah Gibson. He later went on to pursue a PhD in theoretical astrophysics from Cornell, working with Professor Dong Lai. He plans to earn his PhD during the summer of 2013, and will then begin a postdoc at Caltech.

Throughout his life, Jim has been an avid outdoorsman and athlete. As a youth, he participated in Boy Scouts, and he became an Eagle Scout in 2003. Jim loves to backpack, hike, and climb in the mountains. To date, he has climbed over 40 of Colorado's 14,000 foot peaks and 6 of California's 14,000 foot peaks. Jim is also a dedicated ultimate frisbee player, and played in the national college championship tournament with the Cornell Buds in 2010, 2011, and 2012.

This thesis is dedicated to my parents, Melody and Carey. Hopefully this dedication will repay them for the hardships they have endured while parenting me, which include birthing pains, diaper changes, temper tantrums, school concerts, sibling rivalries, cooking catastrophes, adolescence, and six figures of college tuition. Thank you
Mommy and Daddy!

ACKNOWLEDGEMENTS

I am indebted to my adviser, Dong Lai, for the years of extensive assistance (and scrutiny) required to transform my undisciplined scientific floundering into coherent research. I also wish to thank Lars Bildsten, Bill Paxton, Eliot Quataert, Dan Tamayo, Gordon Ogilvie, Yanqin Wu, Matt Hedman, and Phil Nicholson for useful discussions related to the research presented in this thesis. I thank Gilles Fontaine (University of Montreal) for providing the white dwarf models used in this paper and for valuable advice on these models. I acknowledge the hospitality (Fall 2011) of the Kavli Institute for Theoretical Physics at UCSB (funded by the NSF through Grant 11-Astro11F-0016) where part of the work was carried out. This work has been supported in part by NSF grants AST-1008245, AST-1211061, AST 0707628, and NASA grants NNX12AF85G, NNX10AP19G, NNX11AL13H, and NNX07AG81G.

TABLE OF CONTENTS

Biographical Sketch	iii
Dedication	iv
Acknowledgements	v
Table of Contents	vi
List of Tables	x
List of Figures	xi
1 Introduction	1
2 Tidal Excitations of Oscillation Modes in Compact White Dwarf Binaries:	
I. Linear Theory	7
2.1 Introduction	7
2.2 Combined Evolution Equations for Oscillation Modes and the Binary Orbit	10
2.3 White Dwarf G-Modes and Tidal Coupling Coefficients	13
2.4 Numerical Results for Mode-Orbit Evolution Through Resonance	19
2.5 Analytic Estimate of the Resonant Mode Amplitude	23
2.6 Effect of Mode Damping	29
2.7 Discussion	30
3 Dynamical Tides in Compact White Dwarf Binaries: Tidal Synchronization and Dissipation	35
3.1 Introduction	35
3.2 Basic Equations	38
3.3 Boundary Conditions	41
3.4 Angular Momentum and Energy Flux	44
3.5 White Dwarf Models	47
3.6 Numerical Calculations of Tidal Response	49
3.6.1 Numerical Method and Importance of Self-Consistent Stellar Model	49
3.6.2 Calculation with a Toy White Dwarf Model	50
3.6.3 Calculation with Realistic White Dwarf Model	53
3.6.4 Relation to Tidal Overlap Integral	58
3.6.5 Justification of the Outer Boundary Condition	60
3.7 Simple Model for Gravity Wave Excitation: Analytic Estimate	62
3.8 Spin-Orbit Evolution	67
3.8.1 Synchronization	69
3.8.2 Tidal Effect on the Orbital Decay Rate and Phase of Gravitational Waves	72
3.8.3 Tidal Heating	74
3.9 Discussion	76

4	Tidal Novae in Compact Binary White Dwarfs	80
4.1	Introduction	80
4.2	Energy and Angular Momentum of Tidally Excited Gravity Waves . . .	82
4.3	Two Zone Model for Tidal Heat Deposition	83
4.4	Tidal Heating and Unstable Nuclear Burning	86
4.5	Discussion	90
5	Dynamical Tides in Compact White Dwarf Binaries: Helium Core White Dwarfs, Tidal Heating, and Observational Signatures	92
5.1	Introduction	92
5.2	Tidal Dissipation in Helium WDs	95
5.2.1	Wave Dynamics	95
5.2.2	Wave Excitation in He WDs	97
5.3	Orbital and Rotational Evolution of He WDs	103
5.4	Location of Tidal Heat Deposition	107
5.4.1	Non-linear Wave Breaking	107
5.4.2	Wave Absorption at a Critical Layer	111
5.5	Thermal Evolution of Tidally Heated Binary White Dwarfs	115
5.5.1	Details of Calculation	115
5.5.2	Effects of Tidal Heating	116
5.5.3	Heating and Cooling Time Scales	121
5.6	Discussion	124
6	Dynamical Tides in Eccentric Binaries and Tidally-Excited Stellar Pulsations in <i>KEPLER</i> KOI-54	130
6.1	Introduction	130
6.2	Dynamical Tides in Eccentric Binary Stars: General Theory	132
6.3	Stellar Oscillation Modes and Non-Resonant Mode Energies	135
6.4	Flux Variation due to Tidally-Forced Oscillations	140
6.5	Secular Spin-Orbit Evolution and Resonance Locking	146
6.5.1	Need for Resonance Locking	147
6.5.2	Critical Resonance-Locking Mode	148
6.5.3	Evolution Toward Resonance	150
6.5.4	Numerical Examples of Evolution Toward Resonance	156
6.6	Oscillations at Non-Orbital Harmonics	163
6.7	Discussion	165
7	Tidally Induced Oscillations and Orbital Decay in Compact Triple-Star Systems	168
7.1	Introduction	168
7.2	Three-body Tidal Forcing	170
7.3	Mode Excitation and Observation	175
7.3.1	Mode Amplitudes	175
7.3.2	Luminosity Variations	177

7.4	Effect of Modes on Orbital Evolution	179
7.4.1	Hamiltonian Formalism	179
7.5	Observations of HD 181068	182
7.5.1	Fourier Analysis	182
7.5.2	Lack of solar-like oscillations	184
7.6	Comparison With Observations	186
7.6.1	Stellar Model	186
7.6.2	Comparison with Observed Luminosity Fluctuations	190
7.7	Orbital Evolution of HD 181068	193
7.7.1	Results of Orbital Evolution	196
7.7.2	Resonance Locking	199
7.8	Discussion	201
8	Non-radial Oscillations in Rotating Giant Planets with Solid Cores: Appli- cation to Saturn and its Rings	204
8.1	Introduction	204
8.2	Planetary Model	207
8.2.1	The Shear Modulus	209
8.3	Oscillations of Non-rotating Planets	210
8.3.1	Mode Mixing	217
8.4	Rotational Mode Mixing	219
8.4.1	Strength of Coriolis Mode Mixing	223
8.4.2	Two and Three-Mode Rotational Mixing	224
8.4.3	Multi-Mode Rotational Mixing	228
8.5	Effect of Oscillation Modes on the Rings	228
8.5.1	Comparison with Observations	232
8.6	Discussion and Conclusions	235
A	Calculation with Massive Star Model	240
B	Calculation of Equilibrium Tide	244
C	General Scaling for Spin-Orbit Synchronization and Tidal Heating	246
D	Estimating the Core-Envelope Coupling Time Scale	248
E	Non-tidal Orbital Evolution	249
F	Elastic Oscillation Equations	251
F.0.1	Boundary Conditions	254
G	Solving for Rotationally Mixed Modes	258
G.0.2	Alternative Formalism	261
G.0.3	Rotational Coupling Coefficients	262

H	Mode Normalization	264
I	Three-Mode Mixing	265
J	Effect of Modes on the Rings	267
	Bibliography	270

LIST OF TABLES

2.1	Oscillation modes in warm WD model	16
2.2	Oscillation modes in cool WD model	16
7.1	Properties of HD 181068	182
7.2	Fourier peaks in HD 181068	183
8.1	Observed Waves in Saturn's Rings	206

LIST OF FIGURES

2.1	WD model propagation diagram	15
2.2	Mode weight functions in warm WD model	18
2.3	Mode weight functions in cool WD model	19
2.4	Mode evolution through resonance	21
2.5	Post-resonance mode amplitudes vs. mode index	22
2.6	Post-resonance mode amplitudes vs. companion mass	22
2.7	Mode amplitude evolution including damping	30
2.8	Post-resonance mode displacements	34
3.1	Realistic WD models	48
3.2	Toy WD model	51
3.3	Toy model wave function	52
3.4	Toy model tidal torque	53
3.5	Warm WD model peak wave function	54
3.6	Warm WD model trough wave function	55
3.7	Warm WD model tidal torque	56
3.8	Cool WD model tidal torque	57
3.9	Cold WD model tidal torque	57
3.10	Non-linearity of wave function	61
3.11	Simplified wave propagation diagram	63
3.12	WD synchronization	70
3.13	WD spin evolution	71
3.14	Tidal energy deposition	73
4.1	Critical layer evolution	85
4.2	Surface temperature evolution	88
4.3	Internal temperature profiles	89
5.1	Helium WD models	98
5.2	Helium WD wave function	100
5.3	Helium WD tidal torque	101
5.4	Helium WD synchronization	104
5.5	Helium WD energy deposition	106
5.6	Location of non-linear wave breaking	110
5.7	Location of critical layer	113
5.8	Helium WD temperature evolution	117
5.9	CO WD temperature evolution, $0.3M_{\odot}$ companion	118
5.10	CO WD temperature evolution, $0.9M_{\odot}$ companion	119
5.11	Thermal time scales	123
5.12	Comparison with SDSS J0651	125
6.1	A-type star mode propagation diagram	136
6.2	Mode excitation in KOI-54	138

6.3	Mode visibilities	144
6.4	Simple example of resonance locking	157
6.5	Realistic example of resonance locking	160
6.6	Simultaneous resonance locks	162
7.1	Triple star system geometry	171
7.2	Fourier spectrum of HD 181068	184
7.3	HD 181068 light curve	184
7.4	Lack of solar-like oscillations in HD 181068	187
7.5	HD 181068 structure and mode eigenfunctions	188
7.6	Mode displacements and overlap integrals	189
7.7	Tidally excited mode luminosity fluctuations	192
7.8	HD 181068 orbital evolution	197
8.1	Saturn Model	209
8.2	Elastic oscillation mode spectrum	212
8.3	Mode eigenfunctions	213
8.4	F-mode eigenfunctions	214
8.5	Mode potential perturbations	215
8.6	Mode mixing	218
8.7	Two-mode rotational mixing	225
8.8	Three-mode rotational mixing	226
8.9	Multi-mode rotational mixing	227
8.10	Comparison with observations for $\mu = 1.6$ GPa	231
8.11	Comparison with observations for $\mu = 0.32$ GPa	232
8.12	Comparison with observations for $\mu = 8$ GPa	233
A.1	Massive star propagation diagram	241
A.2	Massive star wave function	242
A.3	Massive star tidal torque	243

CHAPTER 1

INTRODUCTION

The physics of tidal interactions in astronomical systems is an old and onerous subject. Indeed, Darwin (1879) realized that the mutual tidal distortion of the Earth and the Moon, created by their mutual gravitational fields, would lead to tidal orbital and spin evolution. Such evolution is caused by the dissipative effects of tidal distortions, which arise from friction in the non-uniform velocity field of particles in a tidally distorted object. The stable end-state of such evolution is a circular orbit in which both bodies rotate synchronously with the orbit, such that the gravitational fields felt by particles in each object are time-independent. Yet, despite more than a century of study, the exact processes creating the tidal friction (and their associated orbital evolution time scales) remain poorly understood in many astronomical systems.

Understanding tidal evolution is essential to our knowledge of the formation and evolution of stars in compact multiple systems. Tidal interactions can cause orbits to expand or to shrink, potentially inducing stellar mergers. In certain situations, tides may create substantial frictional heating. Moreover, observations clearly indicate that tidal friction is important in stellar systems of sufficiently short orbital periods. For instance, binary stars with short orbital periods tend to be in circular orbits (Abt & Boonyarak 2004, Abt 2005, Abt 2006) and the spins of the stellar components tend to be synchronous and aligned with the orbital motion (Abt & Boonyarak 2004).

Despite observations that tidal effects are important in compact stellar systems, a thorough understanding of the physics behind the tidal dissipation remains lacking. One question that must be addressed is whether tidal friction arises primarily due to equilibrium tides (i.e., quasi-static tides) or dynamical tides. The equilibrium tide is simply the hydrostatic tidal bulge induced in a star by the tidal gravitational field of its compan-

ion.¹ Although the time-dependent motion of the equilibrium tide will be damped by the microscopic viscosity associated with the motions of particles in the stellar plasma, the associated time scales are extremely long and can not account for observed tidal effects. If the star contains large convective zones, the turbulent motion of convective eddies may create a greatly increased effective viscosity, leading to tidal dissipation through the turbulent dissipation of the equilibrium tide (Zahn 2008 and references therein).

In this thesis, I attempt to better understand the influence of dynamical tides in various types of stellar systems. Dynamical tides are the result of non-hydrostatic motions induced by the tidal gravitational field of a companion star, and are present in the form of waves that propagate through the stellar interior. These waves have frequencies equal to the tidal forcing frequencies and thus have frequencies that are typically smaller than the star's dynamical frequency (although see Chapter 7 for exceptions to this rule in triple star systems). In stably stratified (i.e., non-convective) regions of a star, these waves exist as gravity waves restored by the buoyancy force.² If the waves are weakly damped and confined to a propagation cavity within the star (i.e., they are reflected at the boundaries of this cavity), they interfere and set up standing waves. Standing gravity waves are referred to as gravity modes (g-modes), while standing acoustic waves are referred to as pressure modes (p-modes).

In the simplest case, tidally excited oscillations can be calculated as adiabatic, linear perturbations to a non-rotating, spherical star. The oscillations are then described by a system of four linear coupled ordinary differential equations which may be easily solved given appropriate boundary conditions. Numerous calculations of tidal dissipation from

¹The assumption that the star remain near hydrostatic equilibrium is usually a good first approximation because the dynamical time of a star is usually much shorter than the orbital period of its companion. In most (but not all) cases, the physical displacements associated with the equilibrium tide are larger than those associated with the dynamical tide.

²In neutrally stratified (convective) regions of a rotating star, inertial waves may exist, whose restoring force is the Coriolis force. However, I do not explicitly investigate the influence of inertial waves in this thesis.

linearly excited waves (given the above simplifications) exist for main sequence stars (e.g., Zahn 1977, Goldreich & Nicholson 1989, Lai 1996,1997, Kumar & Quataert 1998, and Witte & Savonije 1999,2001, Goodman & Dickson 1998, Barker & Ogilvie 2010, Weinberg et al. 2012).

In realistic situations, calculation of the tidal dissipation associated with dynamic tides is hampered by several complicating factors. First, the degree of excitation of gravity waves is strongly dependent on stellar structure, and therefore the resulting dissipation strongly depends on the type of star involved. Second, gravity waves can be significantly altered by rotational effects in the star, including differential rotation, making detailed calculations significantly more difficult. Third, non-adiabatic effects responsible for the dissipation of gravity waves can introduce considerable numerical difficulty into wave excitation and dissipation calculations. Fourth, non-linear effects (i.e., when the tidal effect can no longer be treated as a small perturbation) may be very important in certain types of systems, making the analysis considerably more complex. Finally, non-trivial orbital and spin evolution may result from the combined effects of tidal dissipation and stellar evolution (e.g., due to various types of resonances), making it necessary to understand the coupled orbital, spin, and stellar evolution of systems undergoing tidal dissipation. I discuss all of the above processes at some point within the chapters that follow.

The first four chapters of this thesis are devoted to understanding the tidal dissipation process in short orbital period (less than a few hours) white dwarf (WD) binaries. Compact WD binaries emit gravitational waves, causing orbital decay that eventually triggers mass transfer or a stellar merger. As the orbit decays, tidal interactions become increasingly powerful and may have a profound effect on the pre-merger state of the WDs. The question arises whether the tidal interactions are powerful enough to syn-

chronize the WDs before the onset of mass transfer, and whether the associated tidal heating will substantially effect the thermal state of the WDs.

In Chapter 2, I investigate the excitation of g-modes in inspiraling WD binaries. I find that g-modes are excited to large amplitudes as the orbit decays through resonances between the orbital frequency and the WD's g-mode frequencies. Even before the resonance is reached, the mode amplitudes can be highly non-linear, invalidating a purely linear analysis of standing g-modes. Therefore, in Chapter 3, I investigate the excitation of traveling gravity waves that become highly non-linear in the envelope of the star, causing them to break and locally deposit their energy and angular momentum. I find that the gravity waves are excited at composition gradients within the WD, with a strong dependence on the tidal forcing frequency. Therefore, tidal effects are negligible at long orbital periods (periods greater than roughly two hours), but are powerful at short orbital periods (periods less than about 45 minutes). I find that the gravity waves are capable of bringing the WDs to nearly synchronous rotation rates by the onset of mass transfer. Although tides cause negligible orbital decay compared to gravitational radiation, they will produce substantial deviations to gravitational wave forms detectable by next generation gravitational wave detectors such as *ELISA*.

Chapters 4 and 5 mostly focus on the tidal heating produced in binaries containing both canonical CO WDs of mass $M \sim 0.6M_{\odot}$ and low mass He WDs of mass $M \sim 0.3M_{\odot}$. The tidal heating is localized to the outer layers of the WD where the gravity waves break, although the exact location depends on the non-linear breaking criterion and angular momentum transport processes within the WD. Using the *MESA* stellar evolution code, I find that tidal heating substantially increases the temperatures of the outer $\sim 10^{-4}M_{\odot}$ of the WD, leading to greatly increased luminosities for WDs with orbital periods shorter than ~ 20 minutes. If the tidal heat is deposited relatively deeply,

it cannot quickly diffuse outward and can increase the temperature of the base of the WD's hydrogen shell to $\sim 10^7$ K. At this point, the hydrogen will ignite, potentially producing a tidally induced nova, whose characteristics may be similar to classical novae observed in accreting WDs.

Dynamical tides are important in stars other than WDs, and Chapters 6 and 7 investigate the excitation of tidal oscillation modes in stars observed by the *Kepler* satellite. In Chapter 6, I compare tidal theories to observations of the KOI-54 system, which is composed of two A-type stars in a highly eccentric ($e = 0.83$) 42 day orbit (Welsh et al. 2011). The stars excite g-modes in one another, which oscillate at exact integer harmonics of the orbital frequency. Although most of the observed oscillations can be adequately explained by simple linear tidal theory, the largest pulsations (at 90 and 91 times the orbital frequency, with luminosity fluctuation amplitudes of $\sim 2 \times 10^{-4}$) are more enigmatic. I propose that the pulsations are nearly-resonant oscillation modes that are locked near resonance by the coupled orbital, spin, and stellar evolution.

In Chapter 7, I examine tidally induced pulsations in the hierarchical triple star system HD 181068, composed of a red giant primary orbited every 45 days by a pair of dwarf stars who orbit each another every 0.9 days (Derekas et al. 2012, Borkovits et al. 2012). I show that the orbital motion of the dwarf stars tidally excites p-modes in the red giant primary at a few discrete frequencies. Luminosity fluctuations at these frequencies are observed in the *Kepler* light curve, with amplitudes close to my estimates. I show that these tidally excited p-modes can cause substantial orbital decay in the dwarf binary during certain phases of the system's evolution.

Finally, Chapter 8 examines the properties of oscillation modes in giant planets with solid cores. While these oscillations may be an important aspect of dynamic tides in planetary systems, this chapter focuses on the properties of the oscillations and their

gravitational influence on a planetary ring system. I begin by evaluating the characteristics of oscillation modes in non-rotating planets, focusing on the shear modes that can propagate in a solid planetary core. Next, I study the process of rotationally-induced mode mixing that can cause the shear modes (which are otherwise confined to the core) to mix with envelope modes, thereby obtaining greatly enhanced observable signatures. I conclude by comparing our theoretical expectations to the observations of Hedman et al. (2013), which indicate the presence of waves in Saturn's rings excited by gravitational perturbations from Saturn's oscillation modes. I find that mode mixing between core shear modes and Saturn's fundamental modes provides a possible (although somewhat incomplete) explanation for the wave features observed by Hedman et al. (2013).

CHAPTER 2

TIDAL EXCITATIONS OF OSCILLATION MODES IN COMPACT WHITE DWARF BINARIES: I. LINEAR THEORY

2.1 Introduction¹

It is well known that non-radial gravity modes (g-modes) are responsible for the luminosity variations observed in some isolated white dwarfs (called ZZ Ceti stars) in the instability strip. These g-modes are thought to be excited by a convective driving mechanism operating in the shallow surface convection zone of the star (see Brickhill 1983; Goldreich & Wu 1999; Wu & Goldreich 1999).

In this paper we study the tidal excitation of g-modes in compact binary systems containing a white dwarf (WD) and another compact object (white dwarf, neutron star or black hole). The Galaxy is populated with $\sim 10^8$ WD-WD binaries and several 10^6 of double WD-NS binaries [Nelemans et al. (2001); see also Nelemans (2009) and references therein]. A sizeable fraction of these binaries are compact enough so that the binary orbit will decay within a Hubble time to initiate mass transfer or a binary merger. Depending on the details of the mass transfer process (including the response of the WD to mass transfer), these ultra-compact binaries (with orbital period less than an hour) may survive mass transfer for a long time or merge shortly after mass transfer begins. A number of ultra-compact interacting WD-WD binary systems have already been observed [including RX J0806.3+1527 (period 5.4 min) and V407 Vul (period 9.5 min); see Strohmayer 2005 and Ramsay et al. 2005]. Recent surveys (e.g., SDSS) have also begun to uncover non-interacting compact WD binaries (e.g., Badenes et al. 2009; Mullally et al. 2009; Kilic et al. 2009; Marsh et al. 2010; Kulkarni & van Kerkwijk

¹This chapter is based on Fuller & Lai (2011).

2010; Steinfadt et al. 2010). Depending on the total mass, the systems may evolve into Type Ia supernovae (for high mass), or become AM CVn binaries or R CrB stars (for low mass). Many of these WD binaries are detectable in gravitational waves by the *Laser Interferometer Space Antenna (LISA)* (Nelemans 2009).

In this paper we consider resonant tidal interaction in WD binaries that are not undergoing mass transfer. This means that the binary separation D is greater than D_{\min} , the orbital radius at which dynamical merger or mass transfer occurs, i.e.,

$$D \gtrsim D_{\min} \simeq 2.5 \left(\frac{M_t}{M} \right)^{1/3} R, \quad (2.1)$$

where M is the WD mass, $M_t = M + M'$ is the total mass and R is the WD radius. This corresponds to orbital periods of

$$P \gtrsim P_{\min} = 68.4 \left(\frac{R}{10^4 \text{km}} \right)^{3/2} \left(\frac{M}{M_{\odot}} \right)^{-1/2} \text{ s}. \quad (2.2)$$

Since WD g-mode periods are of order one minute or longer, they can be excited by the binary companion prior to mass transfer. In particular, as the binary orbit decays due to gravitational radiation, the orbital frequency sweeps through a series of g-mode frequencies, transferring orbital energy to the modes. Although the overlap integral of the g-mode eigenfunctions with the tidal potential is generally quite small, a binary system that spends a long time at resonance can still excite g-modes to large amplitudes.

Previous studies of tidal interaction in WD binaries have focused on quasi-static tides (e.g., Iben, Tutukov & Fedorova 1998; Willems, Deloye & Kalogera 2009), which essentially correspond to non-resonant f-modes of the star. Such static tides become important only as the binary approaches the tidal limit (equation 2.1). Racine, Phinney & Arras (2007) recently studied non-dissipative tidal synchronization due to Rossby waves in accreting ultra-compact WD binaries. Rathore, Blandford & Broderick (2005) studied resonant mode excitations of WD modes in eccentric binaries. They focused

on f-modes, for which the resonance occurs when harmonics of the orbital frequency matches the mode frequency. As mentioned above, for circular orbits, such resonance with the f-mode does not occur prior to mass transfer or tidal disruption. Their published analysis also did not include back reaction of the excited mode on the binary orbit.

The problem of resonant mode excitations in compact binaries has been studied before in the context of coalescing neutron star binaries: Reisenegger & Goldreich (1994), Lai (1994) and Shibata (1994) focused on the excitations of g-modes of non-rotating neutron stars; Ho & Lai (1999) and Lai & Wu (2006) studied the effects of NS rotation – including r-modes and other inertial modes; Flanagan & Racine (2006) examined gravitomagnetic excitation of r-modes. In the case of neutron star binaries, the orbital decay rate (for orbital frequencies larger than 5 Hz) is large and the mode amplitude is rather small, so the back reaction of the excited mode on the orbit can be safely neglected (see section 5 of the present paper). By contrast, in the case of WD binaries, the orbital decay is much slower and the excited mode can reach a much larger amplitude. It thus becomes essential to take the back reaction into account.

In this paper, we consider WD binaries in circular orbits, consistent with the observed population of compact WD binaries (e.g. Kulkarni & van Kerkwijk 2010). Such circular orbits are a direct consequence of the circularization by gravitational radiation and/or the common envelope phase leading to their formation. A key assumption of this paper is that we assume the WD is not synchronized with the binary orbit. While it is true that the tidal circularization time scale is much longer than the synchronization time, the observed circular orbit of the WD binaries does not imply synchronization. While there have been numerous studies of tidal dissipation in normal stars and giant planets (e.g., Zahn 1970,1989; Goldreich & Nicholson 1977; Goodman & Oh 1997; Goodman & Dickson 1998; Ogilvie & Lin 2004,2007; Wu 2005; Goodman & Lackner

2009), there has been no satisfactory study on tidal dissipation in WDs. Even for normal stars, the problem is not solved (especially for solar-type stars; see Goodman & Dickson 1999; see Zahn 2008 for review). In fact it is likely that the excitations of g-modes and other low-frequency modes play a role in the synchronization process. The orbital decay time scale near g-mode resonances is relatively short (of order 10^4 years for orbital periods of interest, i.e., minutes), so it is not clear that tidal synchronization can compete with the orbital decay rate. Given this uncertainty, we will consider non-rotating WDs (or slowly-rotating WDs, so that the g-mode properties are not significantly modified by rotation) as a first step, and leaving the study of the rotational effects to a future paper.

The remainder of the paper is organized as follows. In Section 2.2, we present the equations governing the evolution of the orbit and the g-modes. Section 2.3 examines the properties of WD g-modes and their coupling with the tidal gravitational field of the companion. In Section 2.4, we numerically study the evolution of the g-modes through resonances, and in Section 2.5 we present analytic estimates of the resonant g-mode excitation. We study the effect of mode damping on the tidal excitation in Section 2.6 and discuss the uncertainties and implications of our results in Section 2.7.

2.2 Combined Evolution Equations for Oscillation Modes and the Binary Orbit

We consider a WD of mass M and radius R in orbit with a companion of mass M' (another WD, or NS or BH). The WD is non-spinning. The gravitational potential produced

by M' can be written as

$$\begin{aligned} U(\mathbf{r}, t) &= -\frac{GM'}{|\mathbf{r} - \mathbf{D}(t)|} \\ &= -GM' \sum_{lm} \frac{W_{lm} r^l}{D^{l+1}} e^{-im\Phi(t)} Y_{lm}(\theta, \phi), \end{aligned} \quad (2.3)$$

where $\mathbf{r} = (r, \theta, \phi)$ is the position vector (in spherical coordinates) of a fluid element in star M , $\mathbf{D}(t) = (D(t), \pi/2, \Phi(t))$ is the position vector of M' relative to M (D is the binary separation, Φ is the orbital phase or the true anomaly) and the coefficient W_{lm} is given by

$$\begin{aligned} W_{lm} &= (-)^{(l+m)/2} \left[\frac{4\pi}{2l+1} (l+m)!(l-m)! \right]^{1/2} \\ &\times \left[2^l \left(\frac{l+m}{2} \right)! \left(\frac{l-m}{2} \right)! \right]^{-1}. \end{aligned} \quad (2.4)$$

Here the symbol $(-)^p$ is zero if p is not an integer. The dominant $l = 2$ component of the tidal potential has $W_{2\pm 2} = (3\pi/10)^{1/2}$, $W_{20} = (\pi/5)^{1/2}$, $W_{2\pm 1} = 0$, and so only the $m = \pm 2$ modes can be resonantly excited.

The linear perturbation of the tidal potential on M is specified by the Lagrangian displacement $\xi(\mathbf{r}, t)$, which satisfies the equation of motion

$$\frac{\partial^2 \xi}{\partial t^2} + \mathcal{L} \cdot \xi = -\nabla U, \quad (2.5)$$

where \mathcal{L} is an operator that specifies the internal restoring forces of the star. The normal oscillation modes of the star satisfy $\mathcal{L} \cdot \xi_\alpha = \omega_\alpha^2 \xi_\alpha$, where $\alpha = \{n, l, m\}$ is the usual mode index and ω_α is the mode frequency. We write $\xi(\mathbf{r}, t)$ as the sum of the normal modes:

$$\xi(\mathbf{r}, t) = \sum_{\alpha} a_{\alpha}(t) \xi_{\alpha}(\mathbf{r}). \quad (2.6)$$

The (complex) mode amplitude $a_{\alpha}(t)$ satisfies the equation

$$\ddot{a}_{\alpha} + \omega_{\alpha}^2 a_{\alpha} = \frac{GM' W_{lm} Q_{\alpha}}{D^{l+1}} e^{-im\Phi(t)}, \quad (2.7)$$

where Q_α is the tidal coupling coefficient (also used by Press & Teukolski 1977), defined by

$$\begin{aligned} Q_\alpha &= \langle \xi_\alpha | \nabla(r^l Y_{lm}) \rangle \\ &= \int d^3x \rho \xi_\alpha^* \cdot \nabla(r^l Y_{lm}) \\ &= \int d^3x \delta\rho_\alpha^* r^l Y_{lm}. \end{aligned} \quad (2.8)$$

Here $\delta\rho_\alpha = -\nabla \cdot (\rho \xi_\alpha)$ is the Eulerian density perturbation. In deriving (2.7) we have used the normalization

$$\langle \xi_\alpha | \xi_\alpha \rangle = \int d^3x \rho \xi_\alpha^* \cdot \xi_\alpha = 1. \quad (2.9)$$

Resonant excitation of a mode α occurs when $\omega_\alpha = m\Omega$, where Ω is the orbital frequency.

In the *absence* of tidal interaction/resonance, the WD binary orbit decays due to gravitational radiation, with time scale given by (Peters 1964)

$$\begin{aligned} t_D &= \frac{D}{|\dot{D}|} = \frac{5c^5}{64G^3} \frac{D^4}{MM'M_t} \\ &= 3.2 \times 10^{10} \left(\frac{M_\odot^2}{MM'} \right) \left(\frac{M_t}{2M_\odot} \right)^{1/3} \left(\frac{\Omega}{0.1 \text{ s}^{-1}} \right)^{-8/3} \text{ s}, \end{aligned} \quad (2.10)$$

where $M_t = M + M'$ is the total binary mass. When a strong tidal resonance occurs, the orbital decay rate can be modified, and we need to follow the evolution of the orbit and the mode amplitudes simultaneously. The gravitational interaction energy between M' and the modes in star M is

$$\begin{aligned} W &= \int d^3x U(\mathbf{r}, t) \sum_\alpha a_\alpha^*(t) \delta\rho_\alpha^*(\mathbf{r}) \\ &= - \sum_\alpha \frac{M' M R^2}{D^3} W_{lm} Q_\alpha e^{-im\Phi} a_\alpha^*(t), \end{aligned} \quad (2.11)$$

where we have restricted to the $l = 2$ terms and set $G = 1$. The orbital evolution

equations, including the effects of the modes, are then given by

$$\ddot{D} - D\dot{\Phi}^2 = -\frac{M_t}{D^2} - \sum_{\alpha} \frac{3M_t}{D^4} W_{lm} Q_{\alpha} e^{im\Phi} a_{\alpha} - \frac{M_t}{D^2} (A_{5/2} + B_{5/2} \dot{D}), \quad (2.12)$$

$$\ddot{\Phi} + \frac{2\dot{D}\dot{\Phi}}{D} = \sum_{\alpha} im \frac{M_t}{D^5} W_{lm} Q_{\alpha} e^{im\Phi} a_{\alpha} - \frac{M_t}{D^2} B_{5/2} \dot{\Phi}. \quad (2.13)$$

The last terms on the right-hand side of equations (2.12) and (2.13) are the leading-order gravitational radiation reaction forces, with (see Lai & Wiseman 1996 and references therein)

$$A_{5/2} = -\frac{8\mu}{5D} \dot{D} \left(18v^2 + \frac{2M_t}{3D} - 25\dot{D}^2 \right), \quad (2.14)$$

$$B_{5/2} = \frac{8\mu}{5D} \left(6v^2 - \frac{2M_t}{D} - 15\dot{D}^2 \right), \quad (2.15)$$

where $\mu = MM'/M_t$ and $v^2 = \dot{D}^2 + (D\dot{\Phi})^2$. In equations (2.12)-(2.15) we have set $G = c = 1$. We have dropped the other post-Newtonian terms since they have negligible effects on tidal excitations. The mode amplitude equation is given by equation (2.7), or,

$$\ddot{b}_{\alpha} - 2im\Omega \dot{b}_{\alpha} + (\omega_{\alpha}^2 - m^2\Omega^2 - im\dot{\Omega})b_{\alpha} = \frac{M' W_{lm} Q_{\alpha}}{D^{l+1}}, \quad (2.16)$$

where

$$b_{\alpha} = a_{\alpha} e^{im\Phi}. \quad (2.17)$$

2.3 White Dwarf G-Modes and Tidal Coupling Coefficients

The non-radial adiabatic modes of a WD can be found by solving the standard stellar oscillation equations, as given in, e.g., Unno et al. (1989). The g-mode propagation zone in the star is determined by $\omega_{\alpha}^2 < N^2$ and $\omega_{\alpha}^2 < L_l^2$, where $L_l = \sqrt{l(l+1)}a_s/r$ is the

Lamb frequency (a_s is the sound speed), and N is the Brünt-Väisälä frequency, as given by

$$N^2 = g^2 \left[\frac{d\rho}{dP} - \left(\frac{\partial \rho}{\partial P} \right)_s \right], \quad (2.18)$$

where g is the gravitational acceleration, and the subscript “ s ” means that the adiabatic derivative is taken. Alternatively, N^2 can be obtained from (Brassard et al. 1991)

$$N^2 = \frac{\rho g^2 \chi_T}{P \chi_\rho} (\nabla_s - \nabla + B), \quad (2.19)$$

where

$$\begin{aligned} \chi_T &= \left(\frac{\partial \ln P}{\partial \ln T} \right)_{\rho, \{X_i\}}, & \chi_\rho &= \left(\frac{\partial \ln P}{\partial \ln \rho} \right)_{T, \{X_i\}}, \\ \nabla &= \frac{d \ln T}{d \ln P}, & \nabla_s &= \left(\frac{\partial \ln T}{\partial \ln P} \right)_{s, \{X_i\}}. \end{aligned} \quad (2.20)$$

The Ledoux term B accounts for the buoyancy arising from composition gradient:

$$B = - \frac{\chi_Y}{\chi_T} \frac{d \ln Y}{d \ln P}, \quad (2.21)$$

where

$$\chi_Y = \left(\frac{\partial \ln P}{\partial \ln Y} \right)_{\rho, T}, \quad (2.22)$$

and Y is the mass fraction of helium. This equation is valid for a compositional transition zone containing helium and one other element, as is the case for typical compositionally stratified DA WD models.

Figure 2.1 shows the profiles of the Brünt Väisälä and Lamb frequencies for one of the WD models adopted in this paper. These models were provided by G. Fontaine (see Brassard 1991). Since the pressure in the WD core is almost completely determined by electron degeneracy pressure, $N^2 \propto \chi_T$ is very small except in the non-degenerate outer layers. As a result, g-modes are confined to the outer layers of the star below the convection zone. Lower-order modes have higher eigenfrequencies, so they are confined to regions where N^2 is especially large, i.e., just below the convection zone. Higher

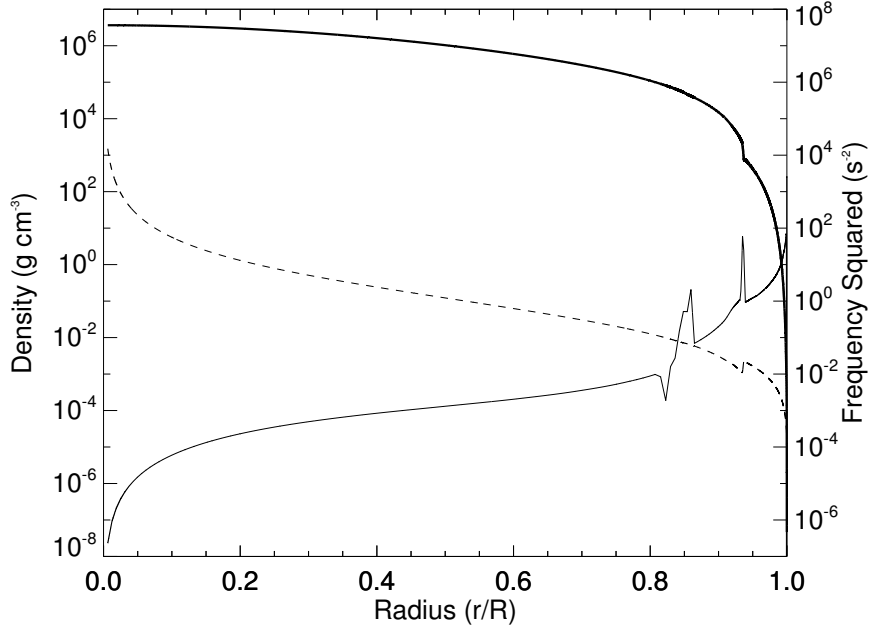


Figure 2.1: The square of the Brünt Väisälä (solid line) and Lamb (dotted line) frequencies and the density (thick solid line) as a function of normalized radius in a DA WD model, with $M = 0.6M_{\odot}$, $R = 8.97 \times 10^3$ km, $T_{\text{eff}} = 10800$ K. The spikes in the Brünt Väisälä frequency are caused by the composition changes from carbon to helium, and from helium to hydrogen, respectively.

order modes have lower eigenfrequencies and can thus penetrate into deeper layers of the star where the value of N^2 is smaller. Cooler WDs have deeper convection zones that cause the modes to be confined to deeper layers where N^2 is smaller. Consequently, the eigenfrequencies and associated values of Q_{α} tend to be smaller in cooler WDs due to the decreased value of N^2 in the region of mode propagation.

The other feature of WDs that strongly effects their g-modes is their compositionally stratified layers. The sharp composition gradients that occur at the carbon-helium transition and the helium-hydrogen transition create large values of the Ledoux term B [equation (2.21)], resulting in sharp peaks in N^2 as seen in Figure 2.1. These peaks have a large effect on the WD g-modes, leading to phenomena such as mode-trapping (e.g., Brassard 1991) and irregular period spectra. Thus, the eigenfrequencies and eigenfunc-

Table 2.1: The eigenfrequency $\bar{\omega}_\alpha$, tidal overlap parameter \bar{Q}_α , and numerical f-mode overlap c_0 for the first six $l = 2$ g-modes of a white dwarf model. The white dwarf model has $T_{\text{eff}} = 10800K$, $M = 0.6M_\odot$, and $R = 8.97 \times 10^3$ km. Note that $\bar{\omega}_\alpha$ and \bar{Q}_α are in dimensionless units such that $G = M = R = 1$, and $(GM/R^3)^{1/2}/(2\pi) = 0.053$ Hz.

n	$\bar{\omega}_\alpha$	$ \bar{Q}_\alpha $	c_0
0	2.08	0.428	1
1	0.298	1.27e-3	-1.80e-6
2	0.186	2.60e-3	3.91e-6
3	0.125	3.25e-5	3.62e-8
4	0.0900	8.91e-5	6.45e-7
5	0.0821	4.24e-4	1.32e-6
6	0.0715	6.91e-5	-2.54e-6

Table 2.2: Same as table 1, for a WD model of identical mass and composition but with $T_{\text{eff}} = 5080K$.

n	$\bar{\omega}_\alpha$	$ \bar{Q}_\alpha $	c_0
0	2.01	0.439	1
1	0.251	1.00e-3	-2.03e-6
2	0.156	2.40e-3	-3.76e-6
3	0.107	1.79e-5	-1.25e-7
4	0.0723	1.53e-5	4.95e-7
5	0.0537	8.42e-5	1.52e-6
6	0.0513	1.26e-4	1.42e-6

tions of WD g-modes are very sensitive to WD models.

Tables 1-2 give the $l = 2$ f-mode and g-mode frequencies and their tidal coupling coefficients for two WD models. While the full oscillation equations need to be solved to accurately determine the f-modes, the Cowling approximation (in which the perturbation in the gravitational potential is neglected) gives accurate results for g-modes. Since high-order g-modes have rather small $|Q_\alpha|$, the mode eigenfunction must be solved accurately to obtain reliable Q_α . To ensure that this is achieved in our numerical integration, we use the orthogonality of the eigenfunctions to check the accuracy of the value of Q_α (see Reisengger 1994 for a study on the general properties of Q_α). Since the numerical determination of an eigenfunction is not perfect, it will contain traces of the other

eigenfunctions, i.e.,

$$(\xi_\alpha)_{\text{num}} = c_\alpha \xi_\alpha + c_0 \xi_0 + c_1 \xi_1 + \dots, \quad (2.23)$$

with $c_\alpha \simeq 1$ and $|c_\beta| \ll 1$ for $\beta \neq \alpha$. This means that the numerical tidal overlap integral is

$$\begin{aligned} (Q_\alpha)_{\text{num}} &= \langle \nabla(r^l Y_{lm}) | (\xi_\alpha)_{\text{num}} \rangle \\ &= c_\alpha Q_\alpha + c_0 Q_0 + c_1 Q_1 + \dots \end{aligned} \quad (2.24)$$

Since $|Q_0|$ (for the f-mode) is of order unity, while $|Q_\alpha| \ll 1$ for g-modes, to ensure $(Q_\alpha)_{\text{num}}$ accurately represents the actual Q_α , we require

$$|c_0| \simeq |\langle \xi_0 | \xi_\alpha \rangle_{\text{num}}| \ll |Q_\alpha|. \quad (2.25)$$

The results shown in tables 1-2 reveal that $|c_0|$ is always more than an order of magnitude less than \bar{Q}_α , so the above condition is satisfied for the modes computed in this paper.

We note from tables 1-2 that while in general higher-order g-modes tend to have smaller $|Q_\alpha|$, the dependence of $|Q_\alpha|$ on the mode index n is not exactly monotonic. This is the result of the mode trapping phenomenon associated with composition discontinuities in the WD. To see this, we note that a mode with amplitude ξ_α has energy given by $E_\alpha = \omega_\alpha^2 \int d^3x \rho |\xi_\alpha|^2$, thus we can define the mode energy weight function

$$\frac{dE_\alpha}{d \ln P} = \omega_\alpha^2 \rho r^2 [\xi_r^2 + l(l+1) \xi_\perp^2] H_p, \quad (2.26)$$

where $H_p = dr/d \ln P = P/(\rho g)$ is the pressure scale height, and we have used

$$\xi_\alpha = [\xi_r(r) \mathbf{e}_r + r \xi_\perp(r) \nabla] Y_{lm} \quad (2.27)$$

(\mathbf{e}_r is the unit vector in the r -direction). Figures 2.2 and 2.3 display the weight functions for several g-modes of WD models. We can see that the weight functions for all the low-order modes are largest in the region below the convective zone near the spikes in N^2

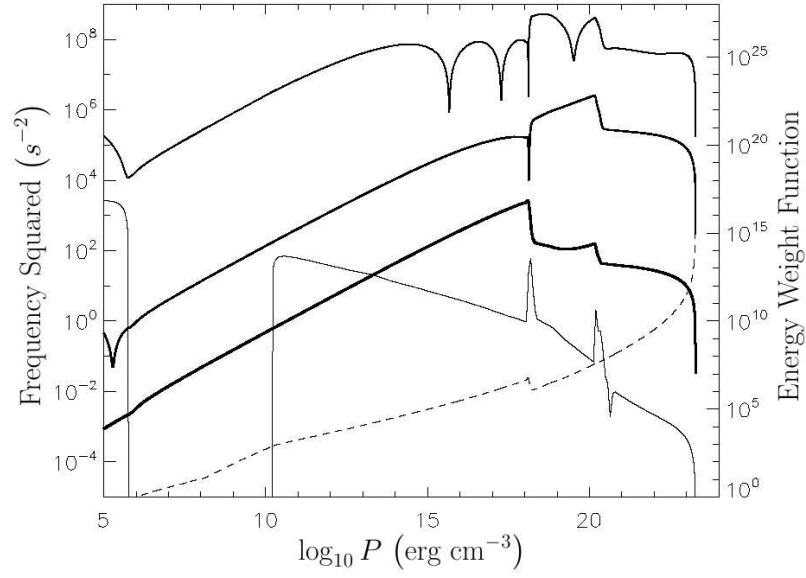


Figure 2.2: The mode energy weight functions for the $n = 1$ (thickest line), $n = 2$ (thick line), and $n = 5$ (top line) modes (all for $l = 2$) for a WD with $T_{\text{eff}} = 10800\text{K}$, $M = 0.6M_{\odot}$, $R = 8.97 \times 10^3\text{km}$, displayed as a function of $\log P$ so that the structure of the outer layers of the WD is more evident. The y-axis for a given mode is intended only to show the relative value of the weight function. The squares of the Brünt Väisälä (thin solid line) and Lamb (dotted line) frequencies are displayed to demonstrate how their values constrain the region of mode propagation.

produced by the composition gradients. For the modes shown in Figure 2.2, the smooth fall-off of the weight function just below the convective zone indicates that these modes are confined by the falling value of the Lamb frequency in this region. The weight functions of higher-order modes and the modes in WDs with deeper convective zones may drop sharply at the convective boundary, indicating that these modes are trapped by the convective zone rather than the decreasing Lamb frequency.

The weight functions also reveal the phenomenon known as mode trapping caused by the composition gradients. Mode trapping is especially evident for the $n = 2$ mode, as it is confined to the helium layer between the spikes in N^2 . It is clear that the mode is reflected by the carbon-helium boundary at larger depths and by the helium-hydrogen boundary at shallower depths. See Brassard (1991) for a more detailed description of

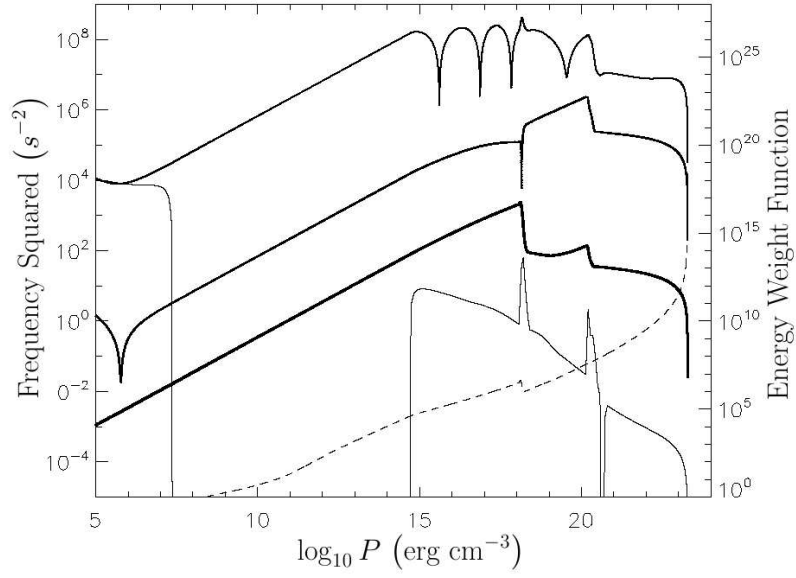


Figure 2.3: Same as Figure 2.2, except for a WD model with $T_{\text{eff}} = 5080\text{K}$. Note that the convection zone extends deeper in this model, pushing the modes to larger depths.

the effects of mode trapping.

The weight function is essentially the energy of a mode as a function of radius, so it tells us where orbital energy is deposited when a mode is excited. Since the weight function is largest in the hydrogen and helium layers just below the convection zone, most of the mode energy exists in this region of the WD. Thus, if the mode is damped, most of the mode energy will be damped out in this region.

2.4 Numerical Results for Mode-Orbit Evolution Through Resonance

Having obtained the mode frequency and the tidal coupling coefficient, we can determine the combined evolution of the resonant mode and the binary orbit using equations (2.7), (2.12), and (2.13). These are integrated from well before resonance until well after

the resonance is complete. The initial mode amplitude b_α and its derivative \dot{b}_α (prior to a resonance) are obtained by dropping the \ddot{b}_α , \dot{b}_α and $\dot{\Omega}$ terms in equation (2.16), giving

$$b_\alpha \simeq \frac{M' W_{lm} Q_\alpha}{D^{l+1}(\omega_\alpha^2 - m^2 \Omega^2)}, \quad (2.28)$$

$$\dot{b}_\alpha \simeq \left[- (l+1) \frac{\dot{D}}{D} + \frac{2m^2 \Omega \dot{\Omega}}{\omega_\alpha^2 - m^2 \Omega^2} \right] b_\alpha, \quad (2.29)$$

with $\dot{\Omega} \simeq -(3\dot{D}/2D)\Omega$. These expressions are valid for $(\omega_\alpha/m\Omega)^2 - 1 \gg \dot{\Omega}/(m\Omega^2) \simeq 3/(2m\Omega t_D)$ (see section 5).

The evolution equations (2.7), (2.12), and (2.13) form a very stiff set of differential equations. The reason for this is that the problem involves two vastly different time scales: the orbital decay time scale which is on the order of thousands of years, and the orbital time scale (or the resonant mode oscillation period) which is on the order of minutes. Consequently, a typical Runge-Kutta scheme would require the integration of millions of orbits, demanding a high degree of accuracy for each orbit. To avoid this problem, we employ the Rossenberg stiff equation technique (Press et al. 2007). The integrator requires a Jacobian matrix of second derivatives, meaning that we need to supply the 8×8 matrix of second derivatives corresponding to our 8 first-order differential equations. The evolution equations are sufficiently simple that this matrix can be found analytically.

Figure 2.4 depicts an example of the mode amplitude and orbit evolution near the resonance for the $n = 3$ g-mode. Before the resonance, the mode must oscillate with the same frequency as the binary companion, so the amplitude $|b_\alpha|$ is smooth. After the resonance, the mode oscillates at its eigenfrequency (which is now different from the forcing frequency). The amplitude of the mode continues to fluctuate after resonance because it is still being forced by the binary companion, although the amplitude of these fluctuations diminishes over time as the orbit moves further from resonance.

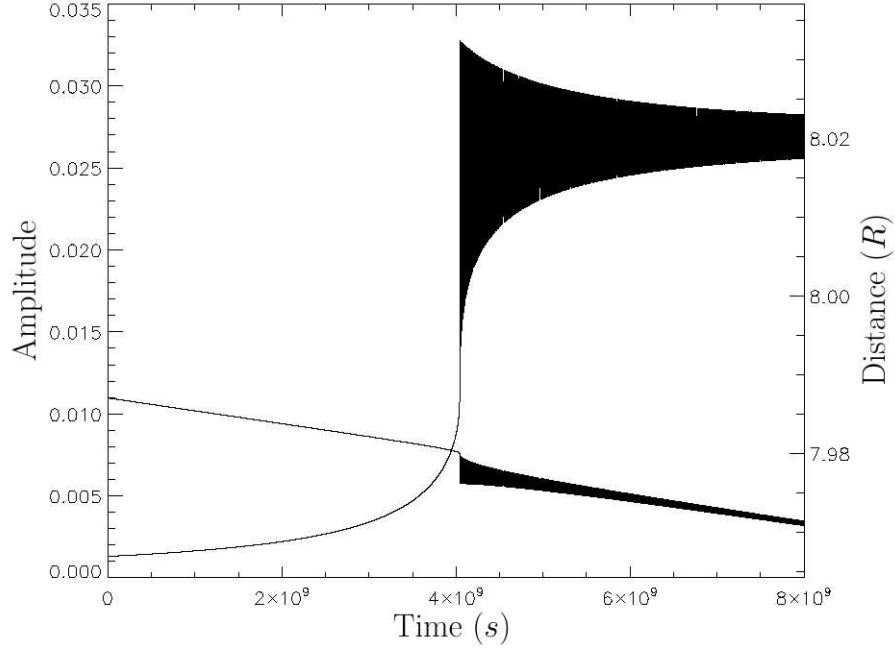


Figure 2.4: Mode amplitude $|b_\alpha|$ and orbital distance D as a function of time during resonance. The amplitude and distance oscillate after resonance, causing the curves to appear as filled shapes due to the short period of the oscillations with respect to the total integration time. These oscillations occur due to the continued interaction between the excited mode and the orbit. Note the sharp drop in orbital distance at resonance, which is caused by the transfer of orbital energy into the mode. The mode parameters are given in table I ($n = 3$). The companion mass is $M' = M = 0.6M_\odot$.

Figure 2.5 displays the average post-resonance amplitudes for the first five modes given in Table I. Note that no mode exceeds a maximum amplitude of $|b_\alpha| = 0.1$, and we expect that our linear approximation is a reasonable first approach to the problem before non-linear effects can be included. In general, lower-order modes reach larger amplitudes (due to their larger coupling coefficients), but higher-order modes with an abnormally high value of Q_α (trapped modes) may reach large amplitudes as well.

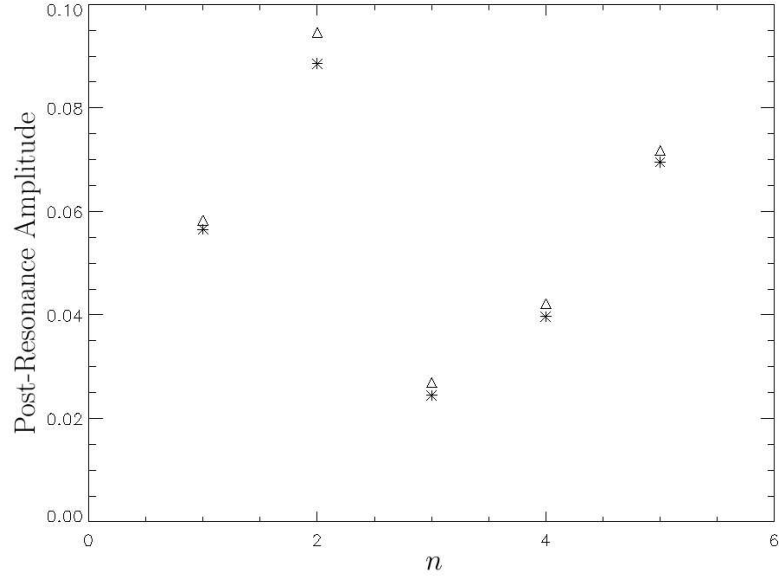


Figure 2.5: The average post-resonance amplitudes for the first five modes given in Table I. The open triangles mark the results obtained from numerical integration, and the asterisks indicate the results predicted by the analytical estimate described in section 2.5. The analytical estimates are usually accurate within a factor of 10%. The $n = 2$ and $n = 5$ modes are trapped modes.

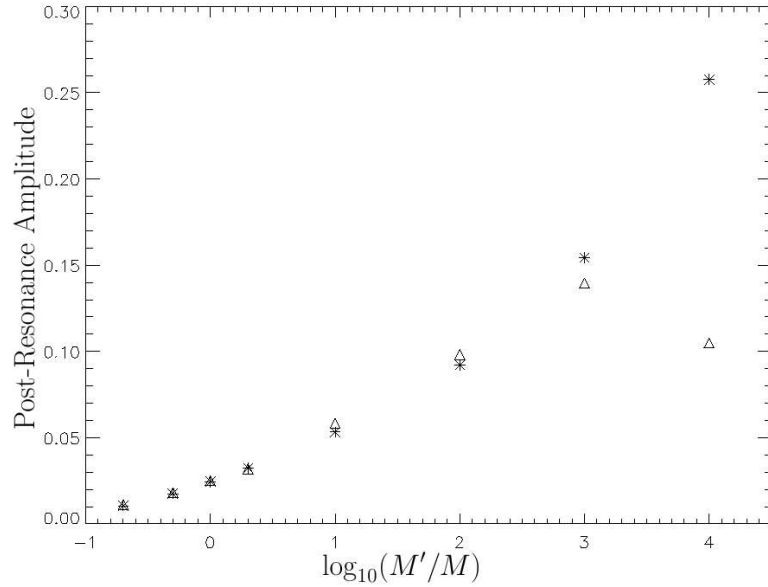


Figure 2.6: The average post-resonance amplitude $|b_\alpha|$ for the $n = 4$ mode given in Table I as a function of the mass of the binary companion. The post-resonance amplitude increases with the mass of the binary companion as predicted by the analytical estimate except for very high companion masses.

2.5 Analytic Estimate of the Resonant Mode Amplitude

Here we provide an analytic estimate of the mode amplitude attained during a resonance as well as the temporal duration of the resonance (i.e., the characteristic time during which the resonant mode receives most of its energy from the orbit).

For a WD oscillation mode with frequency ω_α , the resonant orbital radius is

$$D_\alpha = \left(\frac{m^2 M_t}{\omega_\alpha^2} \right)^{1/3}. \quad (2.30)$$

Prior to the resonance, as the orbital radius D decreases, the mode amplitude grows gradually according to equation (2.28). At the same time, the orbit also loses its energy to gravitational waves (GWs) at the rate

$$\dot{E}_{\text{GW}} = -\frac{32(MM')^2 M_t}{5c^5 D^5} = -\frac{MM'/2D}{t_D}, \quad (2.31)$$

where t_D is given by equation (2.10). We can define the beginning of resonance as the point where the orbital energy is transferred to the mode faster than it is radiated away by GWs. That is, the resonance begins at the radius $D = D_{\alpha+} (> D_\alpha)$, as determined by

$$\dot{E}_\alpha = |\dot{E}_{\text{GW}}|, \quad (2.32)$$

where E_α is the energy contained in the mode. Near the resonance, the mode oscillates at the frequency close to ω_α , so we can write the mode energy as $E_\alpha \simeq 2\omega_\alpha^2 b_\alpha^2$ (including both the $m = 2$ and $m = -2$ terms), assuming $\omega_\alpha \gg |\dot{b}_\alpha/b_\alpha|$. Thus we have $\dot{E}_\alpha \simeq 4\omega_\alpha^2 b_\alpha \dot{b}_\alpha$. Using equations (2.28) and (2.29) for b_α and \dot{b}_α , we find

$$\omega_\alpha^2 - (m\Omega)^2 = \left[\frac{24\omega_\alpha^4 M' (W_{lm} Q_\alpha)^2}{MD^5} \right]^{1/3} \text{ at } D = D_{\alpha+} \quad (2.33)$$

or

$$D_{\alpha+} = D_\alpha \left[1 + 0.436 \left(\frac{M'}{M} \right)^{1/3} \left(\frac{M_t}{M} \right)^{-5/9} \bar{\omega}_\alpha^{4/9} \bar{Q}_\alpha^{2/3} \right], \quad (2.34)$$

where we have used $l = m = 2$ and $\bar{\omega}_\alpha, \bar{Q}_\alpha$ are in dimensionless units where $G = M = R = 1$. The mode energy at $D = D_{\alpha+}$ is

$$E_\alpha(D_{\alpha+}) = 0.0701 \left(\frac{M'}{M} \right)^{4/3} \left(\frac{M_t}{M} \right)^{-8/9} \times \bar{\omega}_\alpha^{10/9} (W_{lm} \bar{Q}_\alpha)^{2/3} \frac{M^2}{R}. \quad (2.35)$$

Since for $D < D_{\alpha+}$, the orbital energy will be deposited into the mode much faster than it is being radiated away, we approximate that all the orbital energy between $D_{\alpha+}$ and D_α is transferred to the mode. Thus the mode energy increases by the amount

$$\Delta E_\alpha = 2 \times \left(\frac{MM'}{2D_\alpha} - \frac{MM'}{2D_{\alpha+}} \right), \quad (2.36)$$

where we have multiplied by a factor of two to account for the fact that energy is also deposited at a nearly equal rate before resonance as it is after resonance. Using equation (2.34), we find

$$\Delta E_\alpha = 0.2804 \left(\frac{M'}{M} \right)^{4/3} \left(\frac{M_t}{M} \right)^{-8/9} \times \bar{\omega}_\alpha^{10/9} (W_{lm} \bar{Q}_\alpha)^{2/3} \frac{M^2}{R}. \quad (2.37)$$

This is exactly four times of equation (2.35). Thus the maximum mode energy after resonance is $E_{\alpha,\max} = E_\alpha(D_{\alpha+}) + \Delta E_\alpha$, or

$$E_{\alpha,\max} \simeq 5.75 \times 10^{-4} \left(\frac{M'}{M} \right)^{4/3} \left(\frac{M_t}{M} \right)^{-8/9} \times \left(\frac{\bar{\omega}_\alpha}{0.2} \right)^{10/9} \left(\frac{\bar{Q}_\alpha}{10^{-3}} \right)^{2/3} \frac{M^2}{R}. \quad (2.38)$$

The corresponding maximum mode amplitude is

$$b_{\alpha,\max} \simeq 8.48 \times 10^{-2} \left(\frac{M'}{M} \right)^{2/3} \left(\frac{M_t}{M} \right)^{-4/9} \times \left(\frac{\bar{\omega}_\alpha}{0.2} \right)^{-4/9} \left(\frac{\bar{Q}_\alpha}{10^{-3}} \right)^{1/3}. \quad (2.39)$$

Figures 2.5 and 2.6 compare our numerical results with the analytical expressions (2.38)-(2.39). We find good agreement for all the WD resonant modes considered. Figure 2.5 verifies the dependence of $b_{\alpha,\max}$ on the mode frequency and the value of \bar{Q}_α , while figure 2.6 verifies the dependence of $b_{\alpha,\max}$ on the mass of the binary companion (except for the highest mass cases discussed below). Therefore equations (2.38) and (2.39) provide fairly accurate estimates of the mode amplitude and energy without performing numerical integrations.

For the very high companion masses ($M' \gtrsim 10^3 M$) shown in Figure 2.6, our analytical formula significantly overestimates the post-resonance amplitude. The reason for this is that the gravitational decay time scale is shorter if the companion is more massive. If the companion is massive enough, the orbit will decay through resonance due to gravitational radiation before the orbital energy of equation (2.37) can be deposited in the mode (see below). Consequently, the amplitude to which a mode is excited decreases if the mass of the companion becomes very high. Therefore our analytical formula overestimates the post-resonance amplitude for extremely massive companions. For any reasonable WD or NS masses, our analytical estimate is accurate, but for a super-massive black hole the estimate may become inaccurate.

It is interesting that the above analytical results for the resonant mode energy is independent of the gravitational wave damping time scale t_D , in contrast to the NS/NS or NS/BH binary cases. In fact, for the above derivation to be valid, the following four conditions must be satisfied at $D_{\alpha+}$:

$$(i) \quad \omega_\alpha \gg |\dot{b}_\alpha/b_\alpha|, \quad (2.40)$$

$$(ii) \quad \omega_\alpha^2 - (m\Omega)^2 \gg m\Omega, \quad (2.41)$$

$$(iii) \quad \omega_\alpha^2 - (m\Omega)^2 \gg 2m\Omega |\dot{b}_\alpha/b_\alpha|, \quad (2.42)$$

$$(iv) \quad \omega_\alpha^2 - (m\Omega)^2 \gg |\ddot{b}_\alpha/b_\alpha|. \quad (2.43)$$

Conditions (i) and (ii) both lead to

$$\omega_\alpha t_D \gg 3 \left[\frac{\omega_\alpha^2}{\omega_\alpha^2 - (m\Omega)^2} \right]; \quad (2.44)$$

condition (iii) gives

$$\omega_\alpha t_D \gg 6 \left[\frac{\omega_\alpha^2}{\omega_\alpha^2 - (m\Omega)^2} \right]^2; \quad (2.45)$$

and condition (iv) yields

$$\omega_\alpha t_D \gg \sqrt{18} \left[\frac{\omega_\alpha^2}{\omega_\alpha^2 - (m\Omega)^2} \right]^{3/2}. \quad (2.46)$$

In equations (2.44)-(2.46), the right-hand sides should be evaluated at $D_{\alpha+}$. Clearly, condition (iii) is most constraining. With

$$\begin{aligned} \frac{\omega_\alpha^2 - (m\Omega)^2}{\omega_\alpha^2} &= 3 \left(\frac{D_{\alpha+} - D_\alpha}{D_\alpha} \right) \\ &= 0.0064 \left(\frac{M'}{M} \right)^{1/3} \left(\frac{M_t}{M} \right)^{-5/9} \left(\frac{\bar{\omega}_\alpha}{0.2} \right)^{4/9} \left(\frac{\bar{Q}_\alpha}{10^{-3}} \right)^{2/3}, \end{aligned} \quad (2.47)$$

we see that condition (iii) is satisfied if

$$\begin{aligned} t_D &\gg 7.3 \times 10^5 \left(\frac{R^3}{GM} \right)^{1/2} \left(\frac{M'}{M} \right)^{-2/3} \left(\frac{M_t}{M} \right)^{10/9} \\ &\times \left(\frac{\bar{\omega}_\alpha}{0.2} \right)^{-17/9} \left(\frac{\bar{Q}_\alpha}{10^{-3}} \right)^{-4/3}. \end{aligned} \quad (2.48)$$

Since t_D is on the order of a thousand years or more for orbital frequencies comparable to WD g-modes, condition (iii) is always satisfied for WD/WD or WD/NS binaries. On the other hand, the conditions (i)-(iv) are not all satisfied for NS/NS or NS/BH binaries.

For very massive companions, the inequality of equation (2.48) may not hold. Using equation (2.10) for t_D , equation (2.48) implies (for $M_t/M \simeq M'/M$)

$$\begin{aligned} \frac{M'}{M} &\ll 5.5 \times 10^4 \left(\frac{\bar{\omega}_\alpha}{0.2} \right)^{-7/10} \left(\frac{\bar{Q}_\alpha}{10^{-3}} \right)^{6/5} \\ &\times \left(\frac{M}{M_\odot} \right)^{-9/4} \left(\frac{R}{10^4 \text{km}} \right)^{9/4}. \end{aligned} \quad (2.49)$$

The above inequality implies our estimates are valid for any feasible companion except a super-massive black hole.² We can also use this inequality to examine the inaccuracy of our estimate in the highest mass cases of Figure 2.6. Figure 2.6 was generated using the $n = 4$ mode parameters listed in Table 1 for a WD of $M = 0.6M_\odot$ and $R = 8.97 \times 10^3$ km. Plugging in these parameters, equation (2.49) requires

$$\frac{M'}{M} \ll 1.7 \times 10^3 \quad (2.50)$$

for our analytical estimates in Figure 2.6 to be accurate. This explains why the analytical estimates of Figure 2.6 are accurate when $M' \lesssim 1000M$ but diverge from the numerical results when $M' \gtrsim 1000M$.

Given the maximum mode amplitude reached during a resonance, we can now estimate the temporal duration of the resonance. Letting $a_\alpha = c_\alpha e^{-i\omega_\alpha t}$, the mode amplitude evolution equation (2.7) becomes

$$\ddot{c}_\alpha - 2i\omega_\alpha \dot{c}_\alpha = \frac{M' W_{lm} Q_\alpha}{D^3} e^{i\omega_\alpha t - im\Phi}. \quad (2.51)$$

Assuming that during the resonance, $\omega_\alpha - m\Omega \simeq 0$, the right-hand-side of equation (2.51) can be taken as a constant, we then have

$$\dot{c}_\alpha \simeq \frac{iM' W_{lm} Q_\alpha}{2\omega_\alpha D^3}, \quad (2.52)$$

i.e., the mode amplitude grows linearly in time. Thus, the duration of the resonance is

²Obviously, our estimate would not apply for a WD in a highly eccentric orbit around an intermediate mass black hole, which may form in dense clusters as described by Ivanov & Papaloizou (2007).

of order

$$\begin{aligned}
t_{\text{res}} &= \left| \frac{b_{\alpha, \text{max}}}{\dot{c}_{\alpha}} \right| \\
&\simeq 3.42 \left(\frac{M'}{M} \right)^{-1/3} \left(\frac{M_t}{M} \right)^{5/9} \bar{\omega}_{\alpha}^{-13/9} \bar{Q}_{\alpha}^{-2/3} \left(\frac{R^3}{M} \right)^{1/2} \\
&= 3.50 \times 10^3 \left(\frac{M'}{M} \right)^{-1/3} \left(\frac{M_t}{M} \right)^{5/9} \\
&\quad \times \left(\frac{\bar{\omega}_{\alpha}}{0.2} \right)^{-13/9} \left(\frac{\bar{Q}_{\alpha}}{10^{-3}} \right)^{-2/3} \left(\frac{R^3}{M} \right)^{1/2}. \tag{2.53}
\end{aligned}$$

Since the dynamical time $(R^3/GM)^{1/2}$ for typical WDs is on the order of one second, the resonance duration is typically an hour or longer. Note that the above estimate is formally valid only when $[\omega - m\Omega(D_{\alpha+})]t_{\text{res}} \ll 1$, so that we can set $\omega_{\alpha} - m\Omega \approx 0$ for the duration of the resonance. Using equations (2.47) and (2.53), we find $[\omega_{\alpha} - m\Omega(D_{\alpha+})]t_{\text{res}} \approx 1$ for typical parameters. Thus we should consider equation (2.53) as an order-of-magnitude estimate only. Also, we can check that the GW energy loss during the resonance, $\Delta E_{\text{gw}} \simeq (MM'/2D_{\alpha})(t_{\text{res}}/t_D)$, is much less than $E_{\alpha, \text{max}}$, justifying our derivation of $E_{\alpha, \text{max}}$ given by equation (2.38). Indeed, the above condition simplifies to equation 2.49, since in both cases it is the energy carried away by gravitational waves that is limiting the mode growth.

We can use the same method to solve for the size of the fluctuations in mode amplitude after resonance. Due to the symmetry of the harmonic oscillator, the fluctuation in mode amplitude about the mean value after the resonance is identical to the zeroth-order estimate of the mode amplitude before resonance [see eq. (2.28)], i.e.,

$$\Delta a \approx \frac{M' W_{lm} Q_{\alpha}}{D^{l+1} (m^2 \Omega^2 - \omega_{\alpha}^2)}. \tag{2.54}$$

These fluctuations occur with frequency $m\Omega - \omega_{\alpha}$, since this is the difference in frequency between the eigenfrequency at which the WD is oscillating and the orbital forcing frequency. So, as the orbital frequency continues to increase after the resonance,

the amplitude of the fluctuations becomes smaller while the frequency of the amplitude oscillations becomes higher.

2.6 Effect of Mode Damping

The results in the previous two sections neglect mode energy damping in the WD. Since the duration of the resonance is much longer than the mode period [see equation (2.53)], internal mode damping could affect the energy transfer during resonance if the damping rate is sufficiently large. To address this issue, we incorporate a phenomenological damping rate $-\gamma_\alpha \omega_\alpha \dot{a}_\alpha$ to the mode equation (2.7) to study how mode damping affects energy transfer during a resonance. Figure 2.7 shows the excitation of a mode through resonance for different values of γ_α . We see that, as expected, when the internal damping time is larger than the resonance duration (equation 2.53), the maximum mode energy achieved in a resonance is unaffected.

G-modes in white dwarfs are damped primarily by radiative diffusion. For sufficiently large mode amplitudes, non-linear damping is also important (e.g., Kumar & Goodman 1996; see section 2.7 for more discussion on this issue). Wu (1998) presents estimates for the non-adiabatic radiative damping rates of WD g-modes in terms of $\omega_i = \gamma \omega_r$. Extrapolating Wu’s values to $l = 2$ modes for a white dwarf of temperature $T = 10800$ K, we find $\gamma \sim 10^{-11}$ for modes near $n = 1$ and $\gamma \sim 10^{-4}$ for high-order modes with $n \gtrsim 20$. So, while the maximum amplitude of low-order modes is completely unaffected by non-adiabatic effects, high-order modes will damp on time scales similar to the excitation time scale. Therefore these high-order modes will attain amplitudes somewhat smaller than estimated in the previous section. This continual process of high-order mode damping may extract energy out of the orbit more efficiently than

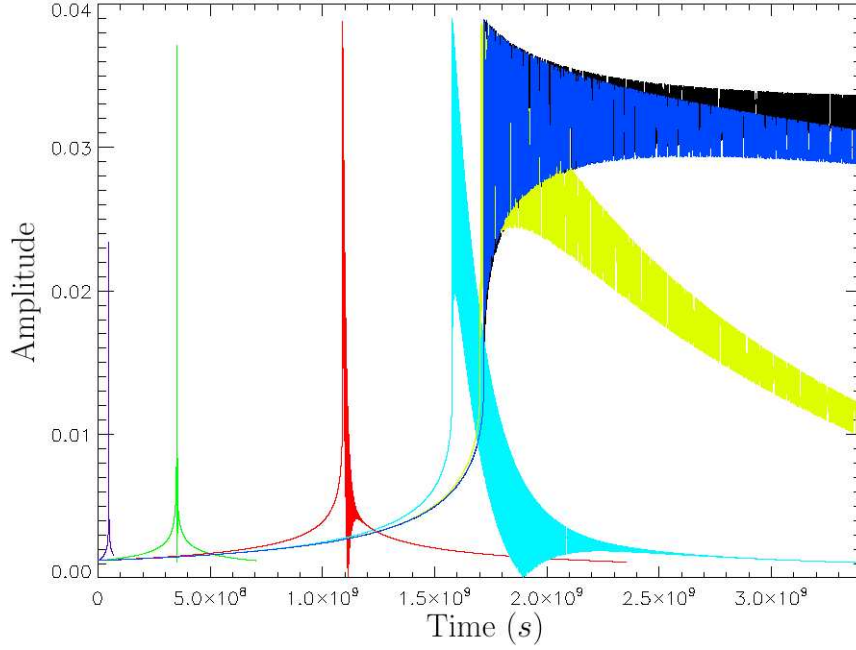


Figure 2.7: The amplitude of a mode as a function of time near its resonance for different values of the damping coefficient γ_α . The curves have $\gamma_\alpha = 0$ (black), $\gamma_\alpha = 10^{-9}$ (dark blue), $\gamma_\alpha = 10^{-8}$ (yellow-green), $\gamma_\alpha = 10^{-7}$ (light blue), $\gamma_\alpha = 10^{-6}$ (red), $\gamma_\alpha = 10^{-5}$ (green), and $\gamma_\alpha = 10^{-4}$ (purple). For this mode, we have set $\omega_\alpha = 0.1\text{s}^{-1}$ and $Q_\alpha = 1 \times 10^{-4}$ so that $t_{\text{res}} \approx 10^5\text{s}$. Note that the damping term does not greatly affect the maximum mode amplitude except when $\gamma_\alpha \gtrsim 10^{-4}$, or when $\gamma_\alpha \omega_\alpha t_{\text{res}} \gtrsim 1$. Also note that modes with larger values of γ_α evolve on a much shorter time scale because their orbits decay quickly due to the conversion of orbital energy into heat via mode damping.

discrete resonance events, causing a steady decay of the binary's orbit.

2.7 Discussion

We have shown that during the orbital decay of compact white dwarf binaries (WD/WD, WD/NS or WD/BH), a series of g-modes can be tidally excited to large amplitudes (up to 0.1 in dimensionless units) as the orbital frequency sweeps through the resonant mode frequencies. Such mode excitations can significantly affect the orbital decay rate near resonance. Indeed, to properly calculate the resonant mode amplitude, it is necessary

to take into account of the back-reaction of the excited modes on the orbit. One consequence of the resonant mode excitations is that the low-frequency ($\lesssim 10^{-2}$ Hz) gravitational waveforms emitted by the binary, detectable by LISA, will deviate significantly from the point-mass binary prediction. This is in contrast to the case of neutron star binaries (NS/NS or NS/BH) studied previously (Reisenegger & Goldreich 1994; Lai 1994; Shibata 1994; Ho & Lai 1999; Lai & Wu 2006; Flanagan & Racine 2006), where the resonant mode amplitude is normally too small to affect the binary orbital decay rate and the gravitational waveforms to be detected by ground-based gravitational wave detectors such as LIGO and VIRGO.

In the case of WD binaries studied in this paper, the number of of orbits skipped as a result of a resonant mode excitation is

$$\Delta N_{\text{orb}} = \frac{t_D}{P_{\text{orb}}} \frac{E_{\alpha, \text{max}}}{E_{\text{orb}}}, \quad (2.55)$$

where t_D is the gravitational wave decay time scale given in equation (2.10), P_{orb} is the orbital period, and E_{orb} is the orbital energy at resonance. Using equation (2.38) for $E_{\alpha, \text{max}}$, we find

$$\Delta N_{\text{orb}} = 3.4 \times 10^6 \left(\frac{M_{\odot}^{17}}{M^9 M'^6 M_t^2} \right)^{1/9} \left(\frac{R}{10^4 \text{km}} \right)^{2/3} \left(\frac{\bar{Q}_{\alpha}}{10^{-3}} \right)^{2/3} \left(\frac{\Omega}{0.1 \text{s}^{-1}} \right)^{-11/9}. \quad (2.56)$$

The number of skipped orbital cycles should be compared to the number of orbits in a decay time, expressed by

$$\begin{aligned} \frac{dN_{\text{orb}}}{d \ln \Omega} &= \frac{1}{3\pi} \Omega t_D \\ &= 3.3 \times 10^8 \left(\frac{M_{\odot}^2}{MM'} \right) \left(\frac{M_t}{2M_{\odot}} \right)^{1/3} \left(\frac{\Omega}{0.1 \text{s}^{-1}} \right)^{-5/3}. \end{aligned} \quad (2.57)$$

The huge number of skipped orbital cycles implies that such a resonant interaction would be important, but because the number of skipped orbital cycles is much smaller

than the number of orbital cycles in a decay time, resonances will not dominate the decay process.

A second possible consequence of resonant mode excitations is that the large mode energy may lead to significant heating of the white dwarf prior to the binary merger. Indeed, equation (2.38) shows that for typical binary parameters, the mode energy can be a significant fraction ($\sim 10^{-4}$ – 10^{-3}) of the gravitational binding energy of the star, and comparable to the thermal energy. Indeed, the thermal energy of the WD is of order $E_{\text{th}} \approx \frac{MkT_c}{Am_p}$, where T_c is the core temperature of the WD and A is the mean atomic weight. The ratio of post-resonance mode energy to thermal energy is then

$$\frac{E_{\alpha,\text{max}}}{E_{\text{th}}} \approx 1.7 \left(\frac{M'}{M} \right)^{4/3} \left(\frac{M_t}{M} \right)^{-8/9} \left(\frac{\bar{\omega}_\alpha}{0.2} \right)^{10/9} \times \left(\frac{\bar{Q}_\alpha}{10^{-3}} \right)^{2/3} \left(\frac{10^7 \text{ K}}{T_c} \right) \left(\frac{M}{M_\odot} \right) \left(\frac{10^4 \text{ km}}{R} \right). \quad (2.58)$$

This implies that the white dwarf may become bright thousands of years before the binary merger.

A third consequence that may result from a resonance is significant spin-up of the WD. If we assume that all the angular momentum transferred to the WD during a resonance eventually manifests as rigid body rotation of the WD, the change in spin frequency of the WD is

$$\Delta\Omega_s = \frac{E_{\alpha,\text{max}}}{I\Omega}, \quad (2.59)$$

where Ω_s is the spin frequency of the WD and I is its moment of inertia. Plugging in our expression for $E_{\alpha,\text{max}}$, we find

$$\Delta\Omega_s = 0.29 \left(\frac{0.2}{\kappa} \right) \left(\frac{M'}{M} \right)^{4/3} \left(\frac{M_t}{M} \right)^{-8/9} \times \left(\frac{\bar{\omega}_\alpha}{0.2} \right)^{-8/9} \left(\frac{\bar{Q}_\alpha}{10^{-3}} \right)^{2/3} \Omega, \quad (2.60)$$

where $\kappa = I/(MR^2) \approx 0.2$. We can thus see that a given resonance may deposit enough angular momentum to completely spin up the WD (or significantly alter its spin) by

the time the mode damps out. This implies that mode resonances are potentially very important in the spin synchronization process.

However, before these implications can be taken seriously, one should be aware of the limitations of the present study. One issue is the assumption that the white dwarf is non-rotating (and not synchronized), already commented on in section 1. More importantly, we have assumed that the white dwarf oscillations can be calculated in the linear regime. While the mass-averaged dimensionless amplitude $|a_\alpha| = |b_\alpha|$ of the excited g-modes are less than 0.1 [see Fig. 5 and Eq. (2.39)], the physical fluid displacements in the stellar envelope are much larger since g-modes of white dwarfs are mainly concentrated in the outer, non-degenerate layers. Figure 2.8 gives some examples: it shows the horizontal and radial displacements of three modes at their post-resonance amplitudes. These are obtained from $\xi = a_\alpha \xi_\alpha$, with ξ_α the normalized eigenfunction (see section 2.3) and a_α computed from equation (2.39) with $M' = M$. In general, the linear approximation is valid only if $|\xi| \ll |k_r|^{-1}$, where k_r is the WKB wave number, given by

$$k_r^2 \simeq \frac{l(l+1)(N^2 - \omega^2)}{\omega^2 r^2}. \quad (2.61)$$

Clearly, the three modes depicted in Fig. 8 strongly violate the linear approximation beyond the radius $r \approx 0.85R$, near the jump in N^2 associated with the carbon-helium boundary.

Therefore, the results presented in this paper should be treated with caution as non-linear effects will likely limit mode growth. Rather than increasing to the large displacements shown in Figure 2.8, the white dwarf oscillations will undergo non-linear processes such as mode coupling that will transfer energy to high-order modes. These high-order modes have much shorter wavelengths and thus damp on very short time scales. As non-linearity is most important in the outer layers of the white dwarf, we expect that excited oscillations will dissipate their energy preferentially in the outer layers

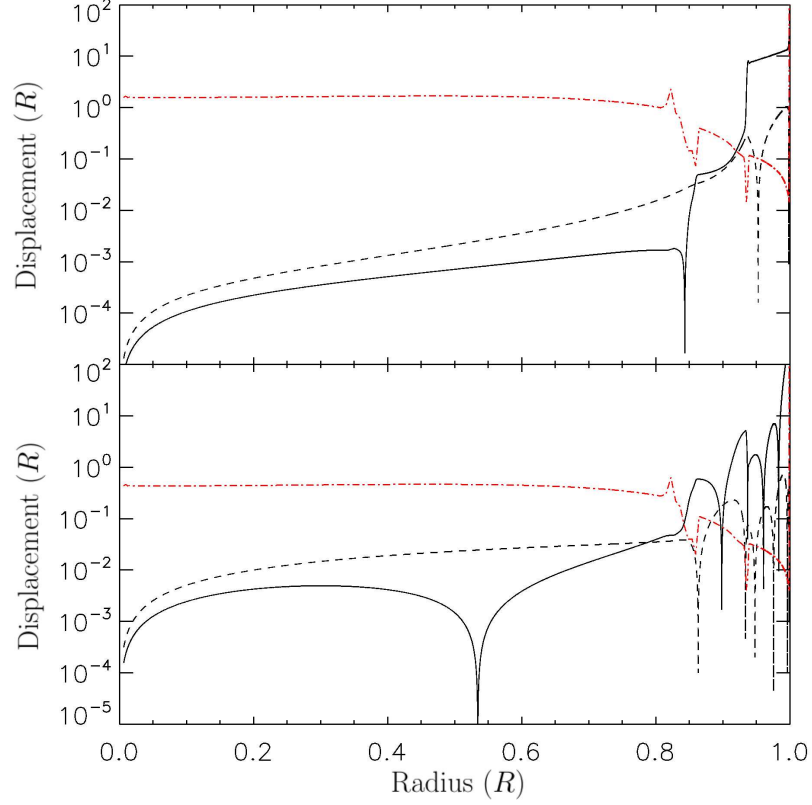


Figure 2.8: The horizontal (solid line) and radial (dashed line) displacements of the $n = 1$ (top panel) and $n = 5$ (bottom panel) modes as a function of radius. The physical displacements are calculated using the analytical estimates for the post-resonance amplitudes given in equation 2.39 using $M = M'$, giving $|a_1| = 0.0566$ and $|a_5| = 0.0695$. Also shown is inverse of the WKB wave number $1/k_r$ (dotted line).

and will not reflect back into the stellar interior. We plan to address these issues in our next paper (Fuller & Lai 2012).

CHAPTER 3

DYNAMICAL TIDES IN COMPACT WHITE DWARF BINARIES: TIDAL SYNCHRONIZATION AND DISSIPATION

3.1 Introduction¹

Compact white dwarf (WD) binary systems (with orbital periods in the range of minutes to hours) harbor many interesting and unanswered astrophysical questions. An increasing number of such systems are being discovered by recent surveys (e.g. Mullally et al. 2009; Kulkarni & van Kerkwijk 2010; Steinfadt et al. 2010; Kilic et al. 2011; Brown et al. 2011; see Marsh 2011 for a review). The orbits of these systems decay via the emission of gravitational waves, which could be detected by the planned *Laser Interferometer Space Antenna (LISA)* (Nelemans 2009). Depending on the WD masses and the physics of the merger process, these merging WD systems may produce single helium-rich sdO/sdB stars, giant stars (R CrB stars), stable mass transfer AM CVn binaries, or possibly underluminous supernovae. Most importantly, compact WD binaries in which the total mass is near the Chandrasekhar limit are thought to be the probable progenitors of type Ia supernovae upon a stellar merger at the end of the orbital decay process (Webbink 1984; Iben & Tutukov 1984). Recent studies have provided support for this “double degenerate” scenario (e.g., Gilfanov & Bogdan 2010; Di Stefano 2010; Maoz et al. 2010) and even sub-Chandrasekhar WD mergers may lead to type Ia supernovae (van Kerkwijk et al. 2010).

Prior to merger, tidal interactions may affect the properties of the binary WDs and their evolutions, including the phase evolution of the gravitational waves. Previous studies have focused on equilibrium tides (e.g., Iben et al. 1998; Willems et al. 2010), cor-

¹This chapter is based on Fuller & Lai (2012B).

responding to quasi-static deformation of the star. Such equilibrium tides are unlikely to play a role in the tidal synchronization/dissipation process. Iben et al. (1998) estimated the effect of tidal heating in the WD based on the assumption that the (spherically averaged) local heating rate is equal to the rate of rotational energy deposition required to maintain synchronization. They suggested that the binary WDs may brighten by several magnitudes before merger.

In fact, in a compact WD binary, as the orbital decay rate due to gravitational wave radiation increases rapidly with decreasing orbital period, it is not clear if tidal effects are sufficiently strong to drive the binary system toward synchronous rotation. The critical orbital period for synchronization is unknown. For this reason, the majority of recent WD merger simulations (e.g., Segretain et al. 1997; Loren-Aguilar et al. 2009; Pakmor et al. 2010,2011) have assumed the merging WDs to be non-synchronized prior to merger. However, whether the WDs are spin-synchronized may affect the merger product and the possible supernova signature: for example, the strong velocity shear between the stars upon contact would be significantly reduced for the merger of a synchronized binary. The degree of synchronization also determines the tidal luminosity of the binary prior to merger. Indeed, it is possible that tidal dissipation contributes significantly to the brightness of some of the recently observed WD binaries (e.g., Brown et al. 2011).

In a recent paper (Fuller & Lai 2011, hereafter Paper I), we used linear theory to calculate the excitation of discrete gravity modes in a WD due to the tidal gravitational field of a compact companion star (a WD, neutron star or black hole). The existence of discrete modes requires that gravity waves be reflected near the surface of the WD. In this case, tidal energy and angular momentum is transferred only near a mode resonance, when the g-mode frequency σ_α equals 2Ω (where Ω is the orbital frequency). Our calculations showed that while the dimensionless (mass-weighted) amplitude of the

resonantly excited g-mode is not extremely non-linear (it approaches ≈ 0.1), the displacement associated with the mode becomes large in the outer layer of the WD where the density is low. In other words, while the mode does not reach a non-linear amplitude in the bulk interior of the star, it becomes very non-linear in the outer layers even before resonance. We concluded that tidally excited gravity waves are likely to continually damp in the outer layer of the WD, preventing the formation of discrete modes. A proper treatment of dynamical tides in binary WDs must take account of this continuous wave damping.

In this paper, we calculate the tidal excitation of gravity waves in binary WDs assuming that the waves are efficiently damped in the WD envelope. To this end, we implement an outgoing wave boundary condition near the WD surface. Unlike gravity modes (which have a set of discrete eigenfrequencies), the outgoing wave boundary condition permits the excitation of gravity waves at all frequencies, and thus allows for a continuous process of tidal dissipation. Similar calculations have been implemented for early-type stars (Zahn 1975, 1977; Goldreich & Nicholson 1989) and solar-type stars (Goodman & Dickson 1998; Ogilvie & Lin 2007). In early-type stars, gravity waves are excited at the boundary between the convective core and radiative envelope, propagate outwards and dissipate in the outer envelope. In solar-type stars, gravity waves are similarly excited at the interface between the radiative core and convective envelope, but propagate inward before dissipating (via non-linear wave breaking) near the center of the star (Barker & Ogilvie 2010, 2011). Unlike main-sequence stars, WDs do not contain a simple two-zone structure of convective and radiative regions, and it is not clear how and to what extent gravity waves are excited. The outgoing wave outer boundary condition allows us to calculate the rate at which energy and angular momentum are transferred to the WD as a function of orbital period. We can then calculate the orbital period at which tidal effects can compete with orbital decay due to gravitational radi-

ation. At this orbital period, the synchronization process can begin. Furthermore, by scaling our results to rotating WDs, we can determine the WD spin period and energy dissipation rate at any orbital period.

This paper is organized as follows. In Sections 3.2-3.4 we derive the basic equations for tidally forced stellar oscillations, the boundary conditions and the tidal angular momentum and energy transfer rates. In Section 3.5 we discuss our numerical method and present several test calculations, where we emphasize the importance of using a self-consistent stellar model in order to obtain reliable amplitudes for tidally excited gravity waves. In Section 3.6 we present our numerical calculations of wave excitation for realistic WD models. Since our numerical results reveal a complicated dependence of the tidal energy transfer rate on the tidal frequency, we examine a simple semi-analytic model in Section 3.7 to shed light on the mechanism of gravity wave excitation. In Section 3.8 we use the results of previous sections to study the long-term spin-orbit evolution of WD binaries, including spin synchronization, the tidal effect on the low-frequency gravitational radiation waveforms and tidal heating of the WDs. We conclude in Section 3.9 with a discussion of theoretical uncertainties and future work.

3.2 Basic Equations

The dynamical tide of the WD (mass M) is driven by the external gravitational potential of the companion (mass M'). The leading order (quadrupole) potential is

$$U_{\text{ex}}(\mathbf{r}, t) = U(r) \left[Y_{22}(\theta, \phi) e^{-i\omega t} + Y_{22}^*(\theta, \phi) e^{i\omega t} \right] \quad (3.1)$$

with

$$U(r) = -\frac{GM'W_{22}}{a^3} r^2. \quad (3.2)$$

Here a is the orbital separation, $\omega = 2\Omega$ is the tidal frequency for a non-spinning WD (we will account for the spin effect in Section 3.8), Ω is the orbital frequency, and $W_{22} = \sqrt{3\pi/10}$. The actual fluid perturbations in the WD can be written as $\xi_{\text{ac}}(\mathbf{r}, t) = \xi(\mathbf{r}, t) + \xi^*(\mathbf{r}, t)$ for the Lagrangian displacement and $\delta P_{\text{ac}}(\mathbf{r}, t) = \delta P(\mathbf{r}, t) + \delta P^*(\mathbf{r}, t)$ for the Eulerian pressure perturbation, and similarly for other quantities. In the following, we shall consider perturbations (ξ , δP , etc.) driven by the potential $U(\mathbf{r}, t) = U(r)Y_{22}(\theta, \phi)e^{-i\omega t}$. We shall adopt the Cowling approximation (so that the gravitational potential perturbation $\delta\Phi$ associated with the density perturbation is neglected, i.e., $\delta\Phi = 0$), which is valid for gravity waves in the star. We will consider adiabatic oscillations, for which the Lagrangian perturbations in pressure and density are related by $\Delta P = a_s^2 \Delta\rho$, where a_s is the adiabatic sound speed. This is a good approximation in the bulk of the star where the thermal time is much longer than the wave period.

Letting

$$\delta P(\mathbf{r}, t) = \delta P(r)Y_{22}(\theta, \phi)e^{-i\omega t}, \quad (3.3)$$

and

$$\xi(\mathbf{r}, t) = [\xi_r(r)\hat{r} + \xi_\perp(r)r\nabla_\perp]Y_{22}(\theta, \phi)e^{-i\omega t}, \quad (3.4)$$

the fluid perturbation equations reduce to

$$\frac{1}{r^2}(r^2\xi_r)' - \frac{g}{a_s^2}\xi_r + \frac{1}{\rho a_s^2}\left(1 - \frac{L_l^2}{\omega^2}\right)\delta P - \frac{l(l+1)U}{\omega^2 r^2} = 0, \quad (3.5)$$

and

$$\frac{1}{\rho}\delta P' + \frac{g}{\rho a_s^2}\delta P + (N^2 - \omega^2)\xi_r + U' = 0, \quad (3.6)$$

where the $'$ denotes d/dr . In equations (3.5) and (3.6), L_l and N are the Lamb and Brünt-Vaisälä frequencies, respectively, given by [note we will continue to use the notations L_l , $l(l+1)$, and m , although we focus on $l = m = 2$ in this paper]

$$L_l^2 = \frac{l(l+1)a_s^2}{r^2} \quad (3.7)$$

and

$$N^2 = g^2 \left(\frac{d\rho}{dP} - \frac{1}{a_s^2} \right). \quad (3.8)$$

The other perturbation variables are related to δP and ξ_r by

$$\xi_\perp = \frac{1}{r\omega^2} \left(\frac{\delta P}{\rho} + U \right), \quad (3.9)$$

$$\delta\rho = \frac{1}{a_s^2} \delta P + \frac{\rho N^2}{g} \xi_r. \quad (3.10)$$

Defining $Z = \chi^{-1/2} r^2 \xi_r$, where

$$\chi = \frac{r^2}{\rho a_s^2} \left(\frac{L_l^2}{\omega^2} - 1 \right), \quad (3.11)$$

equations (3.5) and (3.6) can be combined to yield

$$Z'' + k^2(r)Z = V(r). \quad (3.12)$$

Here,

$$\begin{aligned} k^2(r) = & \frac{\chi \rho (N^2 - \omega^2)}{r^2} + \frac{1}{2} \left(\frac{\chi'}{\chi} \right)' - \frac{1}{4} \left(\frac{\chi'}{\chi} \right)^2 \\ & + \frac{g}{a_s^2} \left[\frac{-(g/a_s^2)'}{g/a_s^2} + \frac{\chi'}{\chi} - \frac{g}{a_s^2} \right] \end{aligned} \quad (3.13)$$

and

$$V(r) = \chi^{-1/2} \left[\frac{l(l+1)}{\omega^2} \left(\frac{-\chi'}{\chi} + \frac{g}{a_s^2} \right) + \frac{2r}{a_s^2} \right] U. \quad (3.14)$$

In the WKB limit $|k| \gg 1/H$ and $|k| \gg 1/r$, where $H = |P/P'| \simeq a_s^2/g$ is the pressure scale height, equation (3.13) simplifies to

$$k^2(r) = \frac{1}{a_s^2 \omega^2} (L_l^2 - \omega^2)(N^2 - \omega^2). \quad (3.15)$$

This is the standard WKB dispersion relation for non-radial stellar oscillations (e.g., Unno et al. 1989). For $\omega^2 \ll L_l^2$ and $\omega^2 \ll N^2$, the wave equation (3.12) reduces to

$$Z'' + \frac{l(l+1)(N^2 - \omega^2)}{r^2 \omega^2} Z \simeq -\chi^{-1/2} \frac{l(l+1)N^2}{\omega^2} \frac{U}{g}. \quad (3.16)$$

Then, as long as $|Z''/Z| \gg |\chi''/\chi|$ (which we expect to be true because $Z'' \approx -k^2 Z$ and $\chi'' \sim \chi/H^2$), equation (3.16) is identical to the oscillation equations used by Zahn (1975) and Goodman & Dickson (1998).

3.3 Boundary Conditions

Equations (3.5) and (3.6) or equation (3.12) can be solved with the appropriate boundary conditions at $r = r_{\text{out}}$ near the stellar surface and at $r = r_{\text{in}} \rightarrow 0$ at the center of the star. The general solution of equation (3.12) can be written as

$$Z(r) = c_+ Z_+(r) + c_- Z_-(r) + Z^{\text{eq}}(r), \quad (3.17)$$

where c_+ , c_- are constants. $Z_+(r)$ and $Z_-(r)$ are two independent solutions of the homogeneous equation $Z'' + k^2 Z = 0$, and $Z^{\text{eq}}(r)$ represents a particular solution of equation (3.12). We choose the outer boundary r_{out} to be in the wave zone ($k^2 > 0$). If $k^2(r)$ varies slowly such that $|k'/k| \ll k > 0$, then the two independent WKB solutions to the homogeneous equation are

$$Z_{\pm}(r) = \frac{1}{\sqrt{k}} \exp\left(\pm i \int_{r_o}^r k dr\right), \quad (3.18)$$

where r_o is an interior point ($r_o < r_{\text{out}}$). For $\omega^2 \ll L_t^2$, the WKB wave dispersion relation [equation (3.15)] reduces to $\omega^2 = N^2 k_{\perp}^2 / (k^2 + k_{\perp}^2)$, where $k_{\perp}^2 = l(l+1)/r^2$, which implies that the radial component of the group velocity is $-\omega k / (k^2 + k_{\perp}^2)$. Thus, with $\omega > 0$ and $k > 0$, $Z_- \propto e^{-i \int_{r_o}^r k dr}$ represents an outgoing wave, while $Z_+ \propto e^{i \int_{r_o}^r k dr}$ represents an ingoing wave. An approximate particular solution of equation (3.12) is

$$Z^{\text{eq}}(r) \simeq \frac{V}{k^2} - \frac{1}{k^2} \left(\frac{V}{k^2} \right)'', \quad (3.19)$$

where the second term is smaller than the first by a factor of $(kH)^2$ or $(kr)^2$. This represents the “non-wave” equilibrium solution.²

Throughout this paper, we adopt the radiative condition at the outer boundary ($r = r_{\text{out}}$), i.e., we require that only an outgoing wave exists:

$$Z(r) \simeq Z^{\text{eq}}(r) + \frac{c_-}{\sqrt{k}} \exp\left(-i \int_{r_o}^r k dr\right). \quad (3.20)$$

This implicitly assumes that waves propagating toward the WD surface are completely damped by radiative diffusion (Zahn 1975) or by non-linear processes. We will check this assumption a posteriori from our numerical results (see Section 3.6.5). Thus, near the outer boundary, the radial displacement ξ_r behaves as (for $\omega^2 \ll L_l^2$)

$$\begin{aligned} \xi_r(r) &= \frac{\chi^{1/2}}{r^2} Z(r) \\ &= \xi_r^{\text{eq}}(r) + \frac{c_-}{\sqrt{\rho r^2 (N^2 - \omega^2)}} \exp\left(-i \int_{r_o}^r k dr\right). \end{aligned} \quad (3.21)$$

Here ξ_r^{eq} represents the equilibrium tide

$$\xi_r^{\text{eq}} \simeq \left(-\frac{U}{g}\right) \frac{N^2}{N^2 - \omega^2} \left[1 - \frac{2gr}{l(l+1)a_s^2} \frac{\omega^2}{N^2}\right], \quad (3.22)$$

where we have retained only the first term of equation (3.19). For $\omega^2 \ll N^2$, this further simplifies to $\xi_r^{\text{eq}} \simeq -U/g$ (Zahn 1975). The constant c_- specifies the amplitude of the outgoing wave which is eventually dissipated in the stellar envelope; this is the constant we wish to determine from numerical calculations.

In practice, to implement equation (3.21) at the outer boundary, we require a very accurate calculation of the non-wave solution ξ_r^{eq} . This can become problematic when the conditions $|k| \gg 1/H$ and $\omega \ll L_l$ are not well satisfied. Since the transverse displacement ξ_\perp for gravity waves is much larger than the radial displacement in the

²Note that the equilibrium tide usually refers to the f-mode response of the star to the tidal force. Here, we use the term “equilibrium” to refer to the “non-wave” solution.

wave zone, it is more convenient to use ξ_\perp in our outer boundary condition. We define

$$Z_1(r) = \left(\frac{\rho}{D}\right)^{1/2} r^2 \omega^2 \xi_\perp(r), \quad (3.23)$$

with $D \equiv N^2 - \omega^2$. Equations (3.5) and (3.6) can be rearranged to yield

$$Z_1'' + k_1^2(r) Z_1 = V_1(r), \quad (3.24)$$

where

$$\begin{aligned} k_1^2(r) = & -\frac{1}{4} \left[\left(\ln \frac{\rho r^2}{D} \right)' \right]^2 - \frac{1}{2} \left(\ln \frac{\rho r^2}{D} \right)'' - \left(\frac{N^2}{g} \right)' \\ & - \frac{N^2}{g} \left(\ln \frac{r^2}{D} \right)' + \frac{\omega^2}{a_s^2} + \frac{l(l+1)D}{r^2 \omega^2} \end{aligned} \quad (3.25)$$

and

$$\begin{aligned} V_1(r) = & -\left(\frac{\rho r^2}{D}\right)^{1/2} \times \\ & \left\{ \frac{N^2}{g} U \left[\ln \left(\frac{r^2 N^2}{D g} U \right) \right]' - \frac{\omega^2}{a_s^2} U \right\}. \end{aligned} \quad (3.26)$$

For $k_1 \gg 1/H$ and $\omega^2 \ll L_l^2$, the functions $k_1^2(r)$ and $V_1(r)$ simplify to

$$k_1^2(r) \simeq \frac{l(l+1)(N^2 - \omega^2)}{\omega^2 r^2} \quad (3.27)$$

and

$$V_1(r) \simeq -\left(\frac{\rho r^2}{D}\right)^{1/2} \frac{D}{r^2} \left(\frac{U r^2 N^2}{g D} \right)'. \quad (3.28)$$

Again, adopting the radiative boundary condition at $r = r_{\text{out}}$, we have

$$Z_1(r) \simeq \frac{V_1}{k_1^2} - \frac{1}{k_1^2} \left(\frac{V_1}{k_1^2} \right)'' + \frac{c_-}{k_1} \exp \left(-i \int_{r_o}^r k_1 dr \right), \quad (3.29)$$

where c_- is a constant. Thus, the transverse displacement $\xi_\perp(r)$ behaves as

$$\begin{aligned} \xi_\perp(r) = & \left(\frac{D}{\rho}\right)^{1/2} \frac{1}{r^2 \omega^2} Z_1(r) \\ = & \xi_\perp^{\text{eq}} + c_- \left(\frac{k_1}{\rho r^2}\right)^{1/2} \exp \left(-i \int_{r_o}^r k_1 dr \right), \end{aligned} \quad (3.30)$$

where several constants have been absorbed into c_- . The equilibrium tidal transverse displacement $\xi_{\perp}^{\text{eq}}(r)$ is given by

$$\xi_{\perp}^{\text{eq}}(r) \simeq -\frac{1}{l(l+1)r} \left(\frac{Ur^2}{g} \frac{N^2}{D} \right)'. \quad (3.31)$$

For $\omega^2 \ll N^2$, this reduces to (for $l = 2$)

$$\xi_{\perp}^{\text{eq}}(r) \simeq -\frac{1}{6r} \left(\frac{Ur^2}{g} \right)', \quad (3.32)$$

in agreement with Goldreich & Nicholson (1989). Thus, we implement the radiative boundary condition at $r = r_{\text{out}}$ as

$$\left(\xi_{\perp} - \xi_{\perp}^{\text{eq}} \right)' = \left[\frac{-(\rho r^2/k_1)'}{2(\rho r^2/k_1)} - ik_1 \right] (\xi_{\perp} - \xi_{\perp}^{\text{eq}}), \quad (3.33)$$

with ξ_{\perp} computed from ξ_r and δP using equation (3.9).

The inner boundary condition can be found by requiring the radial displacement to be finite at the center of the star. This requires

$$\xi_r = \frac{l}{\omega^2 r} \left(\frac{\delta P}{\rho} + U \right) \quad (\text{Near } r = 0). \quad (3.34)$$

3.4 Angular Momentum and Energy Flux

As the wave propagates through the star, it carries an angular momentum flux to the outer layers. At any radius within the star, the z component of the time-averaged angular momentum flux is

$$J_z(r) = \left\langle \oint d\Omega r^2 \rho (\delta v_r + \delta v_r^*) (\delta v_{\phi} + \delta v_{\phi}^*) r \sin \theta \right\rangle, \quad (3.35)$$

where $\langle \dots \rangle$ implies time averaging. With

$$\delta v_r = -i\omega \xi_r(r) Y_{lm} e^{-i\omega t} \quad (3.36)$$

and

$$\delta v_\phi = -i\omega \xi_\perp(r) r \nabla_\phi Y_{lm} e^{-i\omega t} = \frac{m\omega \xi_\perp(r)}{\sin \theta} Y_{lm} e^{-i\omega t}, \quad (3.37)$$

we find

$$\begin{aligned} J_z(r) &= 2 \oint d\Omega r^3 \rho \omega^2 \text{Re} \left[i \xi_r^*(r) Y_{lm}^* m \xi_\perp(r) Y_{lm} \right] \\ &= 2m\omega^2 \rho r^3 \text{Re} \left(i \xi_r^* \xi_\perp \right). \end{aligned} \quad (3.38)$$

In the wave zone, the fluid displacement consists of an equilibrium (“non-wave”) component and a dynamical (wave) component, $\xi = \xi^{\text{eq}} + \xi^{\text{dyn}}$. Since the equilibrium tide component is purely real (assuming negligible dissipation of the equilibrium tide), $\text{Re}(i \xi_r^{\text{eq}*} \xi_\perp^{\text{eq}}) = 0$, and the equilibrium tide does not contribute to angular momentum transfer. The cross terms $\text{Re}(i \xi_r^{\text{dyn}*} \xi_\perp^{\text{eq}})$, and $\text{Re}(i \xi_r^{\text{eq}*} \xi_\perp^{\text{dyn}})$ are opposed by a nearly equal and opposite Reynold’s stress term (see Goldreich & Nicholson 1989) and do not contribute significantly to angular momentum transfer. Thus, the $\text{Re}(i \xi_r^{\text{dyn}*} \xi_\perp^{\text{dyn}})$ term dominates angular momentum transfer.³ Equation (3.38) then becomes

$$J_z(r) = 2m\omega^2 \rho r^3 \text{Re} \left[i \xi_r^{\text{dyn}*} \xi_\perp^{\text{dyn}} \right]. \quad (3.39)$$

In the outer layers of the WD where ξ^{dyn} is a pure outgoing wave ($\propto e^{-ikr}$), equation (3.5) can be rearranged to obtain the relationship between ξ_\perp^{dyn} and ξ_r^{dyn} in the WKB approximation ($k \gg 1/H$) with $\omega^2 \ll L_t^2$:

$$\xi_\perp^{\text{dyn}} \simeq -i \frac{kr}{l(l+1)} \xi_r^{\text{dyn}}. \quad (3.40)$$

Then the angular momentum flux is

$$\begin{aligned} J_z &\simeq 2ml(l+1) \frac{\omega^2 \rho r^2}{k} |\xi_\perp^{\text{dyn}}|^2 \\ &\simeq \frac{4 \sqrt{l(l+1)} \omega^3 \rho r^3}{N} |\xi_\perp^{\text{dyn}}|^2. \end{aligned} \quad (3.41)$$

³It can be shown that in the WKB limit the Reynold’s stress associated with the dynamical response is negligible.

where we have used the dispersion relation (equation 3.27) with $\omega^2 \ll N^2$ and set $m = 2$. This expression agrees with that found in Goldreich & Nicholson (1989). From the scaling of ξ_{\perp}^{dyn} provided in equation (3.33), we see that the angular momentum flux is constant (independent of radius) in the outer layers of the star. Since the wave pattern frequency (in the inertial frame) is Ω (the orbital frequency), the energy flux carried by the wave is given by $\dot{E} = \Omega \dot{J}_z$.

Once we have solved our differential equations (3.5 and 3.6) with the appropriate boundary conditions, we can use equation (3.39) to determine where angular momentum and energy are added to the wave, i.e., where the wave is generated. In the WD interior, the waves travel both inwards and outwards and thus carry no net angular momentum, so the value of \dot{J}_z oscillates around zero. However, near the outer boundary, the value of \dot{J}_z is constant and positive because there only exists an outgoing wave. The region where the value of \dot{J}_z rises to its constant value is the region of wave excitation, because it is in this region where energy and angular momentum are added to the waves (see Section 3.6.3).

The energy and angular momentum carried by the outgoing wave is deposited in the outer envelope of the star. Thus, the constant values of \dot{J}_z and \dot{E} near the outer boundary represent the net angular momentum and energy transfer rates from the orbit to the WD. Since $\xi_{\perp}^{\text{dyn}} \propto M'/a^3$, the angular momentum and energy transfer rates can be written in the form

$$\dot{J}_z = T_0 F(\omega), \quad \dot{E} = T_0 \Omega F(\omega), \quad (3.42)$$

where

$$T_0 \equiv G \left(\frac{M'}{a^3} \right)^2 R^5, \quad (3.43)$$

and F is a dimensionless function of the tidal frequency ω and the internal structure of the star. For WDs with rotation rate Ω_s , the tidal frequency is $\omega = 2(\Omega - \Omega_s)$.

3.5 White Dwarf Models

Figure 3.1 depicts three WD models provided by G. Fontaine (see Brassard et al. 1991). These WD models are taken from an evolutionary sequence of a $M = 0.6M_{\odot}$ WD, at effective temperatures of $T = 10800\text{K}$, $T = 6000\text{K}$, and $T = 3300\text{K}$. The WD has a radius $R \simeq 8.97 \times 10^8\text{cm}$ and a carbon-oxygen core surrounded by a $\sim 10^{-2}M$ helium layer, which in turn is surrounded by a $\sim 10^{-4}M$ layer of hydrogen. The models shown have been slightly altered in order to ensure thermodynamic consistency (see Section 3.6.1).

The Brünt-Väisälä frequency can be expressed as

$$N^2 = \frac{g^2 \rho}{P} \frac{\chi_T}{\chi_P} (\nabla_{\text{ad}} - \nabla + B), \quad (3.44)$$

where the symbols have their usual thermodynamic definitions, and the Ledoux term B accounts for composition gradients (see Brassard et al. 1991). In the core of the WD, the value of N^2 is very small due to the high degeneracy pressure, which causes χ_T in equation (3.44) to be small. The sharp spikes in N^2 are created by the carbon-helium and helium-hydrogen transitions, and are characteristic features of WD models. These sharp features in realistic WDs make it difficult to construct toy WD models or to understand how gravity waves propagate through the WD. From Figure 3.1, it is evident that cooler WDs have smaller values of N^2 throughout their interiors. However, the spikes in N^2 have little dependence on WD temperature because they are produced by composition gradients rather than thermal gradients, thus these features are unlikely to be strongly affected by tidal heating.

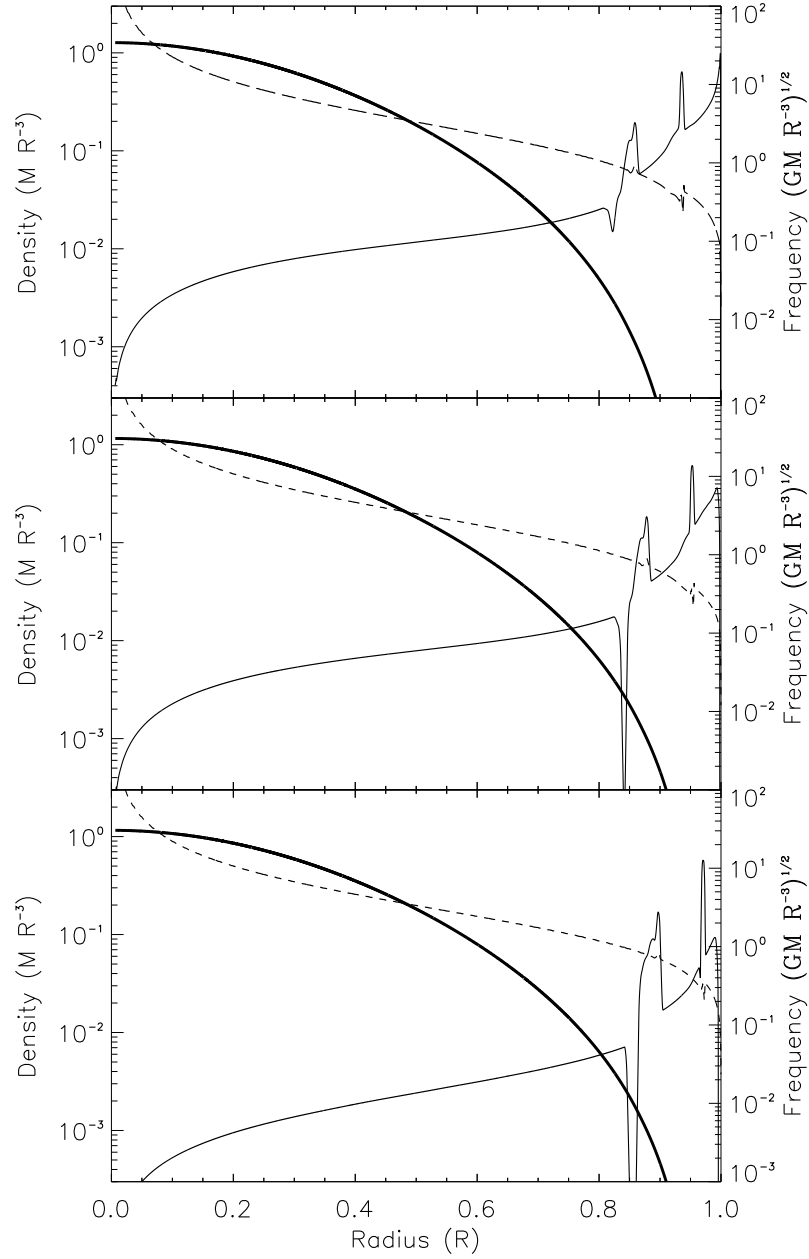


Figure 3.1: The square of the Brünt-Väisälä (thin solid lines) and Lamb (dashed lines) frequencies (for $l = 2$), in units of GM/R^3 , and the density (thick solid line) as a function of normalized radius in three WD models. The models are taken from an evolutionary sequence of a DA WD with $M = 0.6M_{\odot}$, $R = 8.97 \times 10^3$ km, and effective temperatures of $T = 10800\text{K}$ (top), $T = 6000\text{K}$ (middle), and $T = 3300\text{K}$ (bottom). The spikes in the Brünt Väisälä frequency are caused by the composition changes from carbon to helium, and from helium to hydrogen, respectively. Note the formation of a convective zone just below the carbon-helium transition zone as the WD cools.

3.6 Numerical Calculations of Tidal Response

3.6.1 Numerical Method and Importance of Self-Consistent Stellar Model

To calculate the amplitude of the gravity waves excited in a WD by its companion, we integrate the inhomogeneous equations (3.5) and (3.6) with the appropriate boundary conditions given by equations (3.33) and (3.34). We use the relaxation method discussed by Press et al. (2007). The integration requires a grid of points containing stellar properties (ρ , N^2 , a_s^2 , g) as a function of radius, and solves the equations on a grid of (possibly identical) relaxation points.

When creating the grid of data points representing the stellar structure, one must be very careful in ensuring that the stellar properties are consistent with one another. In particular, the Brünt Väisälä frequency is given by

$$N^2 = -g\left(\frac{\rho'}{\rho} + \frac{g}{a_s^2}\right). \quad (3.45)$$

If the value of N^2 in our stellar grid is not exactly equal to the right hand side of the above equation as calculated from the values of ρ , g , and a_s^2 , the stellar properties will not be self-consistent. Such inconsistency may arise from the inaccuracy of the stellar grids, or from the interpolation of the stellar grids (even if the original grids are exactly self-consistent). We have found that even a small inconsistency can lead to a large error in the computed wave amplitude. The reason for this can be understood by examining equation (3.16). When tracing back to equations (3.5) and (3.6), one can see that the N^2 term on the right-hand side is actually the sum of two terms. That is, the value of N^2 on the right-hand side of equation (3.16) is calculated via equation (3.45) from our grid of ρ , a_s^2 , and g values, while the N^2 term on the left hand side of the equation is taken

directly from our grid of N^2 values. If these two values of N^2 differ (by the amount δN^2), then a “false” excitation term will be introduced on the right-hand side of equation (3.16), given by

$$V_f \simeq -\frac{l(l+1)\delta N^2}{r^2\omega^2} \frac{U}{g}. \quad (3.46)$$

This false term can vary rapidly with radius depending on the error in the stellar grid. In Section 3.7, we discuss how sharp changes in the excitation term can be responsible for the excitation of the dynamical component of the tidal response. Thus, the false excitation term introduced by even small numerical inconsistencies can cause large errors in calculations of the dynamical tide.

To test our methods, we calculated the tidal response for a simple massive star model. The results are discussed in Appendix A, and are consistent with previous studies of gravity waves in massive stars (e.g., Zahn 1975, 1977 and Goldreich & Nicholson 1989).

3.6.2 Calculation with a Toy White Dwarf Model

To understand wave excitation in WDs, we first examine a toy model constructed to mimic the structure of a WD. Examining the $T_{\text{eff}} = 10800\text{K}$ model, we see that it contains a sharp rise in N^2 at the carbon-helium boundary, preceded by a small dip in N^2 near the top of the carbon layer. Consequently, we have created a toy model with a similar dip and rise in N^2 in the outer part of the star. To create this model, we first construct a smooth density profile (identical to that of an $n = 2$ polytrope, along with a smooth N^2 profile that mimics the dip-rise features associated with the C-He transition in real WDs. Next, we compute a thermodynamically consistent sound speed profile using the equation

$$a_s^2 = \left(\frac{1}{dP/d\rho} - \frac{N^2}{g^2} \right)^{-1}. \quad (3.47)$$

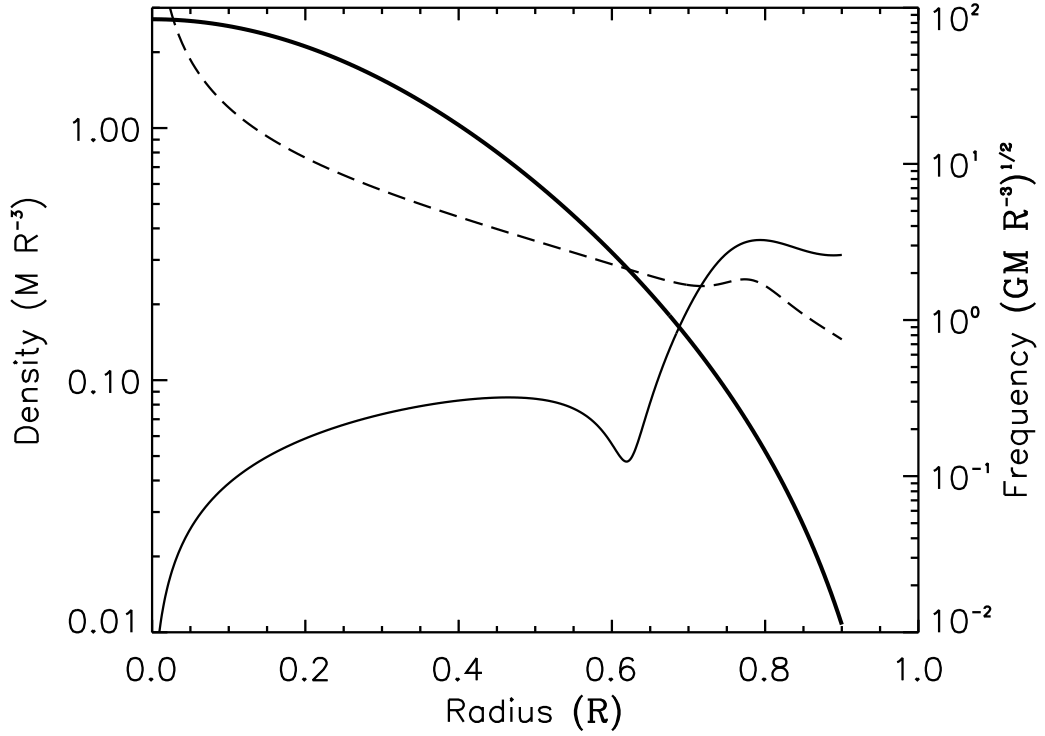


Figure 3.2: The square of the Brünt Vaisälä (thin solid line) and Lamb (dashed line) frequencies (for $l = 2$), in units of GM/R^3 , as a function of normalized radius in a toy WD model. Also plotted is the stellar density (thick solid line). The stellar properties are only plotted out to $r = 0.9R$, the location where the outer boundary condition is imposed in the tidal excitation calculation.

Since the density profile is that of a polytrope, the $dP/d\rho$ term can be calculated analytically.

We solve the forced oscillation equations as a function of the tidal frequency ω . Figure 3.3 shows the energy flux and wave amplitude as a function of radius for a given value of ω . The small oscillations in energy flux are due to imperfect numerical calculation of the dynamical component of the wave and do not actually contribute to energy or angular momentum transfer. We see that waves are excited near the dip of N^2 (before N^2 rises to a maximum). This is similar to the location of wave excitation in real WD models (see Section 3.6.3). The dip in N^2 causes the wave to have a larger wavelength

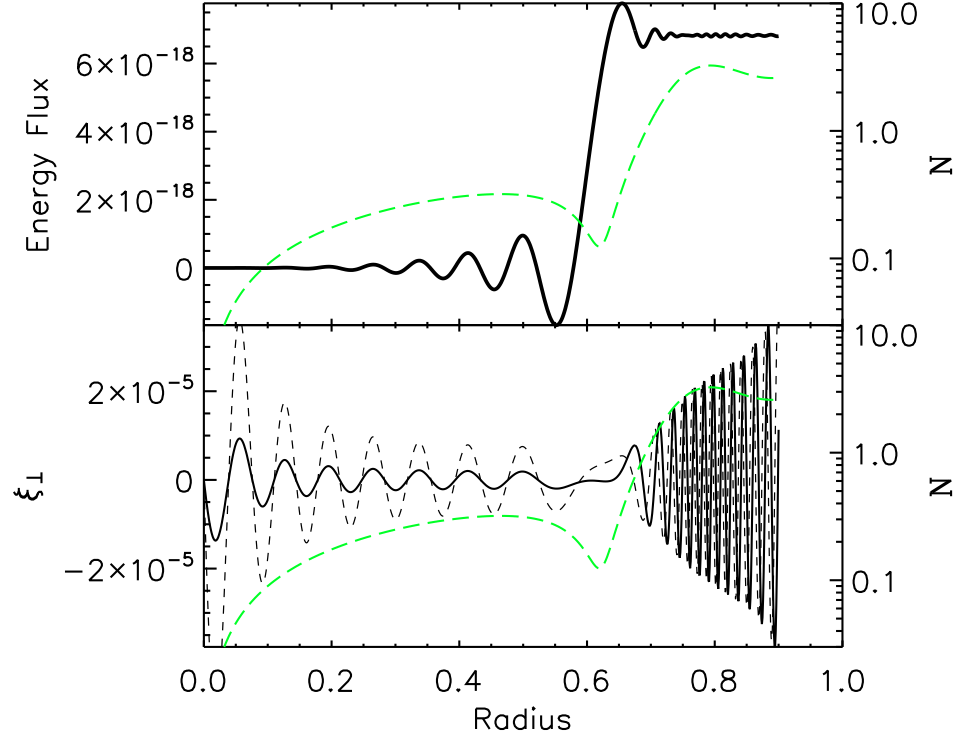


Figure 3.3: Dynamical tide in a toy WD model (based on the model depicted in Figure 3.2) driven by a companion of mass $M' = M$, with the tidal frequency $\omega = 2.3 \times 10^{-2}$. Top: The energy flux $\dot{E} = \Omega \dot{J}_z$ (dark solid line) as a function of radius, with \dot{J}_z calculated from equation (3.39). All values are plotted in units of $G = M = R = 1$. Bottom: The real part of ξ_{\perp}^{dyn} (dark solid line) and imaginary part of ξ_{\perp}^{dyn} (dashed line) as a function of stellar radius. The value of N^2 has been plotted (light solid green line) in both panels. In this model, the energy flux rises to its final value near the dip in N^2 , showing that the wave is excited at this location.

in this region, and so it couples to the companion star's gravitational potential best in this region of the star. Note that although N^2 is smaller near the center of the star, no significant wave is excited there since $U \propto r^2$ is negligible.

Figure 3.4 shows a plot of $F(\omega)$. For this model, $F(\omega)$ is not a smooth, monotonic function of ω as it is for the massive star model studied in Appendix A. Instead, there are many jagged peaks and troughs, causing the value of $F(\omega)$ to vary by two or three orders of magnitude over very small frequency ranges. These features are also present in the real WD models, and will be discussed further in Section 3.7. Our numerical results

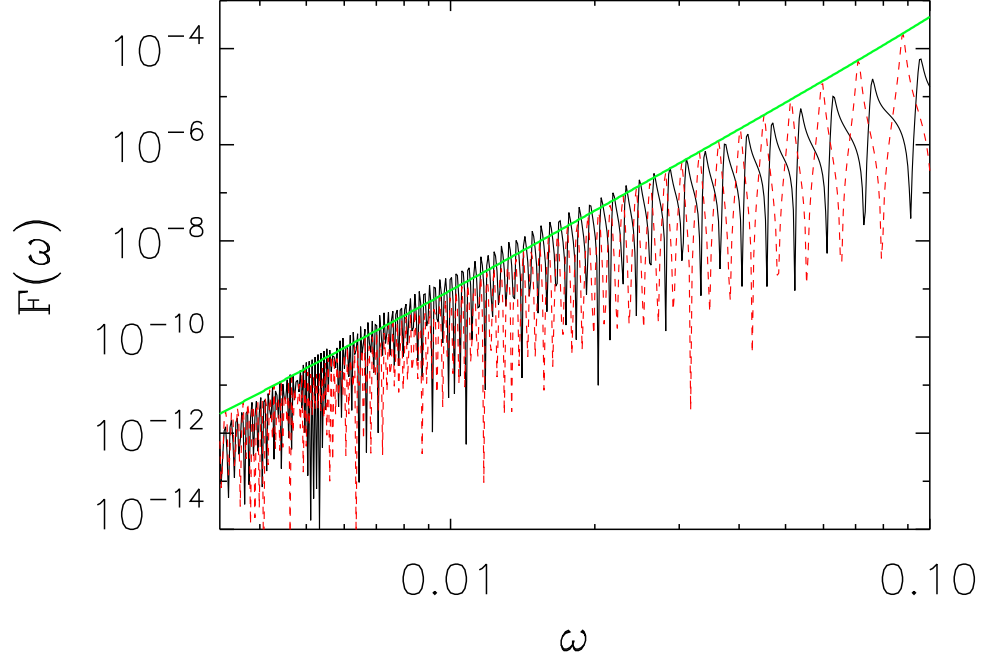


Figure 3.4: The dimensionless tidal torque $F(\omega) = \dot{J}_z/T_o$ [see equation (3.42)] carried by the outgoing gravity wave as a function of the tidal frequency ω (solid line), for the toy WD model depicted in Figure 3.2. The frequency is in units of $G = M = R = 1$. The straight light solid (green) line is calculated from equation (3.68) and is roughly proportional to ω^5 . The dashed (red) line is our semi-analytical approximation, with $\alpha = 1/5$, $\beta = 1/5$, and $\delta = 0$ (see Section 3.7).

indicate that the peaks of $F(\omega)$ can be fitted by $F(\omega) \propto \omega^5$, significantly different from the massive star model.

3.6.3 Calculation with Realistic White Dwarf Model

We now present our numerical results for wave excitation in realistic WD models. Using the outgoing wave outer boundary condition, we solved the oscillation equations (3.5) and (3.6) for the three WD models described in Section 3.6.2 (see Figure 3.1). Figures 3.5 and 3.6 show plots of the outgoing energy flux as a function of radius for the model with $T_{\text{eff}} = 10800\text{K}$ and tidal frequencies of $\omega = 2\Omega = 10^{-2}$ and 1.1×10^{-2} , in units

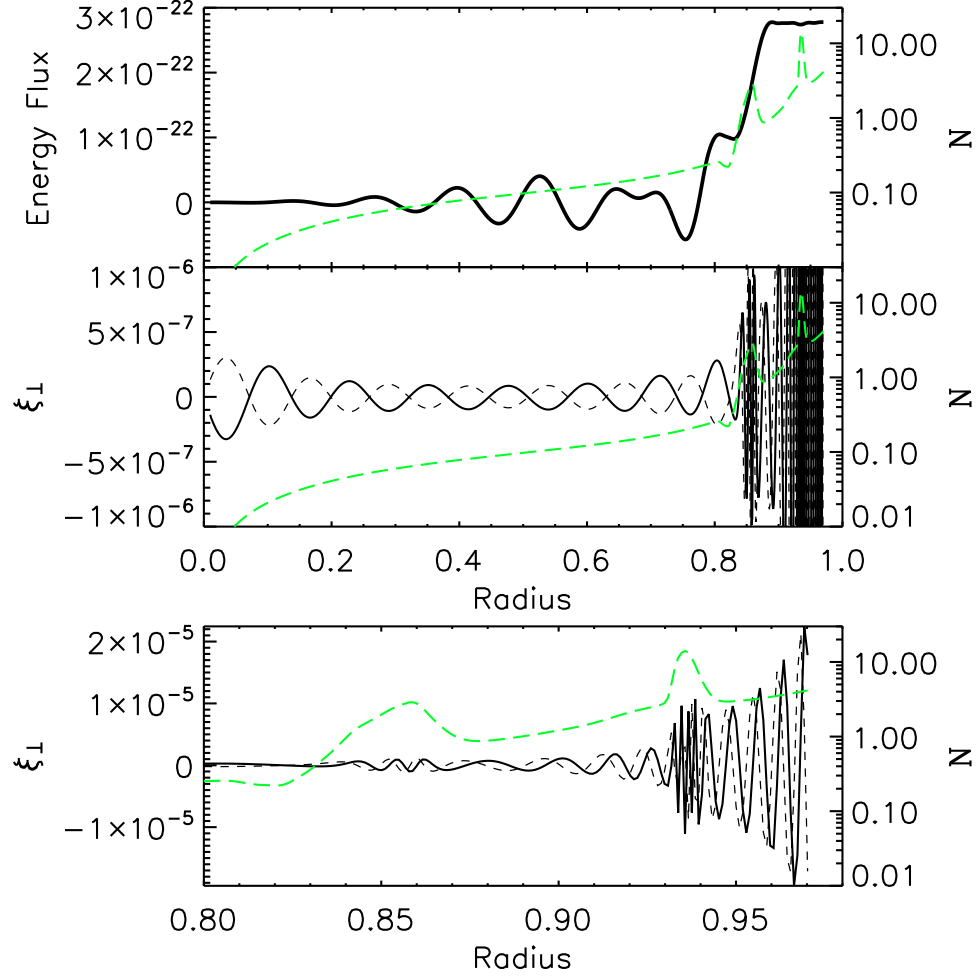


Figure 3.5: Dynamical tide in a realistic WD model (with $M = 0.6M_{\odot}$, $R = 8.97 \times 10^3 \text{ km}$, and $T_{\text{eff}} = 10800 \text{ K}$) driven by a companion of mass $M' = M$, with the tidal frequency $\omega = 2\Omega = 10^{-2}$. Top: The energy flux $\dot{E} = \Omega \dot{J}_z$ (thick solid line) as a function of radius, calculated from equation (3.39). All values are plotted in units of $G = M = R = 1$. Middle: The real part of ξ_{\perp}^{dyn} (solid line) and imaginary part of ξ_{\perp}^{dyn} (dashed line) as a function of stellar radius. Bottom: The same as the middle panel, but zoomed in on the outer layer of the WD. The value of N^2 has been plotted as dashed (green) lines in each panel. The energy flux rises to near its final value around the carbon-helium transition region, showing that the wave is excited at this location.

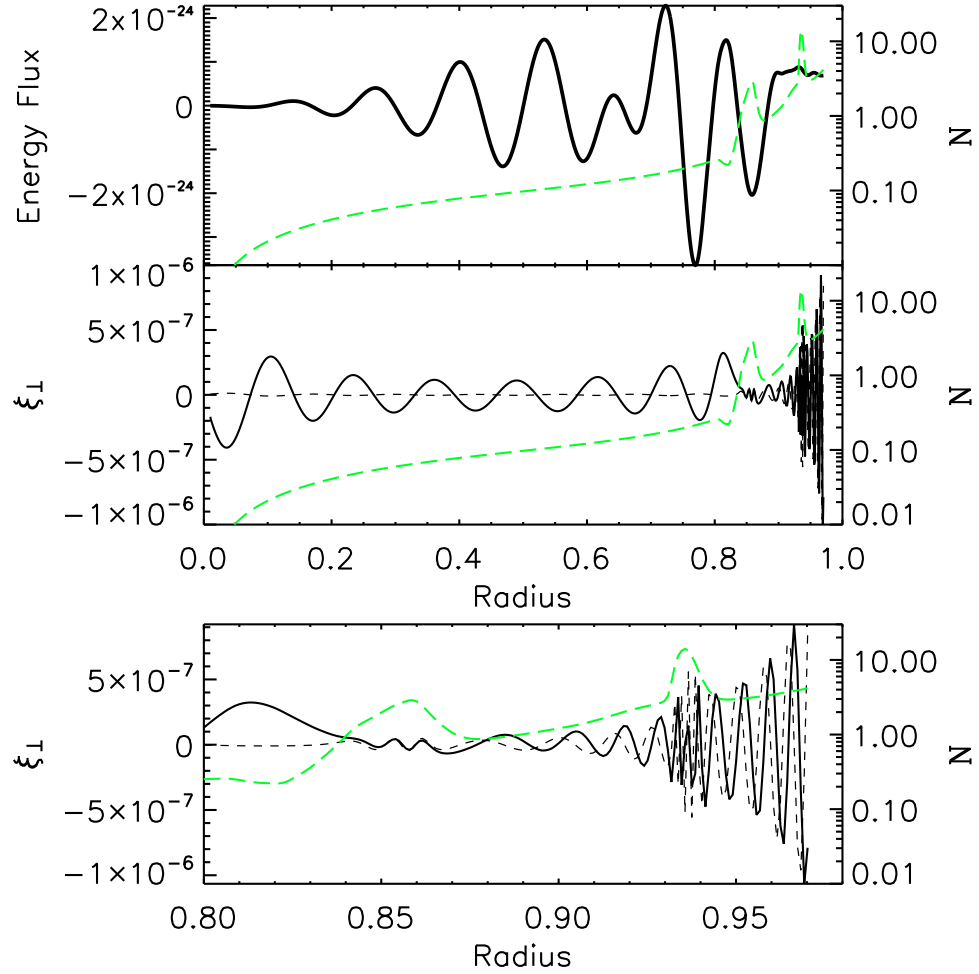


Figure 3.6: Same as Figure 3.5, but for the tidal frequency $\omega = 1.1 \times 10^{-2}$.

of $G = M = R = 1$. The energy flux jumps to its final value near the carbon-helium transition zone. Once again, the oscillations in energy flux are due to imperfect numerical calculation of the dynamical component of the wave and do not actually contribute to energy or angular momentum transfer. In Figures 3.5 and 3.6, we have smoothed the value of the energy flux to minimize the amplitude of the unphysical oscillations. Note that although Figure 3.6 corresponds to a larger tidal frequency, the outgoing energy flux is about 100 times less than in Figure 3.5. Thus, as in our toy WD model (see Section 3.6.2), the tidal energy flux is not a monotonic function of tidal frequency as it is for early-type stars (see Section A).

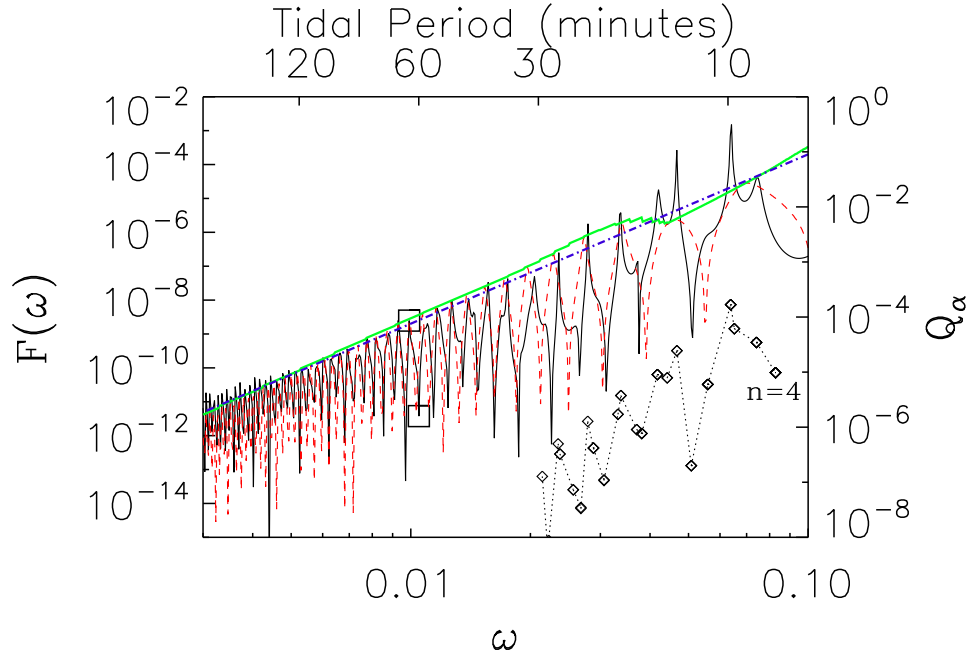


Figure 3.7: The dimensionless tidal torque $F(\omega) = \dot{J}_z/T_o$ [see equation (3.42)] carried by outgoing gravity waves as a function of the tidal frequency ω for our WD model with $T_{\text{eff}} = 10800\text{K}$. The two boxed points correspond to $\omega = 10^{-2}$ and 1.1×10^{-2} , as depicted in Figures 3.5 and 3.6. The dashed (red) line is our semi-analytical approximation [see equation (3.67)], with $\alpha = 1/5$, $\beta = 1/5$, and $\delta = 0$. The smooth solid line corresponds to the maximum values of $F(\omega)$ in our semi-analytical equation, and is calculated from equation (3.69). The dot-dashed (blue) line corresponds to $F(\omega) = 20\hat{\omega}^5$ (see Section 3.8). The diamonds connected by the dotted line are the tidal overlap integrals Q_α associated with nearby gravity modes, and the $n = 4$ mode is the highest frequency mode shown. The frequency and Q_α are plotted in units of $G = M = R = 1$.

We have calculated the dimensionless tidal torque $F(\omega) = \dot{J}_z/T_o$ [see equation (3.42)] as a function of ω for the three WD models depicted in Figure 3.1. The results are shown in Figures 3.7, 3.8, and 3.9. In general, $F(\omega)$ exhibits a strong and complicated dependence on ω , such that a small change in ω leads to a very large change in $F(\omega)$ (see also Figures 3.5-3.6). This dependence is largely due to “resonances” between the radial wavelength of the gravity waves and the radius of the carbon core, as discussed in Section 3.7. We also find that the local maxima of $F(\omega)$ can be approximately fitted by the scaling $F(\omega) \propto \omega^5$, similar to the toy WD model discussed in Section 3.6.2.

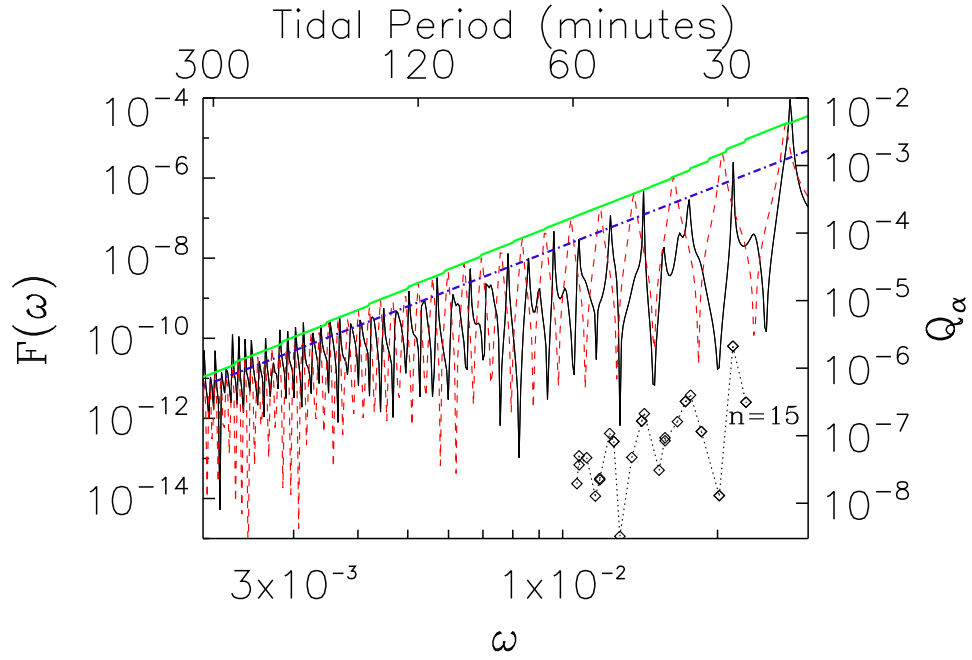


Figure 3.8: Same as Figure 3.7, except for the $T_{\text{eff}} = 6000\text{K}$ WD model. In this plot, the dot-dashed (blue) line corresponds to $F(\omega) = 200\hat{\omega}^5$. The $n = 15$ mode is the highest frequency g-mode shown.

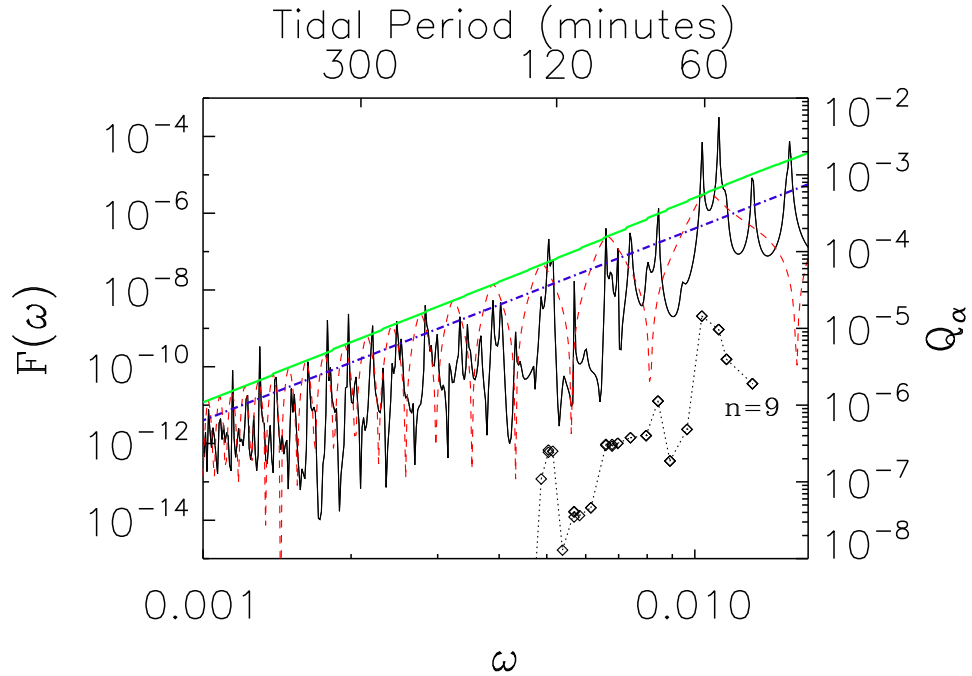


Figure 3.9: Same as Figure 3.7, except for the $T_{\text{eff}} = 3300\text{K}$ WD model. In this plot, the dot-dashed (blue) line corresponds to $F(\omega) = 4 \times 10^3 \hat{\omega}^5$. The $n = 9$ mode is the highest frequency g-mode shown.

3.6.4 Relation to Tidal Overlap Integral

In an attempt to understand the erratic dependence of the tidal energy transfer rate \dot{E} on the tidal frequency ω , here we explore the possible relationship between \dot{E} and the tidal overlap integral. The energy transfer rate to the star due to tidal interactions can be written as

$$\dot{E} = -2 \operatorname{Re} \int d^3x \rho \frac{\partial \xi(\mathbf{r}, t)}{\partial t} \cdot \nabla U^*(\mathbf{r}, t). \quad (3.48)$$

With $\xi(\mathbf{r}, t) = \xi(\mathbf{r})e^{-i\omega t}$ and $U(\mathbf{r}, t) = U(r)Y_{22}e^{-i\omega t}$ [see equations (3.1)-(3.2)], we have

$$\dot{E} = 2\omega \frac{GM'W_{22}}{a^3} \operatorname{Im} \left[\int d^3x \rho \xi(\mathbf{r}) \cdot \nabla(r^2 Y_{22}^*) \right]. \quad (3.49)$$

We decompose the tidal response $\xi(\mathbf{r}, t)$ into the superposition of stellar oscillation modes (with each mode labeled by the index α):

$$\xi(\mathbf{r}, t) = \sum_{\alpha} a_{\alpha}(t) \xi_{\alpha}(\mathbf{r}), \quad (3.50)$$

where the mode eigenfunction ξ_{α} is normalized via $\int d^3x \rho |\xi_{\alpha}|^2 = 1$. Then the mode amplitude $a_{\alpha}(t)$ satisfies the equation

$$\ddot{a}_{\alpha} + \omega_{\alpha}^2 a_{\alpha} + \gamma_{\alpha} \dot{a}_{\alpha} = \frac{GM'W_{22}Q_{\alpha}}{a^3} e^{-i\omega t}, \quad (3.51)$$

where ω_{α} is the mode frequency, γ_{α} is the mode (amplitude) damping rate, and Q_{α} is the *tidal overlap integral* with mode α :

$$Q_{\alpha} = \int d^3x \rho \xi_{\alpha}^*(\mathbf{r}) \cdot \nabla(r^2 Y_{22}). \quad (3.52)$$

The steady-state solution of equation (3.51) is

$$a_{\alpha}(t) = \frac{GM'W_{22}Q_{\alpha}}{a^3(\omega_{\alpha}^2 - \omega^2 - i\gamma_{\alpha}\omega)} e^{-i\omega t}. \quad (3.53)$$

Thus the tidal energy transfer rate to mode α is

$$\dot{E}_{\alpha} = 2\omega \left(\frac{GM'W_{22}|Q_{\alpha}|}{a^3} \right)^2 \frac{\gamma_{\alpha}\omega}{(\omega_{\alpha}^2 - \omega^2)^2 + (\gamma_{\alpha}\omega)^2}. \quad (3.54)$$

In paper I, we have computed ω_α and Q_α for adiabatic g-modes of several WD models used in this paper. The eigenfunctions of these modes satisfy the “reflective” boundary condition (i.e., the Lagrangian pressure perturbation ΔP vanishes) at the WD surface. Our result showed that although the mode frequency ω_α decreases as the radial mode number n increases (for a given $l = 2$), the overlap integral $|Q_\alpha|$ is a non-monotonic function of n (or ω_α) due to various features (associated with carbon-helium and helium-hydrogen transitions) in the N^2 profile of the WD models. On the other hand, our calculation of the tidal response $\xi(\mathbf{r}, t)$ presented in this paper adopts the radiative outer boundary condition; this implies significant wave damping at the outer layer of the star. Because of the difference in the outer boundary conditions, the mode frequency ω_α (as computed using the $\Delta P = 0$ boundary condition) does not have special significance. Nevertheless, we may expect that when $\omega = \omega_\alpha$, the tidal energy transfer is dominated by a single mode (α) and \dot{E} is correlated to $|Q_\alpha|^2$.

In Figures 3.7, 3.8, and 3.9 we show $|Q_\alpha|$ as a function of ω_α for a number of low-order g-modes. It is clear that the peaks and troughs of $F(\omega)$ calculated with an outgoing wave outer boundary condition are associated with the peaks and troughs in the value of $|Q_\alpha|^2$. Thus, the peaks in the value of $F(\omega)$ are *not* due to resonances with g-modes, but approximately correspond to the tidal frequencies near g-modes with large values of $|Q_\alpha|^2$. Note this correspondence between $|Q_\alpha|^2$ and the local peaks of $F(\omega)$ is not precise (as they are calculated using different boundary conditions), as is clear from the $T_{\text{eff}} = 3300\text{K}$ model (Figure 3.9). Another way to understand the erratic dependence of $F(\omega)$ on ω lies in the quasi-resonance cavity of the carbon core of the WD (see Section 3.7).

3.6.5 Justification of the Outer Boundary Condition

Our calculations in this paper adopt the outgoing wave boundary condition near the stellar surface. This implicitly assumes that gravity waves are absorbed in the outer layer of the WD due to nonlinear effects and/or radiative damping. To analyze the validity of this assumption, we plot the magnitude of the displacement, $|\xi^{\text{dyn}}|$, as a function of radius in Figure 3.10. We have shown the results for tidal frequencies of $\omega = 2\Omega = 0.028$ and 0.0053 (corresponding to frequencies near the peaks in $F(\omega)$ shown in Figure 3.7) for our WD model with $T_{\text{eff}} = 10800\text{K}$. We have also plotted the local radial wavelength k_r^{-1} because we expect nonlinear wave breaking to occur when $|\xi^{\text{dyn}}| \gtrsim k_r^{-1}$.

It is evident from Figure 3.10 that at relatively high tidal frequencies, the gravity waves become nonlinear in the outer layers of the star, justifying our outgoing wave boundary condition. In some cases, the waves formally reach nonlinear amplitudes ($k_r^{-1}|\xi^{\text{dyn}}| > 1$) in the helium-hydrogen transition region (demarcated by the dip in k_r^{-1} at $r \simeq 0.935$). This implies that waves may be partially reflected at the helium-hydrogen transition region, although nonlinear damping may also occur before the waves make it to the outermost layers of the WD. The lower frequency gravity waves do not formally reach nonlinear amplitudes in the region depicted in Figure 3.10. However, when extending to the lower-density region near the stellar surface, the wave amplitudes will increase further and nonlinearity will set in, although partial reflection may occur due to the shallow convection zone very near the stellar surface. Also note that our calculations are for $\Omega_s = 0$. If the WD has a non-negligible spin (Ω_s), a given tidal frequency $\omega = 2(\Omega - \Omega_s)$ would correspond to a higher orbital frequency Ω , further increasing the wave amplitudes compared to those shown in Figure 3.10. Furthermore, lower frequency waves may damp efficiently via radiative diffusion near the stellar surface. We therefore expect our outgoing wave outer boundary condition to be a good approxima-

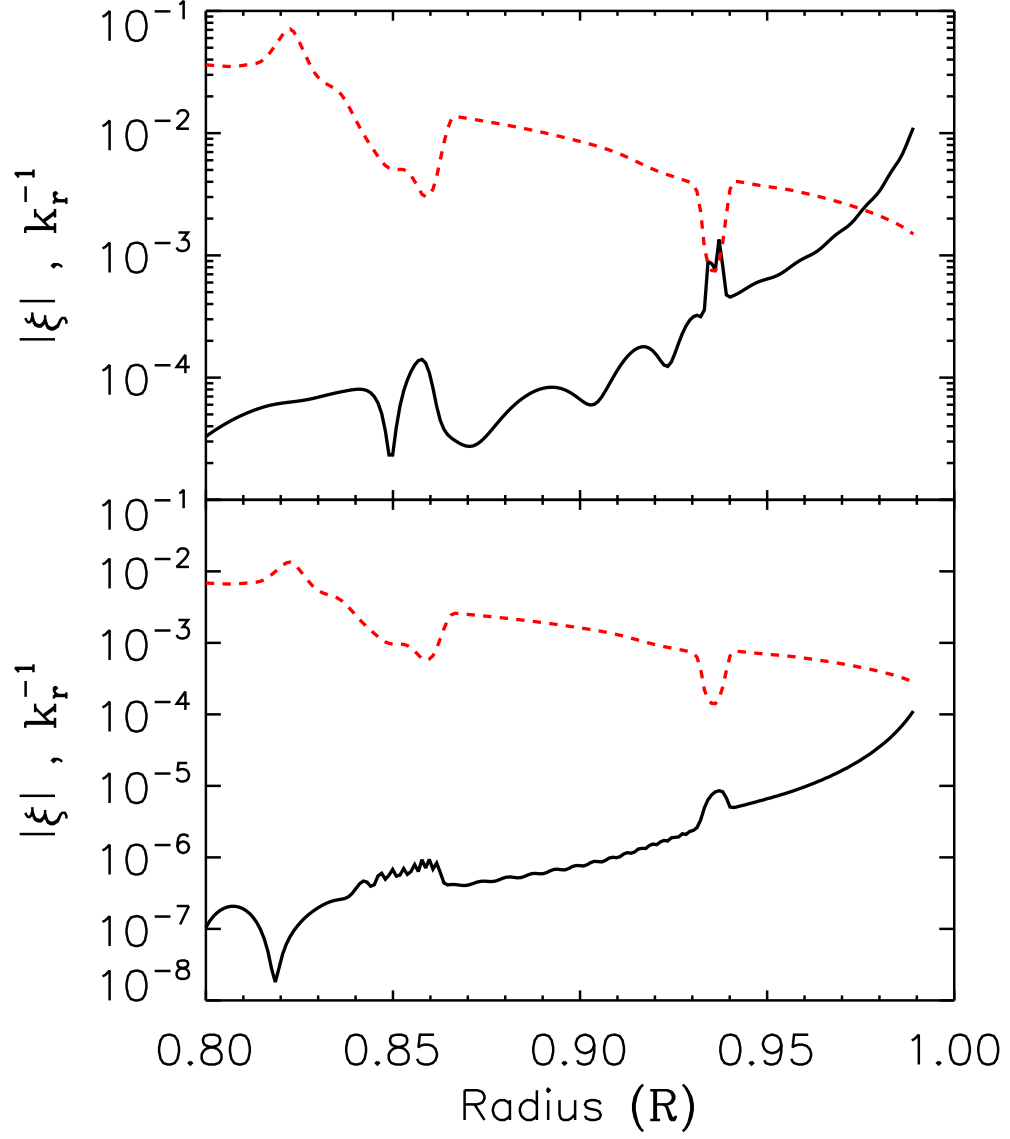


Figure 3.10: The magnitude of the gravity wave displacement vector $|\xi^{\text{dyn}}|$ (solid line) as a function of radius for a tidal frequency of $\omega = 0.028$ (top) and $\omega = 0.0053$ (bottom). Also plotted is the local radial wavelength k_r^{-1} (red dashed line). The wave displacement, wavelength, and frequency are in units where $G = M = R = 1$.

tion for the frequencies considered in this paper for our warmest WD model.

Our cooler WD models with $T_{\text{eff}} = 6000\text{K}$ and $T_{\text{eff}} = 3300\text{K}$ do not formally reach the same nonlinear amplitudes as our warmest model. The cooler models have smaller Brunt-Vaisala frequencies, particularly in their outer layers, as can be seen in Figure 3.1. Consequently, the gravity waves have smaller displacements (recall the WKB scaling $\xi_{\perp}^{\text{dyn}} \propto N^{1/2}$ for a constant \dot{J}_z) and larger wavelengths (recall $k_r \propto N$). Therefore, gravity waves are less likely to damp due to nonlinear effects in our cooler models, and our outgoing wave outer boundary condition may not be justified at all frequencies considered. More detailed analyses of the nonlinear effects in dynamical tides are necessary (e.g., Barker & Ogilvie 2010, Weinberg et al. 2011).

3.7 Simple Model for Gravity Wave Excitation: Analytic Estimate

To understand our numerical result for the tidal energy transfer rate \dot{E} (Section 3.6.3), particularly its dependence on the tidal frequency ω , here we consider a simple stellar model that, we believe, captures the essential physics of tidal excitation of gravity waves in binary WDs. In this model, the star consists of two regions (see Figure 3.11): the outer region with $r > r_a$ (region a) and the inner region with $r < r_b$ (region b). In each region, the stellar profiles are smooth, but N^2 jumps from N_b^2 at $r = r_b$ to N_a^2 (with $N_a^2 \gg N_b^2$) at $r = r_a$. The tidal frequency ω satisfies $\omega^2 \ll N_b^2$. As we will see, although waves can propagate in both regions, the sharp jump in N^2 makes the inner region behave like a resonance cavity—this is ultimately responsible for the erratic dependence of $F(\omega)$ on the tidal frequency ω .

We start from the wave equation (3.12) for $Z(r) = \chi^{-1/2} r^2 \xi_r$:

$$Z'' + k^2(r)Z = V(r), \quad (3.55)$$

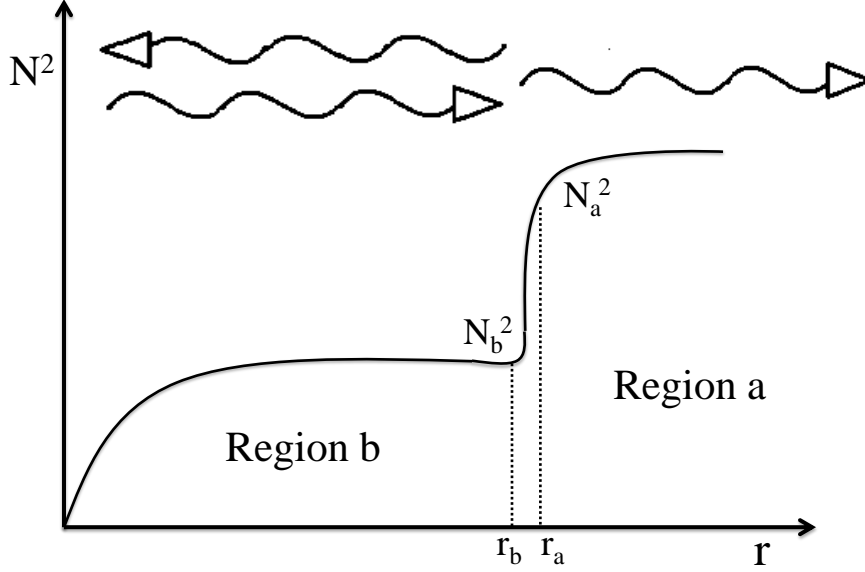


Figure 3.11: A diagram showing a simplified model of a white dwarf used in our analytical estimate for gravity wave excitation. The arrows indicate that region b contains both an inward and outward propagating wave, while region a contains only an outward propagating wave.

with

$$\begin{aligned}
 k^2(r) &= \frac{l(l+1)N^2}{r^2\omega^2} + \Delta k^2(r) \\
 &= \frac{l(l+1)N^2}{r^2\omega^2} \left\{ 1 + O\left[\frac{r^2}{H^2} \frac{\omega^2}{l(l+1)N^2} \right] \right\}
 \end{aligned} \tag{3.56}$$

$$V(r) = -\chi^{-1/2} \frac{l(l+1)N^2}{\omega^2} \frac{U}{g} \left[1 - \frac{2r}{H} \frac{\omega^2}{l(l+1)N^2} \right], \tag{3.57}$$

where $H = a_s^2/g(\lesssim r)$ is the pressure scale height. The above expressions are valid in both regions of the star, and we have assumed $\omega^2 \ll L_l^2$ and $\omega^2 \ll N^2$ [more general expressions are given by equations (3.13) and (3.14)]. Since the stellar profiles are smooth in each of the two regions, the non-wave (“equilibrium”) solution is given by

$$Z^{\text{eq}}(r) \simeq \frac{V}{k^2} - \frac{1}{k^2} \left(\frac{V}{k^2} \right)'' = Z_0 + \Delta Z, \tag{3.58}$$

where

$$Z_0 = -\chi^{-1/2} \frac{r^2 U}{g}, \quad (3.59)$$

$$\Delta Z = Z_0 \frac{\beta}{k^2 H^2}, \quad (3.60)$$

and β is a constant (with $\beta \sim 1$).⁴ Note that the above solution for Z^{eq} breaks down around $r = r_{\text{in}}$ (where $\omega^2 = N^2$). At distances sufficiently far away from r_{in} , we have $k \gg 1/H$.

The general solution to equation (3.12) consists of the non-wave part Z^{eq} and the wave part Z^{dyn} . In region b there exist both ingoing and outgoing waves. Thus

$$\begin{aligned} Z(r) = & Z^{\text{eq}}(r) + A_+ \exp\left(i \int_{r_{\text{in}}}^r k dr\right) \\ & + A_- \exp\left(-i \int_{r_{\text{in}}}^r k dr\right) \end{aligned} \quad (3.61)$$

for $r_{\text{in}} < r < r_b$, where A_+ and A_- are slow-varying functions of r . In region a, we require there be no ingoing wave. Thus for $r > r_a$,

$$Z(r) = Z^{\text{eq}}(r) + A \exp\left(-i \int_{r_0}^r k dr\right) \quad (3.62)$$

where $r_0 > r_a$ is a constant, and A varies slowly with r . Note that Z^{eq} is discontinuous between the two regions.

At the inner boundary $r = r_{\text{in}}$, gravity waves are perfectly reflected. Thus we have $A_- = -e^{i\delta} A_+$, where δ is a constant phase that depends on the details of the disturbance around and inside r_{in} . To determine A and A_+ we must match the solutions in the two regions. Although in reality r_a is somewhat larger than r_b , we shall make the approximation $r_a \simeq r_b$, and label the physical quantities on each side with the subscript “a” or “b”.

⁴From equation (3.13), we find that Δk^2 in equation (3.56) is given by $\Delta k^2 = (H_\rho^{-1})'/2 - (2H_\rho)^{-2} + H_\rho^{-1}[-(\ln H_\rho)' + H_\rho^{-1} - H_\rho^{-1}]$, where $H_p = H$ and $H_\rho = -\rho'/\rho$. In the isothermal region, $H_\rho = H$, and we have $\Delta k^2 = -(2H_\rho)^{-2}$. In the region satisfying $P \propto \rho^{5/3}$, we have $H_\rho = (5/3)H$, and $\Delta k^2 \simeq 1/(12H_\rho^2)$. Thus the parameter β in equation (3.59) ranges from $|\beta| \lesssim 0.1$ to 0.3.

Note that $Z_a^{\text{eq}} - Z_b^{\text{eq}} \simeq -\Delta Z_b$ since $k_a^2 \gg k_b^2$, and $(dZ^{\text{eq}}/dr)_a - (dZ^{\text{eq}}/dr)_b \simeq -(\alpha/H)\Delta Z_b$ where α is a constant ($|\alpha| \sim 1$). Matching Z and dZ/dr across $r = r_b \simeq r_a$, we obtain the expression for the wave amplitude at $r = r_a$:

$$A \exp\left(-i \int_{r_0}^{r_a} k dr\right) = \Delta Z_b \left[\frac{1 - (\alpha/k_b H) \tan \varphi}{1 + i(k_a/k_b) \tan \varphi} \right], \quad (3.63)$$

which entails

$$|A| = |\Delta Z_b| \frac{|1 - (\alpha/k_b H) \tan \varphi|}{[1 + (k_a/k_b)^2 \tan^2 \varphi]^{1/2}}, \quad (3.64)$$

where

$$\varphi = \int_{r_0}^{r_b} k dr - \frac{\delta}{2}. \quad (3.65)$$

Clearly, $|A|$ reaches the maximum $|\Delta Z_b|$ at $\varphi = 0$, and $|A| \simeq |\Delta Z_b(\alpha/k_a H)|$ at $\varphi = \pi/2$.

The Lagrangian displacement for the outgoing gravity wave in region a is given by

$$\begin{aligned} \xi_{\perp}^{\text{dyn}} &\simeq -\frac{ikr}{l(l+1)} \xi_r^{\text{dyn}} \\ &= -\frac{ik\chi^{1/2}}{l(l+1)r} A \exp\left(-i \int_{r_0}^r k dr\right). \end{aligned} \quad (3.66)$$

The tidal energy transfer rate \dot{E} is equal to the energy flux carried by the wave. Using equation (3.41), we have

$$\dot{E} = \Omega \dot{J}_z = 4\Omega k_a |A|^2, \quad (3.67)$$

where $k_a = \sqrt{l(l+1)}N_a/(r_a\omega)$ and $|A|$ are evaluated at $r = r_a$. Using $|A|_{\text{max}} = |\Delta Z_b|$, we obtain the maximum tidal energy transfer rate as a function of the tidal frequency ω and the orbital frequency Ω :

$$\dot{E}_{\text{max}} \simeq \frac{6\pi\beta^2}{5} \frac{\rho_a r_a^7 N_a}{N_b^4 [l(l+1)]^{5/2} g_a^2} \left(\frac{r_a}{H_a}\right)^4 \left(\frac{M'}{M_t}\right)^2 \Omega^5 \omega^5. \quad (3.68)$$

The corresponding dimensionless tidal torque [see equation (3.42)] is

$$F_{\text{max}}(\omega) = \frac{6\pi\beta^2}{5} \frac{G\rho_a r_a^7 N_a}{N_b^4 [l(l+1)]^{5/2} g_a^2 R^5} \left(\frac{r_a}{H_a}\right)^4 \omega^5. \quad (3.69)$$

This scaling [$F(\omega) \propto \omega^5$] agrees with our numerical results for the toy WD models (Section 3.6.2) and realistic WD models (Section 3.6.3).

Realistic WD models are obviously more complicated than the analytical model considered in this section (see Figure 3.11). To evaluate the tidal energy transfer rate \dot{E} using equation (3.67) [with $|A|$ given by equation (3.64)] and \dot{E}_{\max} using equation (3.68) for our WD models, we choose r_b at the location where $d \ln N^2 / dr$ is largest in the helium-carbon transition region. We then set the location of r_a to be one half of a wavelength above r_b , i.e., by finding the location r_a such that the equation $\pi = \int_{r_b}^{r_a} k dr$ is satisfied, where k is given by equation (3.27). For the three models considered in Section 6, we find that r_a thus calculated typically lies near the peak in N^2 associated with the carbon-helium transition region.

In Figures 3.4, 3.7, 3.8, and 3.9, we compare the analytical results based on equations (3.67) and (3.68) to our numerical calculations. We see that the erratic dependence of $F(\omega)$ on the tidal frequency ω can be qualitatively reproduced by our analytical expression (3.67), and the maximum F_{\max} is also well approximated by equation (3.69). Our analytical estimate works best for the WD model with $T_{\text{eff}} = 10800\text{K}$, but it does a poor job of approximating the value of $F(\omega)$ for the WD model with $T_{\text{eff}} = 3300\text{K}$. We attribute this disagreement to the lower value of N^2 in the cool WD model because our assumption that $N^2 \gg \omega^2$ is not satisfied. Instead, we find that gravity waves are excited near the spike in N^2 associated with the helium-hydrogen transition region in the cool WD model.

For each model shown in Figures 3.7-3.9, our model also breaks down at the highest and lowest frequencies shown. These discrepancies are likely related to errors in our numerical methods. At the highest frequencies shown, the approximation $k_r \gg 1/H$ begins to break down, causing error in our outer boundary condition. At the lowest

frequencies shown, extremely fine grid resolution is needed to resolve the dynamical component of the tidal response, and so slight thermodynamic inconsistencies may introduce significant errors (see Section 3.6.1).

3.8 Spin-Orbit Evolution

The dissipation of tidally excited gravity waves cause energy and angular momentum transfer from the orbit to the star, leading to spin-up of the WD over time. In this section, we study the spin-orbit evolution of WD binaries under the combined effects of tidal dissipation and gravitational radiation. In general, the tidal torque on the primary star M from the companion M' and the tidal energy transfer rate can be written as [see equations (3.42) and (3.43)]

$$T_{\text{tide}} = T_0 F(\omega), \quad \dot{E}_{\text{tide}} = T_0 \Omega F(\omega), \quad (3.70)$$

with $T_0 = G(M'/a^3)^2 R^5$. In previous sections, we have computed $F(\omega)$ for various non-rotating ($\Omega_s = 0$) WD models (and other stellar models). To study the spin-orbit evolution, here we assume that for spinning WDs, the function $F(\omega)$ is the same as in the non-rotating case. This is an approximation because a finite Ω_s can modify gravity waves in the star through the Coriolis force (gravity waves become the so-called Hough waves) and introduce inertial waves, which may play a role in the dynamical tides. In other words, the function F generally depends on not only ω but also Ω_s . However, we expect that when the tidal frequency $\omega = 2(\Omega - \Omega_s)$ is larger than Ω_s , i.e., when $\Omega \gtrsim 3\Omega_s/2$, the effect of rotation on the gravity waves is small. Also, we assume that the WD exhibits solid-body rotation, which would occur if different layers of the WD are strongly coupled (e.g., due to viscous or magnetic stresses).⁵

⁵In a medium containing a magnetic field, we expect differential rotation to be smoothed out by magnetic stresses on time scales comparable to the Alfvén wave crossing time. The Alfvén wave crossing time

Before proceeding, we note that in the weak friction theory of equilibrium tides (e.g., Darwin 1879; Goldreich & Soter 1966; Alexander 1973; Hut 1981), the tidal torque is related to the tidal lag angle δ_{lag} or the tidal lag time Δt_{lag} by

$$T_{\text{tide}} = 3k_2 T_0 \delta_{\text{lag}}, \quad \text{with } \delta_{\text{lag}} = (\Omega - \Omega_s) \Delta t_{\text{lag}}, \quad (3.71)$$

where k_2 is the Love number. Often, a dimensionless tidal quality factor Q_{tide} is introduced (e.g. Goldreich & Soter 1966) such that $\Delta t_{\text{lag}} = 1/(|\omega|Q_{\text{tide}})$ (valid only for $\omega \neq 0$). Thus, if we use the weak-friction theory to parametrize our dynamical tide, $F(\omega)$ would correspond to

$$\begin{aligned} F(\omega) &= 3k_2 \delta_{\text{lag}} \\ &= 3k_2 (\Omega - \Omega_s) \Delta t_{\text{lag}} \\ &= \frac{3k_2}{2Q_{\text{tide}}} \text{sgn}(\Omega - \Omega_s). \end{aligned} \quad (3.72)$$

Obviously, the effective Q_{tide} would depend strongly on ω as opposed to being a constant (assuming constant lag angle) or being proportional to $1/|\omega|$ (assuming constant lag time, appropriate for a viscous fluid).

With equation (3.70) and the assumption in $F(\omega)$, the WD spin evolves according to the equation

$$\dot{\Omega}_s = \frac{T_0 F(\omega)}{I}, \quad (3.73)$$

where I is the moment of inertia of the WD ($I \simeq 0.169MR^2$ for our $M = 0.6M_\odot$ WD models). The orbital energy $E_{\text{orb}} = -GMM'/(2a)$ satisfies the equation

$$\dot{E}_{\text{orb}} = -\dot{E}_{\text{tide}} - \dot{E}_{\text{GW}}, \quad (3.74)$$

where $\dot{E}_{\text{GW}}(> 0)$ is the energy loss rate due to gravitational radiation. The evolution

is $t_A = R \sqrt{4\pi\rho}/B \simeq 1\text{yr}$ for a magnetic field strength of $B = 10^5\text{gauss}$ and a density of $\rho = 10^6\text{g/cm}^3$. Since the Alfvén wave crossing time is always much smaller than the inspiral time for WDs, we expect solid body rotation to be a good approximation.

equation for the orbital angular frequency $\Omega = (GM_t/a^3)^{1/2}$ is then

$$\dot{\Omega} = \frac{3T_0 F(\omega)}{\mu a^2} + \frac{3\Omega}{2t_{\text{GW}}}, \quad (3.75)$$

where $\mu = MM'/M_t$ is the reduced mass of the binary, and t_{GW} is the orbital decay time scale ($|a/\dot{a}|$) due to gravitational radiation:

$$\begin{aligned} t_{\text{GW}} &= \frac{5c^5}{64G^3} \frac{a^4}{MM'M_t} \\ &= 3.2 \times 10^{10} \left(\frac{M_\odot^2}{MM'} \right) \left(\frac{M_t}{2M_\odot} \right)^{1/3} \left(\frac{\Omega}{0.1 \text{ s}^{-1}} \right)^{-8/3} \text{ s}, \end{aligned} \quad (3.76)$$

3.8.1 Synchronization

Using our results for the function $F(\omega)$ obtained in previous sections, we integrate equations (3.73) and (3.75) numerically to obtain the evolution of the WD spin. Since at large a (small Ω) the orbital decay time $\sim t_{\text{GW}} \propto \Omega^{-8/3}$ is much shorter than the time scale for spin evolution, $t_{\text{spin}} = \Omega_s/\dot{\Omega}_s \propto 1/(\Omega^4 F)$, we start our integration with $\Omega_s \ll \Omega$ at a small orbital frequency (an orbital period of several hours).

The results for our three WD models are shown in Figures 3.12 and 3.13. Note we only include the effects of tides in the primary star (M), and treat the companion (M') as a point mass. All three models have the same WD masses ($M = M' = 0.6M_\odot$), but different temperatures. Also note that the minimum binary separation (before mass transfer or tidal disruption occurs) is $a_{\text{min}} \simeq 2.5(M_t/M)^{1/3}R$, corresponding to the minimum orbital period

$$P_{\text{min}} \simeq (1.1 \text{ min}) M_1^{-1/2} R_4^{3/2}, \quad (3.77)$$

where $M_1 \equiv M/(1 M_\odot)$ and $R_4 = R/(10^4 \text{ km})$. We see that for all models, appreciable spin-orbit synchronization is achieved before mass transfer or tidal disruption. However, depending in the WD temperature, the rates of spin-orbit synchronization are different.

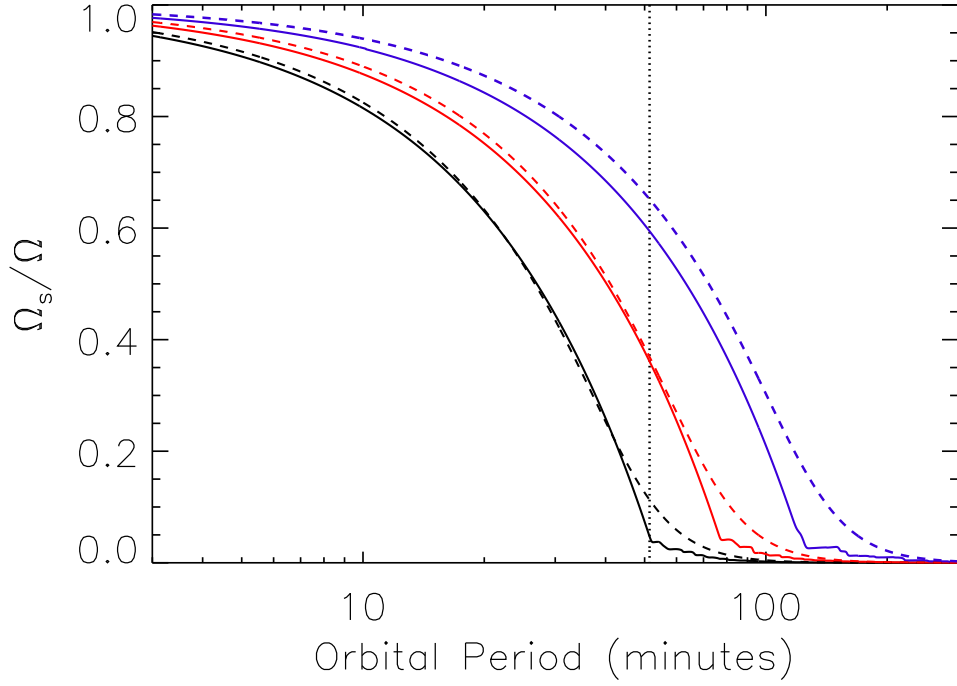


Figure 3.12: Evolution of the spin frequency Ω_s in units of the orbital frequency Ω as a function of the orbital period. The solid black, red, and blue lines correspond to our WD models with $T_{\text{eff}} = 10800\text{K}$, $T = 6000\text{K}$, and $T = 3300\text{K}$, respectively. The black, red, and blue dashed lines correspond to evolutions using $F = 20\hat{\omega}^5$, $F = 200\hat{\omega}^5$, $F = 4 \times 10^3 \hat{\omega}^5$, respectively (these functions $F(\omega)$ approximate the like-colored WD models, see Figures 3.7-3.9). The vertical dotted line denotes the critical orbital period, $2\pi/\Omega_c$ [see equation (3.79)], corresponding to the black dashed line. In these evolutions, $M' = M$ and the WDs initially have $\Omega_s = 0$.

The basic feature of the synchronization process can be obtained using an approximate expression for the dimensionless function $F(\omega)$. We fit the local maxima of our numerical results depicted in Figures 3.7-3.9 by the function

$$F(\omega) = f\omega^5 = \hat{f}\hat{\omega}^5, \quad (3.78)$$

where $\hat{\omega} = \omega/(GM/R^3)^{1/2}$, and $\hat{f} \simeq 20, 200, 4 \times 10^3$ for the $T_{\text{eff}} = 10800\text{K}$, 6000K , and 3300K models, respectively. Suppose $\Omega_s \ll \Omega$ at large orbital separation. We can define the *critical orbital frequency*, Ω_c , at which spinup or synchronization becomes efficient, by equating $\dot{\Omega}$ and $\dot{\Omega}_s$ (with $\Omega_s \ll \Omega$). Note that since the orbital decay rate

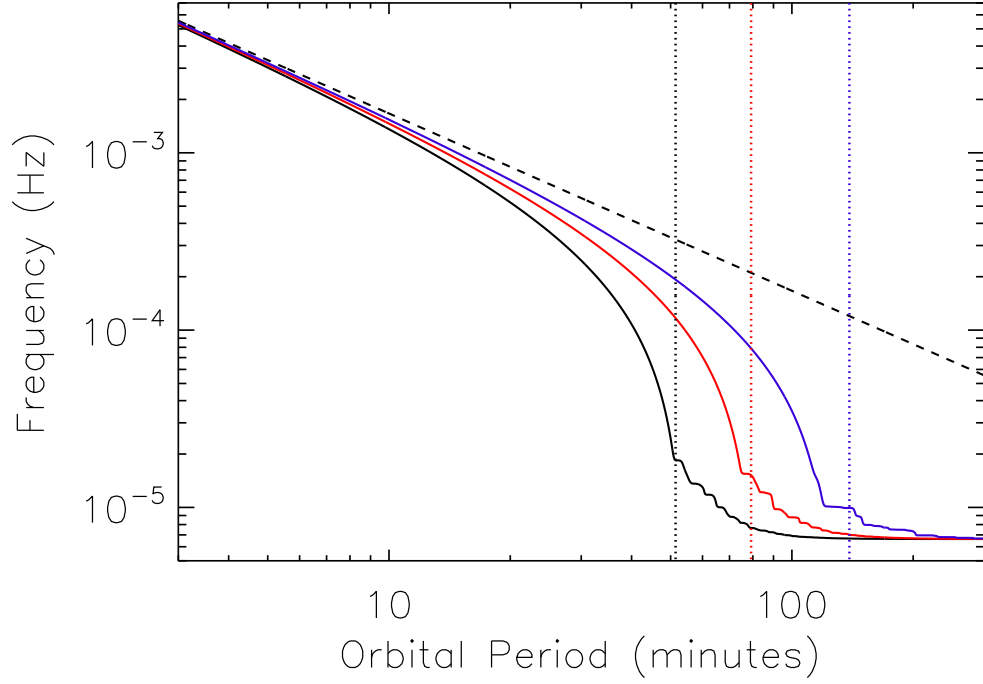


Figure 3.13: The spin frequency $\Omega_s/(2\pi)$ in units of Hz as a function of orbital period. The solid black, red, and blue lines correspond to our WD models with $T_{\text{eff}} = 10800\text{K}$, $T = 6000\text{K}$, and $T = 3300\text{K}$, respectively. The dashed line shows the orbital frequency, $\Omega/(2\pi)$. The dotted vertical black, red, and blue lines are the values of $2\pi/\Omega_c$ for $F = 20\hat{\omega}^5$, $F = 200\hat{\omega}^5$, $F = 4 \times 10^3\hat{\omega}^5$, respectively. In these evolutions, $M' = M$ and the WDs initially have $\Omega_s = \Omega/4$.

due to tidal energy transfer [the first term in equation (3.75)] is much smaller than the spinup rate $\dot{\Omega}_s$, the orbital decay is always dominated by the gravitational radiation, i.e., $\dot{\Omega} \simeq 3\Omega/(2t_{\text{GW}})$. With $T_o = \bar{T}_o\Omega^4$ and $t_{\text{GW}} = \bar{t}_{\text{GW}}\Omega^{-8/3}$, we find

$$\begin{aligned}\Omega_c &\simeq \left(\frac{3I}{64f\bar{T}_o\bar{t}_{\text{GW}}} \right)^{3/16} \\ &= \left[\frac{3\kappa}{5\hat{f}} \frac{M_t^{5/3}}{M'M^{2/3}} \left(\frac{GM}{Rc^2} \right)^{5/2} \right]^{3/16} \left(\frac{GM}{R^3} \right)^{1/2} \\ &= (3.8 \times 10^{-3} \text{s}^{-1}) \left(\frac{\kappa_{0.17} M_{t1}^{5/3} M_1^{9/2}}{\hat{f} M'_1 R_4^{21/2}} \right)^{3/16},\end{aligned}\tag{3.79}$$

where $\kappa = 0.17\kappa_{0.17} = I/(MR^2)$, $M'_1 = M'/(1 M_\odot)$, and $M_{t1} = M_t/(1 M_\odot)$. For $\Omega \lesssim \Omega_c$, tidal synchronization is inefficient. For $\Omega \gtrsim \Omega_c$, the spinup rate $\dot{\Omega}_s$ becomes larger than

$\dot{\Omega}$ and the system will become increasingly synchronized. In fact, when $\Omega \gtrsim \Omega_c$, an approximate analytic expression for the spin evolution can be obtained by assuming *a posteriori* $(\dot{\Omega}_s - \dot{\Omega}) \ll \dot{\Omega}$. With $\dot{\Omega} \simeq 3\Omega/(2t_{\text{GW}}) \simeq \dot{\Omega}_s$, we find

$$\Omega_s \simeq \Omega - \Omega_c^{16/15} \Omega^{-1/15} \quad (\text{for } \Omega \gtrsim \Omega_c). \quad (3.80)$$

This expression provides an accurate representation of the numerical solutions.

Note that we can derive a similar equation as (3.80) for more general tidal torques. For example, assume

$$\dot{\Omega}_s = A\Omega^4(\Omega - \Omega_s)^n, \quad (3.81)$$

where n and A are constants. With $\dot{\Omega} = B\Omega^{11/3}$ (where B is a constant) and assuming $\dot{\Omega}_s \simeq \dot{\Omega}$, we find

$$\Omega_s \simeq \Omega - \Omega_c \left(\frac{\Omega_c}{\Omega} \right)^{1/(3n)}, \quad (3.82)$$

for $\Omega \gtrsim \Omega_c$, where

$$\Omega_c = \left(\frac{B}{A} \right)^{3/(3n+1)}. \quad (3.83)$$

Note that our equation (3.80) corresponds to $n = 5$, which implies $\Omega - \Omega_s \simeq \Omega_c$ for $\Omega \gtrsim \Omega_c$. By contrast, in the equilibrium tide model (with constant lag time), $n = 1$, so $(\Omega - \Omega_s)$ changes moderately as the orbit decays.

3.8.2 Tidal Effect on the Orbital Decay Rate and Phase of Gravitational Waves

Figure 3.14 shows the tidal energy transfer rate (from the orbit to the WD) $\dot{E}_{\text{tide}} = T_0 \Omega F(\omega)$. For $\Omega \lesssim \Omega_c$, $\omega \simeq 2\Omega$ (assuming $\Omega_s \ll \Omega$), we see that \dot{E}_{tide} depends on Ω in a rather erratic manner. However, when $\Omega \gtrsim \Omega_c$, efficient tidal synchronization ensures

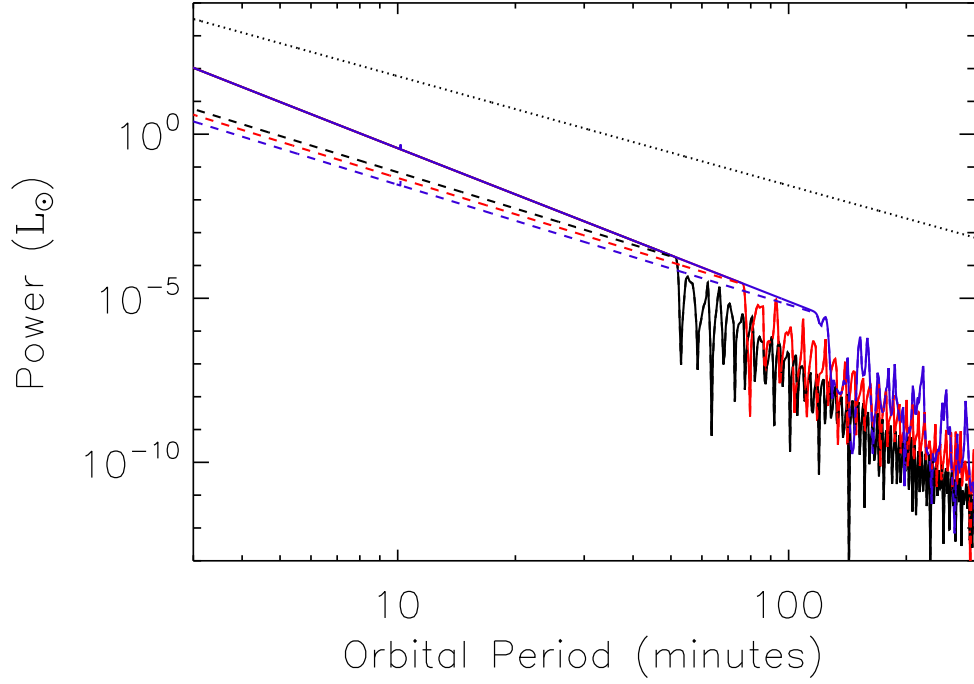


Figure 3.14: The tidal energy dissipation rate \dot{E}_{tide} (solid lines) and the tidal heating rate \dot{E}_{heat} (dashed lines) as a function of orbital period. The black, red, and blue lines correspond to our WD models with $T_{\text{eff}} = 10800\text{K}$, $T = 6000\text{K}$, and $T = 3300\text{K}$, respectively. Note that at small orbital periods, the \dot{E}_{tide} curves overlap for different WD models. The dotted line is the energy dissipation rate due to gravitational waves, \dot{E}_{GW} . In these evolutions, $M' = M$ and the WDs initially have $\Omega_s = 0$.

$\dot{\Omega} \simeq \dot{\Omega}_s$, or $3\Omega/2t_{\text{GW}} \simeq T_0 F(\omega)/I$, and thus \dot{E}_{tide} simplifies to

$$\dot{E}_{\text{tide}} \simeq \frac{3I\Omega^2}{2t_{\text{GW}}} \quad (\text{for } \Omega \gtrsim \Omega_c). \quad (3.84)$$

Since $\dot{E}_{\text{tide}}/\dot{E}_{\text{GW}} \simeq 3I/(\mu a^2) \ll 1$, the orbital decay is dominated by gravitational radiation. Nevertheless, the orbital phase evolution is affected by the tidal energy transfer, and such a phase shift can be measurable for short period binaries such as the recently discovered 12 minute system SDSS J0651 (Brown et al. 2011; see Section 9). Also, low-frequency ($10^{-4} - 10^{-1}$ Hz) gravitational waveforms emitted by the binary, detectable by LISA, will deviate significantly from the point-mass binary prediction. This is in contrast to the case of neutron star binaries (NS/NS or NS/BH) studied pre-

viously (Reisenegger & Goldreich 1994; Lai 1994; Shibata 1994; Ho & Lai 1999; Lai & Wu 2006; Flanagan & Racine 2007), where the resonant mode amplitude is normally too small to affect the gravitational waveforms detectable by ground-based gravitational wave detectors such as LIGO and VIRGO.

The orbital cycle of a WD binary evolves according to

$$dN_{\text{orb}} = \frac{\Omega}{2\pi} \frac{dE_{\text{orb}}}{\dot{E}_{\text{orb}}}. \quad (3.85)$$

Including tidal effects in \dot{E}_{orb} , we find

$$\frac{dN_{\text{orb}}}{d \ln \Omega} = \left(\frac{dN_{\text{orb}}}{d \ln \Omega} \right)_0 \left(1 + \frac{\dot{E}_{\text{tide}}}{\dot{E}_{\text{GW}}} \right)^{-1}, \quad (3.86)$$

where

$$\begin{aligned} \left(\frac{dN_{\text{orb}}}{d \ln \Omega} \right)_0 &= \frac{\Omega t_{\text{GW}}}{3\pi} = \frac{5c^5}{192\pi G^{5/3} \mu M_t^{2/3} (\pi f_{\text{GW}})^{5/3}} \\ &= 2.3 \times 10^9 \left(\frac{M_{\odot}^2}{MM'} \right) \left(\frac{M_t}{2M_{\odot}} \right)^{1/3} \left(\frac{f_{\text{GW}}}{0.01 \text{ Hz}} \right)^{-5/3} \end{aligned} \quad (3.87)$$

is the usual result when the tidal effect is neglected ($f_{\text{GW}} = \Omega/\pi$ is the gravitational wave frequency). Thus, even though $\dot{E}_{\text{tide}}/\dot{E}_{\text{GW}} \ll 1$, the number of “missing cycles” due to the tidal effect,

$$\left(\frac{d\Delta N_{\text{orb}}}{d \ln \Omega} \right)_{\text{tide}} \simeq - \left(\frac{dN_{\text{orb}}}{d \ln \Omega} \right)_0 \frac{\dot{E}_{\text{tide}}}{\dot{E}_{\text{GW}}}, \quad (3.88)$$

can be significant. Since $E_{\text{tide}} \propto I$, proper modelling and detection of the missing cycles would provide a measurement of the moment of inertia of the WD.

3.8.3 Tidal Heating

The tidal energy transfer \dot{E}_{tide} does not correspond to the energy dissipated as heat in the WD, because some of the energy must be used to spin up the WD. Assuming rigid-body

rotation, the tidal heating rate is

$$\dot{E}_{\text{heat}} = \dot{E}_{\text{tide}} \left(1 - \frac{\Omega_s}{\Omega}\right). \quad (3.89)$$

Figure 3.14 shows \dot{E}_{heat} for our three binary WD models. At large binary separations ($\Omega \lesssim \Omega_c$) when $\Omega_s \ll \Omega$, virtually all of the tidal energy transfer to the WD is dissipated as heat. At smaller separations, we have shown that the WD will retain a small degree of asynchronization. Inserting equation (3.80) into equation (3.89), we find

$$\begin{aligned} \dot{E}_{\text{heat}} &\simeq \dot{E}_{\text{tide}} \left(\frac{\Omega_c}{\Omega}\right)^{16/15} \\ &\simeq \frac{3I\Omega^2}{2t_{\text{GW}}} \left(\frac{\Omega_c}{\Omega}\right)^{16/15} \quad (\text{for } \Omega \gtrsim \Omega_c). \end{aligned} \quad (3.90)$$

Thus, as the orbital frequency increases, a smaller fraction of the tidal energy is dissipated as heat. Using equation (3.79) for Ω_c , we have

$$\begin{aligned} \dot{E}_{\text{heat}} &\simeq (6.1 \times 10^{36} \text{ erg s}^{-1}) \kappa_{0.17}^{6/5} \hat{f}^{-1/5} M_1^{29/10} \\ &\quad \times (M_1')^{4/5} R_4^{-1/10} \left(\frac{\Omega}{0.1 \text{ s}^{-1}}\right)^{18/5}. \end{aligned} \quad (3.91)$$

Note that \dot{E}_{heat} is relatively insensitive to \hat{f} , so its precise value is not important. Thus, tidal heating of the WD can become significant well before merger. For example, for our $T_{\text{eff}} = 10800\text{K}$ WD model (with $M = M' = 0.6M_\odot$, $R = 8970 \text{ km}$ and $\hat{f} \sim 20$), we find $\dot{E}_{\text{heat}} \sim 1.2 \times 10^{32} \text{ erg/s}$ at the orbital period $P = 10 \text{ min}$, much larger than the “intrinsic” luminosity of the WD, $4\pi R^2 \sigma_{\text{SB}} T_{\text{eff}}^4 = 3.3 \times 10^{30} \text{ erg/s}$. Note that \dot{E}_{heat} is mainly deposited in the WD envelope, so an appreciable fraction of \dot{E}_{tide} may be radiated, and the WD can become very bright prior to merger. The 12 minute binary SDSS J0651 (Brown et al. 2011) may be an example of such tidally heated WDs (see Section 9).

3.9 Discussion

We have studied the tidal excitation of gravity waves in binary white dwarfs (WDs) and computed the energy and angular momentum transfer rates as a function of the orbital frequency for several WD models. Such dynamical tides play the dominant role in spinning up the WD as the binary decays due to gravitational radiation. Our calculations are based on the outgoing wave boundary condition, which implicitly assumes that the tidally excited gravity waves are damped by nonlinear effects or radiative diffusion as they propagate towards the WD surface. Unlike dynamical tides in early-type main-sequence stars, where gravity waves are excited at the boundary between the convective core and radiative envelope, the excitation of gravity waves in WDs is more complicated due to the various sharp features associated with composition changes in the WD model. We find that the tidal energy transfer rate (from the orbit to the WD) \dot{E}_{tide} is a complex function of the tidal frequency $\omega = 2(\Omega - \Omega_s)$ (where Ω and Ω_s are the orbital frequency and spin frequency, respectively; see Figures 3.7-3.9), and the local maxima of \dot{E}_{tide} scale approximately as $\Omega^5 \omega^5$. For most tidal frequencies considered, the gravity waves are excited near the boundary between the carbon-oxygen core and the helium layer (with the associated dip and sharp rise in the Brunt-Väisälä frequency profile). We have constructed a semi-analytic model that captures the basic physics of gravity wave excitation and reveals that the complex behavior of \dot{E}_{tide} as a function of the tidal frequency arises from the partial trapping of gravity waves in the quasi-resonance cavity provided by the carbon-oxygen core.

We have also calculated the spin and orbital evolution of the WD binary system including the effects of both gravitational radiation and tidal dissipation. We find that above a critical orbital frequency Ω_c [see equation (3.79)], corresponding to an orbital period of about an hour for our WD models, the dynamical tide BEGINS to drive the

WD spin Ω_s towards synchronous rotation, although a small degree of asynchronization is maintained even at small orbital periods: $\Omega - \Omega_s \simeq \Omega_c(\Omega_c/\Omega)^{1/15}$ [see equation (3.80)]. Thus, numerical simulations of WD binary mergers should use synchronized configurations as their initial condition – these may affect the property of the merger product and possible supernova signatures.

We also show that, although gravitational radiation always dominates over tides in the decay of the binary orbit, tidal effects can nevertheless affect the orbital decay and introduce significant phase error to the low-frequency gravitational waveforms. Future detection of gravitational waves from WD binaries by LISA may need to take these tidal effects into account and may lead to measurements of the WDs' moments of inertia. Finally, we have calculated the tidal heating rate of the WD as a function of the orbital period. We show that well before mass transfer or binary merger occurs, tidal heat deposition in the WD envelope can be much larger than the intrinsic luminosity of the star. Thus, the WD envelope may be heated up significantly, leading to brightening of the WD binary well before merger. We plan to study this issue in detail in a future paper.

The recently discovered 12 minute WD binary SDSS J0651 (Brown et al. 2011) can provide useful constraints for our theory. Applying equation (3.79) to this system, we find that the orbital period (12.75 minutes) is sufficiently short that both WDs are nearly (but not completely) synchronized with the orbit. Because of the orbital decay, the eclipse timing changes according to the relation

$$\Delta t = \dot{P}t^2/(2P), \quad (3.92)$$

where t is the observing time. Gravitational radiation gives rise to $\Delta t_{GW} = 5.6s (t/1yr)^2$. Using equation (3.84) to evaluate the orbital decay rate \dot{P}_{tide} due to tidal energy transfer, we find $\Delta t_{\text{tide}} \simeq 0.28s (t/1yr)^2$ (see also Benacquista 2011). Thus, the orbital decay due to tidal effects should be measured in the near future. Also, our calculated heating

rate, equation (3.91), indicates the SDSS J0651 WDs have undergone significant tidal heating, although predicting the luminosity change due to tidal heating requires careful study of the thermal structure of the WDs and knowledge of the location of tidal heating. We note that Piro (2011) also considered some aspects of tidal effects in SDSS J0651, but his results were based on parameterized equilibrium tide theory.

This paper, together with paper I, represents only the first study of the physics of dynamical tides in compact WD binaries, and more works are needed. We have adopted several approximations that may limit the applicability of our results. First, we have not included the effects of rotation (e.g., the Coriolis force) in our wave equations. In addition to modifying the properties of gravity waves (they become generalized Hough waves), rotation also introduces inertial waves that can be excited once the WD spin frequency becomes comparable to the tidal frequency – this may lead to more efficient tidal energy transfer and synchronization. For example, if we parameterize the spinup rate due to various mechanisms (including inertial waves) by equation (87), the critical orbital frequency for the onset of synchronization (Ω_c) is given by equation (3.83). For a stronger tidal torque (larger A), Ω_c is smaller. However, the tidal heating rate at $\Omega \gtrsim \Omega_c$ becomes [cf. equation (3.90)]

$$\dot{E}_{\text{heat}} \simeq \frac{3I\Omega^2}{t_{\text{GW}}} \left(\frac{\Omega_c}{\Omega} \right)^{(3n+1)/(3n)}. \quad (3.93)$$

Thus, for stronger tidal torques, at a given orbital frequency ($\Omega \gtrsim \Omega_c$), the tidal heating rate is reduced because the WD is closer to synchronization.

Second, we have assumed that the WD rotates as a rigid body. As the tidally-excited gravity waves deposit angular momentum in the outer layer of the WD, differential rotation will develop if the different regions of the WD are not well coupled. Thus it may be that the outer layer becomes synchronized with the companion while the core rotates at a sub-synchronous rate, analogous to tidal synchronization in early-type main-sequence

stars (Goldreich & Nicholson 1989). Third, we have implicitly assumed that the outgoing gravity waves are efficiently damped near the WD surface. This may not apply for all WD models or all orbital frequencies. If partial wave reflection occurs, tidal dissipation will be reduced compared to the results presented in this paper except when the tidal frequency matches the intrinsic frequency of a g-mode (cf. Paper I). More detailed studies on nonlinear wave damping (e.g., Barker & Ogilvie 2010; Weinberg et al. 2011) and radiative damping would be desirable.

Finally, we have only studied carbon-oxygen WDs in this paper. Our calculations have shown that the strength of dynamical tides depends sensitively on the detailed internal structure of the WD. Recent observations (see references in Section 1) have revealed many compact WD binaries that contain at least one low-mass helium-core WD. The temperatures of these helium-core WDs tend to be high ($T_{\text{eff}} \gtrsim 10^4 \text{K}$). These observations warrant investigation of tidal effects in hot, helium-core WDs, which have significantly different internal structures from the cool, carbon-oxygen WDs considered in this paper.

CHAPTER 4

TIDAL NOVAE IN COMPACT BINARY WHITE DWARFS

4.1 Introduction¹

Compact white dwarf (WD) binaries (with orbital periods in the range from minutes to hours) are important for several areas of astrophysics. The orbits of these systems decay via the emission of gravitational waves, constituting the largest signals for the next generation of space-based gravitational wave interferometers. Systems of sufficiently short orbital period will merge within a Hubble time, which may produce a variety of exotic objects, such as helium-rich sdB stars, R CrB stars and AM CVn binaries. Most importantly, when the total binary mass is near the Chandrasekhar limit, the merged WDs may collapse into a neutron star or explode as a Type Ia supernova (e.g., Webbink 1984; Iben & Tutukov 1984). Recent studies have provided support for such “double degenerate” progenitors of SNe Ia. (e.g., Gilfanov & Bogdan 2010; Di Stefano 2010; Maoz et al. 2010; Li et al. 2011; Bloom et al. 2012; Schaefer & Pagnotta 2012).

The outcome of a WD binary merger depends on the masses of the WDs and their pre-merger conditions (e.g., Segretain et al. 1997; Yoon et al. 2007; Loren-Aguilar et al. 2009; van Kerkwijk et al. 2010; Dan et al. 2012; Raskin et al. 2012). Most previous studies of pre-merger binary WDs have focused on equilibrium tides and considered tidal dissipation in a parameterized way (e.g., Mochkovitch & Livio 1989; Iben et al. 1998; Willems et al. 2010; Piro 2011). None of these studies has sought to predict the magnitude and location of tidal heating due to dynamical tides, which dominate the tidal responses of the binary WDs.

¹This chapter is based on Fuller & Lai (2012C).

In two recent papers (Fuller & Lai 2011, 2012, hereafter paper I and paper II, respectively), we presented the first *ab initio* calculations of dynamical tides in realistic WD models. In paper I, we considered resonant excitations of WD g-modes during binary decay and showed that the modes reach non-linear amplitudes near the surface of the star. This implies that, rather than exciting discrete g-modes, the binary companion will excite a continuous train of gravity waves, which propagate outward and dissipate in the outer envelope of the WD. We studied such continuous tidally excited waves in paper II. For a canonical carbon-oxygen WD (consisting of a CO core with a He-H envelope), we showed that the outgoing waves are primarily launched at the CO/He transition region, and propagate toward the WD surface, where they are likely dissipated through a combination of non-linear processes and radiative damping. We computed the energy and angular momentum flux carried by the waves in order to predict the orbital and spin evolution of WDs in compact binaries. We found that such dynamical tides cause the binary WDs to be nearly synchronized prior to merger. Furthermore, the tidal heating rate can be quite large at short orbital periods (exceeding tens of solar luminosities just before merger, depending on the system parameters), potentially leading to significant observable signatures.

In this *Letter*, we show that tidal heating may trigger a thermonuclear runaway hydrogen fusion event in a CO WD. The observational consequence of such an event would likely be an outburst that resembles a classical nova. We call this new phenomenon a “Tidal Nova” (TN). Unlike all other types of novae or supernovae, a TN does not rely on mass accretion or collapse. We present a simple two-zone model for the angular momentum evolution of a differentially rotating WD, which we use to calculate the radial tidal heating profile within the WD. We then evolve the WD model including tidal heating to calculate changes in its temperature, luminosity, and internal structure. For a wide range of physically plausible parameters, we demonstrate that tidal heating induces

a thermonuclear runaway event. Finally, we discuss the observational signatures of such an event, and compare our predictions to observations of short-period WD binaries.

4.2 Energy and Angular Momentum of Tidally Excited Gravity Waves

Using the method described in Paper II, we calculate the amplitude of tidally excited gravity waves inside a WD. We consider a circular orbit with angular frequency Ω . The WD spins at an angular frequency Ω_s , and the spin is aligned with the orbit. In the corotating frame, the frequency of the dominant $l = m = 2$ tidal potential is $\omega = 2(\Omega - \Omega_s)$. For a WD of mass M and radius R (and given internal structure) with a companion of mass M' , the energy and angular momentum fluxes carried by the gravity waves can be written as

$$J_z(\Omega, \omega) = T_0(\Omega)F(\omega), \quad (4.1)$$

$$\dot{E}(\Omega, \omega) = \Omega T_0(\Omega)F(\omega), \quad (4.2)$$

where

$$T_0(\Omega) = \frac{GM'^2}{a} \left(\frac{R}{a} \right)^5, \quad (4.3)$$

with $\Omega = \sqrt{GM_t/a^3}$ the orbital angular frequency ($M_t = M + M'$ is the total mass and a is the orbital semi-major axis).

The dimensionless function $F(\omega)$ (similar to the tidal lag angle in the language of equilibrium tide theory) determines the magnitude of wave excitation, and is strongly dependent on the internal structure of the WD and the tidal frequency ω . In Paper II we have calculated $F(\omega)$ for $0.6M_\odot$ CO WD models of various surface temperatures and

slow rotation. We found that $F(\omega)$ is an erratic function of ω because of the “quasi-resonance cavity” formed by the CO core inside the He/H shell. However, because of the strong dependence of $F(\omega)$ on ω [the envelope of $F(\omega)$ approximately scales as ω^5], at sufficiently short orbital periods, tidal spin-up combined with orbital decay via gravitational radiation ensure that ω remains nearly constant. The orbital period at which this transition occurs is $P_c \simeq 40$ minutes, depending on the WD masses and temperatures [see Eq. (79) of Paper II]. At periods $P \lesssim P_c$, the tidal energy transfer rate is

$$\dot{E} \simeq \frac{3I\Omega^2}{2t_{\text{GW}}}, \quad (4.4)$$

where I is the moment of inertia of the WD, and $t_{\text{GW}} = |a/\dot{a}|$ is the binary inspiral time due to gravitational radiation,

$$t_{\text{GW}} = 4.2 \times 10^5 \text{ yr} \left(\frac{M_\odot^2}{MM'} \right) \left(\frac{M_t}{2M_\odot} \right)^{1/3} \left(\frac{P}{10 \text{ min}} \right)^{8/3}. \quad (4.5)$$

When the outgoing gravity waves damp in the WD envelope and locally deposit their angular momentum, some of the wave energy is converted into rotational kinetic energy, while the rest is converted to heat. The heating rate is

$$\dot{E}_{\text{heat}} = \dot{E} \left(1 - \frac{\Omega_s}{\Omega} \right), \quad (4.6)$$

assuming $\Omega_s < \Omega$ throughout the WD. If the WD maintains some differential rotation, Ω_s in the above equation should be the rotation rate of the layer in which the waves damp, and heat will also be generated through viscous angular momentum transport.

4.3 Two Zone Model for Tidal Heat Deposition

Our calculations indicate that the gravity waves reach non-linear amplitudes and break in the outer layers of the WD. The location of wave breaking depends on various parame-

ters (e.g., orbital and tidal frequencies), but is always at $r \gtrsim 0.92R$ and the exterior mass $\Delta M \lesssim 10^{-4}M$ (Paper II). Since a small fraction of the stellar mass absorbs the entire angular momentum flux, the outer layer spins up rapidly. If it spins up faster than angular momentum can be transported to the core, the outer layer will rotate synchronously with the orbit. Outgoing waves approaching the synchronized layer will be absorbed near corotation and deposit their angular momentum, causing the synchronized layer to move to larger depths (see Goldreich & Nicholson 1989).

We consider a simple two-zone model for the spin evolution of the WD. In this model, the envelope of the star rotates synchronously with the orbit ($\Omega_{\text{env}} = \Omega$), while the core rotates sub-synchronously ($\Omega_{\text{core}} < \Omega$). The envelope and core are coupled, with angular momentum being transferred to the core according to a parameterized coupling time, t_{coup} . The angular momentum of the core-envelope system evolves according to

$$\frac{d}{dt}(I_{\text{env}}\Omega_{\text{env}}) = \dot{J}_z(\Omega, \omega_{\text{core}}) - \frac{I_{\text{env}}}{t_{\text{coup}}}(\Omega_{\text{env}} - \Omega_{\text{core}}), \quad (4.7)$$

$$\frac{d}{dt}(I_{\text{core}}\Omega_{\text{core}}) = \frac{I_{\text{env}}}{t_{\text{coup}}}(\Omega_{\text{env}} - \Omega_{\text{core}}), \quad (4.8)$$

where $I_{\text{env}} = I - I_{\text{core}}$ is the moment of inertia of the envelope. Here, \dot{J}_z is the angular momentum flux which can be calculated from equation (4.1). We have assumed that the gravity waves are excited in the core and absorbed in the envelope². Consequently, the angular momentum source term \dot{J}_z is only present in the envelope evolution equation, although it is dependent on the tidal frequency in the core, $\omega_{\text{core}} = 2(\Omega - \Omega_{\text{core}})$. Using $\Omega_{\text{env}} = \Omega$, equations (4.7) and (4.8) can be integrated to find I_{env} and Ω_{core} as a function of time or orbital period. The mass ΔM_{env} of the envelope corresponds to $I_{\text{env}} \simeq (2/3)\Delta M_{\text{env}}R^2$.

The thickness (or ΔM_{env}) of the envelope is dependent on the parameter t_{coup} . In

²This assumption is valid as long as the core-envelope boundary is above the C/He transition layer (with an exterior mass $\Delta M \approx 10^{-2}M_{\odot}$), which is the region where the outgoing gravity waves are excited.

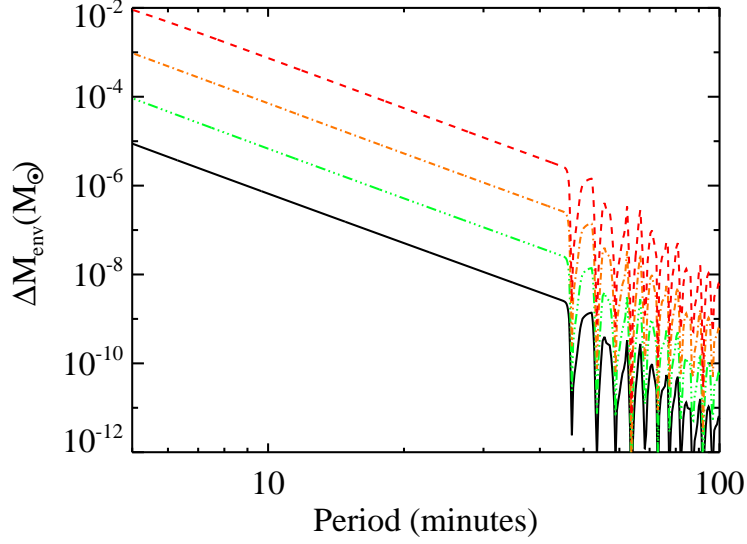


Figure 4.1: The mass ΔM_{env} of the synchronized envelope as a function of orbital period for a $0.6M_{\odot}$ CO WD model with a $0.3M_{\odot}$ companion. The solid (black) line has $t_{\text{coup}} = 1$ yr, the dot-dot-dashed (green) line $t_{\text{coup}} = 10$ yr, the dot-dashed (orange) line $t_{\text{coup}} = 10^2$ yr, and the dashed (red) line $t_{\text{coup}} = 10^3$ yr.

stably stratified stars like WDs, angular momentum can be transported by magnetic fields. In the presence of a poloidal field B connecting the core and envelope, t_{coup} can be estimated from the Alfvén wave crossing time,

$$t_A = \frac{R \sqrt{4\pi\rho}}{B} \simeq 10^2 \text{ yr} \left(\frac{10^3 \text{ G}}{B} \right) \quad (4.9)$$

for our CO WD model. For WDs without an intrinsic magnetic field, angular momentum may be transported via the Tayler-Spruit dynamo (Spruit 2002). To estimate t_{coup} , we calculate the effective viscosity for angular momentum transport via the Tayler-Spruit dynamo, ν_{TS} , as outlined in Spruit 2002.³ We find $t_{TS} \equiv \int_0^R (r/\nu_{TS}) dr \approx 10^3 \text{ yr} (P/45 \text{ min})^{3/2}$. Thus we expect the coupling time to lie in the range $t_{\text{coup}} \lesssim 10^3$ yr for the short orbital periods of interest.

³For simplicity, we have calculated the viscosity ν_{TS} without including the effects of composition gradients in the WD [see equation (32) in Spruit 2002]. A more realistic estimate of the rotational profile of the WD should take composition gradients into account.

Figure 4.1 plots the value of ΔM_{env} as a function of orbital period for our $0.6M_{\odot}$ WD model with a $0.3M_{\odot}$ companion, using values of t_{coup} ranging from 1yr to 10^3yr . We begin our calculation at $P_{\text{orb}} > 1\text{hr}$ and use $I_{\text{env},0} = 0$ and $\Omega_{\text{core},0} = 0$, as appropriate at long orbital periods where tidal effects are negligible. We see that for the range of t_{coup} considered, ΔM_{env} remains small ($\lesssim 10^{-2}M_{\odot}$) at all orbital periods of interest. Thus, the synchronized envelope most likely does not extend down to the C/He transition layer where the gravity waves are excited, justifying our assumption that \dot{J}_z is a function of Ω_{core} . However, the envelope does extend to very large optical depths, suggesting that binary WDs may be observed to be synchronized at large orbital periods even if their cores are not synchronized. Note that since $I_{\text{env}} \ll I$, the core of the star contains most of the angular momentum, and its spin evolves in the same manner as discussed in Paper II.

4.4 Tidal Heating and Unstable Nuclear Burning

In the two-zone model discussed in section 4.3, the total tidal heating rate \dot{E}_{heat} may be calculated from equation (4.6) with $\Omega_s = \Omega_{\text{core}}$, and the tidal heat is deposited entirely at the base of the synchronized envelope where the exterior mass is $\Delta M = \Delta M_{\text{env}}$. In a real WD, the heat deposition will occur over a range of depths that depends on the details of wave breaking and viscous angular momentum transport. For simplicity, here we choose to deposit the tidal heat uniformly per unit mass in the synchronized envelope. The heating rate per unit mass, $\dot{\epsilon}_{\text{heat}}$, is then

$$\begin{aligned} \dot{\epsilon}_{\text{heat}} &= 0 \quad \text{for} \quad \Delta M > \Delta M_{\text{env}} \\ \dot{\epsilon}_{\text{heat}} &= \frac{\dot{E}_{\text{heat}}}{\Delta M_{\text{env}}} \quad \text{for} \quad \Delta M < \Delta M_{\text{env}}. \end{aligned} \tag{4.10}$$

Although the radial dependence of this heating function is unlikely to be realistic, we find that the results below are not strongly dependent on the form of $\dot{\epsilon}_{\text{heat}}$.

To understand the effect of tidal heating on the WD properties, we evolve WD models using the extra heating term calculated via equation (4.10). We use the one-dimensional stellar evolution code MESA (Paxton et al. 2010) to evolve our WD models, starting from an initial orbital period of one hour. We present results for a $0.6M_{\odot}$ CO WD model with a $\sim 10^{-4}M_{\odot}$ hydrogen shell and a $0.3M_{\odot}$ companion.

Figure 4.2 displays the surface temperature as a function of orbital period for our tidally heated WD. For comparison, we also show the temperature of a non-tidally heated WD and the “tidal heating temperature”, defined as

$$T_{\text{eff,heat}} = \left(\frac{\dot{E}_{\text{heat}}}{4\pi R^2 \sigma} \right)^{1/4}. \quad (4.11)$$

At long orbital periods ($P \gtrsim 45$ minutes), the tidal heating has little effect on the surface temperature of the WD. At shorter periods ($P \lesssim 30$ minutes), the temperature becomes substantially larger due to tidal heating. Several of the curves end abruptly due to the ignition of a thermonuclear runaway event, at which point we terminate our evolution calculations.

For small values of t_{coup} , the tidal heat is deposited at shallow depths and quickly diffuses to the surface such that the luminosity of the WD is $L \simeq L_0 + \dot{E}_{\text{heat}}$, where L_0 is the luminosity of a non-tidally heated WD. However, for larger values of t_{coup} , most of the tidal heat is deposited deeper in the WD where it cannot quickly diffuse outward. This leads to lower surface temperatures, although the internal temperature may increase substantially.

Figure 4.3 shows the interior temperature profile of our WD at three different orbital periods, using $t_{\text{coup}} = 10^3$ yr. At long orbital periods, the temperature profile is similar

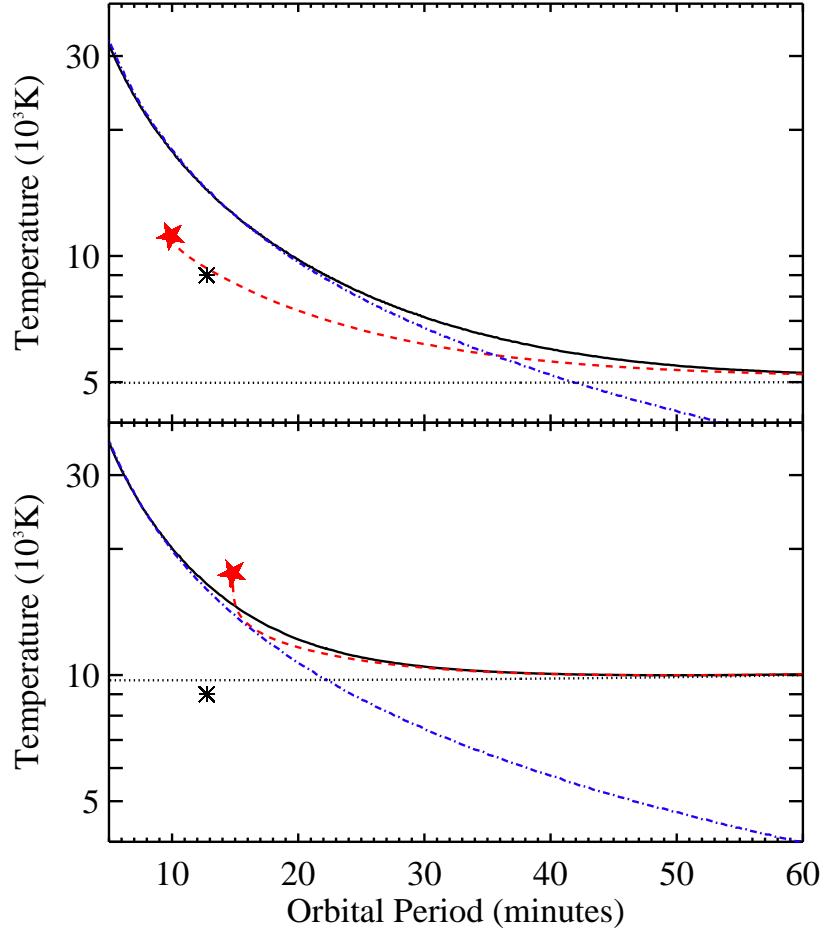


Figure 4.2: The surface temperature of the $0.6M_{\odot}$ CO WD model with a $0.3M_{\odot}$ companion as a function of orbital period, for initial temperatures of 5000 K (top) and 10^4 K (bottom). The solid black lines are calculated with $t_{\text{coup}} = 1$ yr while the dashed (red) lines are calculated with $t_{\text{coup}} = 10^3$ yr. The dotted lines are calculated for a WD with no tidal heating and the same initial temperature. The (blue) dot-dashed lines correspond to equation (4.11). The (red) stars mark the points at which tidal novae occur. The asterisks mark the position of the secondary of the 12.75 minute binary WD system SDSS J065133+284423 (Brown et al. 2011).

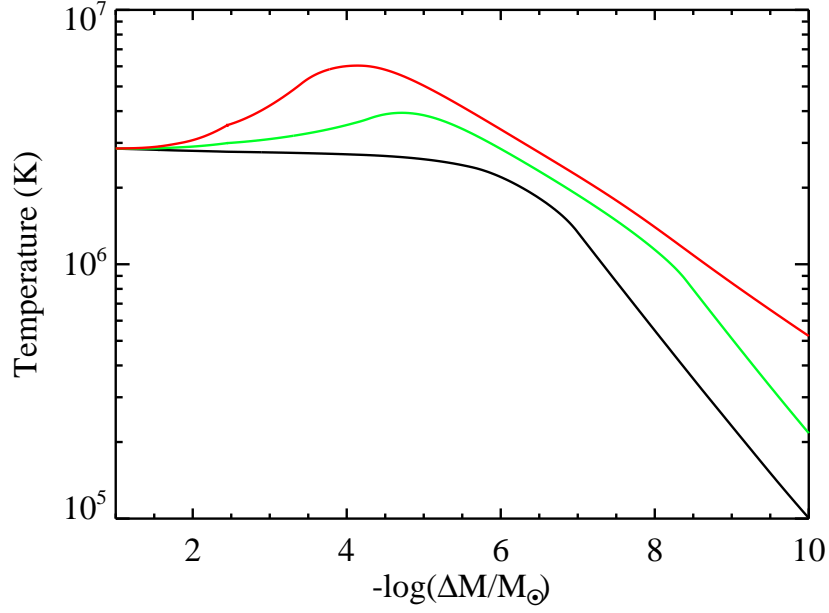


Figure 4.3: Temperature profile of the WD (as a function of exterior mass ΔM) at orbital periods of 45 minutes (black), 20 minutes (green), and 12 minutes (red). These temperatures are calculated for the $0.6M_{\odot}$ WD model with an initial surface temperature of $T_{\text{eff}} = 5000$ K, a $0.3M_{\odot}$ companion and $t_{\text{coup}} = 10^3$ yr. In this model, the H shell extends down to $\Delta M \approx 10^{-4}M_{\odot}$.

to that of a non-tidally heated WD. As the orbital period decreases, the interior heats up, with the local temperature maximum at $\Delta M \sim \Delta M_{\text{env}}$. If the base of the hydrogen layer reaches a temperature of $\sim 10^7$ K, hydrogen burning will be ignited.

In the depicted model, the layer just above the He/H transition (at $\Delta M \approx 10^{-4}M_{\odot}$) is composed of largely degenerate hydrogen gas. The ignition of fusion in this layer can thus spark a thermonuclear runaway. In general, our calculations show that these *tidal novae* occur only in initially cool WDs ($T_{\text{eff}} \lesssim 1.2 \times 10^4$ K in the absence of tidal heating). They do not occur in hotter WDs because the hydrogen is not degenerate and can burn stably. Also, tidal novae require that the waves deposit some of the heat near the base of the hydrogen layer, i.e., $10^{-5}M_{\odot} \lesssim \Delta M_{\text{env}} \lesssim 10^{-3}M_{\odot}$. Overall, we find that the tidal novae occur at orbital periods $5 \text{ min} \lesssim P_{\text{orb}} \lesssim 20 \text{ min}$, depending on the location of heat deposition, initial temperature of the WD, and companion mass.

4.5 Discussion

We do not attempt to predict the detailed observational signal of a tidal nova (TN), but we speculate that it may be very similar to a classic nova. However, in contrast to classical novae in CVs, a TN would occur in a compact system with no evidence for mass transfer. Our results indicate that a TN would precede the beginning of mass transfer or merger by about $t_{\text{GW}}/4 \sim 10^5 - 10^6$ yrs [see Eq. (3.76)].

In most classical novae, the initial outburst is followed by a period of stable hydrogen burning at near the Eddington luminosity, in which the hydrogen shell of the WD inflates to a radius of order R_\odot . However, the ultracompact nature of the WD system involved in a TN (where $a \sim R_\odot/4$) may preclude such a phase because the stably burning hydrogen shell would inflate beyond the WD's Roche lobe. This shell may then accrete on to the companion star or be ejected from the system. Therefore, we expect most of the hydrogen to be burned or ejected during in a TN. In the absence of mass transfer to supply fresh hydrogen, recurrent novae would be unlikely. Thus, the occurrence rate of these TN may be comparable to that of WD mergers involving a CO WD.

Our theory can be constrained by comparing the prediction of our tidal heating calculations to observed compact WD binaries. The 12.75 minute system SDSS J065133+284423 provides the best opportunity (Brown et al. 2011). This system is composed of a primary with $T_{\text{eff}} = 16400$ K and mass $0.25M_\odot$, and a secondary with $T_{\text{eff}} \approx 9000$ K and mass $0.55M_\odot$. Comparison with Figure 4.2 indicates that the luminosity of the secondary is likely dominated by tidal heating. Our result for a CO WD with an initial temperature of 5000 K and a value of $t_{\text{coup}} = 10^3$ yr is most consistent with the observed temperature of the secondary. These results indicate that a TN may occur in this system in the future.

In principle, tidal heating may change the structure of the WD enough to alter the dynamics of gravity wave propagation. However, we find that this is not the case (i.e., no interior convection zone forms), with the exception of a thermonuclear runaway event. Our simple two-zone model for the WD obviously needs improvement, and we have neglected the effects of mixing induced by the breaking gravity waves and viscous angular momentum transport. If the mixing is strong enough to smooth out the WD composition gradients, the dynamics of gravity wave excitation and tidal heat deposition may be altered. Observations of the ejecta of classical novae indicate substantial enrichment with core elements, although the mixing mechanism is not well understood (Truran 2002). These and other aspects of TN in compact WD binaries warrant further study.

CHAPTER 5

**DYNAMICAL TIDES IN COMPACT WHITE DWARF BINARIES: HELIUM
CORE WHITE DWARFS, TIDAL HEATING, AND OBSERVATIONAL
SIGNATURES**

5.1 Introduction¹

In the last decade, compact white dwarf (WD) binaries (with orbital periods in the range of minutes to hours) have become increasingly important for several topics in astrophysics. The orbits of these systems decay via the emission of gravitational waves, constituting the largest signals for next generation space-based gravitational wave detectors. Systems of sufficiently short orbital period will merge within a Hubble time, the result of which may create a variety of exotic astrophysical systems, e.g., isolated sdB and sdO stars, R CrB stars, AM CVn binaries, or high-mass neutron stars. Of most importance, merging WDs may trigger type Ia supernovae (e.g., Webbink 1984; Iben & Tutukov 1984). Recent observations and numerical simulations have provided some support for such “double degenerate” progenitors of SNe Ia. (e.g., Gilfanov & Bogdan 2010; Di Stefano 2010; Maoz et al. 2010; Li et al. 2011; Bloom et al. 2012; Schaefer & Pagnotta 2012, Gonzalez Hernandez et al. 2012).

The outcome of a WD binary merger depends on the masses and compositions of the WDs and their pre-merger conditions (e.g., Segretain et al. 1997; Yoon et al. 2007; Loren-Aguilar et al. 2009; van Kerkwijk et al. 2010; Dan et al. 2012; Raskin et al. 2012). Despite the broad significance of WD mergers in astrophysics, detailed studies of the pre-merger conditions have been relatively scarce. Most studies have focused on equilibrium (non-dynamical) tides (e.g., Iben et al. 1998, Willems et al. 2010) or have

¹This chapter is based on Fuller & Lai (2013).

parameterized the tidal effects (e.g., Piro 2011). None of these studies have sought to calculate both the magnitude and location of tidal heating, and none of them can be used to predict observational signatures of tidal heating. Such predictions are becoming increasingly important as ongoing surveys continue to uncover new compact WD binary systems (e.g. Mullally et al. 2009; Kulkarni & van Kerkwijk 2010; Steinfadt et al. 2010a; Kilic et al. 2012; Brown et al. 2011; see Marsh 2011 for a review).

This paper is the fourth in a series (see Fuller & Lai 2011, 2012a, 2012b, hereafter Papers I, II, and III) where we systematically study dynamical tides and their observational consequences in compact WD binaries. In Paper I, we calculated the tidal excitation of discrete g-modes in carbon-oxygen (CO) WDs. We showed that the excited g-modes reach very non-linear amplitudes near the surface of the star, even far from resonance. Thus, rather than exciting discrete g-modes, the binary companion will excite a continuous train of gravity waves that propagate towards the surface of the WD, where they are likely dissipated through a combination of non-linear processes and radiative damping.

In Paper II, we calculated the gravity wave amplitude as a function of orbital frequency using an outgoing wave boundary condition (i.e., assuming the waves damp completely in the outer layers of the WD rather than reflecting at the surface). Our calculations showed that the train of gravity waves is launched at the C-He composition gradient in the CO WD models we used. We then computed the energy and angular momentum flux carried by the waves in order to predict the orbital and spin evolution of WDs in compact systems. We found that tidal effects are negligible at large separations (orbital periods larger than about an hour), but become increasingly important at smaller periods, causing the WDs to be nearly synchronized upon merger. Furthermore, we found that the heating rate can be quite large at short orbital periods (exceeding $100L_{\odot}$ just before merger, depending on the system parameters), potentially leading to

an observable tidal heating signature. In Paper III, we showed that localized tidal heating in the semi-degenerate region of the hydrogen envelope can lead to thermonuclear run-aways, “tidal novae”, potentially burning the hydrogen layer off the WD in an explosive event similar to a classical nova.

In this paper, we extend our calculations to models of low mass ($M \approx 0.3M_{\odot}$) helium (He) WDs, which are relatively common among observed short-period WD binary systems (Kilic et al. 2012). Since these WDs do not have a C-He compositional gradient (although they do contain a helium-hydrogen composition gradient), the wave excitation mechanism and the resultant amplitude of the gravity waves may be quite different from their higher-mass CO counterparts. We compute the energy and angular momentum fluxes carried by the waves, and the consequent effect on the orbital and spin evolution of He WDs in compact systems.

We also attempt to calculate the observational signatures of tidal heating in both CO and He WDs. Although our calculations of the wave amplitudes are performed in the linear theory, we use these amplitudes to estimate where the waves become non-linear as they propagate toward the surface of the WD. If the waves become sufficiently non-linear, they will overturn the stratification and break, depositing their energy and angular momentum into the surface layers of the star. Also, the WD envelope can develop differential rotation due to the deposition of angular momentum carried by the gravity waves. This in turn produces a “critical layer” at which wave absorption takes place due to corotation resonance. We examine the criteria for non-linear wave breaking and for wave absorption at the critical layer, and estimate where the outgoing waves deposit their energy in He and CO WDs. We then evolve WD models using the MESA stellar evolution code (Paxton et al. 2011) including a tidal heating term (which is a function of both radius and time) calculated according to various criteria. The evolution code

allows us to monitor changes in the WD properties as a function of orbital period and thus allows us to make predictions of observational signatures for WD binaries as a function of their orbital period.

The paper is organized as follows. In Section 5.2, we calculate the amplitude of gravity waves in a He WD model as a function of the tidal forcing frequency, and compare these results to those previously obtained for CO WD models. In Section 5.3, we compute the orbital and spin evolution of a He WD in a compact binary system and estimate the magnitude of the tidal heating. In Section 5.4, we estimate where in the WD the waves will undergo non-linear wave breaking or experience wave absorption at a critical layer, and how the location depends on the orbital period and the internal structure of the WD. In Section 5.5, we evolve WD models under the influence of tidal heating and predict observational signatures of the tidal heating. Finally, in Section 5.6, we compare our predictions to observed systems, and we discuss the uncertainties in our results and how they may be remedied by future studies.

5.2 Tidal Dissipation in Helium WDs

5.2.1 Wave Dynamics

To calculate the amplitude of the tidally excited gravity waves in a He WD model, we use the same method described in Paper II. Here we review only the basic concepts and introduce our notation.

The Lagrangian displacement associated with the dominant (quadrupole) component

of the tidal potential has the form

$$\boldsymbol{\xi}(\mathbf{r}, t) = [\xi_r(r)\hat{r} + \xi_\perp(r)r\nabla_\perp]Y_{22}(\theta, \phi)e^{-i\omega t}, \quad (5.1)$$

where ξ_r is the radial component of the displacement and ξ_\perp is the perpendicular displacement, r is the radius, Y_{22} is the $l = m = 2$ spherical harmonic, and ω is the tidal forcing frequency. In this paper, we consider the orbit of the companion to be circular and aligned such that $\omega = 2(\Omega - \Omega_s)$, where Ω is the angular orbital frequency and Ω_s is the angular spin frequency. The displacement $\boldsymbol{\xi}$ can be further decomposed into an equilibrium component $\boldsymbol{\xi}^{\text{eq}}$ that describes the quasi-static ellipsoidal distortion of the star, and a dynamical component $\boldsymbol{\xi}^{\text{dyn}}$ which describes the non-equilibrium wavelike response of the star to the tidal forcing. Appendix A describes the details (improving upon the treatment of Paper II) of decomposing the equilibrium and dynamical components.

We calculate the waveform of the tidally excited gravity waves by solving the linear inhomogeneous wave equations for stellar oscillations. At the center of the star, we impose the regularity boundary condition. At the outer boundary near the stellar surface, we use the (outgoing) radiative boundary condition:

$$\frac{d}{dr}\xi_\perp^{\text{dyn}} = \left[\frac{-(\rho r^2/k_r)'}{2(\rho r^2/k_r)} - ik_r \right] \xi_\perp^{\text{dyn}}, \quad (5.2)$$

where ρ is the density, k_r is the radial wave number,

$$k_r^2 \simeq \frac{l(l+1)(N^2 - \omega^2)}{\omega^2 r^2}, \quad (5.3)$$

and N is the Brunt-Vaisala frequency. Equation 5.3 is valid as long as $\omega^2 \ll L_l^2$, where

$$L_l^2 = \frac{l(l+1)c_s^2}{r^2} \quad (5.4)$$

is the square of the Lamb frequency, and c_s is the sound speed.

Upon solving the oscillation equations to calculate $\xi_r(r)$ and $\xi_\perp(r)$ for a given value of ω , the angular momentum flux carried by the wave is

$$J_z(r) = 2m\omega^2\rho r^3 \text{Re}\left[i\xi_r^{\text{dyn}*}\xi_\perp^{\text{dyn}}\right]. \quad (5.5)$$

When evaluated at the outer boundary $r = r_{\text{out}}$, equation (5.5) represents the rate at which the dynamical tide deposits angular momentum into the WD envelope. The outgoing angular momentum and energy fluxes can be written as

$$T_{\text{tide}} = \dot{J}_z(r_{\text{out}}) = T_0 F(\omega), \quad (5.6)$$

and

$$\dot{E}_{\text{tide}} = \Omega T_0 F(\omega), \quad (5.7)$$

where

$$T_0 = \frac{GM'^2}{a} \left(\frac{R}{a}\right)^5, \quad (5.8)$$

M' is the mass of the companion star, and a is the orbital semi-major axis. The dimensionless function $F(\omega)$ describes the magnitude of wave excitation in the WD, and is strongly dependent on the internal structure of the WD and the tidal frequency ω . In terms of the commonly used parameterization of tidal dissipation (Goldreich & Soter 1966; Alexander 1973; Hut 1981), $F(\omega)$ is related to the tidal phase lag and tidal Q by $F(\omega) = 3k_2\delta_{\text{lag}} = 3k_2/(2Q)$ (assuming $\Omega > \Omega_s$), where k_2 is the tidal Love number.

5.2.2 Wave Excitation in He WDs

We perform our calculations on an $M = 0.3M_\odot$ He WD with a $\sim 1.2 \times 10^{-3}M_\odot$ hydrogen envelope, generated using the MESA stellar evolution code (Paxton et al. 2011). We evolve the same WD to surface temperatures of $T_{\text{eff}} = 18000\text{K}$, $T_{\text{eff}} = 12000\text{K}$, and $T_{\text{eff}} = 6000\text{K}$, with respective radii of $R = 2.0 \times 10^9\text{cm}$, $R = 1.6 \times 10^9\text{cm}$, and $R =$

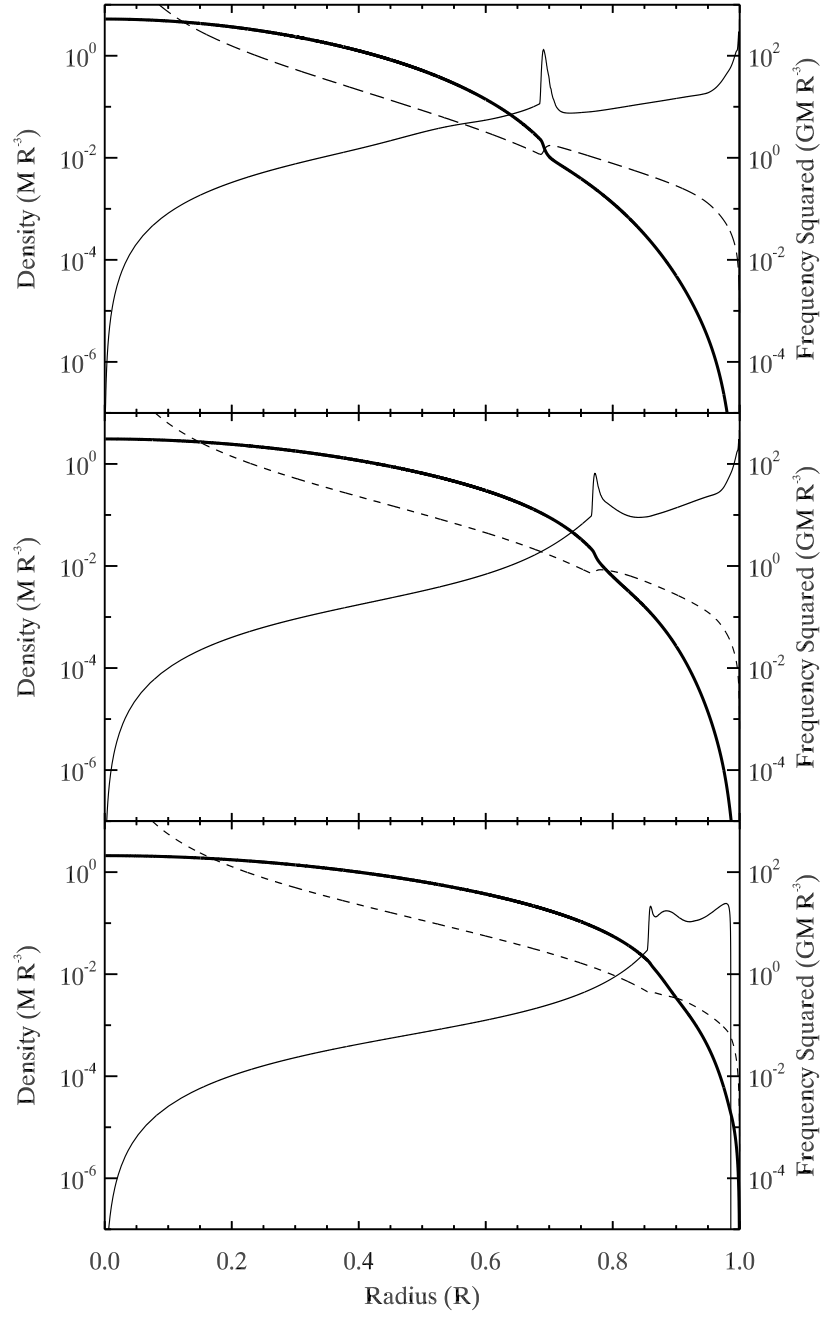


Figure 5.1: Propagation diagrams showing ρ (thick solid line), N^2 (thin solid line), and L_2^2 (dashed line) as a function of radius in our $M = 0.3M_\odot$ He core WD model with a $\sim 10^{-3}M_\odot$ hydrogen shell. The three panels are for WDs with $T_{\text{eff}} = 18000\text{K}$ (top), $T_{\text{eff}} = 12000\text{K}$ (middle), and $T_{\text{eff}} = 6000\text{K}$ (bottom). All quantities are plotted in units with $G = M = R = 1$.

$1.4 \times 10^9 \text{cm}$. Figure 5.1 shows propagation diagrams for our stellar models. The spike in N^2 at $r \simeq 0.8R$ is due to the He-H composition gradient.

We have calculated the fluid displacement $\xi(r)$ as a function of r for tidally excited gravity waves at many values of ω . Figure 5.2 shows the wave function $\xi_\perp(r)$ and dimensionless angular momentum flux $F(\omega, r) = \dot{J}_z(r)/T_0$ as a function of radius for $\omega = 3 \times 10^{-2}$, in units where $G = M = R = 1$. The location of wave excitation can be determined by examining $F(\omega, r)$. Below the wave excitation region there exists both an ingoing and outgoing wave such that $F(\omega, r) \approx 0$, while above the excitation region there exists only an outgoing wave such that $F(\omega, r) \approx \text{constant}$. It is evident from Figure 5.2 that the wave is excited at the sudden increase in N^2 associated with the He-H composition gradient.

Figure 5.3 displays $F(\omega)$ as a function of ω , and reveals that $F(\omega)$ is an erratic, non-monotonic function of ω . The reason is that the core of the WD behaves as a quasi-cavity containing in-going and out-going waves. At some frequencies, these waves constructively interfere at the cavity boundary (the He-H composition gradient) and create a large outgoing wave in the WD envelope. At other frequencies, the waves exhibit destructive interference, creating a small outgoing wave in the envelope (see Paper II for more details). In Paper II we found that on average, $F(\omega)$ has the rough scaling $F(\omega) \propto \omega^5$ for CO WDs, whereas we find here that in a rough sense $F(\omega) \propto \omega^6$ in our He WD models. Moreover, the magnitude of $F(\omega)$ of He WDs is smaller by nearly five orders of magnitude over the frequency range of interest.

The smaller values of $F(\omega)$ in He WDs stem from the dynamics of gravity wave excitation at a composition gradient. In Paper II, we showed that gravity wave excitation due to a composition gradient in CO WDs has a rough scaling

$$F(\omega) \approx \hat{f} \hat{\omega}^5, \quad (5.9)$$

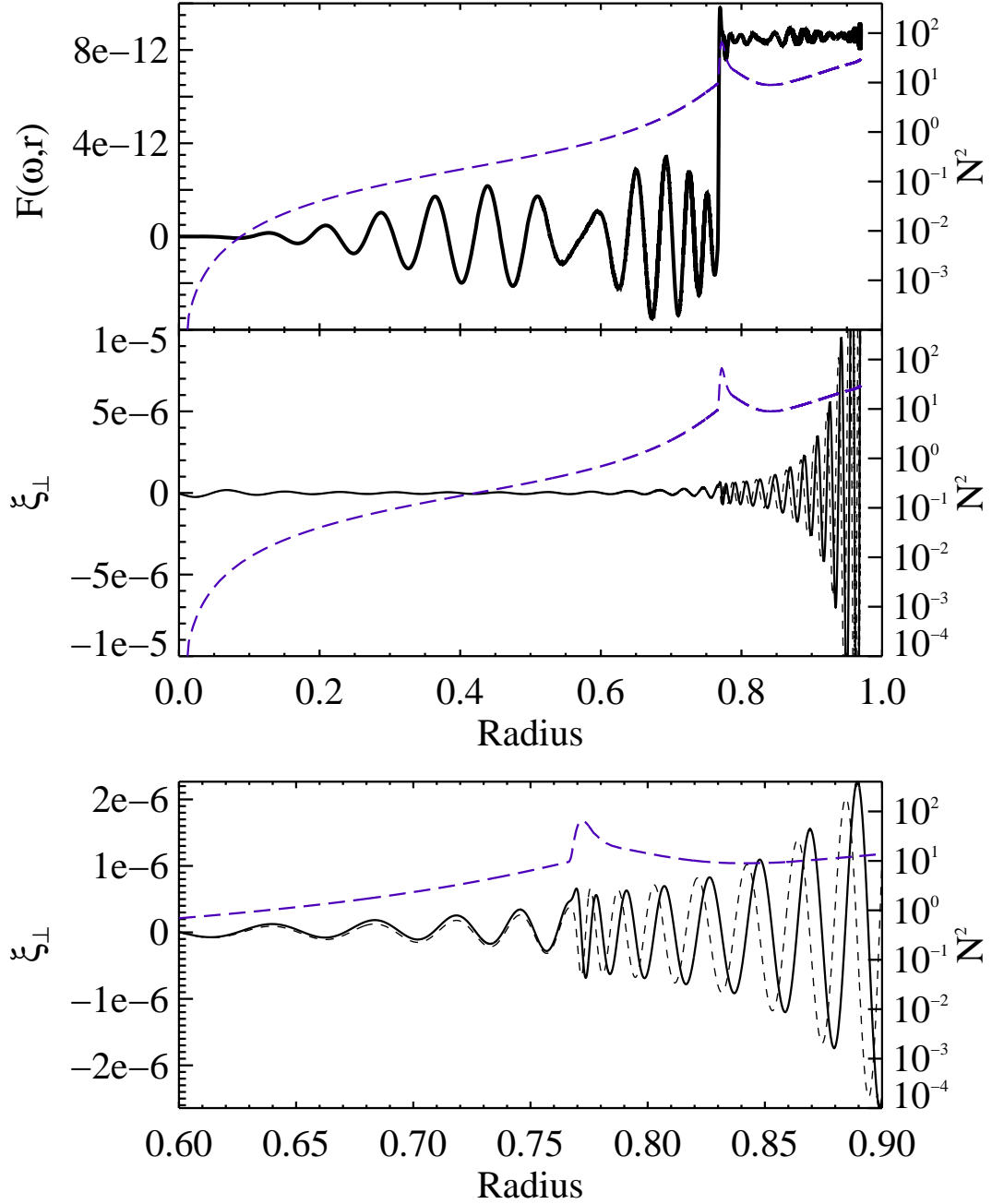


Figure 5.2: Dynamical tide in our He WD model with $T_{\text{eff}} = 12000\text{K}$ driven by a companion of mass $M' = M$, with the tidal frequency $\omega = 3.0 \times 10^{-2}$. Top: The value of $F(\omega, r) = \dot{J}_z(r)/T_0$ (dark solid line) as a function of radius, with \dot{J}_z calculated from equation (5.5). All values are plotted in units of $G = M = R = 1$. Bottom: The real part of ξ_{\perp}^{dyn} (dark solid line) and imaginary part of ξ_{\perp}^{dyn} (dark dashed line) as a function of stellar radius. The value of N^2 has been plotted (dashed purple line) in each panel.

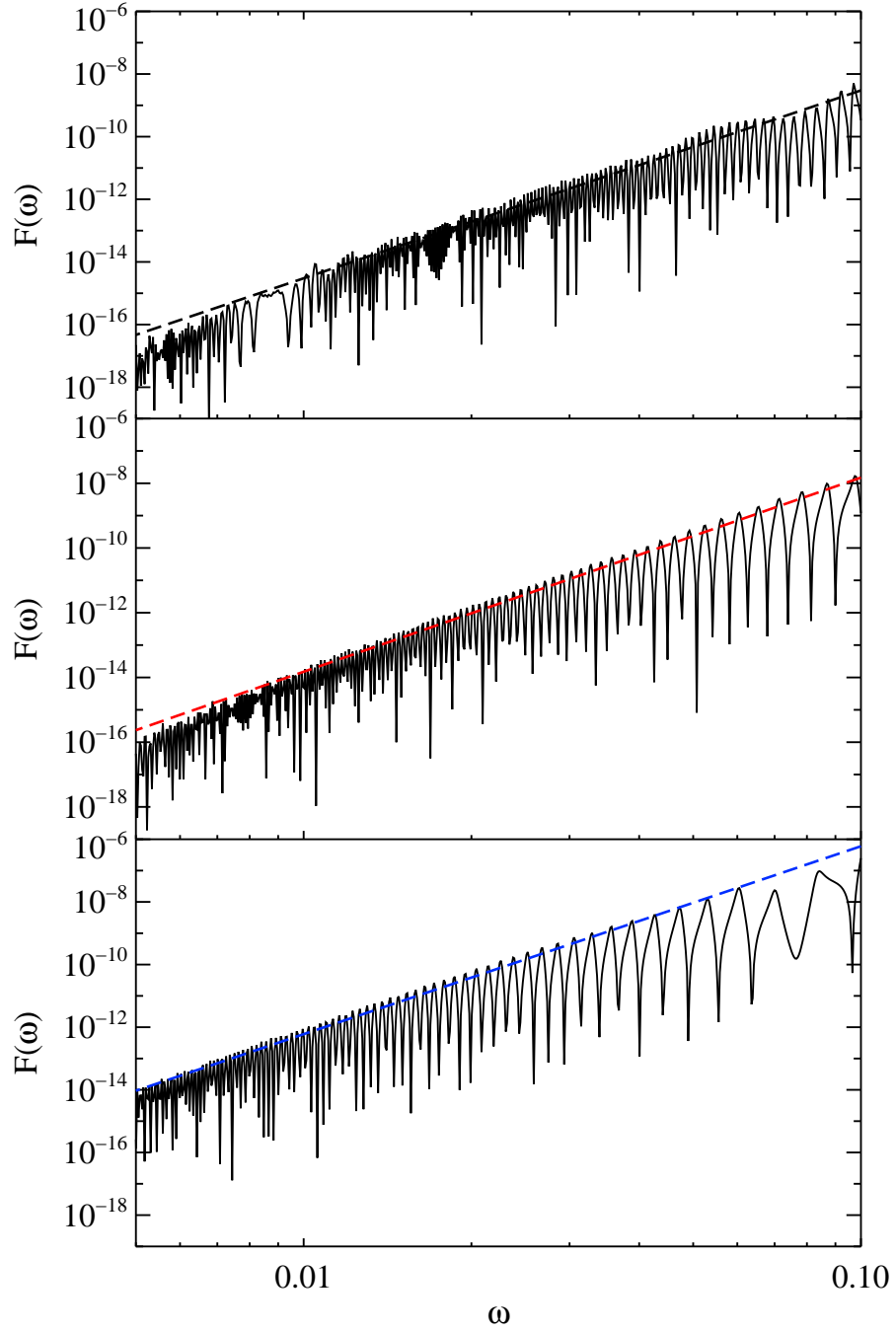


Figure 5.3: The dimensionless tidal torque $F(\omega) = \dot{J}_z/T_o$ [see equation (5.6)] carried by outgoing gravity waves as a function of the tidal frequency ω for our He WD model with $T_{\text{eff}} = 18000\text{K}$ (top), $T_{\text{eff}} = 12000\text{K}$ (middle), and $T_{\text{eff}} = 6000\text{K}$ (bottom). The dashed lines correspond to $F(\omega) = 3 \times 10^{-3} \omega^6$ (top), $F(\omega) = 1.5 \times 10^{-2} \omega^6$ (middle), and $F(\omega) = 6 \times 10^{-1} \omega^6$ (bottom). The frequency is in units of $G = M = R = 1$.

where the notation \hat{x} indicates that the quantity x should be evaluated in dimensionless units with $G = M = R = 1$, and \hat{f} is approximately given by

$$\begin{aligned}\hat{f} &\approx \frac{\hat{\rho}_a \hat{r}_a^7 \hat{N}_a}{\hat{N}_b^4 \hat{g}_a^2} \left(\frac{\hat{r}_a}{\hat{H}_a} \right)^4 \\ &\approx 10^{-1} \left(\frac{\hat{\rho}_a}{10^{-2}} \right) \left(\frac{\hat{r}_a}{0.75} \right)^{11} \left(\frac{\hat{N}_a}{8} \right) \left(\frac{\hat{N}_b}{3} \right)^{-4} \left(\frac{\hat{g}_a}{2} \right)^{-2} \left(\frac{\hat{H}_a}{0.1} \right)^{-4} \quad \text{for He WDs,} \\ &\approx 10^3 \left(\frac{\hat{\rho}_a}{10^{-3}} \right) \left(\frac{\hat{r}_a}{0.8} \right)^{11} \left(\frac{\hat{N}_a}{1.5} \right) \left(\frac{\hat{N}_b}{0.3} \right)^{-4} \left(\frac{\hat{g}_a}{1.5} \right)^{-2} \left(\frac{\hat{H}_a}{0.05} \right)^{-4} \quad \text{for CO WDs,} \quad (5.10)\end{aligned}$$

where H is the pressure scale height. The a and b subscripts indicate these quantities are to be evaluated one wavelength above the base of the composition gradient, and at the base of the composition gradient, respectively. The middle line of equation (5.10) is more appropriate for our He WD models, while the last line is more appropriate for our CO WD models. Waves are more easily excited at larger values of \hat{r}_a due to the longer lever arm available to be torqued by the tidal potential. They are more easily excited at smaller values of \hat{N}_b because smaller values in \hat{N}_b produce longer wavelengths which couple better with the tidal potential.

In our He WD models, the value of \hat{r}_a tends to be smaller than in CO WDs because the hydrogen layer is much thicker. Furthermore, the value of \hat{N}_b^2 tends to be larger in He WDs because they are less degenerate than CO WDs (i.e., they have a larger entropy and a larger entropy gradient). The difference in stellar structure coupled with the strong dependence on \hat{r}_a and \hat{N}_b causes the value of \hat{f} to be orders of magnitude smaller in our He WD models than it is in our CO models. Furthermore, the slight dependence of \hat{r}_a and \hat{N}_a on ω (due to the fact that these quantities are evaluated one wavelength above the base of the composition gradient) creates a slightly steeper scaling $F(\omega) \approx \hat{f} \hat{\omega}^6$ in He WDs.

5.3 Orbital and Rotational Evolution of He WDs

Having computed the dimensionless tidal torque $F(\omega)$, we can calculate the rate at which energy and angular momentum are deposited in a He WD in a compact binary. In our analysis, we assume the WD maintains solid body rotation. The spin frequency of the WD evolves as

$$\dot{\Omega}_s = \frac{T_0 F(\omega)}{I}, \quad (5.11)$$

where I is the moment of inertia of the WD. The orbital frequency of the WD evolves due to both tidal dissipation and gravitational radiation:

$$\dot{\Omega} = \frac{3T_0 F(\omega)}{\mu a^2} + \frac{3\Omega}{2t_{\text{GW}}}. \quad (5.12)$$

Here, μ is the reduced mass of the binary, and $t_{\text{GW}} = |a/\dot{a}|$ is the gravitational wave inspiral time given by

$$\begin{aligned} t_{\text{GW}} &= \frac{5c^5}{64G^3} \frac{a^4}{MM'M_t} \\ &= 3.2 \times 10^{10} \text{s} \left(\frac{M_\odot^2}{MM'} \right) \left(\frac{M_t}{2M_\odot} \right)^{1/3} \left(\frac{\Omega}{0.1 \text{ s}^{-1}} \right)^{-8/3}. \end{aligned} \quad (5.13)$$

At large orbital periods, the second term in equation (5.12) dominates the orbital and spin evolution such that $\dot{\Omega} \gg \dot{\Omega}_s$, and tidal effects are negligible. However, because of the strong dependence of $F(\omega)$ on ω , tidal spin up becomes important at short orbital periods. The critical orbital frequency, Ω_c , at which tidal spin up becomes important is determined by equating $\dot{\Omega} \simeq 3\Omega/(2t_{\text{GW}})$ and $\dot{\Omega}_s$. For our He WD models, we find [cf. equations (79) and (83) of Paper II]

$$\begin{aligned} \Omega_c &= \left[\frac{3\kappa}{10\hat{f}} \frac{M_t^{5/3}}{M'M^{2/3}} \left(\frac{GM}{Rc^2} \right)^{5/2} \right]^{3/19} \left(\frac{GM}{R^3} \right)^{1/2} \\ &= (7.0 \times 10^{-3} \text{s}^{-1}) \left(\frac{\kappa_{0.17} M_{t1}^{5/3} M_1^5}{\hat{f} M_1' R_4^{12}} \right)^{3/19}, \end{aligned} \quad (5.14)$$

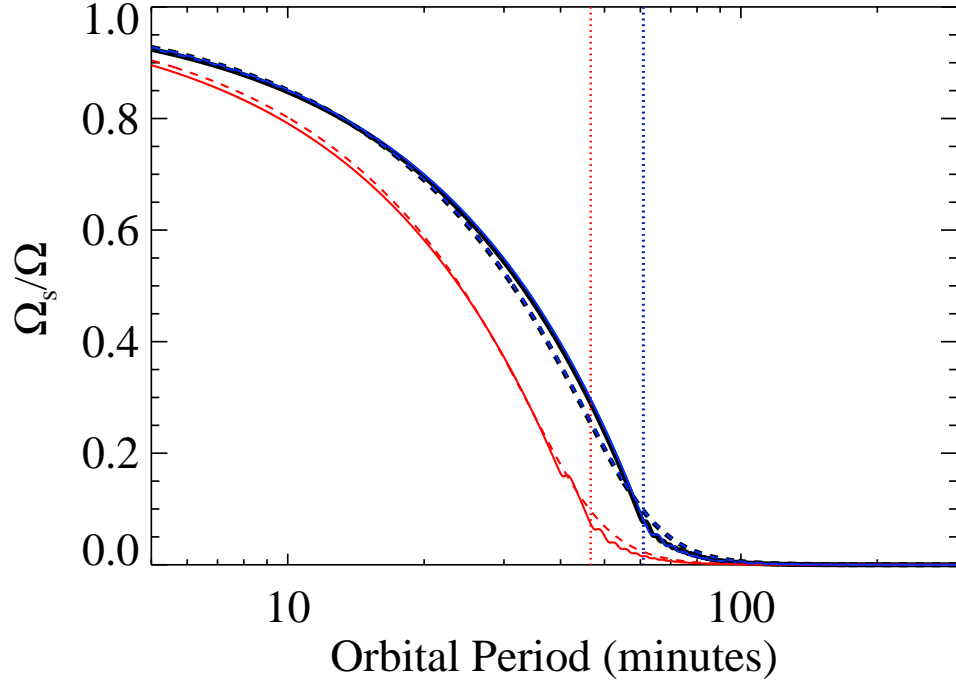


Figure 5.4: Evolution of the spin frequency Ω_s in units of the orbital frequency Ω as a function of the orbital period. The solid lines correspond to our $0.3M_\odot$ WD model with $T_{\text{eff}} = 18000\text{K}$ (black), $T_{\text{eff}} = 12000\text{K}$ (red), and $T_{\text{eff}} = 6000\text{K}$ (blue). The dashed lines correspond to evolutions using $F = 3 \times 10^{-3}\hat{\omega}^6$ (black), $F = 1.5 \times 10^{-2}\hat{\omega}^6$ (red), and $F = 6 \times 10^{-1}\hat{\omega}^6$ (blue) for the WD models of like color. The vertical dotted lines denotes the critical orbital period, $2\pi/\Omega_c$ [see equation (5.14)], for WDs of like color. The black and blue curves are indistinguishable from one another. In these evolutions, $M' = M$ and the WDs initially have $\Omega_s = 0$.

where $M_t = M + M'$ and $\kappa = I/(MR^2)$. Here, $M_{t1} = (M + M')/M_\odot$, $M_1 = M/M_\odot$, $R_4 = R/(10^4\text{km})$, and $\kappa_{0.17} = \kappa/0.17$. Our He WD models have $\kappa = 0.094$, $\kappa = 0.13$, and $\kappa = 0.16$ for $T_{\text{eff}} = 18000\text{K}$, $T_{\text{eff}} = 12000\text{K}$, $T_{\text{eff}} = 6000\text{K}$, respectively.

The scaling shown in equation (5.14) is an important result of our theory.² The dependence on M and R shows that lower mass, larger radius WDs (such as He WDs) should have smaller critical frequencies. So, naively, one would expect tidal dissipation to become important at longer orbital periods for low mass WDs. However, as described

²Equations (5.14) and (5.17) can be derived for the general case $T_{\text{tide}} = T_0\hat{f}\hat{\omega}^n$, as detailed in Appendix C.

in Section 5.2.2, the value of \hat{f} is much smaller in He WDs. These two effects largely offset one another, causing the value of Ω_c to be similar in He and CO WDs. Thus, an He WD in a compact binary will *begin* to evolve toward synchronization with the orbital frequency at roughly the same orbital period as a CO WD, namely, at orbital periods $P \approx 1$ hour.

Figure 5.4 displays the spin frequency, Ω_s , as a function of orbital period for an He WD in a compact binary. At periods longer than about an hour, the spin frequency increases slower than the orbital frequency, and thus the value of Ω_s/Ω remains close to zero. However, when the orbital frequency increases to $\Omega \approx \Omega_c$, the value of Ω_s/Ω begins to increase, i.e., the WD becomes more synchronized with the orbit. The WD does not become completely synchronized, however, but retains a nearly constant degree of asynchronization such that $\Omega - \Omega_s \simeq \Omega_c$ (see Section 8.1 of Paper II for more details).

We can also calculate the amount of heat dissipated in the WD. The heat dissipated in the WD is *not* equal to the tidal energy transfer rate [\dot{E}_{tide} , see equation (5.7)] because some of the tidal energy flux is stored as rotational kinetic energy. Instead,

$$\dot{E}_{\text{heat}} = \dot{E}_{\text{tide}}(1 - \Omega_s/\Omega). \quad (5.15)$$

At long orbital periods where $\Omega_s/\Omega \ll 1$, $\dot{E}_{\text{heat}} \simeq \dot{E}_{\text{tide}}$, with \dot{E}_{tide} given by equation (5.7). However, at shorter orbital periods where $\Omega > \Omega_c$ (see Paper II),

$$\dot{E}_{\text{tide}} \simeq \frac{3I\Omega^2}{2t_{\text{GW}}} \quad \text{for} \quad \Omega > \Omega_c, \quad (5.16)$$

and we find for our He WD model that

$$\begin{aligned} \dot{E}_{\text{heat}} &\simeq \dot{E}_{\text{tide}} \left(\frac{\Omega_c}{\Omega} \right)^{19/18} \\ &\simeq (1.2 \times 10^{37} \text{ erg s}^{-1}) \kappa_{0.17}^{7/6} \hat{f}^{-1/6} M_1^{17/6} (M'_1)^{5/6} (M_{t1})^{-1/18} \left(\frac{\Omega}{0.1 \text{ s}^{-1}} \right)^{65/18}. \end{aligned} \quad (5.17)$$

Comparison with equation (91) of Paper II reveals that the amount of heat dissipated in an He WD is the same order of magnitude as the heat dissipated in a CO WD. At short

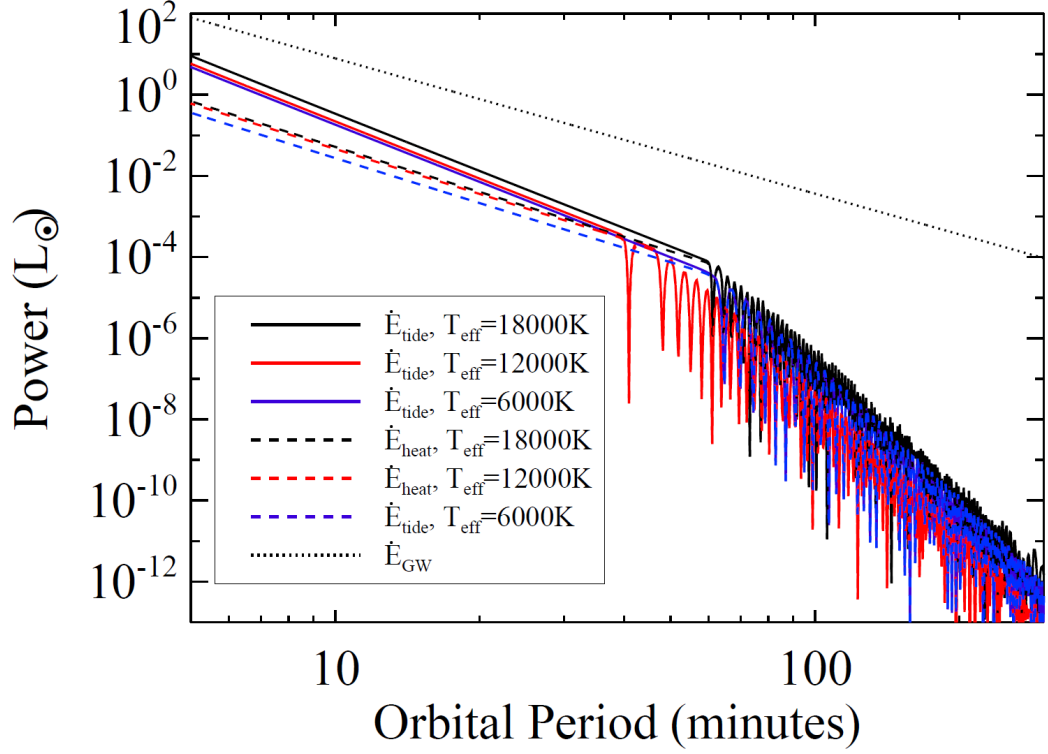


Figure 5.5: The tidal energy dissipation rate \dot{E}_{tide} (solid lines) and the tidal heating rate \dot{E}_{heat} (dashed lines) as a function of orbital period for our $0.3M_\odot$ WD model with $T_{\text{eff}} = 18000\text{K}$ (black), $T_{\text{eff}} = 12000\text{K}$ (red), and $T_{\text{eff}} = 6000\text{K}$ (blue). Note that at long orbital periods, $\dot{E}_{\text{tide}} \simeq \dot{E}_{\text{heat}}$ and these curves overlap. The dotted back line is the energy flux carried away by gravitational waves, \dot{E}_{GW} . In these evolutions, $M' = M$ and the WDs initially have $\Omega_s = 0$.

orbital periods, this heating rate can be much larger than the WD's intrinsic luminosity, and it can thus have a substantial impact on the structure, luminosity, and temperature of the WD (see Section 4).

Figure 5.5 shows the tidal energy flux and heating rate as a function of orbital period for a He WD in a binary with $M' = M$. It is clear that $\dot{E}_{\text{GW}} \gg \dot{E}_{\text{tide}}$ at all orbital periods, where $\dot{E}_{\text{GW}} = GMM'/(2at_{\text{GW}})$ is the energy flux carried away by gravitational waves. At long orbital periods where $\Omega < \Omega_c$, the value of $\dot{E}_{\text{heat}} \simeq \dot{E}_{\text{tide}}$, but the magnitude of the heating is small and has a negligible effect on the WD. At shorter orbital periods where $\Omega > \Omega_c$, the heating rate is well described by equation (5.17).

5.4 Location of Tidal Heat Deposition

Until now, we have not examined the processes that convert the angular momentum and energy carried by gravity waves into the rotational angular momentum and internal energy of the stellar envelope. We have assumed that the gravity waves propagate into the envelope of the WD where they somehow dissipate, depositing their energy and angular momentum. Here, we investigate these processes so that we can estimate the magnitude of tidal heating as a function of depth within the star.

5.4.1 Non-linear Wave Breaking

As the tidally excited gravity waves propagate outward in the WD envelope, their amplitudes increase. In the WKB limit, with $\omega \ll N$ and $\omega \ll L_l$, the radial wave number is given by $k_r \simeq -k_\perp N/\omega$, where the horizontal wave number is $k_\perp = \sqrt{l(l+1)}/r$. The amplitudes of the radial and horizontal displacements scale as

$$\xi_\perp \simeq \frac{ik_r r}{l(l+1)} \xi_r \propto \frac{N}{r^2(\rho|k_r|)^{1/2}}. \quad (5.18)$$

Obviously, $|k_r|/k_\perp = N/\omega \gg 1$ and $|\xi_r/\xi_\perp| = \sqrt{l(l+1)}\omega/N \ll 1$.

As the gravity waves reach sufficiently large amplitudes, they are expected to break and quickly damp, locally depositing their energy and angular momentum. The critical amplitude for wave breaking may be estimated by comparing the Eulerian acceleration $\partial \mathbf{v}/\partial t = -\omega^2 \boldsymbol{\xi}$ (where $\mathbf{v} = -i\omega \boldsymbol{\xi}$ is the fluid velocity) with the non-linear “advective” term $\mathbf{v} \cdot \nabla \mathbf{v} = -\omega^2 \boldsymbol{\xi} \cdot \nabla \boldsymbol{\xi}$. For gravity waves, most of the terms in the advective derivative satisfy the non-linearity condition $\boldsymbol{\xi} \cdot \nabla \boldsymbol{\xi} \simeq \boldsymbol{\xi}$ when

$$|k_r \xi_r| \simeq \frac{l(l+1)}{r} |\xi_\perp| \sim 1. \quad (5.19)$$

Thus, nonlinear effects become important when the radial (horizontal) displacement is comparable to the radial (horizontal) wavelength. Alternatively, one may expect the waves to begin breaking when the shear is large enough to overturn the stratification of the star, i.e., when the Richardson stability criterion, $N^2/|dv_\perp/dr|^2 > 1/4$, is violated. This occurs when $k_\perp|\xi_\perp| \gtrsim 1$, a condition similar to equation (5.19) for $l = 2$. Equation (5.19) is similar to the wave breaking criterion discussed in Ogilvie & Lin (2007) and found in three-dimensional simulations of gravity waves approaching the center of a solar-type star (Barker & Ogilvie 2011).

However, equation (5.19) corresponds to a physical displacement, $|\xi| \simeq |\xi_\perp| \sim R/[l(l+1)]$ in the envelope of the star. It seems unlikely that fluid displacements of order the radius of the star can be realized before non-linear wave breaking occurs. Moreover, the \hat{r} component of the advective derivative contains the term $-\xi_\perp \cdot \xi_\perp/r$. This implies that non-linear effects may become important when $\xi_\perp^2/r \sim \xi_r$, which corresponds to $k_r \xi_\perp \sim l(l+1)$ in the WKB limit. Thus, we will also consider the non-linear breaking criterion

$$|k_r \xi_\perp| \sim \beta, \quad (5.20)$$

where $\beta \gtrsim 1$ is a free parameter. Choosing different values of β will allow us to test how the location of tidal energy deposition depends on different wave breaking criteria.

To implement the non-linear criterion (5.19) or (5.20) for different orbital frequencies and companion masses, we can use our numerically computed wave function $\xi(r)$ and extend it to the near surface region via the WKB amplitude relation (5.18). Alternatively, we can use equations (5.5), (5.6), and (5.18) to find

$$|\xi_\perp(r)| \simeq R \left(\frac{M'}{M_t} \right) \left[\frac{F(\omega)}{2m \sqrt{l(l+1)}} \frac{\Omega^4 N(r)}{G\rho(r)\omega^3} \right]^{1/2}, \quad (5.21)$$

with $l = m = 2$. The radial displacement can be obtained from equation (5.18). The above expression gives the wave amplitude in the outgoing wave region, i.e., the region

above the composition gradient at which the waves are excited.

We denote the location of non-linear wave breaking by ΔM_B , the mass above the point at which the wave amplitude satisfies one of the non-linear criteria discussed above. Figure 5.6 shows ΔM_B as a function of orbital period for both CO and He WD models, calculated according to equations (5.19) and (5.20). At large orbital periods ($P \gtrsim 40$ minutes), the waves do not become non-linear under criterion (5.19) below the surface convection zone (whose depth is $\Delta M_{\text{conv}} \simeq 10^{-12} M_\odot$ for the CO WD and $\Delta M_{\text{conv}} \simeq 10^{-13} M_\odot$ for the He WD). In this case, the g-mode analysis of Paper I and Burkart et al. (2012) may become applicable. At shorter orbital periods, the waves become non-linear according to equation (5.19), but they break near the surface of the WD where $\Delta M_B \lesssim 10^{-8} M_\odot$.

However, under the criterion of equation (5.20) with $\beta = 1$, the waves become non-linear deeper in the star, and nearly always reach non-linear amplitudes before encountering the surface convection zone. In the CO WD model, the value of ΔM_B jumps upward to $\Delta M_B \approx 10^{-4} M_\odot$ at an orbital period of about 30 minutes, while ΔM_B stays below $10^{-5} M_\odot$ in the He WD. The reason is that the CO WD has two composition gradients whereas the He WD has only one. The He-H composition gradient in the CO WD causes the outgoing waves excited at the C-He gradient to have larger values of both $|\xi_\perp|$ and $|k_r|$ in this layer, promoting non-linearity via equation (5.20). No such composition gradient exists above the excitation region in an He WD, so the waves do not reach non-linear amplitudes until they are close to the surface. For reference, Figure 5.6 also shows the value of ΔM_B calculated with the intermediate non-linearity conditions $|k_r \xi_\perp| = 3$ and $|k_r \xi_\perp| = 10$. Using these more conservative criteria yields results similar to the criterion $|k_r \xi_\perp| = 1$, but with generally smaller values of ΔM_B .

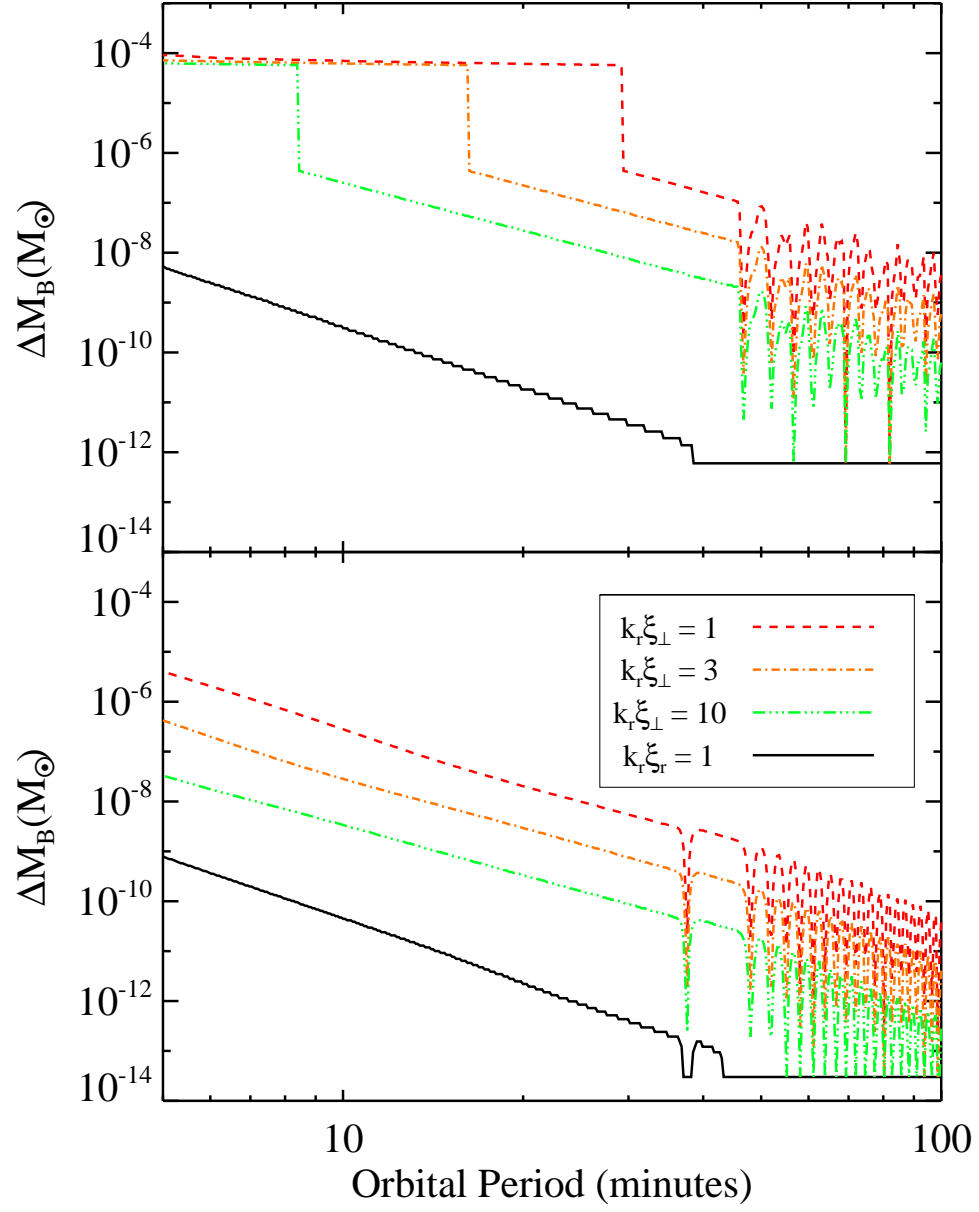


Figure 5.6: The envelope mass ΔM_B above the point at which outgoing waves become non-linear as a function of orbital period for an $M = 0.6M_\odot$ CO WD model with $T_{\text{eff}} = 10000\text{K}$ (top) orbiting an $M = 0.3M_\odot$ He WD model with $T_{\text{eff}} = 12000\text{K}$ (bottom). The solid black lines are calculated from equation (5.19), while the three dashed lines are from equation (5.20) with $\beta = 1, 3, 10$ (from top to bottom). This plot assumes the WD spin and orbital frequencies evolve according to equations (5.11-5.12).

5.4.2 Wave Absorption at a Critical Layer

Until now, we have considered the WD to be rotating as a rigid body. Our results have indicated that in a rigidly rotating WD waves will break and deposit their angular momentum in the outer layers of the star where $\Delta M_B \lesssim 10^{-4} M_\odot$. Since a small fraction of the stellar mass absorbs the entirety of the angular momentum flux carried by waves, the outer layers of the star may spin up rapidly. If the outer layer spins up faster than angular momentum can be transported to the core, it will attain synchronous rotation with the orbit of the companion. The outgoing gravity waves will then encounter a critical layer (corotation resonance), where the wave frequency in the rest frame of the fluid, $\omega = 2[\Omega - \Omega_s(r)]$, equals zero. At the critical layer, the gravity waves are directly absorbed by the fluid since their radial wavelength $|k_r|^{-1} \simeq \omega/(k_\perp N)$ and group velocity $v_g \simeq \omega^2/(k_\perp N)$ both approach zero. As the continuous train of gravity waves deposit their angular momenta in the stellar envelope, the critical layer will move to larger depths. Such an “outside-in” scenario for tidal spin-up was first discussed by Goldreich & Nicholson (1989) for massive (early-type) stellar binaries, and was applied to WD binaries in Paper III.

In this section, we model the spin evolution of the WD using a simple two-zone model. In this model, the envelope of the star forms a critical layer that rotates synchronously with the orbit ($\Omega_{s,\text{env}} = \Omega$), while the core of the star rotates sub-synchronously ($\Omega_{s,\text{core}} < \Omega$). The envelope and core are coupled, with angular momentum being transferred to the core according to a parameterized coupling time, t_{coup} . The angular momentum of the system evolves according to

$$\dot{J}_{\text{env}} = \dot{J}_z(\omega_{\text{core}}) - \frac{I_{\text{env}}}{t_{\text{coup}}}(\Omega_{s,\text{env}} - \Omega_{s,\text{core}}) \quad (5.22)$$

$$\dot{J}_{\text{core}} = \frac{I_{\text{env}}}{t_{\text{coup}}}(\Omega_{s,\text{env}} - \Omega_{s,\text{core}}). \quad (5.23)$$

Here, \dot{J}_z is the angular momentum flux which can be calculated from equation (5.6). We assume that the waves are excited in the core and dissipated in the envelope. Consequently, the angular momentum source term \dot{J}_z is only present in the envelope evolution equation, although it is dependent on the tidal frequency in the core, $\omega_{\text{core}} = 2(\Omega - \Omega_{s,\text{core}})$. Using $\Omega_{s,\text{env}} = \Omega$ and the fact that the star's total moment of inertia is $I = I_{\text{env}} + I_{\text{core}}$, equations (5.22) and (5.23) may be rewritten

$$\dot{I}_{\text{env}} = -\frac{\dot{\Omega}}{\Omega} I_{\text{env}} + \frac{\dot{J}_z(\omega_{\text{core}})}{\Omega} - \frac{\Omega - \Omega_{s,\text{core}}}{\Omega t_{\text{coup}}} I_{\text{env}} \quad (5.24)$$

$$\dot{\Omega}_{s,\text{core}} = \frac{\dot{I}_{\text{env}}}{I - I_{\text{env}}} \Omega_{s,\text{core}} + \frac{I_{\text{env}}}{I - I_{\text{env}}} \frac{\Omega - \Omega_{s,\text{core}}}{t_{\text{coup}}}. \quad (5.25)$$

Since the orbital decay is dominated by the emission of gravitational waves, $\dot{\Omega}/\Omega \simeq 3\Omega/(2t_{\text{GW}})$.

With appropriate initial conditions, we can integrate equations (5.24) and (5.25) to calculate the values of I_{env} and $\Omega_{s,\text{core}}$ as a function of orbital period. We then obtain the mass ΔM_{env} of the envelope corresponding to the value of I_{env} . In this simple two-zone model, the tidal heat is deposited entirely at the base of the envelope where $\Delta M = \Delta M_{\text{env}}$. The thickness of the envelope is dependent on the parameter t_{coup} . Unfortunately, angular momentum transport in stars is not well understood. In stably stratified stars like WDs, angular momentum is likely transported by magnetic torques, e.g., via the Tayler-Spruit dynamo (Spruit 2002). In Appendix D we estimate value of t_{coup} , and find that $1\text{yr} \lesssim t_{\text{coup}} \lesssim 10^4\text{yr}$ for realistic WD parameters.

We can calculate approximate equilibrium solutions to equations (5.24) and (5.25). Since $t_{\text{coup}} \ll t_{\text{GW}}$, the first term on the right hand side of equation (5.24) is negligible. Then at equilibrium,

$$I_{\text{env}} \simeq \frac{\dot{J}_z(\omega_{\text{core}}) t_{\text{coup}}}{\Omega - \Omega_{s,\text{core}}}. \quad (5.26)$$

At large orbital periods where $\Omega \lesssim \Omega_c$ [see equation (5.14)] the system is not synchro-

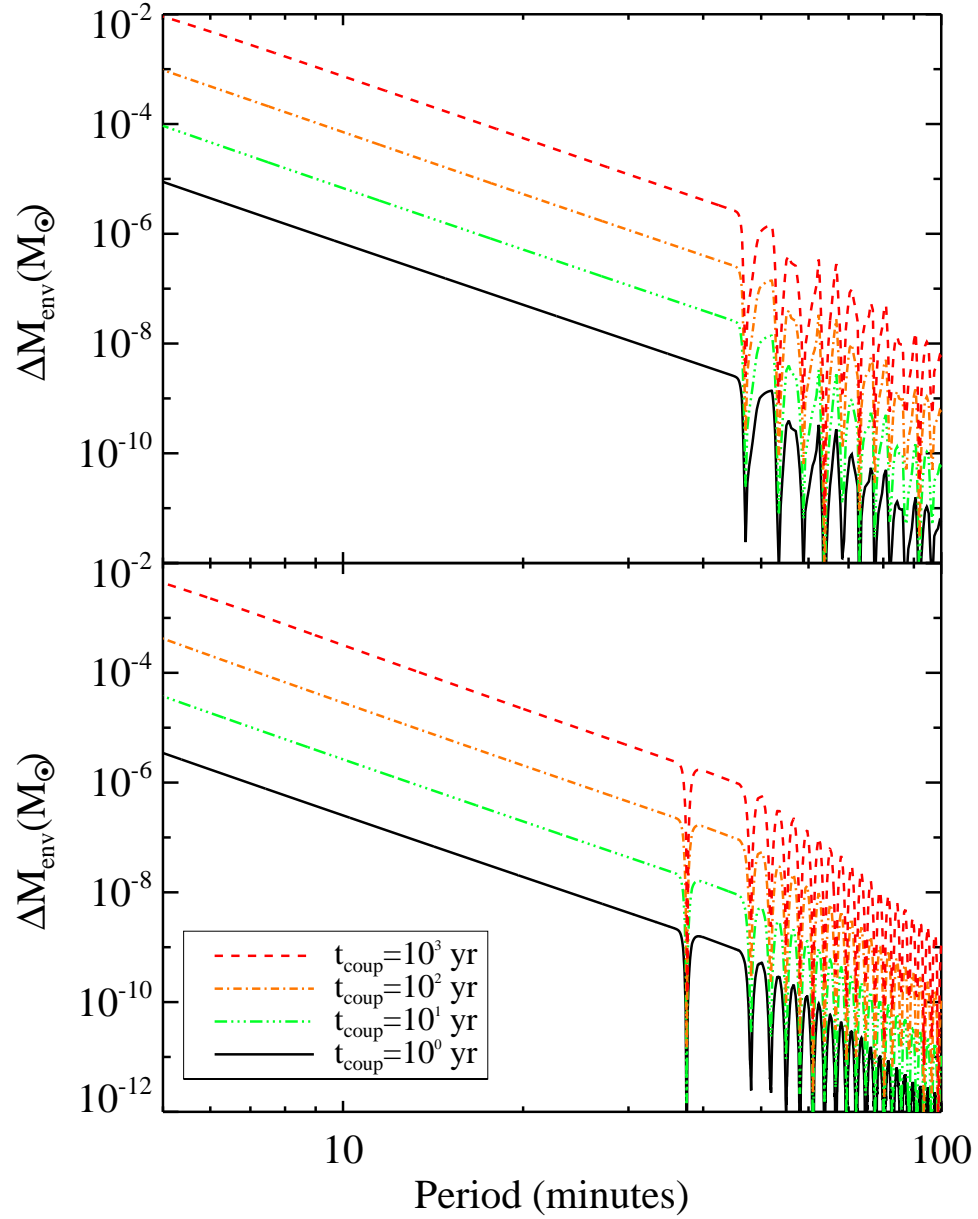


Figure 5.7: The envelope mass ΔM_{env} above the critical layer as a function of orbital period for our $M = 0.6 M_{\odot}$ CO WD model with $T_{\text{eff}} = 10000\text{K}$ (top) orbiting our $M = 0.3 M_{\odot}$ He WD model with $T_{\text{eff}} = 12000\text{K}$ (bottom). The solid black lines have $t_{\text{coup}} = 1\text{yr}$, the dot-dot-dashed green lines have $t_{\text{coup}} = 10\text{yr}$, the dot-dashed orange lines have $t_{\text{coup}} = 10^2\text{yr}$, and the dashed red lines have $t_{\text{coup}} = 10^3\text{yr}$.

nized such that $\Omega_{s,\text{core}} \ll \Omega$ and

$$I_{\text{env}} \simeq \frac{j_z(2\Omega)t_{\text{coup}}}{\Omega} \quad \text{for } \Omega < \Omega_c \quad (5.27)$$

At short orbital periods ($\Omega > \Omega_c$) where synchronization has begun, $\Omega - \Omega_{s,\text{core}} \simeq \Omega_c$. In this regime, $J_z = \dot{E}_{\text{tide}}/\Omega \simeq 3I\Omega/(2t_{\text{GW}})$, and we have

$$I_{\text{env}} \simeq \frac{3\Omega t_{\text{coup}}}{2\Omega_c t_{\text{GW}}} I \quad \text{for } \Omega > \Omega_c. \quad (5.28)$$

Comparison with our numerical integration of equations (5.24) and (5.25) shows that the approximations of equations (5.27) and (5.28) are very accurate.

Figure 5.7 plots the value of ΔM_{env} as a function of orbital period for our two WD models, using values of t_{coup} ranging from 1yr to 10^3 yr. We begin our calculation at $P_{\text{orb}} > 1\text{hr}$ and use $I_{\text{env},0} = 0$ and $\Omega_{s,\text{core}} = 0$, as is appropriate at long orbital periods where tidal effects are small. For the chosen values of t_{coup} , the value of ΔM_{env} remains small at all orbital periods ($\Delta M_{\text{env}} \lesssim 10^{-2}M_{\odot}$). Thus, if a critical layer develops in a real WD, we expect it to be restricted to the outer region of the star. However, the critical layer extends to very large optical depths, suggesting that binary WDs may be observed to be synchronized at large orbital periods even if their cores are not synchronized. Our results indicate that, for our CO WD model, the critical layer most likely does not penetrate as deeply as the C-He composition gradient where gravity waves are excited (or the He-H gradient in our $0.3M_{\odot}$ He WD model), so our assumption that J_z is a function of $\omega_{\text{core}} = 2(\Omega - \Omega_{s,\text{core}})$ is justified. Finally, we note that the values of ΔM_{env} are similar in magnitude to the values of ΔM_B calculated in Section 5.4.1.

5.5 Thermal Evolution of Tidally Heated Binary White Dwarfs

In Section 5.2 (and in Paper II), we demonstrated that the tidal heating rate \dot{E}_{heat} of a WD in a compact binary may be substantially larger than the intrinsic luminosity of the WD. However, the consequence of this tidal heating is not clear a priori and depends on the location of heat deposition (Section 5.4). The assumption that the WD reaches a state of thermal equilibrium is not justified because the WD cooling time can be much larger than the gravitational inspiral time. In this section, we calculate the effect of the tidal heating on the WD structure and on its surface temperature and luminosity.

5.5.1 Details of Calculation

To calculate the effect of tidal heating, we first calculate the value of ΔM_B according to the wave breaking criteria of Sections 5.4.1 and 5.4.2 (for the purposes of this calculation, we refer to the value of ΔM_{env} as ΔM_B , because it determines the depth at which tidal heat is deposited). We deposit the tidal heat uniformly per unit mass in the outer layers of the WD that have $\Delta M < \Delta M_B$. Although the radial dependence of this heating function is unlikely to be realistic, we find that the results are not strongly dependent on the form of the radial heat deposition (although they are sensitive to the value of ΔM_B). The heating rate per gram of material, $\dot{\epsilon}_{\text{heat}}$, is then

$$\dot{\epsilon}_{\text{heat}} = 0 \quad \text{for} \quad \Delta M > \Delta M_B \quad (5.29)$$

$$\dot{\epsilon}_{\text{heat}} = \frac{\dot{E}_{\text{heat}}}{\Delta M_B} \quad \text{for} \quad \Delta M < \Delta M_B, \quad (5.30)$$

with the value of \dot{E}_{heat} calculated from equation (5.17) (and its counterpart in Paper II for CO WDs).

To understand the effect of tidal heating on the WD properties, we evolve WD

models using the extra heating term calculated via equation (5.30). We use the one-dimensional stellar evolution code MESA (Paxton et al. 2011) to evolve our WD models. At the beginning of the evolutions, the WDs have the same profiles used to calculate the magnitude of wave excitation (e.g., the models shown in Figure 5.1 for our He WD models). The initial orbital period is one hour, with companion masses discussed below.

During the course of our evolutions, we do not calculate new values of $F(\omega)$ and Ω_c at each time step. In principle, these values change as the stellar structure adjusts to tidal heating (and WD cooling). However, since waves are excited at a depth well below where they deposit their energy as heat, the properties of the WD at the location of wave excitation experience little change during the evolution. Hence, we expect the values of $F(\omega)$ and Ω_c to remain roughly constant. In contrast, the value of ΔM_B is strongly dependent on orbital period, and is updated at each time step.

In general, the amount of tidal heat depends on the masses of the two WDs. We do not attempt to cover the whole spectrum of WD masses. Instead, we consider only two cases: a $0.6M_\odot$ CO WD paired with a $0.3M_\odot$ He WD (in this case we examine the heating of both WDs), and a $0.6M_\odot$ CO WD paired with a $0.9M_\odot$ companion star (in this case we examine only the $0.6M_\odot$ WD). We present results for the $0.6M_\odot$ CO WDs at initial temperatures of 5000K, 10000K, and 15000K, and for the $0.3M_\odot$ He WDs at initial temperatures of 6000K, 12000K, and 18000K. These temperatures roughly span the observed temperatures in compact WD binaries (Kilic et al. 2012).

5.5.2 Effects of Tidal Heating

Figure 5.8 displays the surface temperature of the $0.3M_\odot$ He WD as a function of orbital period. For comparison, we also plot the temperature of a non-tidally heated WD (i.e.,

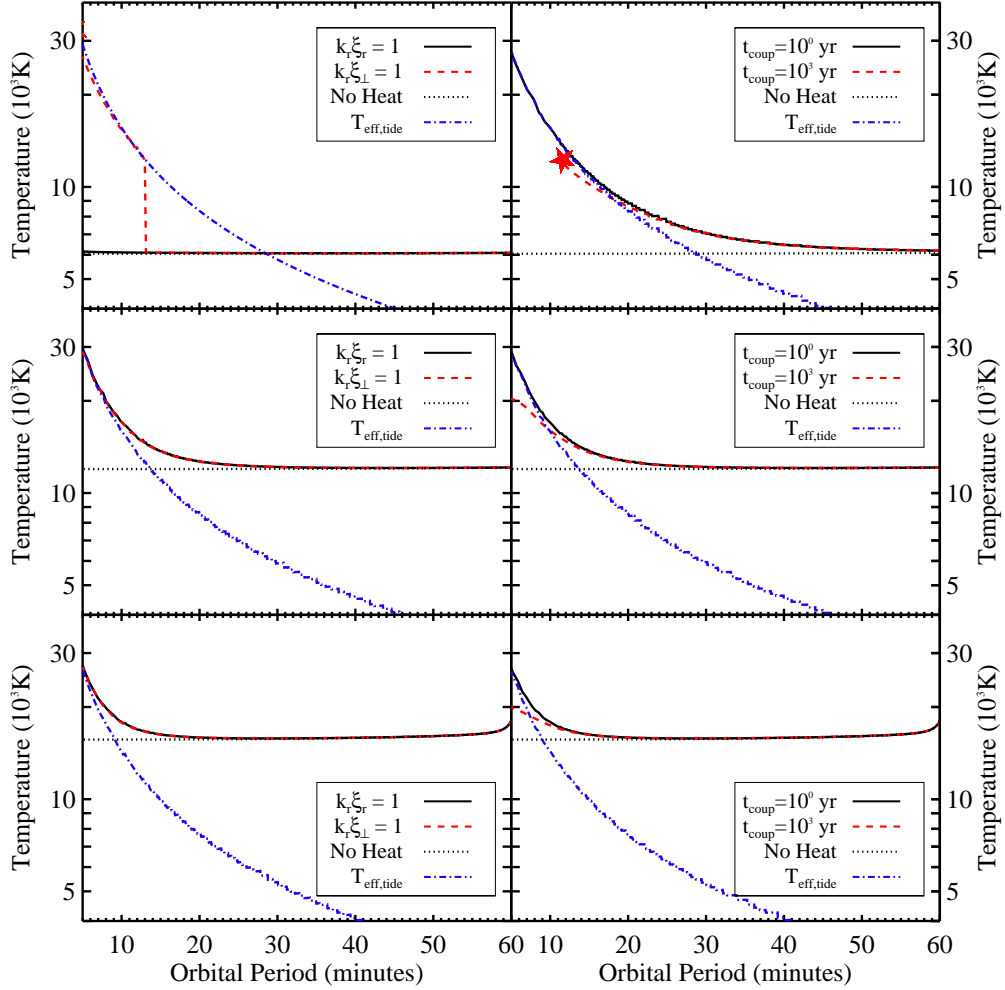


Figure 5.8: The surface temperature of our $0.3M_{\odot}$ He WD model with a $0.6M_{\odot}$ companion as a function of orbital period, for initial temperatures of 6000K (top), 12000K (middle), and 18000K (bottom). On the left-hand side, the solid black lines are calculated with the wave breaking criterion of equation (5.19), while the dashed red lines are calculated with equation (5.20). On the right-hand side, the solid black lines are calculated via the two-zone model with $t_{\text{coup}} = 1\text{ yr}$, while the dashed red lines are calculated with $t_{\text{coup}} = 10^3\text{ yr}$. The dotted lines are calculated for a WD with no tidal heating and the same initial temperature. The blue dot-dashed lines are the values of $T_{\text{eff,tide}}$ from equation (5.31). The black and red lines overlap at large orbital periods, while the black and blue lines often overlap at small orbital periods. Discontinuities in temperature are due to sudden changes in the location of heat deposition (see text). Stars indicate the occurrence of a tidal nova. The plot extends to an orbital period of 5 minutes, the approximate orbital period at which Roche lobe overflow occurs.

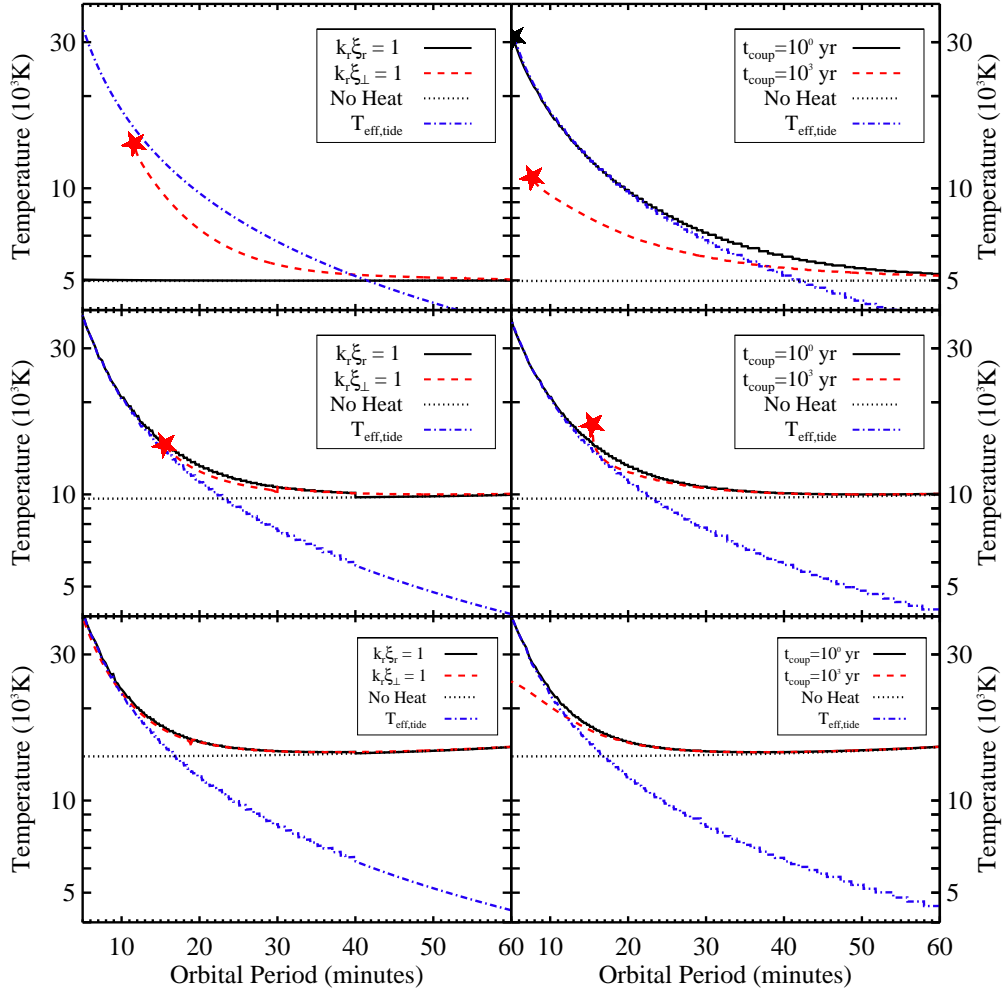


Figure 5.9: Same as Figure 5.8, but for our $0.6M_{\odot}$ CO WD model with a $0.3M_{\odot}$ companion.

we set $\dot{E}_{\text{heat}} = 0$ in our evolutions). At long orbital periods ($P \gtrsim 30$ minutes), the tidal heating has little effect on the luminosity or temperature of the WD, except to slightly raise the temperature of the $T_0 = 5000\text{K}$ model. In this phase of its evolution, the WD remains well described by the cooling track for a non-tidally heated WD. At shorter periods ($P \lesssim 20$ minutes), the luminosity and temperature become substantially larger due to tidal heating. At the smallest orbital periods ($P \lesssim 8$ minutes), the WD has a temperature in excess of 18000K regardless of its initial temperature, and the luminosity is dominated by escaping tidal heat. The case with $t_{\text{coup}} = 10^3\text{yr}$ and initial temperature

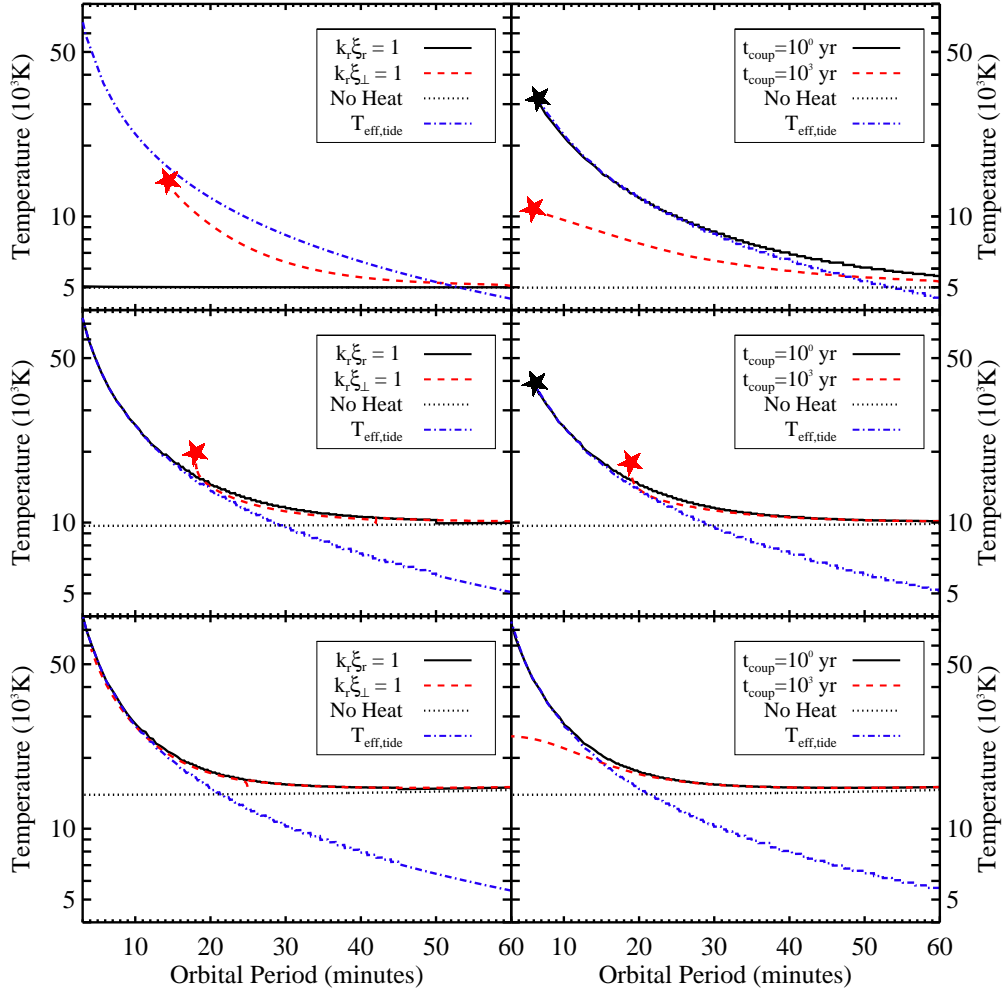


Figure 5.10: Same as Figure 5.8, but for our $0.6M_{\odot}$ CO WD model with a $0.9M_{\odot}$ companion.

$T_{\text{eff}} = 6000\text{K}$ (top right panel) ends abruptly, indicating that the surface hydrogen layer ignited to create a tidally induced nova, which we discuss in greater detail below (see also Paper III).

The top left panel of Figures 5.8, 5.9 and 5.10 are calculated for cool WDs with deep convection zones. In these WDs, the waves do not become non-linear below the convection zone according to equation (5.19) at any orbital period, and they may become non-linear according to equation (5.20) at orbital periods below one hour. When the

waves do not become non-linear, we distribute tidal heat evenly throughout the WD, but a more accurate calculation should use the discrete g-mode formalism discussed in Paper I (c.f. Burkart et al. 2012, Valsecchi et al. 2012).

Figures 5.8-5.10 also show the tidal heating temperature, defined as

$$T_{\text{eff,tide}} = \left(\frac{\dot{E}_{\text{heat}}}{4\pi R^2 \sigma} \right)^{1/4}, \quad (5.31)$$

where σ is the Stefan-Boltzmann constant. In the $0.3M_{\odot}$ WD, the tidal heat diffuses to the surface very quickly (see Section 5.5.3 for more discussion), regardless of the non-linear breaking criterion. In this case, the observed luminosity is roughly $L \simeq L_{\text{int}} + \dot{E}_{\text{heat}}$, where L_{int} is the intrinsic luminosity of the cooling, non-tidally heated WD.

Figures 5.9-5.10 display the temperature of a $0.6M_{\odot}$ WD as a function of orbital period, for companion masses of $0.3M_{\odot}$ and $0.9M_{\odot}$. For the cases using the non-linear breaking criterion of equation (5.19) and critical layer absorption with $t_{\text{coup}} = 1\text{yr}$, the results are very similar to those of the $0.3M_{\odot}$ He WD models. When the luminosity is dominated by tidal heating, the $0.6M_{\odot}$ WD models have slightly larger surface temperatures than the $0.3M_{\odot}$ models. Although the value of \dot{E}_{heat} is comparable between the $0.3M_{\odot}$ and $0.6M_{\odot}$ models, the smaller radius of the $0.6M_{\odot}$ WD models requires a larger surface temperature to radiate the same amount of energy. Finally, the luminosities and temperatures are usually larger for the $0.9M_{\odot}$ companion, as expected from the scaling of equation (5.17).

However, for the non-linear breaking criterion of equation (5.20) and the critical layer absorption with $t_{\text{coup}} = 10^3\text{yr}$, the results are markedly different. For these criteria, most of the tidal heat is deposited deeper in the WD where it cannot quickly diffuse outward to be radiated away. These criteria thus lead to generally lower WD surface temperatures. However, because the tidal heat is not quickly radiated away, the layers in which the heat is deposited may heat up substantially.

The layers just above the He-H composition gradient are primarily composed of degenerate hydrogen. If these layers are able to trap enough heat, their temperature will increase until hydrogen fusion begins. Due to the degeneracy of the hydrogen, the ignition of fusion starts a thermonuclear runaway similar to a classical nova. Our evolutions show that these tidally induced novae occur in our two cooler $0.6M_{\odot}$ CO WD models and in our coolest $0.3M_{\odot}$ He WD model. The novae occur only if the gravity waves deposit their heat near the base of the hydrogen layer, i.e., only for the heat deposition criteria which yield $10^{-5}M_{\odot} \lesssim \Delta M_B \lesssim 10^{-3}M_{\odot}$ for our CO WD model and $10^{-4}M_{\odot} \lesssim \Delta M_B \lesssim 10^{-2}M_{\odot}$ for our He WD model. Novae do not occur for the warmer models because the hydrogen is not degenerate, so these models are able to burn the hydrogen stably.

In a thermonuclear runaway event, most of the hydrogen will be burned to helium or will be ejected from the system (Truran 2002). We do not attempt to predict a detailed observational signal of such an event, other than to speculate that it will be very similar to a classical nova. The thermonuclear runaway may dramatically change the dynamics of subsequent tidal heat deposition. Assuming the hydrogen shell is much thinner after the nova event, tidal heat may be deposited closer to the surface where it can quickly diffuse outwards, similar to the results for our warm He WDs.

5.5.3 Heating and Cooling Time Scales

The effect of tidal heating can be better understood by examining the relative time scales of the WD inspiral, heating, and cooling processes. The WD inspiral time due to gravitational radiation, t_{GW} , is given by equation (3.76). The inspiral time scale ranges from more than a Hubble time at large orbital periods (several hours), to less than a million

years at short orbital periods (less than about fifteen minutes). Any process that acts on a time scale longer than the inspiral time is irrelevant, because the WDs will have merged (or begun stable mass transfer) by the time the process makes a substantial change.

The temperature evolution of the WD is determined not only by the amount of tidal heat deposited, but also by the rate at which that heat is able to diffuse to the surface. The time scale on which a shell of material heats up (in the absence of cooling) is

$$t_{\text{heat}}(r, \Omega) = \frac{c_p T}{\dot{\epsilon}_{\text{heat}}}, \quad (5.32)$$

where c_p is the specific heat at constant pressure. The radial profile of the heating time depends primarily on the magnitude and radial dependence of the tidal heating. As tidal heat is deposited in a shell of the WD, it will diffuse on a thermal time scale,

$$t_{\text{therm}}(r, \Omega) = \frac{P c_p T}{g F}, \quad (5.33)$$

where P is the pressure and F is the heat flux through the shell. The thermal time scale has a very sensitive dependence on the depth of the shell in question (see Figure 5.11). In the core of the WD, $t_{\text{therm}} \approx 10^9$ years, whereas near the surface, $t_{\text{therm}} \ll 1$ year.

Figure 5.11 shows a plot of t_{GW} , t_{heat} , and t_{therm} as a function of ΔM for our $0.6M_{\odot}$ WD with a $0.3M_{\odot}$ companion at orbital periods of 45 and 15 minutes. At long orbital periods, $t_{\text{therm}} \ll t_{\text{heat}}$ at all radii. The tidal heat is able to quickly diffuse to the surface and be radiated away. The temperature of the WD reaches a thermal equilibrium such that tidal heat is radiated at the same rate it is deposited. We find this is also the case for our $0.3M_{\odot}$ He WD model at most orbital periods.

At short orbital periods, $t_{\text{therm}} \approx t_{\text{heat}}$ near the base of the heat deposition zone. The temperature profile will adjust so as to re-establish thermal equilibrium such that $t_{\text{therm}} < t_{\text{heat}}$, thereby changing the internal structure of the star. When ΔM_B is calculated with equation (5.19), the star is able to adjust to the heating by steepening its

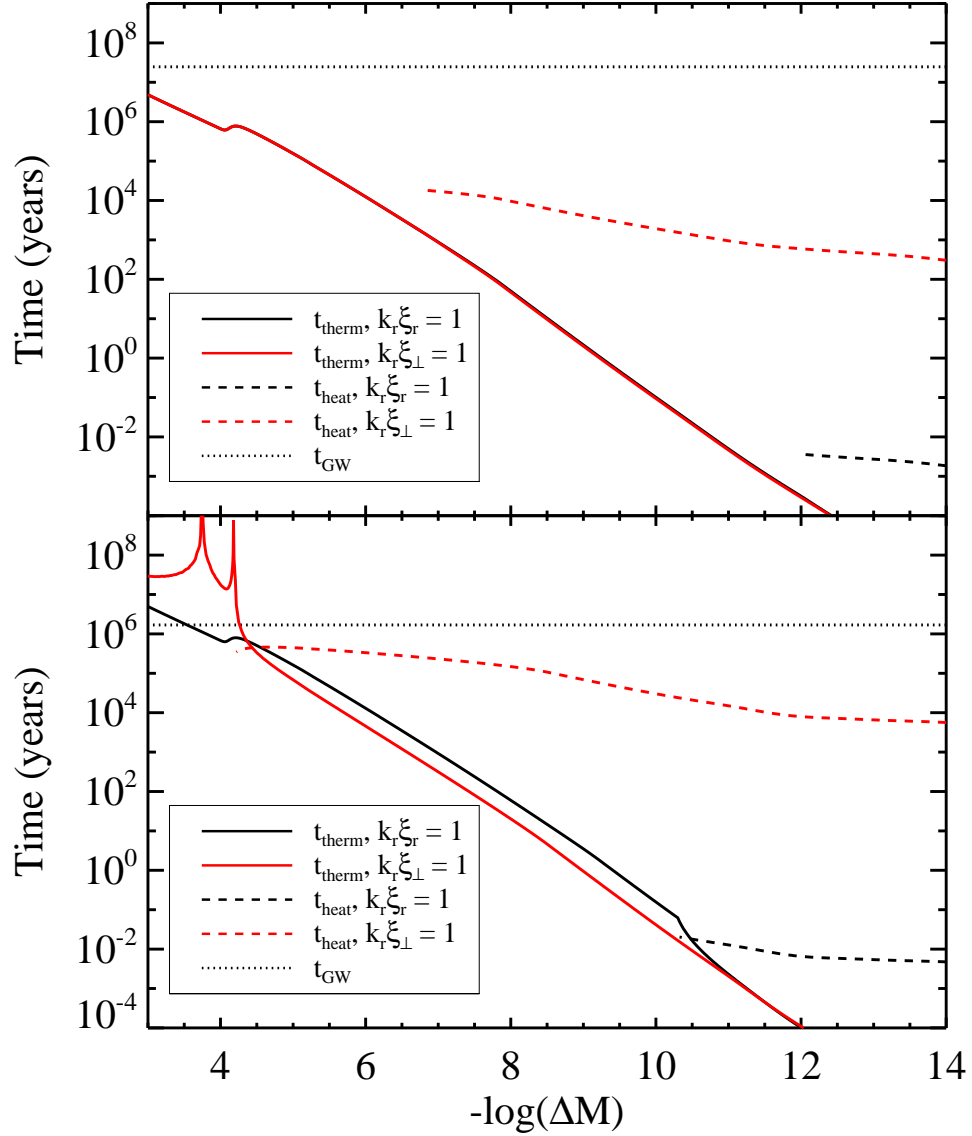


Figure 5.11: The thermal time [solid lines, equation (5.33)], heating time [dashed lines, equation (5.32)], and inspiral time [dotted lines, equation (3.76)] as a function of exterior mass, ΔM , in our $0.6M_{\odot}$ CO WD model with initial temperature $T_{\text{eff}} = 10000\text{K}$. The black lines are calculated using the breaking criterion of equation (5.19), while the red lines are calculated using the breaking criterion of equation (5.20). The top panel is calculated for an orbital period of 45 minutes, while the bottom is for an orbital period of 15 minutes. Both panels are calculated for a $0.3M_{\odot}$ companion.

temperature gradient (thus increasing its luminosity) such that $t_{\text{therm}} \lesssim t_{\text{heat}}$ at all radii.³ However, when ΔM_B is calculated with equation (5.20), the star is unable to reach thermal equilibrium and $t_{\text{therm}} > t_{\text{heat}}$ at the base of the heat deposition zone. The shell at $\Delta M \approx 10^{-4} M_{\odot}$ heats up, and eventually it reaches temperatures high enough to trigger run-away hydrogen fusion.

In principle, tidal heating may change the structure of the WD enough to alter the dynamics of wave excitation and wave breaking. However, we find that this is not the case, with the exception of the instance of a run-away hydrogen fusion event. At and below the location of wave excitation ($\Delta M \gtrsim 6 \times 10^{-3}$), $t_{\text{GW}} \ll t_{\text{heat}}$, so these layers are not affected by tidal heating. At shallower depths ($\Delta M \lesssim 6 \times 10^{-5} M_{\odot}$), significant heating may occur, creating large temperature gradients. However, in our evolutions no interior convection zone forms, despite the large temperature gradients. We thus conclude that the locations of wave excitation and breaking will not be significantly altered by the tidal heating, except in the case of a run-away hydrogen fusion event.

5.6 Discussion

We have calculated the amplitude of tidally excited gravity waves in a $0.3 M_{\odot}$ He WD in a compact binary system, using an outgoing radiative boundary condition. This amplitude translates directly into the rate at which tidal energy and angular momentum are transferred into the WD as a function of the tidal forcing frequency. As in the case of CO WDs (see Paper II), we find that the tidal torque and energy flux depends on the

³In Figure 5.11, the value of t_{therm} goes to infinity at some values of ΔM because the heat flux goes to zero at these locations. This can occur when the amount of tidal heat diffusing inwards from the surface is equal to the amount of intrinsic WD heat diffusing outwards from the core (i.e., there is a local temperature minimum). It can also occur where the tidal heat diffuses equally in both directions (i.e., there is a local temperature maximum).

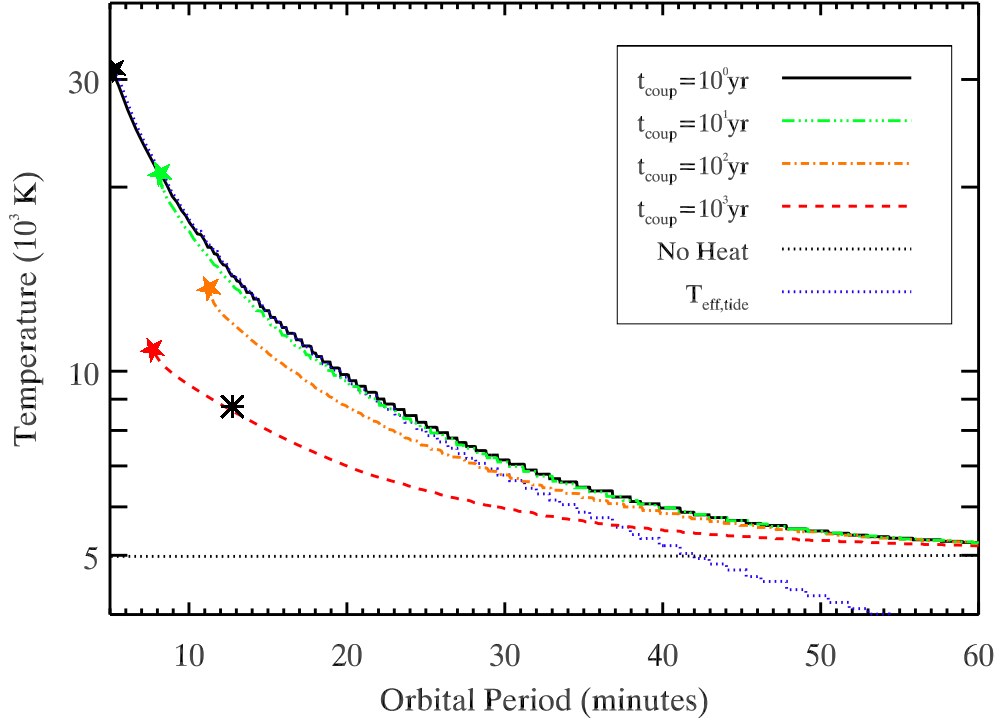


Figure 5.12: Same as the top right panel of Figure 5.9, except that we have also included the temperature calculated using $t_{\text{coup}} = 10^2 \text{ yr}$ (orange dot-dashed line) and $t_{\text{coup}} = 10 \text{ yr}$ (green dot-dot-dashed line). The asterisk marks the position of the secondary in SDSS J0651+2844.

tidal forcing frequency in an erratic way. On average, the dimensionless tidal dissipation rate $F(\omega)$ [related to the inverse of the tidal quality factor, see equation (5.6)], is several orders of magnitude smaller for He WDs than for the $0.6M_{\odot}$ CO WDs studied in Paper II. This difference arises from the larger entropy gradients in low-mass WDs, causing decreased coupling between gravity waves and the tidal potential [see equation (5.10)]. Nevertheless, since low-mass He WDs have larger radii, we find that the critical orbital frequency above which spin-orbit synchronization starts is similar in He and CO WDs, both occurring at an orbital period of about an hour. Furthermore, the amount of tidal heat deposited is similar in He and CO WDs, exceeding the intrinsic luminosity at short orbital periods ($P \lesssim 30$ minutes).

We have also estimated the location of tidal heating due to the non-linear breaking

of outgoing gravity waves or resonant absorption at a critical layer in the WD envelope. The tidal heat is likely deposited in the outer layers of the WD with $\Delta M \lesssim 10^{-2} M_{\odot}$, although the precise location depends on the details of non-linear wave breaking and the efficiency of rotational coupling between the WD core and surface layers. We have evolved WD models to evaluate the effect of tidal heating as function of orbital period. Tidal heating is unimportant at long orbital periods ($P_{\text{orb}} \gtrsim 1$ hour), but can dominate the luminosity of the WD at small orbital periods ($P_{\text{orb}} \lesssim 15$ minutes). We have also found that if the tidal heat is deposited deep enough in a WD (near the He-H composition gradient), it may build up enough to trigger a nova-like hydrogen burning event (a “tidal nova”).

Our theory can be constrained by comparing the predictions of our tidal heating calculations to observed compact WD binaries. The two 39 minute systems J0106-1000 (Kilic et al. 2011a) and J1630+4233 (Kilic et al. 2011b), and the 12.75 minute system J0651+2844 (Brown et al. 2011) provide the best opportunities. We find that the warm temperatures of the He WD primaries in the two 39 minute systems ($T_{\text{eff}} = 16490\text{K}$ in J0106 and $T_{\text{eff}} = 14670\text{K}$ in J1630) can not be explained by tidal heating. These WDs are likely young or kept warm by residual hydrogen shell burning (Steinfadt et al. 2010b). The unseen companions in these two systems do not have measured effective temperatures, but they are unlikely to be substantially increased by tidal heating.

The 12.75 minute system J0651 likely exhibits strong tidal heating signatures. This system is composed of a primary He WD with $T_{\text{eff}} = 16530\text{K}$ and $M = 0.26 M_{\odot}$, and a secondary CO WD with $T_{\text{eff}} \approx 8700\text{K}$ and $M = 0.50 M_{\odot}$ (Hermes et al. 2012). Comparison with Figure 5.8 indicates that the luminosity of the primary is mostly due to intrinsic heat, but that tidal heat may slightly increase its temperature and luminosity. In contrast, comparison with Figure 5.12 indicates the luminosity of the secondary is likely

dominated by tidal heat. In fact, Figure 5.12 predicts that T_{eff} is typically *larger* than the observed surface temperature, except for relatively deep tidal heat deposition.

Our results indicate that the secondary in J0651 is fairly old (it takes a WD several 10^9 yr to cool to $T_{\text{eff}} = 5000\text{K}$), and that tidal heat deposition occurs relatively deep in the star, at $\Delta M_B \gtrsim 10^{-4} M_{\odot}$. Such deep tidal heat deposition could arise due to a thick critical layer created by inefficient rotational coupling between the surface layer and the core, or it could be due to non-linear wave breaking at the He-H composition gradient. Furthermore, Figure 5.12 indicates that a tidal nova may occur in the future of J0651.

However, there are other possible explanations for the cool observed surface temperature of the secondary in J0651. One possibility is that the value of \dot{E}_{heat} used in our calculations is too large. This would require the value of Ω_c to be smaller than suggested by our calculations, i.e., tidal effects become important at *longer* orbital periods than we have predicted. Stronger tidal effects may be possible if some other tidal dissipation mechanism (e.g., inertial waves, non-linear wave excitation, or spin-up via resonance locking, see Burkart et al. 2012 and discussion below) plays an important role in tidal synchronization. This would cause the tidal heating rate at shorter periods to become *smaller*, which could explain the low observed value of T_{eff} .

We find that the ignition of run-away hydrogen fusion is a general characteristic of the tidal heating process for CO WDs with hydrogen envelopes, provided that a significant fraction of the tidal heat is deposited near the base of the hydrogen shell. Thermonuclear runaway only occurs in WDs with initial surface temperatures $T_{\text{eff}} \lesssim 1.2 \times 10^4\text{K}$, otherwise tidal heating promotes steady hydrogen burning. The thermonuclear runaway usually occurs at orbital periods $5\text{min} \lesssim P_{\text{orb}} \lesssim 20\text{min}$, depending on the location of heat deposition, initial temperature of the WD, and companion mass. We speculate that the thermonuclear runaway will create an event very similar to a classical nova. Since most

of the hydrogen would likely be burned or ejected in such an event, recurrent novae are unlikely. Thus, the occurrence rate of these tidally induced novae may be comparable to that of WD mergers involving a CO WD.

Finally, we note that we have ignored the effect of mixing in our WD evolutions. Substantial mixing may be caused by the turbulence of breaking gravity waves or by shear instabilities due to differential rotation. If mixing occurs faster than the gravitational settling time, the composition gradients inside the WD may be smoothed out. Since the composition gradients play important roles in the excitation and breaking of gravity waves, substantial mixing may change the dynamics of the tidal synchronization and heating process. We have also ignored the effect of crystallization on the wave dynamics. Although this issue is unlikely to affect He WDs because of their long cooling times, it may be important for cool CO WDs.

Soon after our paper was submitted, Burkart et al. (2012) posted an article on arXiv studying tides in WD binaries. In addition to examining gravity waves that break [using the criterion of equation (5.19)] in systems with short orbital periods, they discussed resonance locking with WD g-modes at larger orbital periods ($P \gtrsim 1\text{hr}$). This may cause substantial tidal spin-up of the WD in the orbital period range $1\text{hr} \lesssim P \lesssim 4\text{hr}$ if the associated gravity waves do not break. At shorter orbital periods ($P \lesssim 45\text{min}$), Burkart et al. (2012) found that gravity waves indeed break, producing tidal torques and spin evolution similar to ours. Note that if gravity waves break via the non-linearity criterion of equation (5.20), then the resonance locking regime will be limited to long orbital periods. This will reduce the effectiveness of tidal spin-up prior to the onset of continual gravity wave breaking, bringing their results more in line with ours for $P \sim \text{hrs}$. In another recent paper on WD binaries, Valsecchi et al. (2012) discussed possible “anti-resonance locking” of g-modes in the linear theory. The nature of this

“anti-resonance” locking is not clear, nor is the parameter regime where such locking is effective. Overall, it appears that there is a general agreement that at short orbital periods ($P \lesssim 1\text{hr}$), the WD spins up on the orbital decay timescale, with Ω_s/Ω approaching unity as Ω increases, but maintaining an approximately constant $(\Omega - \Omega_s)$ until binary merger or the onset of mass transfer [see Figure 4 or equation (C.3); see also Section 8.1 of Paper II].

Future observations and simulations can further constrain these theories. We are hopeful that more compact WD systems with $P_{\text{orb}} \lesssim 30$ minutes will be discovered in the near future. Measurements of the masses, luminosities, temperatures, and spins of these systems will provide more data points for comparison with our theory. Finally, simulations of gravity waves propagating through a WD envelope could be used to understand the non-linear criterion that governs wave breaking in WDs and could more conclusively determine where tidal heat is deposited in a WD.

CHAPTER 6

DYNAMICAL TIDES IN ECCENTRIC BINARIES AND TIDALLY-EXCITED STELLAR PULSATIONS IN *KEPLER* KOI-54

6.1 Introduction¹

Tides play an important role in binary star systems and in star-planet systems. While numerous studies of tidal effects have been based on the so-called equilibrium tide theory, which parameterizes tidal dissipation by an effective tidal lag angle/time or tidal quality factor (e.g., Darwin 1880; Goldreich & Soter 1966; Alexander 1973; Hut 1981), the underlying physics of tides in fluid stars and planets involves dynamical excitations of waves and oscillations by the tidal force (see Ogilvie & Lin 2007 and Zahn 2008 for recent reviews). Tides in highly eccentric systems are particularly rich in their dynamical behavior, since wave modes with a wide range of frequencies can be excited and participate in the tidal interaction. Various aspects of dynamical tides in eccentric binaries have been studied by Lai (1996,1997), Kumar & Quataert (1998), Witte & Savonije (1999,2001), Willems et al. (2003), Ivanov & Papaloizou (2004) and Papaloizou & Ivanov (2010).

Recent observations of the binary star system HD 187091 (KOI-54) by the *Kepler* satellite provide a unique opportunity for studying dynamical tides in eccentric binaries. KOI-54 consists of two A stars (mass $M_{1,2} = 2.32, 2.38 M_{\odot}$ and radius $R_{1,2} = 2.19, 2.33 R_{\odot}$) in an eccentric ($e = 0.8342$) orbit with period $P = 41.805$ days (Welsh et al. 2011). The binary is nearly face-on with orbital inclination $i_{\text{orb}} = 5.52^{\circ}$. In addition to periodic brightening events caused by tidal distortion and irradiation of the two stars during their close periastron passages, the power spectrum of the *Kepler*

¹This chapter is based on Fuller & Lai (2012A).

light curve revealed 30 significant (with a signal-to-noise ratio $\gtrsim 7$) stellar pulsation modes. The observed mode periods range from 45 hours to 11 hours, corresponding to the mode frequency f_α ranging from $22.42 f_{\text{orb}}$ to $91 f_{\text{orb}}$ (where $f_{\text{orb}} = P^{-1}$ is the orbital frequency). Most interestingly, twenty-one of these mode frequencies are integer multiples of f_{orb} (with the ratio f_α/f_{orb} differing from an integer by 0.01 or less). The two dominant modes have frequencies that are exactly 90 and 91 times f_{orb} , with the corresponding flux amplitudes of $297.7 \mu\text{mag}$ and $229.4 \mu\text{mag}$, respectively.

While dynamical tides in massive-star binaries have been studied before (e.g., Zahn 1977, Goldreich & Nicholson 1989 for circular binaries; Lai 1996,1997, Kumar & Quataert 1998 and Witte & Savonije 1999,2011 for eccentric binaries), KOI-54 represents the first example where tidally excited oscillations are directly observed and therefore serves as an explicit demonstration of dynamical tides at work in the system. As discussed in Welsh et al. (2011), the observed oscillation modes are puzzling: over 20 of the observed modes are nearly exact integer multiples of the orbital frequency, yet several others are not. It is not clear why the dominant modes are so prominent, e.g., why modes with frequencies 90, 91, 44, and 40 times f_{orb} are clearly visible, and yet modes with frequencies greater than $91 f_{\text{orb}}$ and those less than $20 f_{\text{orb}}$ appear to be absent.

The goal of this paper is to explain some of the observational puzzles related to KOI-54 and to develop the general theoretical framework for studying tidally-excited oscillations in eccentric binary systems.

Our paper is organized as follows. In Section 6.2, we derive the general equations for calculating the energies of tidally excited oscillation modes in an eccentric binary. Our theory improves upon previous (and less rigorous) works, and provides a clear relationship between the resonant mode energy and non-resonant mode energy. In Section

6.3 we study the properties of non-radial g-modes relevant to the stars in the KOI-54 system and calculate the non-resonant mode energies – these serve as a benchmark for examining the effect of resonances. In Section 6.4 we present our calculations of the flux variation due to tidally-forced oscillations. We show that the observed flux variation in KOI-54 can be largely explained when a high-frequency mode is locked into resonance (with the mode frequency equal to $90f_{\text{orb}}$). In Section 6.5 we study the possibility of resonance locking. We show that the combination of the secular tidal orbital/spin evolution and the intrinsic spindown of the star (e.g., due to stellar evolution) may naturally lead to resonance locking of a particular mode. Our analysis demonstrates that (in the KOI-54 system) a mode with frequency around $90f_{\text{orb}}$ can be resonantly locked, while modes with higher frequencies cannot. In Section 6.6 we discuss the origin of the observed modes in KOI-54 with frequencies that are not an integer multiple of f_{orb} , including the evidence of nonlinear mode coupling. We conclude in Section 6.7 with a discussion of future prospects and remaining puzzles.

6.2 Dynamical Tides in Eccentric Binary Stars: General Theory

We consider the tidally-excited oscillations of the primary star of mass M and radius R by the companion of mass M' . The gravitational potential produced by M' can be written as

$$U(\mathbf{r}_i, t) = -GM' \sum_{lm} \frac{W_{lm} r^l}{D^{l+1}} e^{-im\Phi(t)} Y_{lm}(\theta, \phi_i), \quad (6.1)$$

where $\mathbf{r}_i = (r, \theta, \phi_i = \phi + \Omega_s t)$ is the position vector (in spherical coordinates) relative to the center of star M (the azimuthal angle ϕ is measured in the rotating frame of the star, with the rotation rate Ω_s and the spin axis aligned with the orbital angular momentum), $D(t)$ is the binary separation and Φ is the orbital true anomaly. The dominant terms have $l = |m| = 2$ and $l = 2, m = 0$, and for these terms $W_{2\pm 2} = (3\pi/10)^{1/2}$ and $W_{20} = (\pi/5)^{1/2}$.

The linear response of star M is specified by the Lagrangian displacement $\xi(\mathbf{r}, t)$, which satisfies the equation of motion (in the rotating frame of the star)

$$\frac{\partial^2 \xi}{\partial t^2} + 2\mathbf{\Omega}_s \times \frac{\partial \xi}{\partial t} + \mathbf{C} \cdot \xi = -\nabla U, \quad (6.2)$$

where \mathbf{C} is a self-adjoint operator (a function of the pressure and gravity perturbations) acting on ξ (see, e.g., Friedman & Schutz 1978). A free mode of frequency ω_α (in the rotating frame) with $\xi_\alpha(\mathbf{r}, t) = \xi_\alpha(\mathbf{r}) e^{-i\omega_\alpha t} \propto e^{im\phi - i\omega_\alpha t}$ satisfies

$$-\omega_\alpha^2 \xi_\alpha - 2i\omega_\alpha \mathbf{\Omega}_s \times \xi_\alpha + \mathbf{C} \cdot \xi_\alpha = 0, \quad (6.3)$$

where $\{\alpha\}$ denotes the mode index, which includes the radial mode number n , the polar mode number L (which reduces to l for spherical stars) and the azimuthal mode number m . We carry out phase space mode expansion (Schenk et al. 2002)

$$\begin{bmatrix} \xi \\ \partial \xi / \partial t \end{bmatrix} = \sum_\alpha c_\alpha(t) \begin{bmatrix} \xi_\alpha(\mathbf{r}) \\ -i\omega_\alpha \xi_\alpha(\mathbf{r}) \end{bmatrix}, \quad (6.4)$$

where the sum includes not only mode indices, but also both positive and negative ω_α . Note that the usual mode decomposition, $\xi = \sum_{\alpha'} c_{\alpha'} \xi_{\alpha'}$ (with the sum including only mode indices), adopted in many previous studies (e.g., Lai 1997, Kumar & Quataert 1998; Witte & Savonije 1999), are rigorously valid only for non-rotating stars. Using the orthogonality relation $\langle \xi_\alpha, 2i\mathbf{\Omega}_s \times \xi_{\alpha'} \rangle + (\omega_\alpha + \omega_{\alpha'}) \langle \xi_\alpha, \xi_{\alpha'} \rangle = 0$ (for $\alpha \neq \alpha'$), where $\langle A, B \rangle \equiv \int d^3x \rho (A^* \cdot B)$, we find (Lai & Wu 2006)²

$$\begin{aligned} \dot{c}_\alpha + (i\omega_\alpha + \gamma_\alpha) c_\alpha &= \frac{i}{2\varepsilon_\alpha} \langle \xi_\alpha(\mathbf{r}), -\nabla U \rangle \\ &= \frac{iGM' W_{lm} Q_\alpha}{2\varepsilon_\alpha D^{l+1}} e^{im\Omega_s t - im\Phi}, \end{aligned} \quad (6.5)$$

where γ_α is the mode (amplitude) damping rate, and

$$Q_\alpha \equiv \langle \xi_\alpha, \nabla(r^l Y_{lm}) \rangle, \quad (6.6)$$

$$\varepsilon_\alpha \equiv \omega_\alpha + \langle \xi_\alpha, i\mathbf{\Omega}_s \times \xi_\alpha \rangle, \quad (6.7)$$

²As noted before, in this paper we restrict to aligned spin-orbit configurations for simplicity. Generalization to misaligned systems is straightforward (Lai & Wu 2006; see also Ho & Lai 1999).

and we have used the normalization $\langle \xi_\alpha, \xi_\alpha \rangle = 1$. The quantity Q_α (called the “tidal overlap integral” or “tidal coupling coefficient”) directly relates to the tidally excited mode amplitude. We shall focus on $l = 2, m = 0$ and $|m| = 2$ modes in the following (although we will continue to use the notations l and m so that it would be easy to generalize to high-order tides).

The general solution equation (6.5) is

$$c_\alpha(t) = e^{-i\omega_\alpha t - \gamma_\alpha t} \int_{t_0}^t \frac{iGM'W_{lm}Q_\alpha}{2\varepsilon_\alpha D^{l+1}} e^{i\sigma_\alpha t + \gamma_\alpha t - im\Phi} dt, \quad (6.8)$$

assuming $c_\alpha(t_0) = 0$, where

$$\sigma_\alpha = \omega_\alpha + m\Omega_s \quad (6.9)$$

is the mode frequency in the inertial frame. Let $t_j = (2j - 1)P/2$ (with $j = 0, 1, 2, \dots$) be the times at apastron. After the k th periastron passage, the mode amplitude becomes

$$c_\alpha(t_k) = (\Delta c_\alpha) e^{im\Omega_s t_k - (i\sigma_\alpha + \gamma_\alpha)P/2} \times \left[\frac{1 - e^{-(i\sigma_\alpha + \gamma_\alpha)kP}}{1 - e^{-(i\sigma_\alpha + \gamma_\alpha)P}} \right], \quad (6.10)$$

with

$$\Delta c_\alpha = \int_{-P/2}^{P/2} dt \frac{iGM'W_{lm}Q_\alpha}{2\varepsilon_\alpha D^{l+1}} e^{i\sigma_\alpha t + \gamma_\alpha t - im\Phi}. \quad (6.11)$$

For $\gamma_\alpha kP \gg 1$, the steady-state mode energy in the inertial frame

$$E_\alpha = 2\sigma_\alpha \varepsilon_\alpha |c_\alpha|^2 \quad (6.12)$$

becomes (Lai 1997)³

$$E_\alpha = \frac{\Delta E_\alpha}{2(\cosh \gamma_\alpha P - \cos \sigma_\alpha P)} \simeq \frac{\Delta E_\alpha}{4 \sin^2(\sigma_\alpha P/2) + (\gamma_\alpha P)^2}, \quad (6.13)$$

³Equation (6.13) was derived in Lai (1997) in an approximate manner (since mode decomposition was not done rigorously), and physical arguments were used to get rid of a fictitious term.

where the second equality assumes $\gamma_\alpha P \ll 1$. Here ΔE_α is the energy transfer to the mode in the “first” periastron passage:

$$\Delta E_\alpha = \frac{GM'^2}{R} \left(\frac{R}{D_p} \right)^{2(l+1)} \frac{2\pi^2 \sigma_\alpha}{\varepsilon_\alpha} |Q_\alpha K_{lm}(\sigma_\alpha)|^2, \quad (6.14)$$

where $D_p = a(1 - e)$ is the periastron distance (a is the orbital semi-major axis) and

$$K_{lm}(\sigma_\alpha) = \frac{W_{lm}}{2\pi} \int_{-P/2}^{P/2} dt \left(\frac{R}{D} \right)^{l+1} e^{i\sigma_\alpha t - im\Phi}. \quad (6.15)$$

Note that in equation (6.14), both Q_α and K_{lm} are dimensionless (in units such that $G = M = R = 1$).

Equation (6.13) shows that when $\sigma_\alpha P$ is not close to $2\pi N$ (where N is an integer), the steady-state mode energy is approximately ΔE_α . Thus ΔE_α serves as a benchmark for the non-resonant mode energy. Equation (6.13) provides a simple relationship between the actual mode energy E_α and the non-resonant mode energy ΔE_α .

6.3 Stellar Oscillation Modes and Non-Resonant Mode Energies

We construct an $M = 2.35 M_\odot$ stellar model using the MESA code (Paxton et al. 2010). We assume solar metallicity and evolve the star until its radius reaches $R = 2.34 R_\odot$. These parameters are close to star M_2 in KOI-54. Figure 6.1 displays a propagation diagram for our stellar model. The star has a small convective core inside radius $r = 0.09R$. We make sure that the stellar model has thermodynamically consistent pressure, density, sound speed and Brunt-Väsälä frequency profiles. We have computed the $l = 2$ adiabatic g-modes for this non-rotating stellar model, including ω_α , Q_α , and the mode mass $M_\alpha \equiv \langle \xi_\alpha \cdot \xi_\alpha \rangle / |\xi_\alpha(R)|^2$. Here, the magnitude of the surface displacement is defined

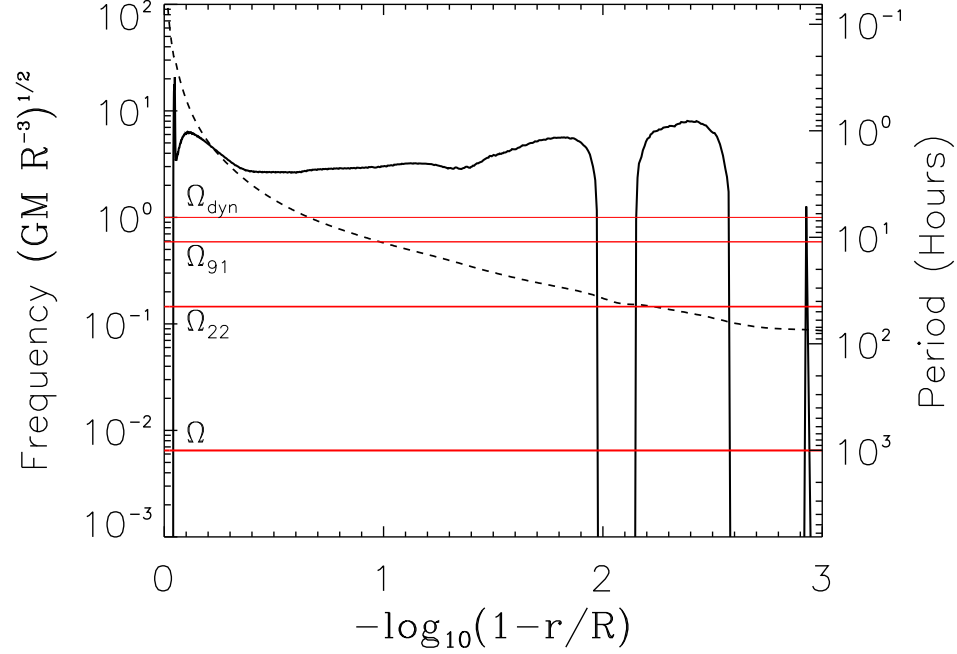


Figure 6.1: Propagation diagram for our $M = 2.35M_{\odot}$, $R = 2.34R_{\odot}$ stellar model, showing the value of N (solid black line) and the Lamb frequency, L_2 (dashed black line), in units of $(GM/R^3)^{1/2}$. The horizontal red lines denote important angular frequencies for the KOI-54 system, including (from top) the dynamical frequency of the star, $(GM/R^3)^{1/2}$; the highest frequency mode observed in KOI-54 ($\sigma_{\alpha} = 91\Omega$); the lowest frequency mode observed ($\sigma_{\alpha} = 22.42\Omega$); and the orbital angular frequency, Ω . The y-axis on the right-hand side displays the corresponding periods, in units of hours.

by

$$\begin{aligned}
 |\xi_{\alpha}(R)|^2 &= \int d\Omega \xi_{\alpha}(R) \cdot \xi_{\alpha}^*(R) \\
 &= \xi_{r\alpha}^2(R) + l(l+1)\xi_{\perp\alpha}^2(R),
 \end{aligned} \tag{6.16}$$

where the r and \perp subscripts denote the radial and horizontal components of the displacement vector, respectively.

We use equation (6.14) to compute the non-resonant mode energy $E_{\alpha} \sim \Delta E_{\alpha}$. The

corresponding surface displacement $\xi_\alpha(R)$ is then obtained from

$$|\xi_\alpha(R)| \equiv \left(\frac{E_\alpha}{M_\alpha \sigma_\alpha^2} \right)^{1/2}. \quad (6.17)$$

Figure 6.2 shows the energy ΔE_α and surface amplitude of the radial component of the displacement, $\xi_{r\alpha}(R)$, of tidally excited modes away from resonances for KOI-54 parameters. The radial displacement is directly related to the flux variation due to the oscillation mode (see Section 4). The most energetic modes have frequencies $80\Omega \lesssim \sigma_\alpha \lesssim 140\Omega$, where Ω is the orbital angular frequency, depending on the stellar spin rate and the value of m . Low-order (high frequency) modes have larger values of Q_α but have smaller values of $K_{lm}(\sigma_\alpha)$, so medium-order ($n \approx 15$) modes have the largest values of ΔE_α .⁴

Figure 6.2 also shows the magnitude of the displacement $|\xi_\alpha(R)|$ for $m = 2$ modes in the zero spin limit. The total displacement is much larger than the radial displacement for low-frequency modes because these modes are characterized by large horizontal displacements and are concentrated near the surface. Consequently, these modes have lower mode mass and the maximum of $|\xi_\alpha(R)|$ shifts to lower frequencies compared to the maximum of ΔE_α .

The rotation rates of the KOI-54 stars are unknown. Spectroscopic observations constrain $V_{\text{rot}} \sin i_s \lesssim 10 \text{ km s}^{-1}$, corresponding to $V_{\text{rot}} \lesssim 100 \text{ km s}^{-1}$, if the spin inclination angle i_s is equal to that of the orbital inclination angle $i_{\text{orb}} = 5.5^\circ$ (Welsh et al. 2011). This implies that the spin period $P_s \gtrsim 1.2$ days and that $\Omega_s \lesssim 30\Omega$. Although the classical equilibrium tide theory (e.g., Hut 1981) is not expected to be valid for our system (Lai 1997), we can adopt the pseudosynchronous rotation frequency $\Omega_s = \Omega_{\text{ps}} = 16.5\Omega$ [corresponding to $f_{\text{ps}} = 1/(2.53 \text{ days})$] as a fiducial value.

⁴The orbital frequency at periastron is $f_p = f_{\text{orb}}(1+e)^{1/2}/(1-e)^{3/2} = 20.06 f_{\text{orb}} = 1/(2.084 \text{ d})$, thus $m = 2$ modes with $\sigma_\alpha/\Omega \sim 40$ have the largest values of K_{lm} . For $m = 0$, modes with $\sigma_\alpha/\Omega \sim 1$ have the largest values of K_{lm} .

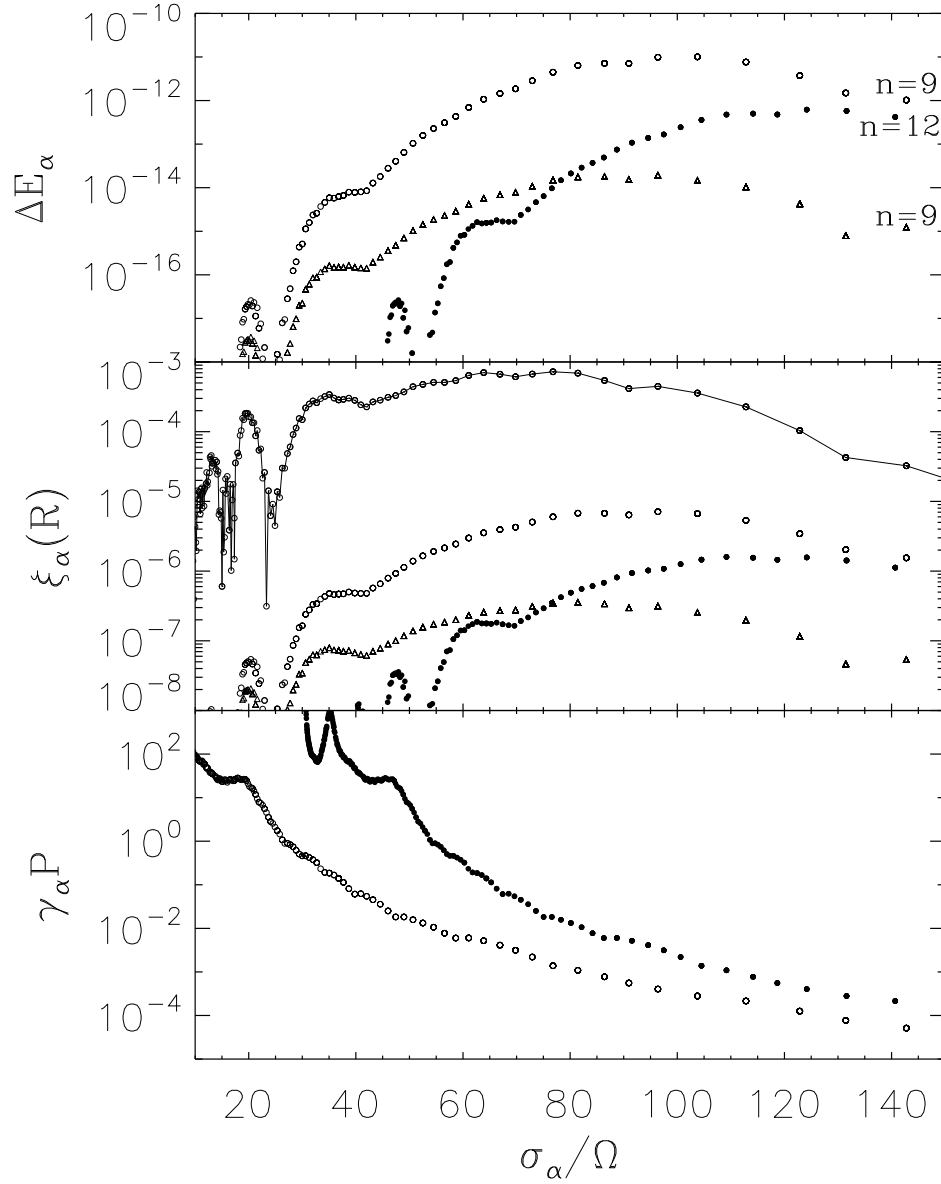


Figure 6.2: Non-resonant mode energy ΔE_α (top), amplitude of the radial surface displacement $\xi_{r\alpha}(R)$ (middle), and mode damping rates $\gamma_\alpha P$ (bottom) as a function of mode frequency σ_α (in units of the orbital frequency Ω). The $l = m = 2$ modes are plotted as open circles for $\Omega_s = 0$ and filled circles for $\Omega_s = 16.5\Omega$, while $m = 0$ modes are plotted as triangles. The middle panel also displays the magnitude of the surface displacement, $|\xi_\alpha(R)|$, for the $l = m = 2$ modes with $\Omega_s = 0$ (open circles connected by lines). The highest frequency modes shown are the g_9 mode for the $m = 0$ and non-spinning $m = 2$ cases, and the g_{12} mode for the spinning $m = 2$ case. The mode energy is in units of GM^2/R and the displacement is in units of R .

To account for the effect of stellar rotation on the tidally excited modes, we adopt the perturbative approximation, valid when Ω_s is less than $\omega_\alpha^{(0)}$ (the mode frequency in the zero-rotation limit). The mode wave functions and Q_α are unchanged by the stellar rotation, while the mode frequencies are modified according to $\omega_\alpha = \omega_\alpha^{(0)} - mC_{nl}\Omega_s$ and $\sigma_\alpha = \omega_\alpha^{(0)} + m(1 - C_{nl})\Omega_s$, where $C_{nl} > 0$ is a constant (e.g. Unno et al. 1989) — our calculation gives $C_{nl} \simeq 0.16$ for all relevant modes. Note that in this approximation, $\varepsilon_\alpha = \omega_\alpha^{(0)}$. More accurate results can be obtained using the method of Lai (1997).

Stellar rotation increases the inertial-frame frequency σ_α of the $m > 0$ modes, causing the dominant modes to have higher observed frequencies. However, rotation also shifts the tidal response to higher order g-modes with smaller values of Q_α , so we expect rotation to lower the mode energies. Figure 6.2 confirms that finite (prograde) stellar rotation indeed shifts the dominant mode energy and surface amplitude to higher-order g-modes, giving rise to smaller ΔE_α and $\xi_{r\alpha}(R)$.

The somewhat erratic features of ΔE_α and ξ_α as seen in Figure 6.2 for high-order (low frequency) modes are due to mode trapping effects created by the thin sub-surface convection zone in our stellar model. For these high-order modes, the tidal overlap integrals (Q_α) depend on the precise shape of the mode wave function, and they can be easily affected by the detailed properties of the stellar envelope. Care must be taken in order to obtain reliable tidal overlap integrals for these high-order modes (see Fuller & Lai 2010).

The damping rate of a mode, γ_α , can be estimated in the quasi-adiabatic limit via

$$\gamma_\alpha \approx \int_{r_-}^{r_+} k_r^2 \chi (\xi_r^2 + l(l+1)\xi_\perp^2) \rho r^2 dr, \quad (6.18)$$

where χ is the thermal diffusivity, $k_r^2 \simeq l(l+1)N^2/(r^2\omega^2)$ is the local radial wave number, and r_+ and r_- are the boundaries of the mode's propagation cavity. Equation (6.18) can be derived in the WKB limit from the quasi-adiabatic work function of a mode (Unno

et al. 1989).⁵ The bottom panel of Figure 6.2 shows the values of γ_α calculated via equation (6.18) for the modes of our stellar model. Lower frequency g-modes have larger damping rates due to their larger wavenumbers and because they propagate closer to the surface of the star where the diffusivity is larger. Equation (6.18) provides an estimate for mode damping rates via radiative diffusion in the quasi-adiabatic limit; however, fully adiabatic oscillation equations must be solved for low-frequency modes for which γ_α is comparable to the mode frequency. Furthermore, modes may also damp via nonlinear processes (see Section 6.6).

6.4 Flux Variation due to Tidally-Forced Oscillations

In section 6.2, we considered the tidal response to be composed of the sum of the star's natural oscillation modes, each having its own steady-state energy E_α . This provides a simple relation between the resonant mode energy and non-resonant energy. The observed magnitude variation of KOI-54 has over 20 components with frequencies that are almost exact multiples of the orbital frequency, i.e., they have $\sigma_\alpha = (N + \epsilon)\Omega$ with $|\epsilon| \leq 0.01$. In this section, we examine the tidal response as a sum of oscillations at exact multiples of the orbital frequency. Each component U_{lm} of the tidal potential can be decomposed as

$$U_{lm} = -\frac{GM'W_{lm}r^l}{a^{l+1}}Y_{lm}(\theta, \phi_i) \sum_{N=-\infty}^{\infty} F_{Nm} e^{-iN\Omega t}, \quad (6.19)$$

where F_{Nm} is defined by the expansion

$$\left(\frac{a}{D}\right)^{l+1} e^{-im\Phi} = \sum_{N=-\infty}^{\infty} F_{Nm} e^{-iN\Omega t} \quad (6.20)$$

⁵While our paper was under review, we became aware of the paper by Burkart et al. (2011), who also used equation (6.18) to estimate the mode damping rate. The bottom panel of Figure 6.2 was added after we saw the Burkart et al. paper.

and is given by

$$F_{Nm} = \frac{1}{\pi} \int_0^\pi d\Psi \frac{\cos [N(\Psi - e \sin \Psi) - m\Phi(t)]}{(1 - e \cos \Psi)^l}. \quad (6.21)$$

Here, a is the semi-major axis of the orbit, and Ψ is the eccentric anomaly. Note that F_{Nm} is related to K_{lm} [see equation (6.15)] by $K_{lm}(\sigma_\alpha = N\Omega) = W_{lm}(1 - e)^{l+1}\Omega^{-1}F_{Nm}$. Inserting equation (6.19) into equation (6.5) yields

$$\begin{aligned} \dot{c}_\alpha + (i\omega_\alpha + \gamma_\alpha)c_\alpha &= \frac{iGM'W_{lm}Q_\alpha}{2\varepsilon_\alpha a^{l+1}} \\ &\times \sum_{N=-\infty}^{\infty} F_{Nm} e^{i(m\Omega_s - N\Omega)t}, \end{aligned} \quad (6.22)$$

whose non-homogeneous solution is

$$c_\alpha(t) = \frac{GM'W_{lm}Q_\alpha}{2\varepsilon_\alpha a^{l+1}} \sum_{N=-\infty}^{\infty} \frac{F_{Nm} e^{-i(N\Omega - m\Omega_s)t}}{(\sigma_\alpha - N\Omega) - i\gamma_\alpha}. \quad (6.23)$$

The total tidal response is $\xi(\mathbf{r}, t) = \sum_\alpha c_\alpha(t) \xi_\alpha(\mathbf{r})$, where $\xi_\alpha(\mathbf{r}) \propto e^{im\phi}$. When the displacements are expressed in terms of $\mathbf{r}_i = (r, \theta, \phi_i)$ (the position vector in the inertial frame, with $\phi_i = \phi + m\Omega_s t$), we have

$$\begin{aligned} \xi(\mathbf{r}_i, t) &= \sum_{N=-\infty}^{\infty} \sum_{\alpha'} \frac{GM'W_{lm}Q_\alpha}{2\varepsilon_\alpha a^{l+1}} \frac{F_{Nm} \xi_\alpha(\mathbf{r}_i)}{(\sigma_\alpha - N\Omega) - i\gamma_\alpha} e^{-iN\Omega t} \\ &= \sum_{N=1}^{\infty} \sum_{\alpha'} \frac{GM'W_{lm}Q_\alpha}{2\varepsilon_\alpha a^{l+1}} \xi_\alpha(\mathbf{r}_i) \\ &\times \left[\frac{F_{Nm} e^{-iN\Omega t}}{(\sigma_\alpha - N\Omega) - i\gamma_\alpha} + \frac{F_{-Nm} e^{iN\Omega t}}{(\sigma_\alpha + N\Omega) - i\gamma_\alpha} \right] + c.c. \end{aligned} \quad (6.24)$$

where $c.c.$ denotes the complex conjugate, and $\sum_{\alpha'}$ implies that the sum is restricted to modes with $\omega_\alpha > 0$ (including both $m > 0$ and $m < 0$ modes) (by contrast, \sum_α includes both $\omega_\alpha > 0$ and $\omega_\alpha < 0$ terms, as well as both $m > 0$ and $m < 0$). We have omitted the $N = 0$ term for simplicity because it is not part of the dynamical response. Each ξ_N (oscillating at frequency $N\Omega$) is then a sum over the star's oscillation modes, with large contributions coming from nearly-resonant modes with $\sigma_\alpha \approx N\Omega$.

We use the results of Buta & Smith (1979) (see also Robinson et al. 1982) to estimate the magnitude variation (Δmag) associated with each component of the tidal response.

The magnitude variation of the star has two primary components: a geometrical component, $(\Delta\text{mag})_G$, due to distortions in the shape of the star, and a temperature component, $(\Delta\text{mag})_T$, due to perturbations in the surface temperature of the star's photosphere.

For an $l = m = 2$ mode with surface radial displacement $\xi_{r\alpha}(R)$, the amplitudes of the bolometric magnitude variations are

$$(\Delta\text{mag})_{\alpha T}^{(m=2)} \simeq -1.7 \gamma_l \sin^2 i_s \frac{\Gamma_2 - 1}{\Gamma_2} \times \left[\frac{l(l+1)}{\hat{\omega}_\alpha^2} - 4 - \hat{\omega}_\alpha^2 \right] \frac{\xi_{r\alpha}(R)}{R} \quad (6.25)$$

and

$$(\Delta\text{mag})_{\alpha G}^{(m=2)} \simeq -0.42 (\alpha_l + \beta_l) \sin^2 i_s \frac{\xi_{r\alpha}(R)}{R}. \quad (6.26)$$

Here, $\Gamma_2 \simeq 5/3$ is the adiabatic index of gas at the surface of the star, $\hat{\omega} = \omega_\alpha / \sqrt{GM/R^3}$ is the dimensionless mode frequency, and $\gamma_l \approx 0.3$ and $\alpha_l + \beta_l \approx -1.2$ are bolometric limb darkening coefficients appropriate for A stars. For KOI-54, the value of the spin inclination angle i_s (the angle between the spin axis and the line of sight) is unknown, but we may use the system's orbital inclination of $i_{\text{orb}} = 5.5^\circ$ as a first guess, although it is possible that the star's spin axis is inclined relative to the orbital angular momentum axis. Similarly, for $l = 2, m = 0$ modes, the amplitudes of the magnitude variations are

$$(\Delta\text{mag})_{\alpha T}^{(m=0)} \simeq -1.4 \gamma_l (3 \cos^2 i_s - 1) \frac{\Gamma_2 - 1}{\Gamma_2} \times \left[\frac{l(l+1)}{\hat{\omega}_\alpha^2} - 4 - \hat{\omega}_\alpha^2 \right] \frac{\xi_{r\alpha}(R)}{R} \quad (6.27)$$

and

$$(\Delta\text{mag})_{\alpha G}^{(m=0)} \simeq -0.34 (\alpha_l + \beta_l) (3 \cos^2 i_s - 1) \frac{\xi_{r\alpha}(R)}{R}. \quad (6.28)$$

In equations (6.25) and (6.27), the factor of $[l(l+1)/\hat{\omega}_\alpha^2 - 4 - \hat{\omega}_\alpha^2]$ arises from the outer boundary condition formulated by Baker & Kippenhahn (1965) (see also Dziembowski 1971), in which the radial derivative of the Lagrangian pressure perturbation vanishes

at the outer boundary (in our case, the stellar photosphere), such that the mode energy vanishes at infinity in an isothermal atmosphere. It is not clear how well this boundary condition applies for a real star, nor how it should be modified when non-adiabatic effects are taken into account. For the g -modes considered here, the factor $l(l+1)/\hat{\omega}_\alpha^2 \gg 1$, causing the temperature effect to overwhelm the geometrical effect for magnitude variations.

The magnitude variation for each frequency $N\Omega$ is a sum of the variations due to individual modes:

$$(\Delta \text{mag})_N = \sum_{\alpha'} \frac{GM' W_{lm} Q_\alpha a_\alpha}{2\varepsilon_\alpha a^{l+1}} \frac{\xi_{r\alpha}(R)}{R} \times \left[\frac{F_{Nm} e^{-iN\Omega t}}{(\sigma_\alpha - N\Omega) - i\gamma_\alpha} + \frac{F_{-Nm} e^{iN\Omega t}}{(\sigma_\alpha + N\Omega) - i\gamma_\alpha} \right] + c.c., \quad (6.29)$$

where a_α is the constant in front of $\xi_{r\alpha}(R)/R$ in equations (6.25)-(6.28), and $N > 0$.

Using the values of ε_α , Q_α , $\xi_\alpha(r)$, and γ_α calculated in Section 6.2, we compute each term $(\Delta \text{mag})_N$ in equation (6.29). Figure 6.3 shows a plot of the magnitude variation as a function of N , along with the observed magnitude variations in KOI-54 as determined by Welsh et al. (2011). To make this plot, we have subtracted out the contribution from the “equilibrium tide”, because the equilibrium tide is responsible for the periodic brightening of KOI-54 near periastron and was subtracted out by Welsh et al. (2011) in order to obtain the magnitude variations due to tidally-induced stellar oscillations. The equilibrium tide can be computed by taking the limit $\sigma_\alpha \gg N\Omega$, i.e., by setting $N\Omega = 0$ for each term inside the sum in equation (6.29). We adopt a spin inclination angle $i_s = 10^\circ$.

Figure 6.3 includes the magnitude variations due to the temperature effect and those due to geometrical effects. For the adopted spin inclination (10°), the $m = 0$ modes dominate the observed magnitude variations, although a nearly-resonant $m = 2$ mode

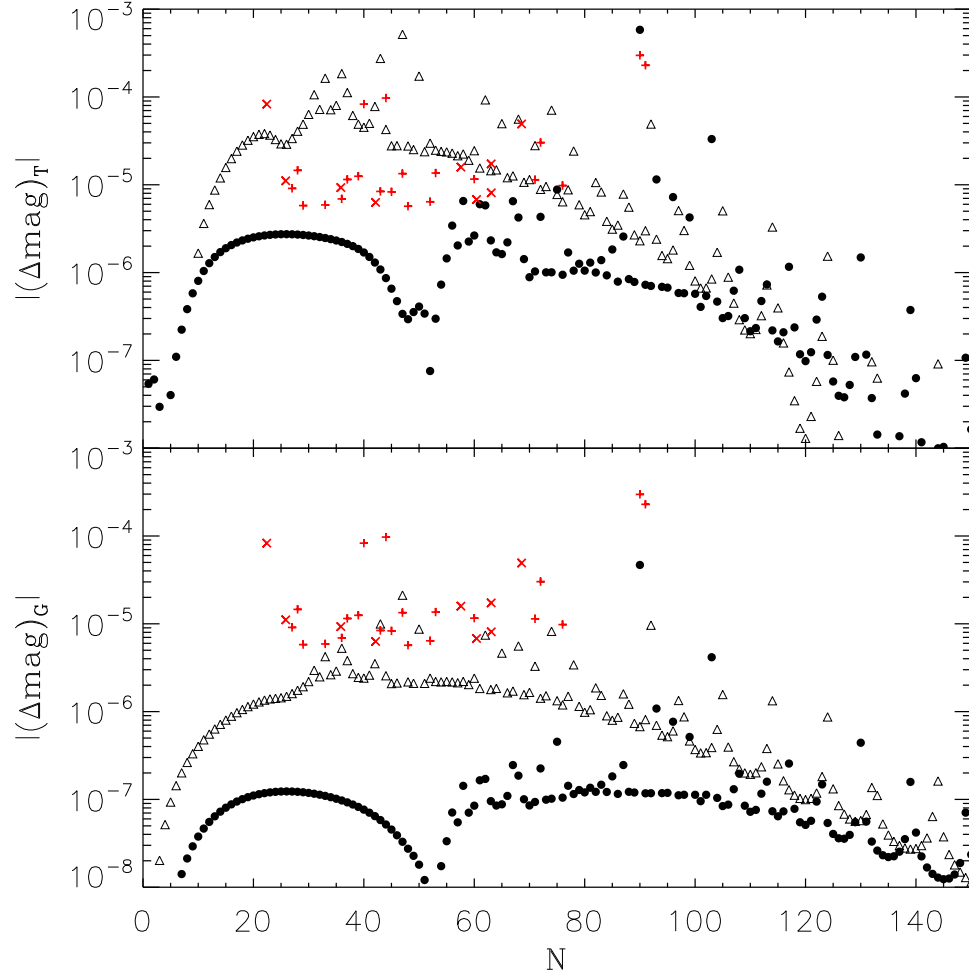


Figure 6.3: Magnitude variation Δmag_N as a function of N due to the temperature effect (top) and geometrical effect (bottom) for $l = m = 2$ modes (filled circles) and $l = 2, m = 0$ modes (triangles). We also plot the observed magnitude variations that are an integer multiple of the orbital frequency (red plus symbols), and those that are not an integer multiple of the orbital frequency (red x symbols). The plot uses $i_s = 10^\circ$ and $\Omega_s \approx 15\Omega$.

can be visible. However, it is obvious from Figure 6.3 that our computed variations due to the temperature effect of $m = 0$ modes are appreciably larger than those observed. In fact, the magnitude variations due to geometrical effects reproduce the observed variations much more accurately. The over-prediction of the magnitude variations from the temperature effect is mostly likely due to non-adiabatic effects in the stellar atmosphere, which renders equations (6.25) and (6.27) inaccurate for low-frequency modes. Indeed, Buta & Smith (1979) also found that for main sequence B stars, the predicted magnitude variations due to the temperature effect for low-frequency modes were much larger than what was observed, and they speculated that the mismatch was due to non-adiabatic effects in the outer layers of the star.

Our results depicted in Figure 6.3 suggest that most of the observed magnitude variations (with the exception the highest-frequency modes) in KOI-54 are due the geometrical surface distortions produced by $m = 0$ modes that happen to be nearly resonant with a harmonic of the orbital frequency. The actual magnitude variations due to the temperature effect (when non-adiabatic effects are properly taken into account near the stellar photosphere) should not be much larger than the geometric effect. Note that in Figure 6.3, we have plotted the absolute values of the magnitude variations for the temperature and geometrical effects, but the temperature and geometrical effects have opposite sign.

To produce the highest-frequency modes ($90f_{\text{orb}}$ and $91f_{\text{orb}}$) observed in KIO-54, in Figure 6.3 we have fine-tuned the spin of the star to $\Omega_s \simeq 15\Omega$ such that the $N = 90$ oscillation is nearly resonant with one of the star's oscillation modes. In section 5 we argue that the $N = 90$ and $N = 91$ oscillations are likely due to an $m = 2$ mode in each star that is locked in resonance. The fine-tuning produces a magnitude variation due to the temperature effect that is comparable to one of the observed oscillations, although the predicted geometrical magnitude variation is somewhat less than what is observed.

If the $N = 90$ and $N = 91$ oscillations are indeed due to resonant $m = 2$ modes, then it is likely that the predicted magnitude variation due to the temperature effect (based on the adiabatic approximation) is more accurate for these modes due to their higher frequencies. This is not unreasonable since non-adiabatic effects in the stellar photosphere are expected to be less important for low-order (high frequency) modes, a point also emphasized by Buta & Smith (1979). In any case, a more in-depth analysis of the non-adiabatic oscillation modes (particularly their flux variations) for the stars of the KOI-54 system is needed.

6.5 Secular Spin-Orbit Evolution and Resonance Locking

In the previous sections we proposed that a resonance with $\sigma_\alpha \sim 90\Omega$ creates the largest observed magnitude variations in KOI-54. Here we study the secular evolution of the stellar spin and binary orbit, and how resonances may naturally arise during the evolution. Several aspects of tidal resonance locking in massive-star binaries were previously explored by Witte & Savonije (1999, 2001).

Dynamical tides lead to spin and orbital evolution, with the orbital energy and angular momentum evolving according to

$$\dot{E}_{\text{orb}} = - \sum_{\alpha} 2\gamma_{\alpha} E_{\alpha}, \quad \dot{J}_{\text{orb}} = - \sum_{\alpha} 2\gamma_{\alpha} E_{\alpha} \frac{m}{\sigma_{\alpha}}, \quad (6.30)$$

where we have used the fact that the mode angular momentum (in the inertial frame) is related to the mode energy by $J_{\alpha} = (m/\sigma_{\alpha})E_{\alpha}$. The orbital frequency Ω therefore evolves as

$$\frac{\dot{\Omega}}{\Omega} = \sum_{\alpha} \frac{f_{\alpha}}{t_{d\alpha}}, \quad (6.31)$$

where

$$f_{\alpha} = \left[4 \sin^2(\pi\sigma_{\alpha}/\Omega) + (\gamma_{\alpha}P)^2 \right]^{-1}, \quad (6.32)$$

and $t_{d\alpha}^{-1}$ specifies the orbital decay rate due to a single non-resonant mode α :

$$\begin{aligned} t_{d\alpha}^{-1} &= \frac{3\gamma_\alpha \Delta E_\alpha}{|E_{\text{orb}}|} \\ &= \frac{12\pi^2 \gamma_\alpha}{(1-e)^6} \left(\frac{M'}{M} \right) \left(\frac{R}{a} \right)^5 \left(\frac{\sigma_\alpha}{\varepsilon_\alpha} \right) |Q_\alpha K_{lm}|^2. \end{aligned} \quad (6.33)$$

Using the KOI-54 parameters and assuming $\sigma_\alpha \sim \varepsilon_\alpha$, we have

$$t_{d\alpha}^{-1} \simeq 8.9 \times 10^{-10} \gamma_\alpha \left(\frac{Q_\alpha K_{lm}}{10^{-4}} \right)^2. \quad (6.34)$$

Resonance occurs when a mode has frequency $\sigma_\alpha = N\Omega$ for an integer value of N .

6.5.1 Need for Resonance Locking

We first consider how likely it is to observe a mode near resonance when σ_α is held constant (i.e., it does not change during the period of resonance-crossing).

As can be seen from Figure 6.2, the $m = 2$ modes dominate tidal energy transfer in the KOI-54 system, yet (as evidenced from Figure 6.3), most of the visible modes (except $N = 90, 91$) are $m = 0$ modes. Consider a particular $m = 0$ mode near resonance, with $\sigma_\alpha = (N + \epsilon)\Omega$ and $|\epsilon| \ll 1$. Since the mode contributes little to the tidal energy transfer, the probability of being close to resonance ($|\epsilon| < \epsilon_0$) is simply $P_{\text{res}} \simeq 2\epsilon_0$. Figure 6.3 indicates that an $m = 0$ mode with $25 \lesssim N \lesssim 80$ requires $|\epsilon_0| \lesssim 0.1$ to be visible [mode visibility scales as $|\Delta \text{mag}| \propto 1/|\epsilon|$]. In each star there are about forty $m = 0$ modes in this frequency range, thus we should expect about 8 of these modes from each star to be visible, in rough agreement with Figure 6.3 and the observations.

Now let us consider modes that significantly influence the tidal energy transfer (these include $m = 2$ modes such as the $N = 90, 91$ modes, but may also include $m = 0$ modes very near resonance – if they occur). For the KOI-54 system, the modes that contribute

significantly to the tidal energy transfer have $\sigma_\alpha \gtrsim 2\Omega_p \simeq 40\Omega$, thus $N = \sigma_\alpha/\Omega \gtrsim 40$. Consider a particular mode near resonance, and suppose that the tidal energy transfer is dominated by the resonant mode (α). The orbital decay rate during the resonance is given by $\dot{P}/P = -t_{d\alpha}^{-1}[(2\pi\epsilon)^2 + (\gamma_\alpha P)^2]^{-1}$. Thus the time that the system spends “in resonance” ($|\epsilon| < \epsilon_0$) is $(\Delta t)_{\epsilon_0} = t_{d\alpha}(2\epsilon_0/N)[(2\pi\epsilon_0)^2/3 + (\gamma_\alpha P)^2] \sim 8\pi^2 t_{d\alpha} |\epsilon_0|^3 / (3N)$. By contrast, the time it takes the orbit to evolve between resonances (for the same mode) is $(\Delta t)_{\text{nr}} \sim t_d/N$, where t_d is the orbital decay timescale due to all non-resonant modes (t_d may be a factor of ~ 10 smaller than $t_{d\alpha}$). The probability of seeing a mode very near resonance is thus

$$P_{\text{res}} = \frac{(\Delta t)_{\epsilon_0}}{(\Delta t)_{\text{nr}}} \simeq \frac{8\pi^2}{3} \frac{t_{d\alpha}}{t_d} |\epsilon_0|^3. \quad (6.35)$$

Figure 6.3 indicates that (for an inclination of $i_s = 10^\circ$) we require $|\epsilon_0| \lesssim 10^{-2}$ for an $m = 2$ mode to be visible, for which the probability is $P_{\text{res}} \lesssim 3 \times 10^{-4}$. Thus, at first glance, the chances of observing even a single tidally-excited $m = 2$ mode in the KOI-54 system are slim. The $N = 90, 91$ modes require $|\epsilon_0| \lesssim 10^{-2}$, even if they are produced by $m = 0$ modes. It is therefore extremely unlikely to observe the system with such large amplitude modes, unless (by some mechanism) they are locked into resonance. In the sections that follow, we outline such a resonance locking mechanism and how it applies to the KOI-54 system.

6.5.2 Critical Resonance-Locking Mode

We now consider the possibility of resonance locking for the $m = 2$ modes. Tidal angular momentum transfer to the star increases the stellar spin Ω_s , thereby changing the mode frequency σ_α . There exists a particular resonance, $\sigma_\alpha = N_c \Omega$, for which σ_α

and Ω change at the same rate, i.e.,

$$\frac{\dot{\sigma}_\alpha}{\sigma_\alpha} = \frac{\dot{\Omega}}{\Omega}, \quad (6.36)$$

so that the resonance can be maintained once it is reached. With $\dot{J}_s = -\dot{J}_{\text{orb}}$ and the mean stellar rotation rate $\bar{\Omega}_s = J_s/I$ (where I is the moment of inertia), we have $\dot{\sigma}_\alpha = mB_\alpha\dot{J}_s/I$, where $B_\alpha \equiv (d\sigma_\alpha/d\bar{\Omega}_s)/m$. Assuming that a single resonant mode dominates the tidal energy and angular momentum transfer, we find $\dot{\sigma}_\alpha/\sigma_\alpha = -m^2B_\alpha\dot{E}_{\text{orb}}/(IN^2\Omega^2)$. Thus

$$\left(\frac{\dot{\sigma}_\alpha}{\sigma_\alpha}\right)_{\text{tide}} = \left(\frac{N_c}{N}\right)^2 \left(\frac{\dot{\Omega}}{\Omega}\right)_{\text{tide}}, \quad (6.37)$$

where

$$N_c = m \left(\frac{B_\alpha \mu a^2}{3I} \right)^{1/2} \quad (6.38)$$

(with $\mu = MM'/M_t$ the reduced mass of the binary) corresponds to the critical resonance-locking mode. The subscript “tide” in equation (6.37) serves as a reminder that the changes of σ_α and Ω are due to the tidal interaction.

For KOI-54 parameters (with $a \simeq 39R$ and $m = 2$), we have

$$N_c \simeq 131 \left(\frac{B_\alpha}{0.84} \right)^{1/2} \left(\frac{\kappa}{0.05} \right)^{-1/2}, \quad (6.39)$$

where $\kappa = I/(MR^2)$. If we assume that the star maintains rigid-body rotation during tidal spin up, then $B_\alpha = 1 - C_{nl}$. Numerical calculation for our stellar model gives $B_\alpha \simeq 0.84$ (with very weak dependence on modes) and $\kappa \simeq 0.040$, giving $N_c \simeq 146$; a less evolved star would have $\kappa \simeq 0.047$, giving $N_c \simeq 135$. Note that in the above we consider only tides in one star (M) – when tides in the other star are considered, $\dot{\Omega}$ would be larger and the effective value of N_c would be reduced. If identical resonances occur in the two stars, the effective value of N_c would be reduced by a factor of $\sqrt{2}$ to $N_c \simeq 92$ (for $\kappa = 0.05$). See section 5.3.3 and equations (6.70)-(6.71) below.

The above consideration assumes that the spin evolution of the star is entirely driven by tides. In reality, the star can experience intrinsic spindown, either due to a magnetic

wind or due to radius expansion associated with stellar evolution. We may write $\dot{\Omega}_s = (\dot{\Omega}_s)_{\text{tide}} - |\dot{\Omega}_s|_{\text{sd}}$, where the second term denotes the contribution due to the intrinsic spindown. The corresponding rate of change for σ_α is then

$$\frac{\dot{\sigma}_\alpha}{\sigma_\alpha} = \left(\frac{\dot{\sigma}_\alpha}{\sigma_\alpha} \right)_{\text{tide}} - \left| \frac{\dot{\sigma}_\alpha}{\sigma_\alpha} \right|_{\text{sd}}. \quad (6.40)$$

On the other hand, the orbital evolution remains solely driven by tides:

$$\frac{\dot{\Omega}}{\Omega} = \left(\frac{\dot{\Omega}}{\Omega} \right)_{\text{tide}} = \left(\frac{N}{N_c} \right)^2 \left(\frac{\dot{\sigma}_\alpha}{\sigma_\alpha} \right)_{\text{tide}}. \quad (6.41)$$

Comparing equations (6.40) and (6.41), we see that N_c *represents the upper boundary for resonance locking*: for $N > N_c$, resonance locking ($\dot{\sigma}_\alpha/\sigma_\alpha = \dot{\Omega}/\Omega$) is not possible. For $N < N_c$, resonance locking can be achieved: the value of $(\dot{\sigma}_\alpha/\sigma_\alpha)_{\text{tide}}$ depends on the closeness to the resonance, which in turn depends on the intrinsic spindown timescale of the star [see equations (6.54) and (6.55) below].

The fact that N_c naturally falls in the range close to $N = 90$ and $N = 91$, the most prominent modes observed in KOI-54, is encouraging. In the next subsection, we consider how the system may naturally evolve into a resonance-locking state with $N < N_c$.

6.5.3 Evolution Toward Resonance

As noted above, even in the absence of tides, the star can experience spin-down, either due to magnetic winds or due to radius expansion associated with stellar evolution. Furthermore, the intrinsic mode frequencies will change as the internal structure of the star evolves. We now show that these effects can naturally lead to evolution of the system toward resonance locking.

The evolution equation for the stellar spin reads $\dot{\Omega}_s = -(J_{\text{orb}}/I) - (\Omega_s/t_{\text{sd}})$, where t_{sd} is the “intrinsic” stellar spin-down time scale associated with radius expansion and/or

magnetic braking. Using equation (6.30), we have

$$\frac{\dot{\Omega}_s}{\Omega_s} = \sum_{\alpha} \left(\frac{m\mu a^2}{3I} \right) \left(\frac{\Omega^2}{\Omega_s \sigma_{\alpha}} \right) \frac{f_{\alpha}}{t_{d\alpha}} - \frac{1}{t_{sd}}. \quad (6.42)$$

From equation (6.30), we find that the orbital frequency and eccentricity evolve according to

$$\frac{\dot{\Omega}}{\Omega} = \sum_{\alpha} \frac{f_{\alpha}}{t_{d\alpha}}, \quad (6.43)$$

$$\frac{e \dot{e}}{1 - e^2} = -\frac{1}{3} \sum_{\alpha} \frac{f_{\alpha}}{t_{d\alpha}} \left[1 - \frac{m\Omega}{\sigma_{\alpha}(1 - e^2)^{1/2}} \right]. \quad (6.44)$$

To leading order in Ω_s , the mode frequency depends on Ω_s via

$$\sigma_{\alpha} = \omega_{\alpha}^{(0)} + mB_{\alpha}\Omega_s. \quad (6.45)$$

For simplicity, we assume that the secular change of σ_{α} is only caused by the Ω_s -evolution (e.g., we neglect the variation of $\omega_{\alpha}^{(0)}$ due to stellar evolution – this effect can be absorbed into the spindown effect on the mode; see Witte & Savonije 1999).

Single Mode Analysis

To gain some insight into the evolutionary behavior of the system, we first consider the case where one of the modes is very close to resonance, i.e.,

$$\sigma_{\alpha} = (N + \epsilon)\Omega, \quad (6.46)$$

while all the other modes are non-resonant. We then write the orbital and spin frequency evolution equations as

$$\frac{\dot{\Omega}}{\Omega} = \frac{f_{\alpha}}{t_{d\alpha}} + \frac{1}{t_d}, \quad (6.47)$$

$$\frac{\dot{\Omega}_s}{\Omega_s} = \frac{N_c^2}{mB_{\alpha}} \frac{\Omega^2}{\Omega_s \sigma_{\alpha}} \frac{f_{\alpha}}{t_{d\alpha}} - \frac{1}{t_{sd}} + \frac{1}{t_{su}}. \quad (6.48)$$

Here t_d^{-1} and t_{su}^{-1} are the orbital decay rate and spin up rate due to all the non-resonant modes.⁶ They are approximately given by

$$t_d^{-1} \simeq \sum_{\alpha} 3\gamma_{\alpha} \frac{\Delta E_{\alpha}}{|E_{\text{orb}}|} \sim \frac{3\gamma\Delta E}{|E_{\text{orb}}|}, \quad (6.49)$$

$$t_{su}^{-1} \simeq \frac{1}{I\Omega_s} \sum_{\alpha} 2\gamma_{\alpha} \frac{m}{\sigma_{\alpha}} \Delta E_{\alpha} \sim \frac{2\gamma\Delta J}{I\Omega_s}, \quad (6.50)$$

where $\Delta E = \sum_{\alpha} \Delta E_{\alpha}$ and $\Delta J = \sum_{\alpha} (m/\sigma_{\alpha}) \Delta E_{\alpha}$ are the energy and angular momentum transferred from the orbit to the star in the “first” periastron passage (see Section 6.2), and γ is the characteristic mode damping rate of the most important modes in the energy transfer. Since $\Delta J \sim \Delta E/\Omega_p$ (where Ω_p is the orbital frequency at periastron), we find

$$\frac{t_{su}^{-1}}{t_d^{-1}} \sim \frac{\mu a^2}{3I} \frac{\Omega^2}{\Omega_s \Omega_p}. \quad (6.51)$$

Note that t_d^{-1} can be a factor of a few (~ 10) larger than $t_{d\alpha}^{-1}$, and t_{su}^{-1} is a factor of a few larger than t_d^{-1} .

Equations (6.46)-(6.48) can be combined to yield the evolution equation for $\epsilon = \sigma_{\alpha}/\Omega - N$:

$$\frac{\dot{\epsilon}}{N} = \left[\left(\frac{N_c}{N} \right)^2 - 1 \right] \frac{f_{\alpha}}{t_{d\alpha}} - \frac{1}{t_D}, \quad (6.52)$$

where

$$\frac{1}{t_D} = \frac{mB_{\alpha}\Omega_s}{N\Omega} \left(\frac{1}{t_{sd}} - \frac{1}{t_{su}} \right) + \frac{1}{t_d}. \quad (6.53)$$

Equation (6.52) provides the key for understanding the condition of achieving mode locking:

(i) For $N > N_c$: The RHS of Equation (6.52) is always negative, and the system will pass through the resonance ($\epsilon = 0$) without locking. Physically, the reason is that for $N > N_c$, the orbit decays faster (during resonance) than the mode frequency can catch up, so the system sweeps through the resonance.

⁶For simplicity, here we do not consider the possibility where the star rotates so fast that dynamical tides spindown the star – such possibility occurs when the star rotates at a rate somewhat beyond Ω_p (see Lai 1997).

(ii) For $N < N_c$ and $t_D^{-1} \gg t_{d\alpha}^{-1}$: Starting from a non-resonance initial condition ($\epsilon_{\text{in}} \sim 0.5$, or $f_\alpha \sim 1$), the system will evolve toward a resonance-locking state ($\dot{\epsilon} = 0$), at which

$$f_\alpha = \frac{t_{d\alpha}}{\delta_N t_D} \gg 1 \quad (6.54)$$

where $\delta_N \equiv (N_c/N)^2 - 1$. The “equilibrium” value of ϵ is given by

$$\epsilon_{\text{eq}} \simeq \frac{1}{2\pi} \left[\frac{t_D \delta_N}{t_{d\alpha}} - (\gamma_\alpha P)^2 \right]^{1/2} \ll 1. \quad (6.55)$$

This resonance-locking state can be achieved when

$$t_D \delta_N / t_{d\alpha} > (\gamma_\alpha P)^2, \quad (6.56)$$

as otherwise resonance “saturation” [$f_\alpha \leq (\gamma_\alpha P)^{-2}$] occurs, and the system will sweep through the resonance. Note that during the resonance-locking phase, the stellar spin increases as

$$\frac{\dot{\Omega}_s}{\Omega_s} = \frac{1}{\delta_N} (t_{sd}^{-1} - t_{su}^{-1}) + \frac{N_c^2 \Omega}{N \delta_N m B_\alpha \Omega_s} t_d^{-1}, \quad (6.57)$$

and the orbital frequency increases as

$$\frac{\dot{\Omega}}{\Omega} = \frac{m B_\alpha}{N \delta_N} \frac{\Omega_s}{\Omega} (t_{sd}^{-1} - t_{su}^{-1}) + \frac{N_c^2}{N^2 \delta_N} t_d^{-1}. \quad (6.58)$$

The above analysis assumes $t_D^{-1} > 0$. In the absence of the intrinsic stellar spin-down (i.e., $t_{sd}^{-1} = 0$), we have

$$t_D^{-1} \sim -\frac{N_c^2}{mN} \left(\frac{20\Omega}{\Omega_p} \right) t_d^{-1} + t_d^{-1}. \quad (6.59)$$

Thus t_D can be negative for $N \lesssim N_c^2/40$. In this case, one may expect mode-locking for $N > N_c$. Nevertheless, t_D^{-1} is only moderately larger (a factor of 10 or so) than $t_{d\alpha}^{-1}$ without intrinsic spin-down, so a close resonance with $f_\alpha \gg 1$ (or $|\epsilon| \ll 1$) is unlikely.

Resonance Locking for $m = 0$ Modes

Above (and in other sections of this paper), we considered the frequency of a mode in the inertial frame to first order in Ω_s : $\sigma_\alpha = \varepsilon_\alpha + mB_\alpha\Omega_s$. In this approximation, $m = 0$ modes have constant frequency and thus cannot lock into resonance. However, Lai (1997) find that to second order in Ω_s , the frequency of $m = 0$ modes can be approximated by

$$\frac{\sigma_{\alpha,m=0}}{\varepsilon_\alpha} \simeq 1 + \frac{6}{7} \left(\frac{\Omega_s}{\varepsilon_\alpha} \right)^2. \quad (6.60)$$

Recall that ε_α is the mode frequency in the absence of rotation. Thus, to second order, the frequency of $m = 0$ modes can change and resonance locking is possible.

Let us examine the scenario in which an $m_\alpha = 2$ mode with $N_{m=2} \simeq 90$ is locked in resonance, as we suspect is the case for KOI-54. Assuming this mode dominates the tidal interaction, the system evolves such that

$$\begin{aligned} N_{m=2}\dot{\Omega} &= \dot{\sigma}_{\alpha,m=2} \\ &= m_\alpha B_\alpha \dot{\Omega}_s, \end{aligned} \quad (6.61)$$

Then there will be a value of $N_{m=0}$ for an $m = 0$ mode such that

$$N_{m=0}\dot{\Omega} = \dot{\sigma}_{\alpha,m=0}. \quad (6.62)$$

Using equation (6.61) for the LHS of equation (6.62), equation (6.60) for the RHS of equation (6.62), and the condition $\sigma_{\alpha,m=0} = N_{m=0}\Omega$, we find

$$N_{m=0} = \left[\frac{12N_{m=2}}{7m_\alpha B_\alpha [\Omega/\Omega_s - m_\alpha B_\alpha / (2N_{m=2})]} \right]^{1/2}. \quad (6.63)$$

Using $N_{m=2} = 90$, $m_\alpha = 2$, $B_\alpha = 0.84$, and $\Omega_s = \Omega_{ps} = 16.5\Omega$, we find that $N_{m=0} \simeq 42$. Thus, an $m = 0$ mode with $\sigma_\alpha \simeq 42\Omega$ may be able to stay close to resonance for an extended period of time. KOI-54 has two very visible modes at $\sigma_3 = 44\Omega$ and $\sigma_4 = 40\Omega$. We speculate that these modes may correspond to an $m = 0$ mode in each

star that is nearly locked in resonance due to the orbital evolution produced by a locked $m = 2$ mode with $N_{m=2} \simeq 90$. However, because the value of $N_{m=0}$ depends on Ω_s (which is currently unknown for KOI-54), we will not consider $m = 0$ mode locking in the remainder of this paper.

Resonance Locking in Both Stars

In Section 5.3.1, we considered resonant locking of an $m = 2$ mode in the primary star M . Since the two stars in the KOI-54 system are quite similar, resonant locking may be achieved in both stars simultaneously. We now consider the situation in which an $m = 2$ mode σ_α in star M and an $m' = 2$ mode $\sigma_{\alpha'}$ in star M' are both very close to orbital resonance, i.e.,

$$\sigma_\alpha = (N + \epsilon)\Omega, \quad \sigma_{\alpha'} = (N' + \epsilon')\Omega, \quad (6.64)$$

while all other modes (in both stars) are non-resonant. Here, all primed quantities refer to star M' , and unprimed quantities refer to star M . The orbital evolution equation then reads

$$\frac{\dot{\Omega}}{\Omega} = \frac{f_\alpha}{t_{d\alpha}} + \frac{f_{\alpha'}}{t_{d\alpha'}} + \frac{1}{t_d}, \quad (6.65)$$

while the spin evolution is governed by equation (6.57) for star M and a similar equation for M' . We then find

$$\frac{\dot{\epsilon}}{N} = \left[\left(\frac{N_c}{N} \right)^2 - 1 - x \right] \frac{f_\alpha}{t_{d\alpha}} - \frac{1}{t_D}, \quad (6.66)$$

$$\frac{\dot{\epsilon}'}{N'} = \left[\left(\frac{N'_c}{N'} \right)^2 - 1 - \frac{1}{x} \right] \frac{f_{\alpha'}}{t_{d\alpha'}} - \frac{1}{t'_D}, \quad (6.67)$$

where

$$x \equiv \frac{f_{\alpha'}/t_{d\alpha'}}{f_\alpha/t_{d\alpha}} = \frac{\dot{E}_{\alpha'}}{\dot{E}_\alpha}, \quad (6.68)$$

with \dot{E}_α and $\dot{E}_{\alpha'}$ the energy dissipation rates (including resonances) due to the resonant modes in star M and M' , respectively. Thus, analogous to Section 5.3.1, for $t_D > 0$ and

$t'_D > 0$, the necessary conditions for resonant mode locking in both stars are

$$N < N_{c,\text{eff}}, \quad \text{and} \quad N' < N'_{c,\text{eff}}, \quad (6.69)$$

with

$$N_{c,\text{eff}} = \frac{N_c}{\sqrt{1+x}} = m \left[\frac{B_\alpha \mu a^2}{3I(1+x)} \right]^{1/2}, \quad (6.70)$$

$$N'_{c,\text{eff}} = \frac{N'_c}{\sqrt{1+x^{-1}}} = m' \left[\frac{B_{\alpha'} \mu a^2}{3I'(1+x^{-1})} \right]^{1/2}. \quad (6.71)$$

Obviously, if the two stars have identical resonances ($x = 1$), then $N_{c,\text{eff}}$ would be smaller than N_c by a factor of $\sqrt{2}$. If the energy dissipation rates in the two stars differ by at least a factor of a few (e.g., $x \sim 0.2$), then $N_{c,\text{eff}}$ is only slightly modified from N_c , while $N'_{c,\text{eff}}$ will be a factor of a few smaller than N'_c .

6.5.4 Numerical Examples of Evolution Toward Resonance

For a given set of modes, the solution of the system of equations (6.42)-(6.44) depends on the dimensionless parameters $t_{d\alpha}/t_{sd}$, N_c and $\gamma_\alpha P$, as well as the initial conditions. In general, these parameters change as the system evolves.

A Simple Example

To illustrate the essential behavior of the secular evolution toward resonance locking, we first consider the simple case where $t_{d\alpha}/t_d$ and $\gamma_\alpha P$ are assumed to be constant and identical for all modes considered. Figure 6.4 depicts an example: we include two $m = 2$ modes (σ_1 and σ_2), both have $t_{d\alpha}/t_{sd} = 10^2$, $\gamma_\alpha P = 10^{-2}$ and $B_\alpha = 0.8$. The parameter N_c has an initial value of 110, but we allow N_c to evolve via $N_c \propto \Omega^{-2/3}$. At $t = 0$, the spin frequency is $\Omega_s = 15\Omega$, and the two modes have $\sigma_1/\Omega = 100.5$ and

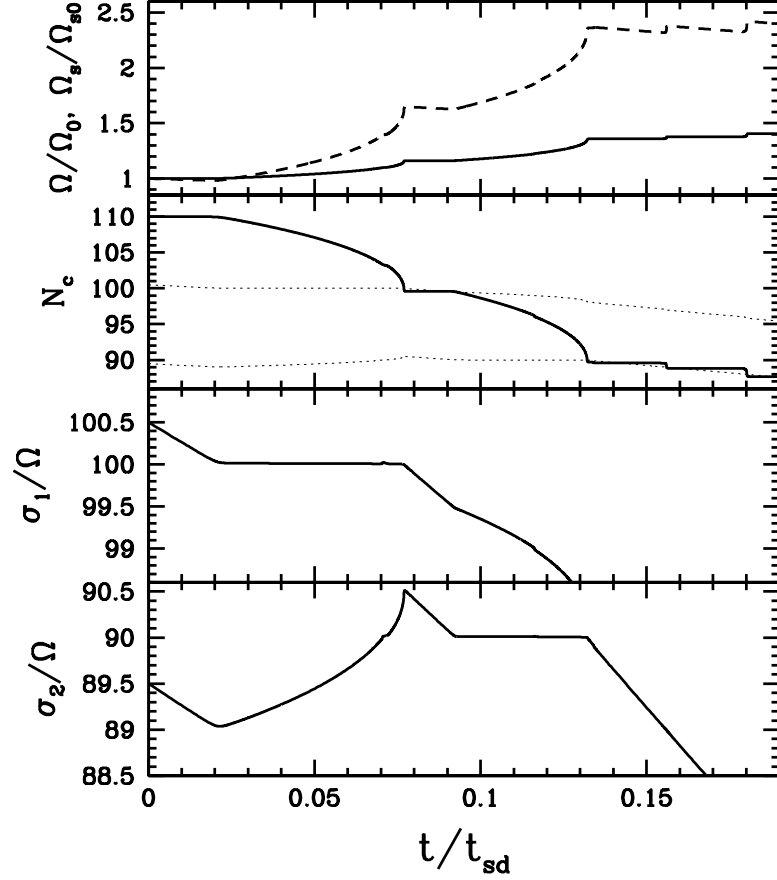


Figure 6.4: Secular evolution of the stellar spin and binary orbit driven by dynamical tides and “intrinsic” stellar spin-down. Two modes are included, both having $m = 2$, $t_{d\alpha}/t_{sd} = 100$ and $\gamma_\alpha P = 0.01$. The initial spin frequency is $\Omega_s = 15\Omega$. The top panel shows the orbital frequency (solid line) and the spin frequency (dashed line), both in units of their initial values. The second panel shows N_c as defined by equation (6.38). The bottom two panels show the mode frequencies in units of Ω . The two light dotted lines on the third panel also show σ_1/Ω and σ_2/Ω . The time (on the horizontal axis) is expressed in units of t_{sd} , the intrinsic spindown time of the star. The system first evolves into resonance locking at $\sigma_1 = 100\Omega$ and then a different resonance locking at $\sigma_2 = 90\Omega$. Note that resonance locking cannot occur when $\sigma_\alpha/\Omega > N_c$.

$\sigma_2/\Omega = 89.5$ (i.e., both are initially “off-resonance”). We see that the stellar spindown first causes σ_1 to lock into resonance at $\sigma_1/\Omega = 100$. The star then spins up, driven by the resonant tidal torque. The second mode passes through the $N = 90$ resonance, but it produces a negligible effect on the $\sigma_1/\Omega = 100$ resonance. In the meantime, the orbit decays, reducing N_c . When N_c becomes less than 100, the resonance locking can no longer be maintained, and σ_1 breaks away from the $N = 100$ resonance. The stellar spin then decreases (due to the $1/t_{sd}$ term), which leads to σ_2 to capture into the $N = 90$ resonance. Eventually, as N_c decreases (due the resonant tidal torque) below 90, the second mode breaks away from the $N = 90$ resonance. This example corroborates our analytic results in section 5.3, and demonstrates that resonance locking can indeed be achieved and maintained for an extended period during the evolution of the binary system.

More Realistic Examples

Having demonstrated how resonance locking can occur in a simplified system consisting of only two oscillation modes, we now investigate how resonance locking is likely to occur in the actual KOI-54 system. We solve the orbital evolution equations (6.42)-(6.45) using the actual values of ε_α , Q_α , and γ_α found in section 6.3 to calculate each $t_{d\alpha}$. We include eighteen modes in our equations: they are the $l = 2$, $m = 0$, $m = \pm 2$ modes for six values of ε_α such that the initial frequencies of the $m = 2$ modes range from 40Ω to 170Ω . We allow the value of K_{lm} to evolve as the values of σ_α , Ω , and e change with time.

Figures 6.5 and 6.6 display the evolution of Ω , Ω_s , N_c , and the values of σ_α and E_α for a selected sample of modes over a time span of tens of millions years. We use initial values of $\Omega_o = 0.95\Omega_{\text{obs}}$ (here Ω_{obs} is the observed orbital frequency of KOI-54),

$e_o = 0.84$, $\Omega_{s,o} = \Omega_{ps} \simeq 16.5\Omega_o$, and a spindown time of $t_{sd} = 3 \times 10^8$ years. In Figure 6.6, we have doubled the orbital decay rate to account for an equal amount of energy dissipation in the companion star.

Let us start by examining Figure 6.5. The system quickly enters a resonance locking state with the $\sigma_{3,2}$ mode, where the notation $\sigma_{k,m}$ identifies the mode with the k th largest frequency in our simulation with azimuthal number m . The resonance locking lasts for over 100 million years, until the $\sigma_{2,2}$ mode reaches resonance. The $\sigma_{2,2}$ mode then locks in resonance for over 100 million years. During resonance locking, the orbital frequency and spin frequency increase rapidly. The energies E_α of the resonant locked modes can exceed 700 times their non-resonant values ΔE_α , corresponding to an increase in visibility of over 25 times the visibility during a non-resonant state. When no mode is locked in resonance, the orbital evolution is relatively slow, with the dominant effect being the spindown of the star due to the t_{sd} term.

For the initial conditions and orbital evolution depicted in Figure 6.5, only two of our 18 modes pass through resonant locking phases: two $m = 2$ modes with initial frequencies of $\sigma_{2,2,o} \simeq 103$ and $\sigma_{3,2,o} \simeq 90$. The highest frequency $m = 2$ mode included in our evolution does not lock in resonance because it has $N > N_c$ at all times. The lowest frequency modes do not lock in resonance because they do not satisfy equation (6.56), i.e., they become saturated before they can begin to resonantly lock. This occurs because the value of Q_α for these high-order modes is small, resulting in a small orbital decay rate $t_{d\alpha}^{-1}$ for these modes.

Which mode locks into resonance is dependent on the initial conditions. However, as can be seen in Figure 6.5, the resonance with the $\sigma_{2,2}$ mode ends the resonance with the $\sigma_{3,2}$ mode because the $\sigma_{2,2}$ mode has a larger value of E_α and will thus dominate the orbital decay. Therefore, we can expect the system to evolve into a state in which the

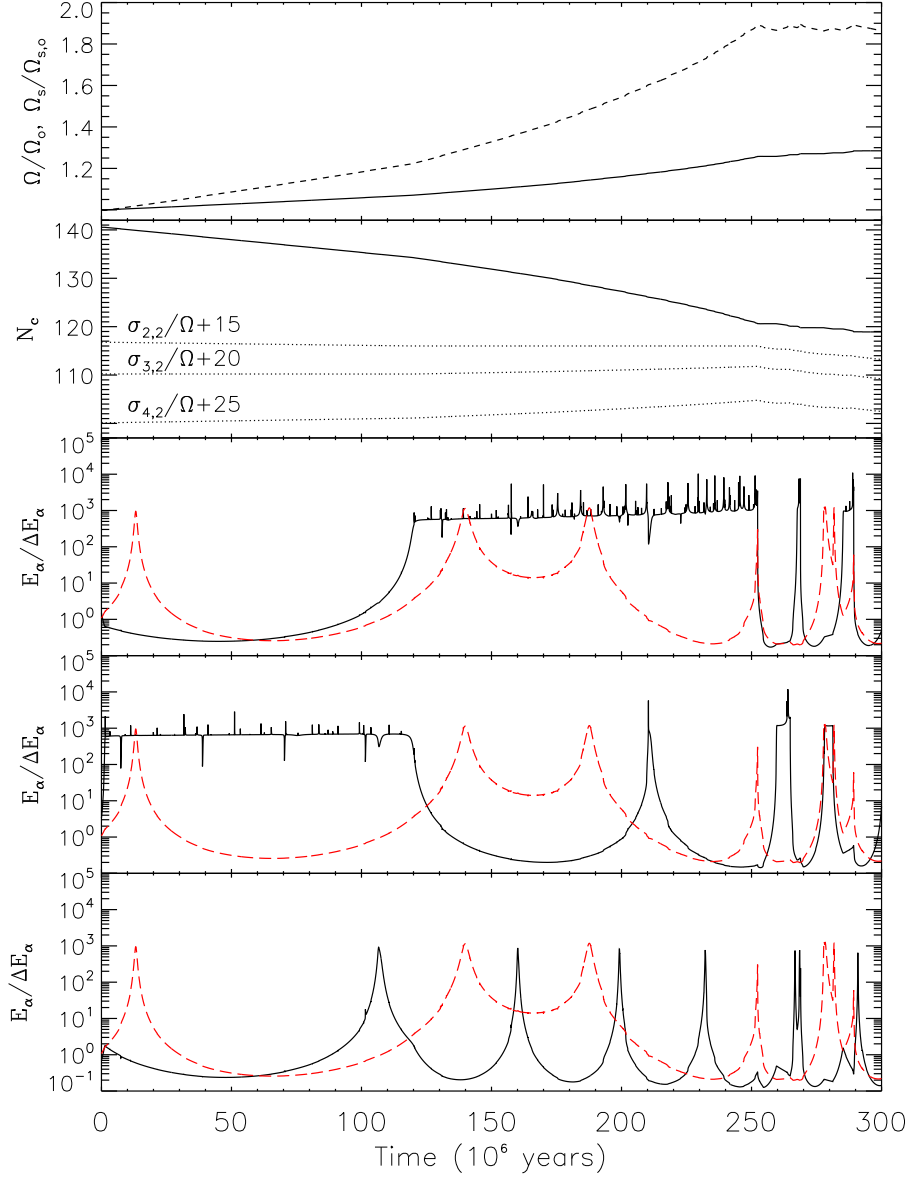


Figure 6.5: Secular evolution of the KOI-54 system driven by a sample of 18 oscillation modes and intrinsic stellar spindown. Top: orbital frequency Ω (solid line) and spin frequency Ω_s (dashed line) in units of their initial values. Top middle: the value of N_c (solid line) and the mode frequencies $\sigma_{2,2}/\Omega + 15$, $\sigma_{3,2}/\Omega + 20$, and $\sigma_{4,2}/\Omega + 35$ (dotted lines) of the modes depicted in the bottom three panels. Middle: the mode energy E_α in units of ΔE_α for the $\sigma_{2,2}$ mode (solid line) and the $\sigma_{4,0}$ mode (red dashed line). Bottom middle: same as middle except the solid line is for the $\sigma_{3,2}$ mode. Bottom: same as bottom middle except the solid line is for the $\sigma_{4,2}$ mode. The initial spin frequency is $\Omega_s \simeq 16.5\Omega$, and the spindown time is $t_{sd} = 3 \times 10^8$ years.

mode with the largest value of E_α (and with $N < N_c$) is locked in resonance.

In Figure 6.5, the resonance locking with the $\sigma_{2,2}$ mode is ended by a resonance with the $\sigma_{4,0}$ mode. The $\sigma_{4,0}$ mode does not lock into resonance because an $m = 0$ mode cannot change the stellar spin frequency. However, its resonance causes the value of $\dot{\Omega}/\Omega$ to exceed the value of $\dot{\sigma}_\alpha/\sigma_\alpha$ for the locked mode, so that the system sweeps through the resonance. In other words, the non-locked resonant mode temporarily decreases the value of t_d , decreasing the value of t_D such that resonant saturation occurs for the locked mode, causing it to pass through resonance. Also note that even though the $\sigma_{4,0}$ mode does not lock into resonance, it maintains a relatively large energy ($E_\alpha > 10\Delta E_\alpha$) for a period of over 50 million years. This is indicative of the pseudo-resonance locking for $m = 0$ modes described in Section 6.5.3.

Let us now examine Figure 6.6, in which the orbital decay rate has been doubled (i.e., we multiply $\dot{\Omega}$ by 2) to account for an equal tidal response in the companion star. The results are significantly different: due to the increased orbital decay rate, the initial effective value of $N_{c,\text{eff}}$ has dropped to ~ 100 (see section 5.3.3) so that the $\sigma_{2,2}$ mode can no longer lock into resonance. Also, the maximum energy $E_\alpha/\Delta E_\alpha$ of the modes is larger in this scenario (because the modes must enter deeper into resonance to become locked), so the modes can create larger magnitude variations while being locked in resonance.

However, the resonance locking events are shorter because the modes are nearly saturated during resonance locking, allowing resonances with $m = 0$ modes or higher frequency $m = 2$ modes to easily disrupt the resonance locking state. In the bottom three panels of Figure 6.6, we have plotted the energy E_α of the $\sigma_{2,0}$ mode. In Figure 6.6, three of the resonant locking events for the $\sigma_{3,2}$ mode are ended due to a resonance with the $\sigma_{2,0}$ mode. We have examined the results carefully and found that all of the resonance locking events were ended due a resonance with an $m = 0$ mode or an $m = 2$ mode

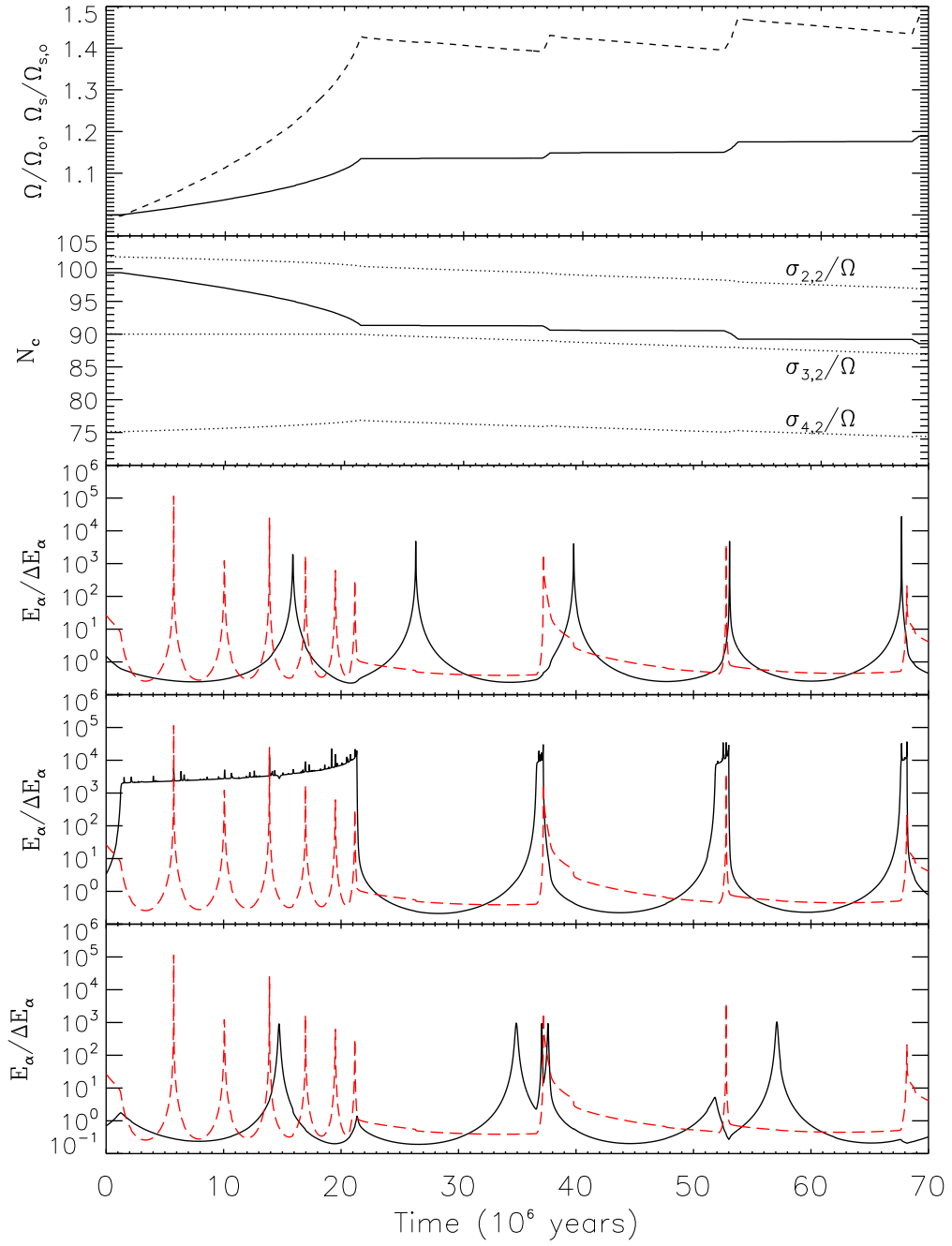


Figure 6.6: Same as Figure 6.5, except this evolution doubles the orbital decay rate due to each mode, and the red dashed line corresponds to the $\sigma_{2,0}$ mode.

for which $N > N_c$. Although the resonance locking events are brief at the end of the simulation, the locking event with the $\sigma_{3,2}/\Omega = 90$ mode lasts for about 20 million years at the beginning of the simulation when the system’s parameters most closely resemble those of KOI-54. We thus conclude it is likely to observe a system such as KOI-54 in a resonance locking state.

We note the secular evolution analysis presented above does not take into account the fluctuation of mode amplitudes due to the changing strength of the tidal potential in an elliptical orbit. Therefore, in addition to the results displayed above, we have also performed calculations of the full dynamic evolution of the stellar oscillations and binary orbit, including the back-reaction of the modes on the orbit. We find that resonance locking can indeed be maintained for extended periods of time, and that non-secular effects have little impact on the results discussed above.

6.6 Oscillations at Non-Orbital Harmonics

As discussed in section 4, in the linear theory, tidally-forced stellar oscillations give rise to flux variations at integer multiples of the orbital frequency. Many of these oscillations have been observed in the KOI-54 system. However, Welsh et al. (2011) also reported the detection of nine modes that do not have frequencies that are integer multiples of the orbital period, and their observation requires an explanation.

One possibility is that one (or both) of the stars in KOI-54 are δ -Scuti variable stars. The masses, ages, and metallicities of the KOI-54 stars put them directly in the instability strip and so δ -Scuti-type pulsations are not unexpected. However, as pointed out by Welsh et al. (2011), the complete absence of any modes detected with periods less than 11 hours is troublesome for the δ -Scuti interpretation, as most observed δ -Scuti

pulsations have periods on the order of a few hours. One would then have to explain why only long period ($P > 11$ hours) δ -Scuti-type oscillations are visible in this system.

Another possibility is that some (or all) of the non-harmonic modes are excited via nonlinear couplings with resonant modes. In particular, it is thought that three-mode resonant coupling (parametric resonance) plays an important role in limiting the saturation amplitudes of overstable g-modes in ZZ-Ceti stars (Wu & Goldreich 2001) and δ -Scuti stars (Dziembowski & Krolikowska 1985). In the KOI-54 system, when a resonantly excited mode reaches sufficiently large amplitude, it will couple to two non-resonant, lower-frequency daughter modes (see Kumar & Goodman 1996), thereby explaining the observed non-harmonic oscillations.

Parametric resonance can occur when $\omega_\gamma \simeq \omega_\alpha + \omega_\beta$, where ω_γ is the frequency of the parent mode and ω_α and ω_β are the frequencies of the two daughter modes. The additional requirement that $m_\gamma = m_\alpha + m_\beta$, where m is the azimuthal number of the mode, implies that $\sigma_\gamma \simeq \sigma_\alpha + \sigma_\beta$. Examination of the KOI-54 data given in Welsh et al. (2011) reveals that $f_2 = f_5 + f_6$ ($25.195 \mu\text{Hz} = 6.207 \mu\text{Hz} + 18.988 \mu\text{Hz}$) exactly to the precision of the measurements, where f_p is the frequency of the oscillation with the p th largest magnitude variation. This provides strong evidence that the $p = 5$ and $p = 6$ oscillations are due to modes excited via parametric resonance and not via direct tidal forcing.

However, no other pair of observed non-harmonic magnitude oscillations have frequencies which add up to that of an observed oscillation. Some of these non-resonant oscillations may be due to modes excited via parametric resonance that have undetected sister modes. This possibility is especially appealing if one considers the scenario in which one of the two daughter modes has $m = 0$ (and could thus be easily detected for small values of i_s), while its sibling has $m = 2$ (and is thus very difficult to detect

for small i_s). We therefore suggest that all non-harmonic flux oscillations are produced by nonlinear mode coupling. Deeper observations may reveal additional evidence for nonlinear mode couplings in the KOI-54 system

6.7 Discussion

We have shown that many properties of brightness oscillations detected in the KOI-54 binary system by *KEPLER* can be understood using the theory of dynamical tidal excitation of g-modes developed in this paper. In particular, our analysis and calculation of the resonance mode locking process, which is driven by dynamical tides and intrinsic stellar spindown, provides a natural explanation for the fact that only those modes with frequencies (σ_α) less than about 90-100 times the orbital frequency (Ω) are observed. Our result suggests that the KOI-54 system is currently in a resonance-locking state in which one of the stars has a rotation rate such that it possesses a $m = 2$ mode with frequency $\sigma_\alpha = 90\Omega$ and the other star has a similar mode with $\sigma_{\alpha'} = 91\Omega$ — these modes produce the largest flux variations detected in KOI-54. Our analysis shows that the system can evolve into and stay in such a resonance locking state for relatively long time periods, and it is reasonable to observe the system in such a state. Other less prominent flux variations at lower frequencies can be explained by $m = 0$ tidally forced oscillations, many of which are enhanced by resonance effects. We have also found evidence of nonlinear three-mode coupling from the published *KEPLER* data and suggested that the nonlinear effect may explain the flux variabilities at non-harmonic frequencies.

In our study, we have used approximate quasi-adiabatic mode damping rates. Obviously, it would be useful to repeat our analysis using more realistic mode damping

rates, calculated with the full non-adiabatic oscillation equations. Our calculations of the flux variations of tidally induced oscillations have also highlighted the importance of accurate treatment of non-adiabatic effects in the stellar photosphere. We have only considered g-modes (modified by stellar rotation) in this paper. Our general theory allows for other rotation-driven modes, such as inertial/Rossby modes. It would be interesting to study tidal excitation of these modes and non-linear 3-mode coupling effects in the future.

More detailed modeling of the observed oscillations may provide useful constraints on the parameters of the KOI-54 system, particularly the stellar rotation rates and spin inclinations. On a more general level, KOI-54 may serve as a “laboratory” for calibrating theory of dynamical tides, which has wide applications in stellar and planetary astrophysics (see references in Section 1).

While we believe that our current theory provides the basis for understanding many aspects of the KOI-54 observations, some puzzles remain. In our current interpretation, the most prominent oscillations (at 90Ω and 91Ω) occur in the two different stars, each having a $m = 2$ mode resonantly locked with the orbit. While one can certainly appeal to coincidence, it is intriguing that the strongest observed oscillations are at the two consecutive harmonics ($N = 90, 91$) of the orbital frequency. More importantly, as discussed in Section 5.3.3, when both stars are involved in resonance locking, the effective N_c (above which resonance locking cannot happen) is reduced. For example, using our canonical stellar parameters ($\kappa = 0.05$), we find $N_c \simeq 131$ [see equation (6.39)], but the effective N_c would be reduced to 92 if the two stars have identical modes in resonance locking. In the case where the resonant energy dissipation rates in the two stars differ by a factor of more than a few, the effective N_c of one star would remain close to 131, while the effective N_c for the other star would likely be reduced to a value below 90. In

this case, it would be unlikely to find the binary system in the resonance-locking state involving both stars with N, N' close to 90, because it is most likely for modes with N just less than N_c to be locked in resonance (see Section 5.4.2.). Thus, we find it likely that the energy dissipation rates are nearly equal (to within a factor of 2) in each star in the KOI-54 system.

Finally, we may use our results to speculate on the evolutionary history (and future) of the KOI-54 system. The star with $M_2 = 2.38M_\odot$ and radius $R_2 = 2.33R_\odot$ has an age of about 3×10^8 years, according to our stellar model generated by the MESA code. During the resonance locking phase, the orbital eccentricity decreases on a relatively short time scale (of order $\sim 10^8$ years). The current large eccentricity of KOI-54 then suggests that resonance locking has not operated for a large fraction of the system's history. When resonance locking is in effect, the orbital evolution time scale is set by primarily by the spindown time scale, t_{sd} , and the value of δ_N for the resonant mode [see equation (6.58)]. In the future, the stars will continue to expand into red giants and the spindown time scale will decrease. This will cause the orbital evolution time scale to correspondingly decrease, leading to rapid orbital decay and circularization of the system.

While our paper was under review, a paper by Burkart et al. (2011) appeared on arXiv. Burkart et al. carried out non-adiabatic mode calculations and also attribute most of the oscillations to $m = 0$ modes, although they do not reach a definite conclusion on the source of the $N = 90, 91$ oscillations. They did not consider resonance locking (instead they consider the qualitatively different phenomenon of “pseudosynchronous locks”), and appeared to attribute all resonances to random chance. They also showed that 3-mode coupling (see Section 6) is possible.

CHAPTER 7

TIDALLY INDUCED OSCILLATIONS AND ORBITAL DECAY IN COMPACT TRIPLE-STAR SYSTEMS

7.1 Introduction¹

Tidal interactions are known to profoundly impact the orbital evolution of close binary star systems, exoplanetary systems, and moon systems. In binary systems, tides drive the components of the systems toward a synchronized state in which the orbit is circular, and the components have spins that are synchronized and aligned with the orbit. In a compact triple system, no equilibrium state exists, and the endpoint of the orbital evolution is not immediately obvious. Furthermore, the dynamics of tidal interactions coupled with multi-body orbital effects can be quite complex and can lead to the formation of astrophysically interesting systems (e.g., the Jupiter moon system, short-period exoplanetary systems, and compact binary star systems).

Although there have been many studies of three-body orbital dynamics including tidal dissipation (e.g., Mazeh & Shaham 1979, Ford et al. 2000, Eggleton & Kisileva-Eggleton 2001, Fabrycky & Tremaine 2007, Correia et al. 2011), these studies have primarily treated tides in a parameterized fashion. Some of these studies take resonant orbital effects into account, but their parameterization of tidal interactions ignores resonant tidal effects which may significantly impact the orbital evolution. Furthermore, these studies only consider tidal interactions between two components of the system (i.e., they incorporate tidal interactions between objects 1 and 2, but ignore interactions with object 3). This approximation is justified in most systems because the third body is relatively distant. However, in sufficiently compact triple systems, a more thorough

¹This chapter is based on Fuller et al. (2013).

study of three-body tidal effects is necessary.

Observing tidal effects is very difficult because of the long time scales associated with tidal evolution, and tidal orbital decay has only been observed in a few rare circumstances (such as the orbital decay of a pulsar-MS binary, see Lai 1996,1997; Kumar & Quataert 1998). Until recently, the direct observation of tidally induced oscillations was difficult because of the extreme precision required (\sim one part in a thousand) over base lines of several days. Fortunately, the continuous observation and high accuracy of the *Kepler* satellite is allowing for the direct observation of tidal effects (e.g., Welsh et al. 2011, Thompson et al. 2012) and detailed analyses of tidally excited stellar oscillations (Fuller & Lai 2012, Burkart et al. 2012). Recently, observations of luminosity variations in the compact triple system HD 181068 (also known as KIC 5952403 or the Trinity system, see Derekas et al. 2011) have provided evidence for three-body tidal effects. To our knowledge, no detailed study of dynamical tides exists for compact triple systems.

We present the first detailed investigation of the tidal excitation of stellar oscillation modes in stars in compact triple systems. Hierarchical three-body systems can experience tidal forcing at frequencies unattainable for two-body systems, allowing for the tidal excitation of high frequency p-modes in the convective envelopes of the stellar components. We investigate the observational signatures of three-body tides, calculate the amplitudes to which stellar oscillation modes are tidally excited, and study the orbital evolution induced by three-body tides.

We also compare our theory to the observations of luminosity fluctuations in HD 181068, accurately characterized by Derekas et al. 2011 and Borkovits et al. 2012. HD 181068 is a triply eclipsing hierarchical star system, with a red giant primary orbited by two dwarf stars. The dwarf stars orbit each other every 0.906 days, and their cen-

ter of mass orbits the primary every 45.47 days. In addition to eclipses, the lightcurve shows oscillations at combinations of the orbital frequencies. We demonstrate that these oscillations are tidally excited oscillations in the red giant primary excited by the orbital motion of the dwarf stars.

Our paper is organized as follows. In Section 7.2 we derive the strength and frequencies of tidal forcing unique to three-body systems. In Section 7.3 we calculate the amplitudes to which modes are tidally excited, and estimate the resulting stellar luminosity variations. In Section 7.4 we calculate the orbital evolution induced by the tidally excited modes. In Section 7.5, we describe observations of tidally excited modes in HD 181068, and in Section 7.6 we compare these observations to our theory. In Section 7.7 we calculate the possible past and future orbital evolution of systems like HD 181068. Finally, in Section 7.8, we discuss our results.

7.2 Three-body Tidal Forcing

Let us consider a triple-star system composed of a central primary star (Star 1), orbited by a pair of companion stars (Stars 2 and 3) at frequency Ω_1 . Stars 2 and 3 orbit one another at a much higher frequency $\Omega_{23} \gg \Omega_1$. Figure 7.1 shows a diagram of the orbital configuration. We adopt a coordinate system centered on Star 1 with z -axis in the direction of its spin angular momentum vector. We consider the case in which all three stars have circular coplanar orbits that are aligned with the stellar spins. We choose a direction of reference such that the observer is located at the azimuthal angle $\phi = 0$.

We wish to calculate the form of the time-varying gravitational potential of the short-period binary (Stars 2 and 3) as seen by Star 1. The tidal potential due to Stars 2 and 3

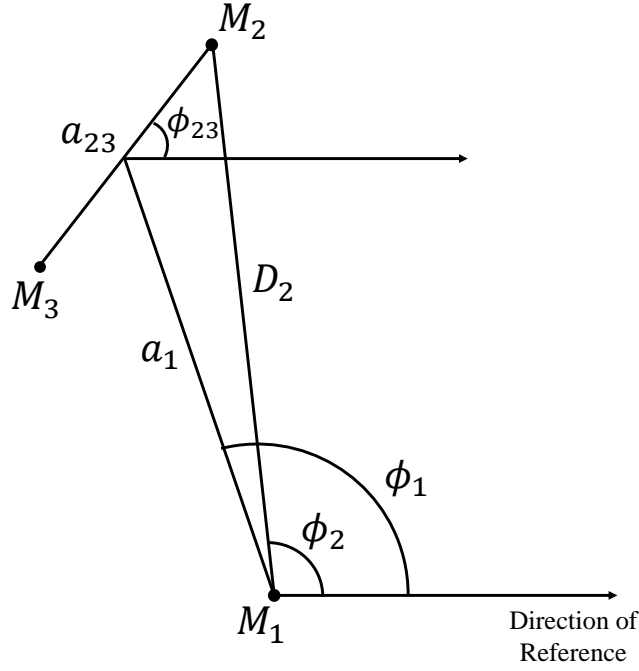


Figure 7.1: This diagram (not to scale) depicts the geometry of a triple-star system at arbitrary orbital phase. a_1 is the semimajor axis between the center of Star 1 and the center of mass of Stars 2 and 3. a_{23} is the semimajor axis between Stars 2 and 3. D_2 is the distance between Stars 1 and 2. ϕ_1 is the orbital phase (relative to a direction of reference) of the center of mass of Stars 2 and 3, while ϕ_2 is the orbital phase of Star 2 about Star 1. ϕ_{23} is the orbital phase of Stars 2 and 3 about each other relative to the same direction of reference.

can be decomposed into spherical harmonics as

$$U_{l,m} = \frac{4\pi}{2l+1} \left[\frac{-GM_2}{D_2^{l+1}} r^l Y_{lm}^*(\theta_2, \phi_2) + \frac{-GM_3}{D_3^{l+1}} r^l Y_{lm}^*(\theta_3, \phi_3) \right] Y_{l,m}(\theta, \phi). \quad (7.1)$$

Here, M_2 , D_2 , θ_2 , and ϕ_2 are the mass, distance, polar angle, and azimuthal angle of Star 2 (M_3 , D_3 , θ_3 , and ϕ_3 are the same quantities for Star 3), while G is the gravitational constant. The dominant terms have $l = |m| = 2$ and $l = 2$, $m = 0$, so we will consider only these terms in our analysis. Since we restrict our analysis to coplanar orbits aligned with the primary spin, $\theta_2 = \theta_3 = \pi/2$.

We wish to express the potential in terms of the angular orbital frequencies Ω_1 and Ω_{23} . Some trigonometry reveals that the distance from Star 1 to Star 2 is

$$D_2^2 = a_1^2 + \left(\frac{M_3}{M_2 + M_3} a_{23} \right)^2 + 2 \frac{M_3}{M_2 + M_3} a_1 a_{23} \cos(\phi_{23} - \phi_1), \quad (7.2)$$

where ϕ_1 is the phase of the orbit of Stars 2 and 3 about Star 1, ϕ_{23} is the phase of the orbit of Star 2 around Star 3, a_1 is the semi-major axis between Star 1 and the center of mass of Stars 2 and 3, and a_{23} is the semi-major axis between Stars 2 and 3. Also, the law of sines reveals

$$\sin(\phi_2 - \phi_1) = \frac{M_3}{M_2 + M_3} \frac{a_{23}}{D_2} \sin(\phi_{23} - \phi_1). \quad (7.3)$$

In a hierarchical triple system, $a_{23} \ll a_1$, so we expand distances and angles in powers of the small parameter

$$\epsilon \equiv a_{23}/a_1. \quad (7.4)$$

We find

$$D_2^{-3} \simeq a_1^{-3} \left[1 - 3\epsilon \frac{M_3}{M_2 + M_3} \cos(\phi_{23} - \phi_1) + \frac{3}{4} \epsilon^2 \left(\frac{M_3}{M_2 + M_3} \right)^2 \left(3 + 5 \cos[2(\phi_{23} - \phi_1)] \right) \right] \quad (7.5)$$

and

$$e^{-im\phi_2} \simeq e^{-im\phi_1} \left[1 - im\epsilon \frac{M_3}{M_2 + M_3} \sin(\phi_{23} - \phi_1) + \epsilon^2 \left(\frac{M_3}{M_2 + M_3} \right)^2 \left(\frac{im}{2} \sin[2(\phi_{23} - \phi_1)] - \frac{m^2}{4} + \frac{m^2}{4} \cos[2(\phi_{23} - \phi_1)] \right) \right]. \quad (7.6)$$

The values of D_3^{-3} and $e^{-im\phi_3}$ are the same as equations (7.5) and (7.6), but with the 2 and 3 subscripts reversed, and with $\phi_{23} \rightarrow \phi_{23} + \pi$.

Inserting equations (7.5) and (7.6) and their counterparts for Star 3 into equation (7.1), we find that the zeroth order contribution (the term proportional to ϵ^0) for $l = 2$ to the tidal potential is

$$U_{2m}^{(0)} = \frac{-G(M_2 + M_3)W_{l,m}r^2}{a_1^3} e^{-im\phi_1} Y_{2,m}(\theta, \phi), \quad (7.7)$$

where $W_{2,0} = -\sqrt{\pi/5}$ and $W_{2,\pm 2} = \sqrt{3\pi/10}$. To zeroth order, the tidal potential due to stars 2 and 3 is simply that of a single star of mass $M_2 + M_3$ at a semi-major axis a_1 .

Upon summing the contributions from both stars, the first-order terms (proportional to ϵ) in equation (7.1) vanish. However, the second-order terms produce an additional component of the tidal potential. Dropping terms with no ϕ_1 or ϕ_{23} dependence because they have no time dependence, we find that the second-order component of the tidal potential is

$$U_{2,m}^{(2)} = -A_{2,m}r^2Y_{2,m}(\theta, \phi)\left[F_me^{2i(\phi_{23}-\phi_1)-im\phi_1} + F_{-m}e^{-2i(\phi_{23}-\phi_1)-im\phi_1}\right], \quad (7.8)$$

where

$$A_{2,m} = \epsilon^2 \frac{G\mu_{23}W_{2,m}}{a_1^3}, \quad (7.9)$$

$\mu_{23} = M_2M_3/(M_2 + M_3)$, and

$$F_m = \frac{15 + 8m + m^2}{8}. \quad (7.10)$$

Then the $m = 0$ component yields

$$U_{2,0}^{(2)} = -\frac{15}{4}A_{2,0}r^2P_{2,0}(\cos\theta)\cos[2(\phi_{23} - \phi_1)]. \quad (7.11)$$

We further illuminate the nature of the tidal forcing by adding the $U_{2,2}^{(2)}$ and $U_{2,-2}^{(2)}$ components to find

$$U_{2,2}^{(2)} + U_{2,-2}^{(2)} = -A_{2,2}r^2P_{2,2}(\cos\theta)\left[\frac{35}{4}\cos(2\phi + 2\phi_{23} - 4\phi_1) + \frac{3}{4}\cos(2\phi - 2\phi_{23})\right]. \quad (7.12)$$

The first term in brackets produces retrograde forcing, i.e., it will excite modes with negative angular momentum that rotate in the opposite direction to the orbital motion of Stars 2 and 3 about one another. The second term in brackets produces prograde forcing, exciting modes with positive angular momentum.

We define $\phi_1 = \Omega_1 t$ and $\phi_{23} = \phi_{2,0} + \Omega_{23}t$, where $\phi_{2,0}$ is the phase ϕ_{23} of the short-period orbit $t = 0$, when their center of mass is closest to the line of sight. The second-order $m = 0$ component of the tidal potential produces forcing at a frequency $\sigma_0 =$

$2(\Omega_{23} - \Omega_1)$. The $m = \pm 2$ components produce forcing at two frequencies, $\sigma_{-2} = 2\Omega_{23}$ and $\sigma_2 = 2(\Omega_{23} - 2\Omega_1)$. These frequencies arise because they are the conjunction frequency in a frame corotating with the long-period orbit, but are Doppler shifted by $m\Omega_1$ when viewed in the inertial frame. Due to the hierarchical structure of the system, these frequencies can be larger than the dynamical frequency of Star 1, causing tidal forcing at high frequencies seldom occurring in binary systems.

Equation (7.8) describes the tidal potential in the inertial frame, but we also wish to calculate the forcing frequencies in the rotating reference frame of Star 1. To do so, we make the transformation $\phi = \phi_r + \Omega_s t$, where ϕ_r is the azimuthal angle in the rotating frame and Ω_s is the angular spin frequency of Star 1. Then in the rotating frame,

$$U_{2,m,r}^{(2)} = -A_{2,m} r^2 Y_{2,m}(\theta, \phi_r) \left[F_2 e^{2i(\phi_{23} - \phi_1) - im\phi_1 + im\Omega_s t} + F_{-2} e^{-2i(\phi_{23} - \phi_1) - im\phi_1 + im\Omega_s t} \right]. \quad (7.13)$$

Thus,

$$U_{2,0,r}^{(2)} = -A_{2,0} r^2 P_{2,0}(\cos \theta) F_0 \cos [2(\phi_{23} - \phi_1)], \quad (7.14)$$

and

$$U_{2,2,r}^{(2)} + U_{2,-2,r}^{(2)} = -A_{2,2} r^2 P_{2,2}(\cos \theta) \left[F_2 \cos (2\phi_r + 2\phi_{23} - 4\phi_1 + 2\Omega_s t) + F_{-2} \cos (2\phi_r - 2\phi_{23} + 2\Omega_s t) \right]. \quad (7.15)$$

Equations (7.13)-(7.15) are general for circular coplanar orbits aligned with the stellar spin. If Star 1 is synchronized with the orbit of Stars 2 and 3 such that $\Omega_{s,1} = \Omega_1$,²

$$U_{2,2,r}^{(2)} + U_{2,-2,r}^{(2)} \simeq -A_{2,2} r^2 P_{2,2}(\cos \theta) \left[F_2 \cos (2\phi_r + 2\phi_{23} - 2\phi_1) + F_{-2} \cos (2\phi_r - 2\phi_{23} + 2\phi_1) \right]. \quad (7.16)$$

²In compact triple systems in which three-body tides operate, it is very likely that $\Omega_{s,1} \simeq \Omega_1$ because the tidal synchronization time due to the zeroth order tidal potential of equation 7.7 will be much shorter than tidal time scales due to the three-body tides of equation (7.8).

Thus, when the spin of Star 1 is aligned with the orbit of Stars 2 and 3, the absolute values of the forcing frequencies of all three modes (the axisymmetric $m = 0$ mode, and the prograde and retrograde $m = \pm 2$ azimuthal modes) in the corotating frame are identical, namely, $|\nu| = 2(\Omega_{23} - \Omega_1)$.

7.3 Mode Excitation and Observation

7.3.1 Mode Amplitudes

With the tidal potential known, we may calculate the amplitude of the tidally forced modes. In this section we consider only tidal forcing by the $l = 2$ second-order component of the tidal potential. We use the subscript α to refer to a mode of angular degree l and m , with a frequency in the rotating frame of ω_α . In this frame, the mode amplitude c_α satisfies (Schenk et al. 2001)

$$\begin{aligned} \dot{c}_\alpha + (i\omega_\alpha + \gamma_\alpha)c_\alpha &= \frac{i}{2\varepsilon_\alpha} \langle \xi_\alpha(\mathbf{r}), -\nabla U \rangle \\ &= \frac{iA_\alpha Q_\alpha}{2\varepsilon_\alpha} e^{im(\Omega_s - \Omega_1)t} \left[F_m e^{2i(\Omega_{23} - \Omega_1)t + 2i\phi_{2,0}} + F_{-m} e^{-2i(\Omega_{23} - \Omega_1)t - 2i\phi_{2,0}} \right]. \end{aligned} \quad (7.17)$$

Here, $\omega_\alpha = \varepsilon_\alpha - mC_\alpha\Omega_s \text{sgn}(\varepsilon_\alpha)$ is the mode frequency in the rotating frame, ε_α is the unperturbed frequency for a non-rotating star, C_α is the rotational kernel (see Fuller & Lai 2012), and γ_α is the mode damping rate. In this formalism, both m and ε_α can have positive or negative values. The dimensionless coefficient Q_α is the overlap integral of the mode with the tidal potential, defined as

$$\begin{aligned} Q_\alpha &= \frac{1}{M_1 R_1^l} \langle \xi_\alpha | \nabla(r^l Y_{lm}) \rangle \\ &= \frac{1}{M_1 R_1^l} \int d^3x \rho \xi_\alpha^* \cdot \nabla(r^l Y_{lm}), \end{aligned} \quad (7.18)$$

where ξ_α is the mode eigenvector normalized via the condition

$$\langle \xi_\alpha | \xi_\alpha \rangle = M_1 R_1^l, \quad (7.19)$$

and R_1 is the radius of Star 1.

The non-homogeneous solution of equation (7.17) is

$$c_\alpha = \frac{A_\alpha Q_\alpha}{2\varepsilon_\alpha} \left[\frac{F_m e^{i\nu_m t + 2i\phi_{2,0}}}{\omega_\alpha + \nu_m - i\gamma_\alpha} + \frac{F_{-m} e^{-i\nu_{-m} t - 2i\phi_{2,0}}}{\omega_\alpha - \nu_{-m} - i\gamma_\alpha} \right] \quad (7.20)$$

where

$$\nu_m = 2(\Omega_{23} - \Omega_1) + m(\Omega_s - \Omega_1). \quad (7.21)$$

The total tidal response of the star is $\xi(\mathbf{r}, t) = \sum_\alpha c_\alpha(t) \xi_\alpha(\mathbf{r})$. We assume that the star is slowly rotating ($\Omega_s \ll \omega_\alpha$) such that $\xi_\alpha(r)$ and Q_α are independent of m or Ω_s , and $\omega_\alpha \simeq \varepsilon_\alpha$. Summing over both signs of ω_α yields

$$\xi(\mathbf{r}, t) = \sum_{\alpha, \omega > 0} A_\alpha Q_\alpha \xi_\alpha(\mathbf{r}) \left[\frac{F_m e^{i\nu_m t + 2i\phi_{2,0}}}{\omega_\alpha^2 - \nu_m^2 + 2i\nu_m \gamma_\alpha + \gamma_\alpha^2} + \frac{F_{-m} e^{-i\nu_{-m} t - 2i\phi_{2,0}}}{\omega_\alpha^2 - \nu_{-m}^2 - 2i\nu_{-m} \gamma_\alpha + \gamma_\alpha^2} \right]. \quad (7.22)$$

Summing over both signs of m then yields

$$\xi(\mathbf{r}, t, m = 0) = \sum_{\alpha, \omega > 0, m=0} 2A_\alpha Q_\alpha P_{2,m}(\cos \theta) \xi_\alpha(r) F_m D_{\alpha,m} \cos(\nu_m t + 2\phi_{2,0} + \psi_{\alpha,m}), \quad (7.23)$$

$$\begin{aligned} \xi(\mathbf{r}, t, m = \pm 2) = & \sum_{\alpha, \omega > 0, m=2} 2A_\alpha Q_\alpha P_{2,m}(\cos \theta) \xi_\alpha(r) \left[F_m D_{\alpha,m} \cos(\nu_m t + 2\phi_r + 2\phi_{2,0} + \psi_{\alpha,m}) \right. \\ & \left. + F_{-m} D_{\alpha,-m} \cos(\nu_{-m} t - 2\phi_r + 2\phi_{2,0} + \psi_{\alpha,-m}) \right], \end{aligned} \quad (7.24)$$

with

$$D_{\alpha,m} = \left[(\omega_\alpha^2 - \nu_m^2)^2 + 4\nu_m^2 \gamma_\alpha^2 + \gamma_\alpha^4 \right]^{-1/2} \quad (7.25)$$

and

$$\psi_{\alpha,m} = \frac{\pi}{2} + \tan^{-1} \left(\frac{\omega_\alpha^2 - \nu_m^2 + \gamma_\alpha^2}{2\nu_m \gamma_\alpha} \right). \quad (7.26)$$

The $m = 0$ modes produce a radial displacement

$$\xi_r(\mathbf{r}, t, m = 0) = \sum_{\alpha, \omega > 0, m=0} 2A_\alpha Q_\alpha F_m D_{\alpha, m} \xi_{r, \alpha}(r) P_{2,0}(\cos \theta) \cos(\nu_m t + 2\phi_{2,0} + \psi_{\alpha, m}). \quad (7.27)$$

The $m = \pm 2$ modes produce a radial displacement

$$\begin{aligned} \xi_r(\mathbf{r}, t, m = \pm 2) \simeq & \sum_{\alpha, \omega > 0, m=2} 2A_\alpha Q_\alpha F_m D_{\alpha, m} \xi_{r, \alpha}(r) P_{2,2}(\cos \theta) \cos(\nu_m t + 2\phi_r + 2\phi_{2,0} + \psi_{\alpha, m}) \\ & + 2A_\alpha Q_\alpha F_{-m} D_{\alpha, -m} \xi_{r, \alpha}(r) P_{2,2}(\cos \theta) \cos(\nu_{-m} t - 2\phi_r + 2\phi_{2,0} + \psi_{\alpha, -m}). \end{aligned} \quad (7.28)$$

The first term is the radial displacement due to the retrograde mode, and the second is due to the prograde mode.

7.3.2 Luminosity Variations

The luminosity variation produced by a mode, $\Delta L_\alpha / L$, is not trivial to calculate, because the temperature fluctuation produced by the mode is sensitive to non-adiabatic effects and subtleties in the outer boundary condition. We refer the reader to other studies (e.g., Buta & Smith 1979, Robinson et al. 1982) which have attempted to quantify the visibility of a mode given its amplitude and eigenfunction. If the mode is adiabatic, its luminosity fluctuation is

$$\frac{\Delta L_\alpha}{L} = 2A_\alpha Q_\alpha F_m D_{\alpha, m} \xi_{r, \alpha}(R) V_\alpha Y_{l, m}(\theta_o, \phi_o) \cos(\sigma_m t + 2\phi_{2,0} + \psi_{\alpha, m}) \quad (7.29)$$

with

$$\sigma_m = 2(\Omega_{23} - \Omega_1) - m\Omega_1, \quad (7.30)$$

and here $m = 2$ corresponds to the retrograde mode and $m = -2$ corresponds to the prograde mode. The angular coordinates θ_o and ϕ_o indicate the direction of the observer relative to the symmetry axis of the mode, here assumed to be the spin axis of Star 1.

We define V_α to be the visibility function of the mode, which is dependent on geometrical, opacity, and non-adiabatic effects. In high-inclination systems like HD 181068, $\theta_o \simeq 90^\circ$, and we have chosen our coordinate system such that $\phi_o = 0$. In this case, $Y_{l,m}(\theta_o, \phi_o) \simeq -\sqrt{5/(16\pi)}$ for $m = 0$ modes and $Y_{l,m}(\theta_o, \phi_o) \simeq \sqrt{15/(32\pi)}$ for $m = \pm 2$ modes.

The value of V_α is uncertain. If non-adiabatic effects are significant, V_α will be complex and the luminosity variation will be phase-shifted from equation (7.29). Here we consider adiabatic modes, but we remember that an observation of a phase shift is indicative of non-adiabatic effects. In the adiabatic limit, Buta & Smith (1979) find

$$V_\alpha = \alpha_l + \beta_l + 4\nabla_{\text{ad}}\gamma_l H_\alpha, \quad (7.31)$$

where α_l , β_l , and γ_l are coefficients of order unity that depend on the spherical harmonic l of the mode and the stellar limb-darkening function (we use the values given in Buta & Smith 1979), and ∇_{ad} is the adiabatic temperature gradient at the surface. The first term in equation (7.31) is due to surface area distortions, the second is due to surface normal distortions, and the third term is due to temperature effects. The function H_α describes the magnitude of the pressure perturbation compared to the radial surface displacement, i.e., $\Delta T_\alpha/T = H_\alpha \xi_{r,\alpha}/R$. According to Dziembowski (1971), the value of H_α for adiabatic oscillations is

$$H_\alpha = \left[\frac{l(l+1)}{\bar{\omega}_\alpha^2} - 4 - \bar{\omega}_\alpha^2 \right], \quad (7.32)$$

where

$$\bar{\omega}_\alpha = \frac{\omega_\alpha}{\omega_{\text{dyn}}}, \quad (7.33)$$

and $\omega_{\text{dyn}} = \sqrt{GM_1/R_1^3}$ is the dynamical frequency of Star 1. In this description, H_α is large for high-order g-modes (low values of $\bar{\omega}_\alpha$) or high-order p-modes (high values of $\bar{\omega}_\alpha$).

Gouttebroze & Toutain (1994) have attempted to estimate the value of V_α for p-modes in a solar model. They calculated non-adiabatic mode eigenfunctions, and then calculated luminosity variations by adding up the perturbed flux from a grid of emitting surface elements. They found that V_α is of order unity for low-order p-modes, but has substantially larger values for the high-order p-modes that typically produce solar-like oscillations. In the analysis of Section 7.6, we calculate V_α from equation (7.31), considering a lower limit of $H_\alpha \approx 1$ and an upper limit of equation (7.32).

7.4 Effect of Modes on Orbital Evolution

7.4.1 Hamiltonian Formalism

The tidally excited modes draw energy and angular momentum from the orbit and deposit them in Star 1. The effect of the modes on the orbits can be calculated from the Hamiltonian of the gravitational interaction between the modes and the stars. This Hamiltonian is

$$H = \int d^3r U(\mathbf{r}, t) \sum_{\alpha} c_{\alpha}^*(t) \delta \rho_{\alpha}^*(\mathbf{r}), \quad (7.34)$$

where $\delta \rho$ is the Eulerian density perturbation associated with each mode. Performing the integration over the volume of Star 1, and considering only $l = 2$ terms yields

$$H = -M_1 R_1^2 \sum_{\alpha, \omega > 0} A_{\alpha} Q_{\alpha} \left[F_m e^{2i(\phi_{23} - \phi_1) - im\phi_1 + im\Omega_s t} + F_{-m} e^{-2i(\phi_{23} - \phi_1) - im\phi_1 + im\Omega_s t} \right] c_{\alpha}^*(t). \quad (7.35)$$

Inserting equation (7.20) into equation (7.35), we find

$$H = -M_1 R_1^2 \sum_{\alpha, \omega > 0} (A_{\alpha} Q_{\alpha})^2 \frac{\omega_{\alpha}}{\varepsilon_{\alpha}} \left[F_m e^{2i(\phi_{23} - \phi_1) - im\phi_1} + F_{-m} e^{-2i(\phi_{23} - \phi_1) - im\phi_1} \right] \times \left[\frac{F_m e^{-i\sigma_{f1} t}}{\omega_{\alpha}^2 - \nu_m^2 - 2i\nu_m \gamma_{\alpha} + \gamma_{\alpha}^2} + \frac{F_{-m} e^{-i\sigma_{f2} t}}{\omega_{\alpha}^2 - \nu_{-m}^2 + 2i\nu_{-m} \gamma_{\alpha} + \gamma_{\alpha}^2} \right], \quad (7.36)$$

with $\sigma_{f1} = 2(\Omega_{23} - \Omega_1) - m\Omega_1$, and $\sigma_{f2} = -2(\Omega_{23} - \Omega_1) - m\Omega_1$.

The orbital evolution equations are $\dot{L}_1 = -dH/d\phi_1$, $\dot{L}_{23} = -dH/d\phi_{23}$, where $L_1 = \mu_1 a_1^2 \Omega_1$ and $L_{23} = \mu_{23} a_{23}^2 \Omega_{23}$ are the angular momenta of the outer and inner orbit, respectively, and $\mu_1 = M_1(M_2 + M_3)/(M_1 + M_2 + M_3)$. In the limit $\Omega_s \ll \omega_\alpha$ we find

$$\begin{aligned} \dot{L}_1 = M_1 R_1^2 \sum_{\alpha, \omega > 0} (A_\alpha Q_\alpha)^2 i \left[\frac{-(2+m)F_m^2}{\omega_\alpha^2 - \nu_m^2 - 2i\gamma_\alpha \nu_m + \gamma_\alpha^2} \right. \\ \left. + \frac{(2-m)F_{-m}^2}{\omega_\alpha^2 - \nu_{-m}^2 + 2i\gamma_\alpha \nu_{-m} + \gamma_\alpha^2} \right] \end{aligned} \quad (7.37)$$

and

$$\begin{aligned} \dot{L}_{23} = M_1 R_1^2 \sum_{\alpha, \omega > 0} (A_\alpha Q_\alpha)^2 i \left[\frac{2F_m^2}{\omega_\alpha^2 - \nu_m^2 - 2i\gamma_\alpha \nu_m + \gamma_\alpha^2} \right. \\ \left. + \frac{-2F_{-m}^2}{\omega_\alpha^2 - \nu_{-m}^2 + 2i\gamma_\alpha \nu_{-m} + \gamma_\alpha^2} \right]. \end{aligned} \quad (7.38)$$

We have discarded rapidly oscillating terms because they produce no secular variations.

The torque due to the $m = 0$ modes is

$$\dot{L}_1(m=0) = 8M_1 R_1^2 \sum_{\alpha, \omega > 0, m=0} (A_\alpha Q_\alpha)^2 F_m^2 \Gamma_{\alpha, m}, \quad (7.39)$$

where

$$\Gamma_{\alpha, m} = \frac{\nu_m \gamma_\alpha}{(\omega_\alpha^2 - \nu_m^2)^2 + 4(\nu_m \gamma_\alpha)^2 + \gamma_\alpha^4}, \quad (7.40)$$

and $\dot{L}_{23}(m=0) = -\dot{L}_1(m=0)$. The torque due to $m = \pm 2$ modes is

$$\dot{L}_1(m = \pm 2) = 16M_1 R_1^2 \sum_{\alpha, \omega > 0, m=2} (A_\alpha Q_\alpha)^2 F_m^2 \Gamma_{\alpha, m} \quad (7.41)$$

and

$$\dot{L}_{23}(m = \pm 2) = -8M_1 R_1^2 \sum_{\alpha, \omega > 0, m=2} (A_\alpha Q_\alpha)^2 \left[F_m^2 \Gamma_{\alpha, m} + F_{-m}^2 \Gamma_{\alpha, -m} \right]. \quad (7.42)$$

Equations (7.39-7.42) may be written in terms of a dimensionless damping rate $\bar{\Gamma}_{\alpha, m} = \Gamma_{\alpha, m} \omega_{\text{dyn}}^2$, such that we obtain the more familiar scaling for tidal dissipation:

$$\begin{aligned} \dot{L}_1(m=0) = 8 \frac{GM_1^2}{R_1} \epsilon^2 \left(\frac{\mu_{23}}{M_1} \right)^2 \left(\frac{R_1}{a_1} \right)^6 \sum_{\alpha, \omega > 0} (W_\alpha Q_\alpha F_0)^2 \bar{\Gamma}_{\alpha, 0}, \quad \text{for} \\ \text{for } m = 0 \text{ modes,} \end{aligned} \quad (7.43)$$

$$\dot{L}_1(m = \pm 2) = 16 \frac{GM_1^2}{R_1} \epsilon^2 \left(\frac{\mu_{23}}{M_1} \right)^2 \left(\frac{R_1}{a_1} \right)^6 \sum_{\alpha, \omega > 0} (W_\alpha Q_\alpha F_2)^2 \bar{\Gamma}_{\alpha, 2}$$

for $m = \pm 2$ modes, (7.44)

$$\dot{L}_{23}(m = 0) = -8 \frac{GM_1^2}{R_1} \epsilon^2 \left(\frac{\mu_{23}}{M_1} \right)^2 \left(\frac{R_1}{a_1} \right)^6 \sum_{\alpha, \omega > 0} (W_\alpha Q_\alpha F_0)^2 \bar{\Gamma}_{\alpha, 0}$$

for $m = 0$ modes. (7.45)

$$\dot{L}_{23}(m = \pm 2) = -8 \frac{GM_1^2}{R_1} \epsilon^2 \left(\frac{\mu_{23}}{M_1} \right)^2 \left(\frac{R_1}{a_1} \right)^6 \sum_{\alpha, \omega > 0} (W_\alpha Q_\alpha)^2 \left[F_2^2 \bar{\Gamma}_{\alpha, 2} + F_{-2}^2 \bar{\Gamma}_{\alpha, -2} \right]$$

for $m = \pm 2$ modes. (7.46)

Conservation of angular momentum requires that the torque on Star 1 is $\dot{L}_* = -\dot{L}_1 - \dot{L}_{23}$,
or

$$\dot{L}_* = -8 \frac{GM_1^2}{R_1} \epsilon^2 \left(\frac{\mu_{23}}{M_1} \right)^2 \left(\frac{R_1}{a_1} \right)^6 \sum_{\alpha, \omega > 0} (W_\alpha Q_\alpha)^2 \left[F_2^2 \bar{\Gamma}_{\alpha, 2} - F_{-2}^2 \bar{\Gamma}_{\alpha, -2} \right]. \quad (7.47)$$

We can see that $m = 0$ modes draw angular momentum from the inner orbit and transfer it to the outer orbit. The $m = 2$ (retrograde) modes take angular momentum from the inner orbit and the spin of Star 1, depositing it in the outer orbit. The $m = -2$ (prograde) modes draw angular momentum from the inner orbit and transfer it to the spin of Star 1. Thus, in all cases, three-body tides cause the inner orbit to decay and the outer orbit to expand, although the outer orbit expands by a much smaller factor because of its larger moment of inertia. Star 1 can be either spun up or spun down, depending on which mode (prograde or retrograde) contains more energy. Under most circumstances, Star 1 will usually be spun down because $F_2 > F_{-2}$. In the limit of zero eccentricity, the orbital energies change as $\dot{E}_1 = \Omega_1 \dot{L}_1$ and $\dot{E}_{23} = \Omega_{23} \dot{L}_{23}$. Consequently, $\dot{e}_1 = \dot{e}_{23} = 0$, and the orbits remain circular. Finally, we note that three-body tides tend to increase the stability of hierarchical triples because they cause the period ratio P_1/P_{23} to increase.

Table 7.1: Properties of the HD 181068 system as measured by Borkovits et al. 2012.

	$M(M_{\odot})$	$R(R_{\odot})$	$T_{\text{eff}}(K)$
Star 1	3.0 ± 0.1	12.46 ± 0.15	5100 ± 100
Star 2	0.915 ± 0.034	0.865 ± 0.010	5100 ± 100
Star 3	0.870 ± 0.043	0.800 ± 0.020	4675 ± 100

7.5 Observations of HD 181068

We now apply our theory to the compact triple-star system HD 181068, also known as the Trinity system, whose properties are listed in Table 1 (see Derekas et al. 2011, Borkovits et al. 2012). Stars 2 and 3 orbit about Star 1 at an angular frequency $\Omega_1 = 0.138 \text{ d}^{-1}$, while Stars 2 and 3 orbit about each other at $\Omega_{23} = 6.94 \text{ d}^{-1}$. All three stars are nearly exactly coplanar, with orbital inclinations of $i \simeq 90^\circ$. The red giant primary has a radius and surface temperature typical of red clump stars, with $R_1 = 12.46 \pm 0.15 R_{\odot}$ and $T_{\text{eff}} = 5100 \pm 100 \text{ K}$, but has a fairly large mass of $M_1 = 3.0 \pm 0.1 M_{\odot}$.

In the discovery paper of HD181068 (Derekas et al. 2011), 218 days of *Kepler* data were analyzed. One of the most surprising results was that the main component of the system, which is a red giant star, did not show solar-like oscillations. Instead, other pulsations were detected with frequencies close to double the orbital frequency of the short-period binary. Derekas et al. 2011 suggested that these pulsations might be tidally forced oscillations and that there might be a mechanism which suppresses the solar-like oscillations.

7.5.1 Fourier Analysis

As of writing, 11 quarters of data from Kepler have been made available to us, representing almost three years of essentially uninterrupted observations. The first six quarters of

Table 7.2: The significant peaks of the period analysis for HD 181068. A number of peaks located $< 0.1\text{d}^{-1}$ were left out of the analysis.

No.	Frequency (d^{-1})	Orbital Relation	Amplitude (mmag)	Phase	S/N
f_1	2.1203	$2(\Omega_{23} - 2\Omega_1)/(2\pi)$	0.44	0.0403	58
f_2	2.1643	$2(\Omega_{23} - \Omega_1)/(2\pi)$	0.25	0.2889	35
f_3	1.1065	$\Omega_{23}/(2\pi)$	0.08	0.2843	3.4
f_4	2.2084	$2\Omega_{23}/(2\pi)$	0.048	0.8719	6.8

data were obtained in long-cadence mode (one point every 29.4 minutes), while Q7 to Q11 were taken in short-cadence mode (one point every 58.9 seconds). Here we present a period analysis of the combined long-cadence and short-cadence data, the latter covering 450 days.

As a first step, we subtracted the eclipses and rotational variations by using the light curve fit of Borkovits et al. 2012, which resulted in a nearly continuous data set containing the pulsations. For the period analysis, we used Period04 by Lenz & Breger 2005. In the Fourier-spectra, a number of the peaks were located $< 0.1\text{d}^{-1}$ indicating long term variability, remnants of the light curve fit, or instrumental effects that are negligible in the present analysis. Peaks with significance are listed in Table 7.2 and the Fourier-spectrum is shown in Figure 7.2.

The most intriguing result of the period analysis is that f_1 and f_2 are linear combinations of the two orbital frequencies, suggesting a tidal origin. Their angular frequencies are separated by $2\Omega_1$, creating a beat pattern in which they are in phase near the primary eclipses and occultations (see Figure 7.3). The frequencies f_3 and f_4 correspond to one and two times the orbital frequency of Stars 2 and 3, and may be caused by the imperfect subtraction of the eclipses or spots on the components. However, they could have a tidal component as well.

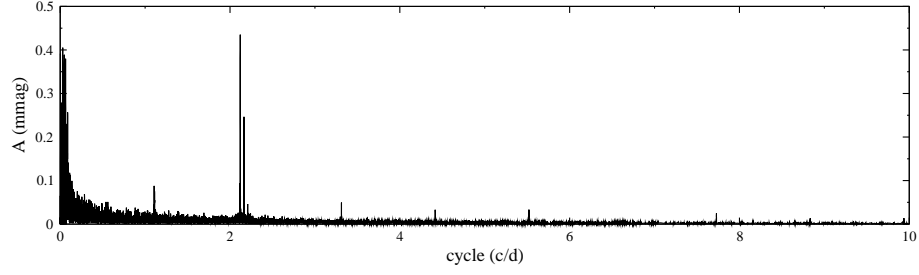


Figure 7.2: Fourier spectrum of 11 quarters of long-cadence data.

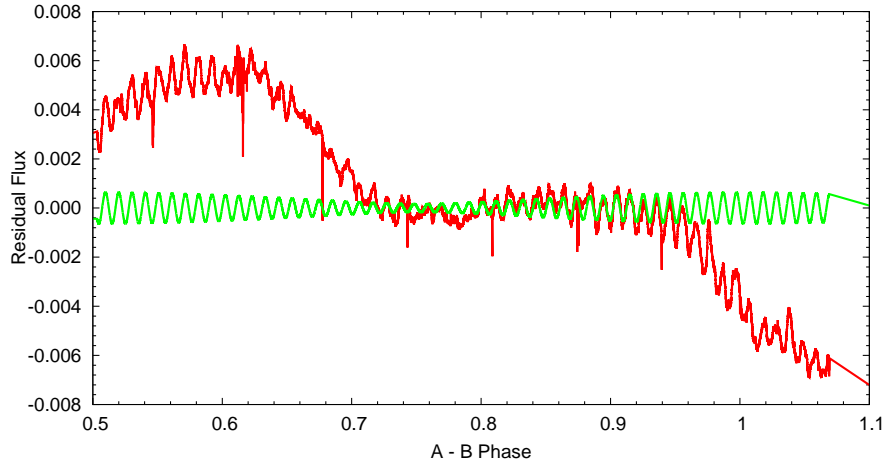


Figure 7.3: *Red curve*: Sample of light curve of HD 181068 between long duration eclipses. The x -axis is the phase of the long-period orbit, measured from the primary minimum at BJD 55545.466. *Green curve*: The simulated light curve of the oscillations. Note the beating pattern due to two close frequency oscillations.

7.5.2 Lack of solar-like oscillations

Red giant stars are well known to show solar-like oscillations (De Ridder et al. 2009, Chaplin et al. 2011a) which are excited by near-surface convection (see, e.g., Houdek et al. 1999, Samadi et al. 2007). Nearly all red giants observed by Kepler show detectable oscillations (Huber et al. 2010, Kallinger et al. 2010, Hekker et al. 2011), which can be used to probe the internal properties of the star (e.g., Bedding et al. 2011, Beck et al. 2012, Mosser et al. 2012). The frequency of maximum power (ν_{\max}) of solar-like

oscillations can be estimated using the scaling relation (Brown et al. 1991)

$$\nu_{\max} = \frac{M/M_{\odot}(T_{\text{eff}}/T_{\text{eff},\odot})^{3.5}}{L/L_{\odot}}\nu_{\max,\odot}, \quad (7.48)$$

with $\nu_{\max,\odot} = 3090\mu\text{Hz}$. Using the fundamental properties given by Borkovits et al. 2012, we calculate $\nu_{\max} = 64 \pm 7\mu\text{Hz}$ (5.5 ± 0.6 c/d) for the red giant component. To search for solar-like oscillations in HD181068, we first remove all primary and secondary eclipses from the data using the ephemeris given by Borkovits et al. 2012. To further remove long-periodic variability we then apply a Savitzky-Golay filter (Savitzky & Golay 1964) with a width of 5 days. Finally, we pre-whiten the most significant low frequency variations due to tidal oscillations, as discussed in the previous section.

The upper panel of Figure 7.4 shows a power spectrum of the residual Q1-Q11 long-cadence light curve. For comparison the middle panel shows the power spectrum of KIC4662939, a Helium-core burning red giant with similar fundamental properties as red giant component in HD181068 (Bedding et al. 2011). Despite an increase of the data set length by a factor of three compared to Derekas et al. 2011, the lack of solar-like oscillations in HD181068 A is clearly confirmed. On the other hand, we observe that both stars exhibit a similar decrease of power from low to high frequencies, which is the typical signature of granulation (see Mathur et al. 2011). This confirms that both stars indeed have similar fundamental properties, but that solar-like oscillations are suppressed in HD181068 A.

We speculate that the lack of solar-like oscillations of the main component is related to the close multiplicity of the components of HD 181068. Derekas et al. 2011 measured a rotational velocity of Star 1 of $v \sin i = 14 \pm 1 \text{ km s}^{-1}$, corresponding to $\Omega_{s,1} = 0.14 \pm 0.01 \text{ d}^{-1}$. This spin frequency is consistent with Star 1 being synchronized with the long-period orbit, indicating that it has been tidally synchronized. It is also an abnormally large spin frequency for red giants (de Medeiros et al. 1996), and the

rapid rotation may generate a strong magnetic dynamo. Indeed, the light curve of HD 181068 exhibits flaring events (some events occur during occultations of Stars 2 and 3, indicating the flares originate from Star 1, see Borkovits et al. 2012) that indicate high levels of magnetic activity. Chaplin et al. 2011b has shown that solar-like oscillations are suppressed in abnormally active stars, presumably due to their rapid rotation or due to the effects of strong magnetic fields. We therefore speculate that the tidal synchronization of the primary in HD 181068 creates rapid rotation and high magnetic activity that suppress the excitation of solar-like oscillations.

The available short-cadence data also allow us to search for solar-like oscillations in the dwarf components. Using equation (7.48), we expect the dwarf components to oscillate at frequencies between $3500 - 5000 \mu\text{Hz}$. The bottom panel of Figure 7.4 shows the power spectrum of the short-cadence data after performing the same corrections as described above. We do not detect any significant power excess in the data. Given the much lower luminosities of the dwarf companions and the amplitude dilution by the brighter giant component, this implies that the amplitudes are too small to be detected with the data at hand. Solar-like oscillations in the dwarfs may be also suppressed by the same mechanisms described above.

7.6 Comparison With Observations

7.6.1 Stellar Model

We generate a $M = 3.0M_{\odot}$, $R = 12.4R_{\odot}$, $T_{\text{eff}} = 5100\text{K}$, $z = 0.015$ helium burning red giant stellar model using the MESA stellar evolution code (Paxton et al. 2011). Figure 7.5 shows a propagation diagram for the stellar model. The high Brunt-Vaisala

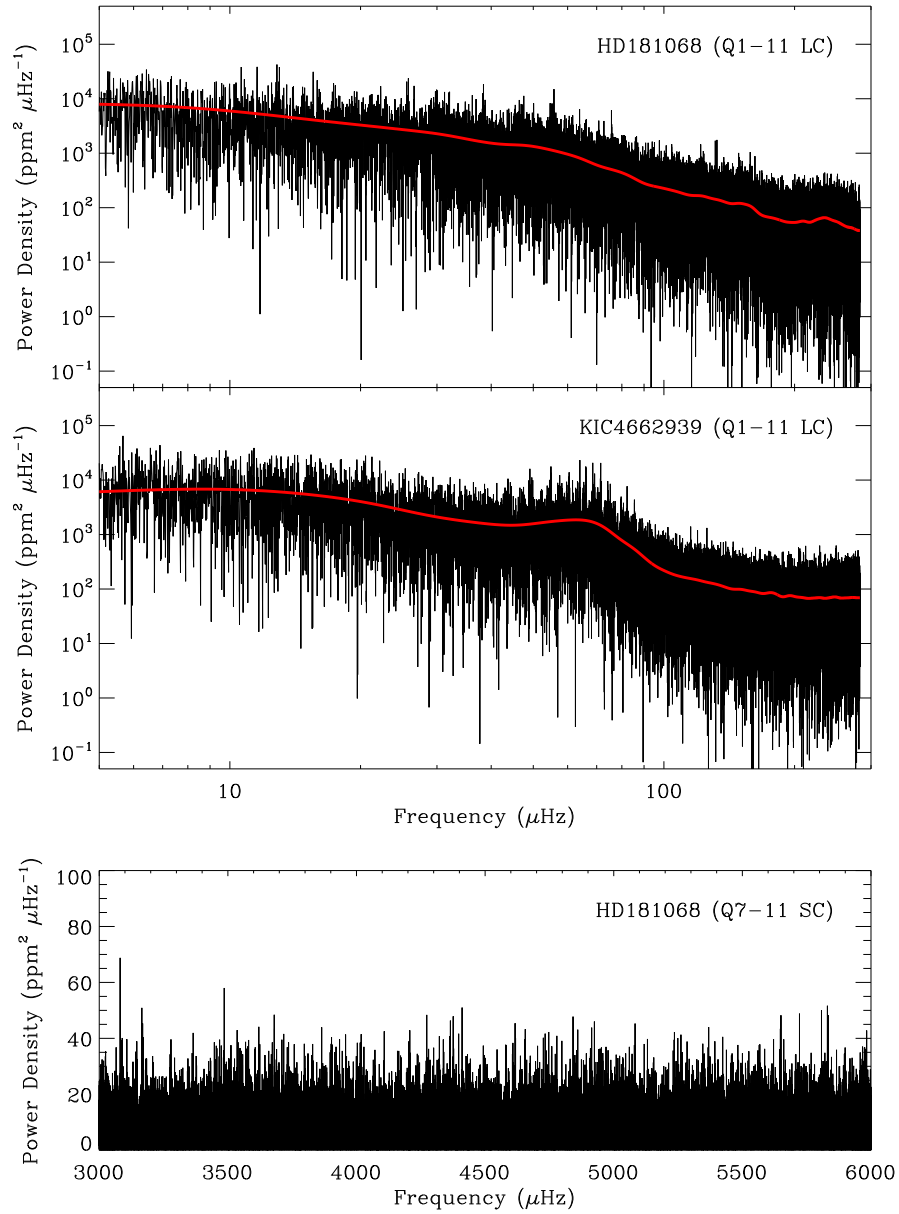


Figure 7.4: Top panel: Power spectrum of the Q1-Q11 long-cadence data of HD 181068 after removing eclipses and low frequency variability. The red line shows the power spectrum smoothed with a Gaussian filter with a full-width at half maximum of $5\mu\text{Hz}$. Middle panel: Same as top panel but for KIC 4662939. Bottom panel: Power spectrum of the Q7-11 short-cadence data of HD 181068 after removing eclipses and low frequency variability.

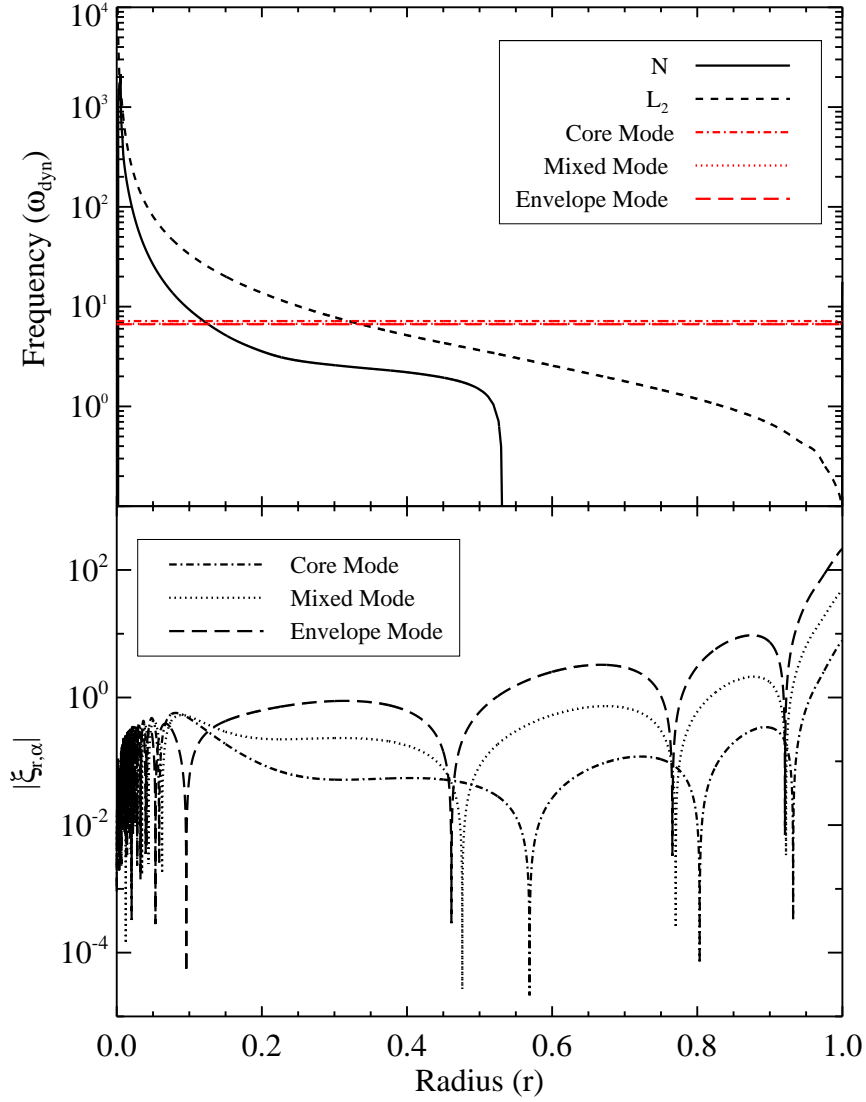


Figure 7.5: Top: the Brunt Vaisala frequency N (solid line) and Lamb frequency L_2 (dashed line) as function of radius r . The red horizontal (overlapping) lines mark the eigenfrequencies $\bar{\omega}_\alpha$ of the modes shown in the bottom panel. Bottom: mode eigenfunctions $\xi_{r,\alpha}$ for an envelope mode with $\bar{\omega}_\alpha = 6.66$ (long dashed line), a neighboring mixed mode with $\bar{\omega}_\alpha = 6.71$ (dotted line), and a core mode with $\bar{\omega}_\alpha = 7.17$. All quantities are calculated for our $M = 3.0M_\odot$, $R = 12.4R_\odot$ helium burning red giant model, and are plotted in units of $G = M = R = 1$. The modes are normalized via equation (7.19).

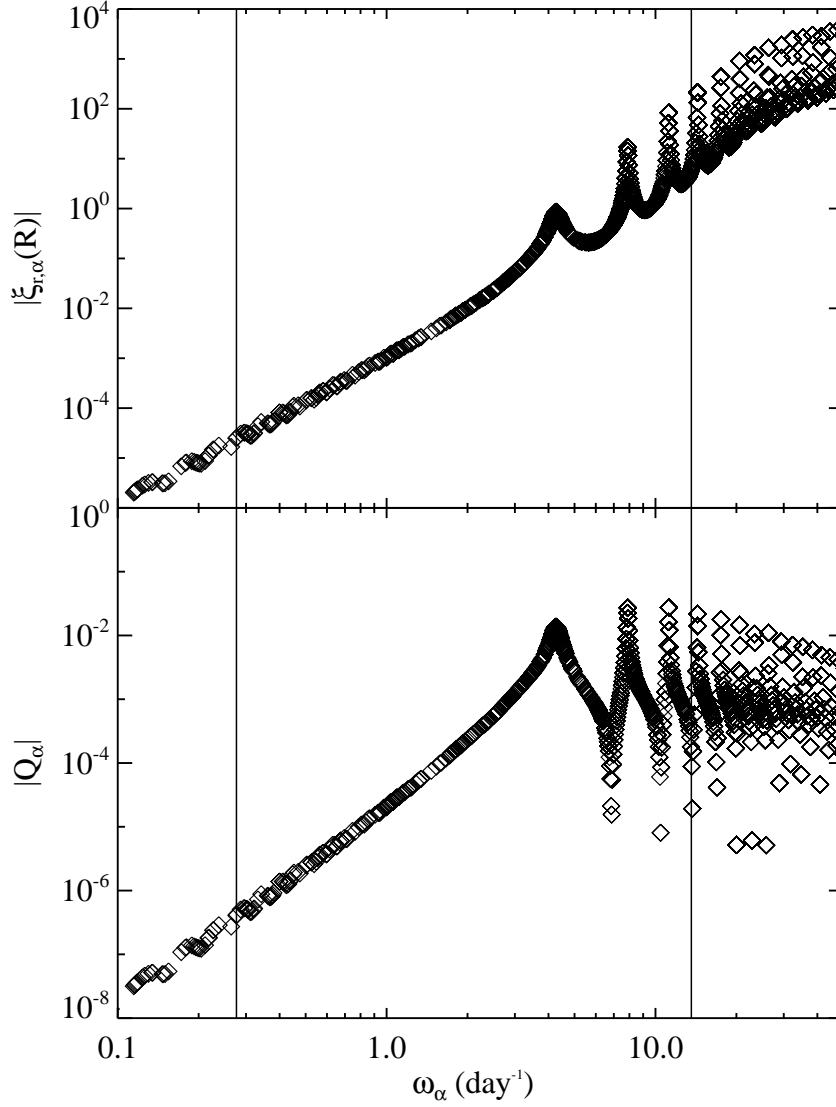


Figure 7.6: Radial displacement at the stellar surface $\xi_{r,\alpha}(R)$ (top) and overlap integral Q_α (bottom) for stellar oscillation modes as a function of mode eigenfrequency ω_α . The modes are calculated from our $M = 3.0M_\odot$, $R = 12.4R_\odot$ red giant model. The modes at the tips of the spikes are envelope dominated mixed modes, while the surrounding modes are mixed modes whose inertia is split between the core and envelope. The vertical lines mark the values of $2\Omega_1$ and $2\Omega_{23}$ in the HD 181068 system.

and Lamb frequencies in the radiative interior of the star allow high-order g-modes to propagate in the stellar interior, while the small Brunt-Vaisala and Lamb frequencies in the convective envelope of the star allow for p-mode propagation.

Using the model described above, we calculate the adiabatic stellar oscillation modes using the usual boundary conditions (see e.g., Unno et al. 1989), and normalized according to equation (7.19). Figure 7.6 shows the values of $\xi_{r,\alpha}(R)$ and Q_α as a function of ω_α for our stellar model. Low frequency modes g-modes (lower than $\omega_\alpha \approx 1$) are trapped in the core. Higher frequency modes still have g-mode character in the core, but have p-mode character in the convective envelope of the star. Modes whose inertia lies primarily in the convective envelope are the envelope dominated mixed modes, while the inertia of the neighboring mixed modes is split between the core and envelope. Figures 7.5 and 7.6 demonstrate that the envelope modes have large values of $\xi_{r,\alpha}(R)$ and Q_α compared to neighboring mixed modes. Consequently, the envelope modes are easily excited to large amplitudes (because of the larger values of Q_α) and produce large luminosity fluctuations [because of the larger values of $\xi_{r,\alpha}(R)$]. The envelope modes thus dominate the visible and energetic response of the star to high frequency tidal forcing.

7.6.2 Comparison with Observed Luminosity Fluctuations

Here, we compare our theory to observations of HD 181068. Unfortunately, it is difficult to predict the amplitude of a tidally excited mode, even if the system parameters are relatively well constrained. Part of the reason is that the value of the frequency detuning $D_{\alpha,m}$ (see equation 7.25) can vary by orders of magnitude over small changes in ω_α . Since the values of ω_α depend on the precise mass, radius, and internal structure of the star, accurately calculating $D_{\alpha,m}$ for each mode is very difficult.

Instead, we choose to calculate the amplitude of the luminosity fluctuations as a function of the stellar radius R_1 , which is constrained to be $R_1 = 12.46 \pm 0.15 R_\odot$. We compute the dimensionless values of $\bar{\omega}_\alpha$ for the stellar model described in Section 7.6.1,

and then scale them to dimensional frequencies ω_α using equation (7.33). The range of radii R_1 is meant to encompass uncertainties in $\bar{\omega}_\alpha$, M_1 , R_1 , $\Omega_{s,1}$, non-adiabatic effects, etc., that affect the precise values of ω_α in HD 181068.

Figure 7.7 displays the theoretical and observed luminosity variations produced at the tidal forcing frequencies $2(\Omega_{23} - 2\Omega_1)$, $2(\Omega_{23} - \Omega_1)$, and $2\Omega_{23}$. Recall that the observed variation at $2\Omega_{23}$ may be contaminated by imperfect eclipse subtraction and/or spotting effects. The luminosity variations are calculated using equation (7.29), using Ω_{23} and Ω_1 observed in HD 181068, and using $M_2 = M_3 = 0.9M_\odot$ and $\theta_o = 87.5^\circ$ (as measured by Borkovits et al. 2012). The top panel uses $H_\alpha = 1$, while the bottom panel uses $H_\alpha = [l(l+1)/\bar{\omega}^2 - 4 - \bar{\omega}_\alpha^2]$. The luminosity variations have peaks and dips at values of R_1 for which the frequency of a mode is nearly resonant with the forcing frequency. For $H_\alpha = 1$, the theoretical luminosity variations are well below the observed variations, except very near a resonance with an envelope p-mode (i.e., at $R_1 \simeq 12.8R_\odot$). Unless the HD 181068 is in a resonance locking state (see Section 7.7), it is unlikely to observe it so close to resonance.

In contrast, the theoretical luminosity variations are closer to the observed variations for $H_\alpha = [l(l+1)/\bar{\omega}^2 - 4 - \bar{\omega}_\alpha^2]$. The best agreement is obtained for $R_1 \simeq 12.6R_\odot$, and matches the luminosity variation for each theoretical and observed frequency to within a factor of 2. We conclude that the luminosity variations in HD 181068 are likely dominated by temperature effects, characterized by large values of H_α . The ordering of the amplitudes of the oscillations is naturally explained by our theory, i.e., $\Delta L/L(m=2) > \Delta L/L(m=0) > \Delta L/L(m=-2)$, because $F_2 > F_0 > F_{-2}$. However, the measured amplitude ratios are slightly different than what we expect away from exact resonances, and the cause of the discrepancy is unclear.

For non-adiabatic modes, our theory also predicts the phases of the observed oscil-

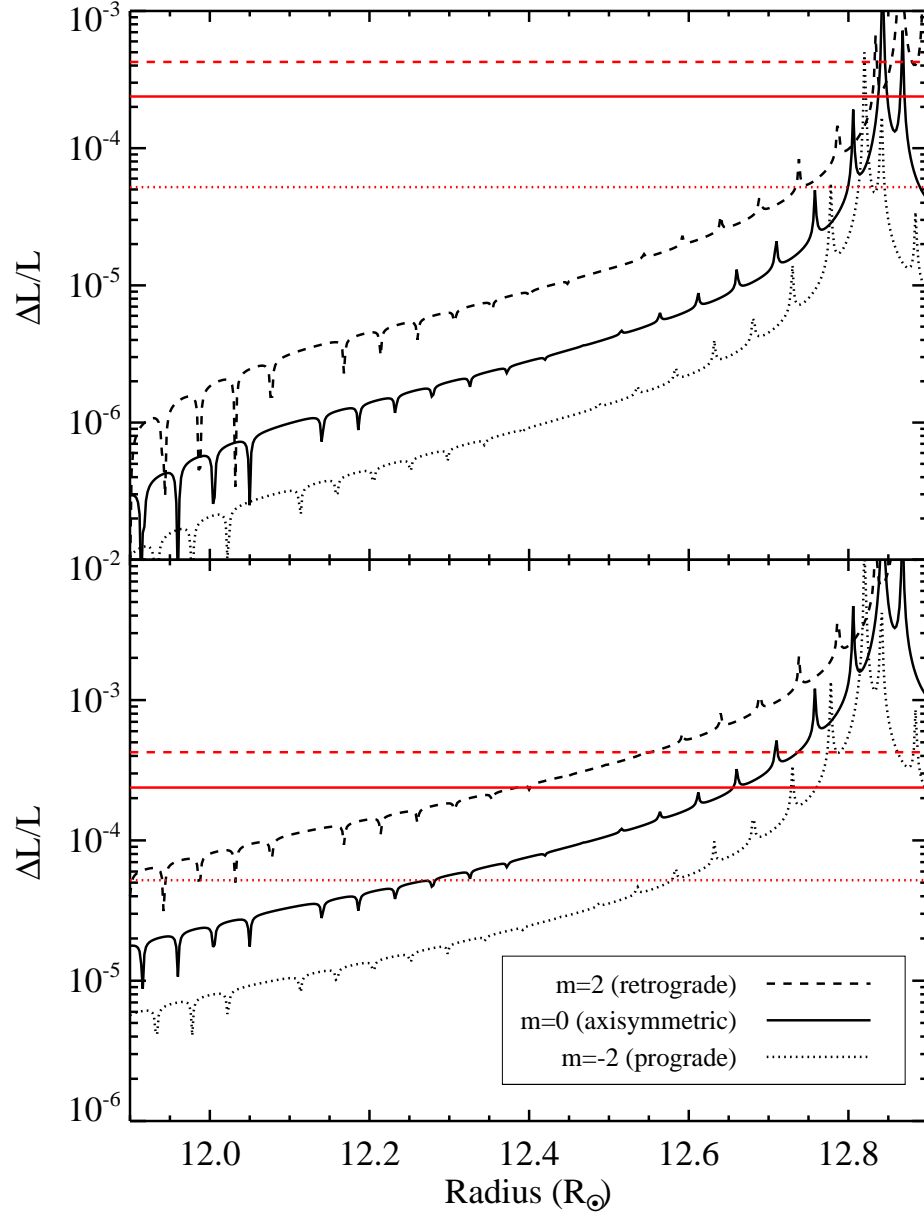


Figure 7.7: Luminosity variations $\Delta L/L$ as a function of stellar radius, using $H_{\alpha} = 1$ (top panel) and $H_{\alpha} = \omega_{\alpha}$ (bottom panel), for our stellar model. The actual stellar model has $R_1 = 12.4R_{\odot}$, but to make this plot we consider identical models scaled to different radii. The black lines are the luminosity variations of the mode at frequencies $2(\Omega_{23} - 2\Omega_1)$ (dashed line), $2(\Omega_{23} - \Omega_1)$ (solid line), and $2\Omega_{23}$ (dotted line). The horizontal red lines are the observed luminosity variations in HD 181068 at the same frequencies.

lations. In particular, equation (7.29) shows that for non-resonant adiabatic modes (i.e., V_α is real and $\psi_\alpha \simeq 0$ or $\psi_\alpha \simeq \pi$), the phase difference between two oscillation frequencies is $\Delta\phi \simeq m\phi_1$. This implies that the prominent frequencies f_1 and f_2 (which have $m = 2$ and $m = 0$, respectively) should be in phase at $\phi_1 \simeq 0$ and $\phi_1 \simeq \pi$, i.e., they should be in phase during the eclipses and occultations of Star 1. Indeed, the measured oscillations are in phase at these times, as can be seen from the simulated light curve in Figure 7.3. This suggests that the observed luminosity fluctuations are being produced by non-resonant modes, consistent with our findings above.

7.7 Orbital Evolution of HD 181068

We now wish to calculate the orbital evolution induced by the tidally excited modes in realistic systems such as HD 181068. The quantity in the orbital evolution equations (7.43)-(7.46) with the most uncertainty is the damping rate γ_α . An accurate calculation of γ_α requires a fully non-adiabatic calculation of mode eigenfrequencies, and must also include the turbulent damping of modes in the convection zone, which is not well understood. We choose to estimate γ_α using a quasiadiabatic WKB damping rate (see Burkart et al. 2012). We check that the damping rate calculated in this manner is the same order of magnitude as the damping rate inferred from observations of mode lifetimes of solar-like oscillations in red giants (see Belkacem 2012) for modes with $\omega_\alpha \approx \nu_{\max}$.

To understand the effects of tidally excited modes on the orbital evolution of a realistic triple system, we calculate the orbital evolution of a system resembling HD 181068 using equations (7.43)-(7.46). We consider coplanar, circular orbits, as observed in HD

181068. The orbital frequencies change as

$$\dot{\Omega}_1 = -\frac{3\dot{L}_1}{\mu_1 a_1^2} \quad (7.49)$$

and

$$\dot{\Omega}_{23} = -\frac{3\dot{L}_{23}}{\mu_{23} a_{23}^2}, \quad (7.50)$$

and the orbital semi-major axes change as $\dot{a}/a = -2\dot{\Omega}/(3\Omega)$. We define the tidal dissipation time scale as

$$t_{\text{tide}} = \frac{a_{23}}{\dot{a}_{23}} = \frac{\mu_{23} a_{23}^2 \Omega_{23}}{2\dot{L}_{23}}. \quad (7.51)$$

The orbital evolution timescales due to tidally excited modes can be comparable to the stellar evolution time scales of the stars in the system. Hence, it is important to evolve the properties of the stars in the system simultaneously with the orbital elements. In our evolutions, we compute the radius of Star 1 as a function of time using the MESA stellar evolution code (Paxton 2011). The changing value of R_1 affects not only the values of \dot{L} in equations (7.43)-(7.46), but it also affects the eigenfrequencies ω_α because the stellar oscillation frequencies scale as $\omega_\alpha \propto \sqrt{GM_1/R_1^3}$. Accounting for the changing eigenfrequencies is important because it can lead to resonance locking (Witte & Savonije 1999, Fuller & Lai 2012), allowing for tidal evolution on stellar evolutionary timescales rather than the longer non-resonant tidal evolution time scales.

In our calculations, we do not calculate new eigenfrequencies $\bar{\omega}_\alpha$ and associated eigenfunctions at each time step. We find that in the red giant phase of stellar evolution, the variations in Q_α as a function of time are relatively small, and that the variations in ω_α are dominated by variations in ω_{dyn} due to the changing value of R_1 . We use the values of $\bar{\omega}_\alpha$ and Q_α shown in Figure 7.6, and calculate ω_α from equation (7.33).

In addition to the tidally excited modes discussed in this paper, our evolutionary calculations should account for “two-body” tidal effects, i.e., the tidal effects due to the

zeroth order component of the tidal potential in equation (7.7). These tidal forces have no dependence on the small parameter ϵ , and hence they act on much shorter time scales. Furthermore, tidal forces between Stars 2 and 3 will act on even shorter time scales due to their close separation. Therefore, two-body tidal forces cause Stars 2 and 3 to have a circular orbit around each other, rotating synchronously with that orbit. They also cause the center of mass of Stars 2 and 3 to have a circular orbit around Star 1, with Star 1 rotating synchronously with that orbit. Thus, in our evolution, we enforce $\Omega_{s,1} = \Omega_1$ and $\Omega_{s,2} = \Omega_{s,3} = \Omega_{23}$ at all times. We account for the angular momentum redistribution associated with these processes, although the stellar spins contain only a small fraction of the total angular momentum of the system.

Because the moment of inertia of Star 1 is much less than that of the orbit of Stars 2 and 3 about Star 1, a small amount of orbital angular momentum deposited in Star 1 by three-body tidal effects can drastically change its spin frequency. This angular momentum will then be transferred back to the orbit of Stars 2 and 3 about Star 1 by two-body tidal effects until synchronism is restored. Therefore, after each time step in our evolution, we calculate ΔL_1 , ΔL_{23} and ΔL_* from equations (7.43)-(7.47). We then adjust the values of $\Omega_{s,1}$ and Ω_1 such that $\Omega_{s,1} = \Omega_1$ and the total angular momentum is conserved. Since $L_{*,1} \ll L_1$ for realistic parameters for a hierarchical triple system, the coupled tidal evolutions ensure that $\dot{L}_1 \simeq -\dot{L}_{23}$.

We also include orbital evolution due to induced eccentricity, magnetic braking, and gravitational radiation, as described in Appendix A. However, we find that the timescales associated with these processes are generally longer than the lifetime of a system such as HD 181068, so we do not discuss these effects in detail below.

7.7.1 Results of Orbital Evolution

Figure 7.8 shows an example of our evolutionary calculations. We plot the stellar radius, R_1 , orbital frequencies Ω_1 and Ω_{23} , and orbital decay time scales (t_{tide} , t_{ecc} , t_{mag} , and t_{GW}) as a function of time. We begin our orbital calculations as Star 1 is moving off the main sequence. The properties of the oscillation modes (calculated for helium burning red-giant model described in Section 7.6.1) are not appropriate for the initial model main sequence model, but become realistic as Star 1 moves up the red giant branch. We begin our calculation with orbital frequencies of $\Omega_{23,i} = 0.2\Omega_{23,o}$ and $\Omega_{1,i} = 1.15\Omega_{1,o}$, where $\Omega_{23,o}$ and $\Omega_{1,o}$ are the observed orbital frequencies in HD 181068.

Let us start by examining the top panel of Figure 7.8. The spike in radius at $t = 1 \times 10^7 \text{ yr}$ corresponds to the largest radius obtained during the red giant phase, while the long flat period between $2 \times 10^7 \text{ yr} < t < 10^8 \text{ yr}$ is the core helium burning phase. Figure 7.8 indicates that Star 1 in HD 181068 could be ascending the red giant branch, but is most likely a horizontal branch star. The measured temperature of Star 1 is also consistent with these possibilities.

The middle panel of Figure 7.8 shows that the orbits evolve substantially due to tidal dissipation. The outer orbital frequency, Ω_1 becomes slightly smaller as angular momentum is transferred from the inner to the outer orbit. The inner orbital frequency Ω_{23} changes substantially, increasing by a factor of roughly five. The tidal dissipation begins as Star 1 moves up the red giant branch, increasing the value of R_1 and hence \dot{L}_{23} . Tidal dissipation also becomes much stronger during this stage because the frequencies of envelope p-modes (which couple strongly with the tidal potential) become comparable to the tidal forcing frequencies. The tidal dissipation remains strong as Star 1 shrinks and descends the red giant branch because the system enters into a resonance locking configuration (see Section 7.7.2). Once Star 1 settles onto the horizontal branch, the

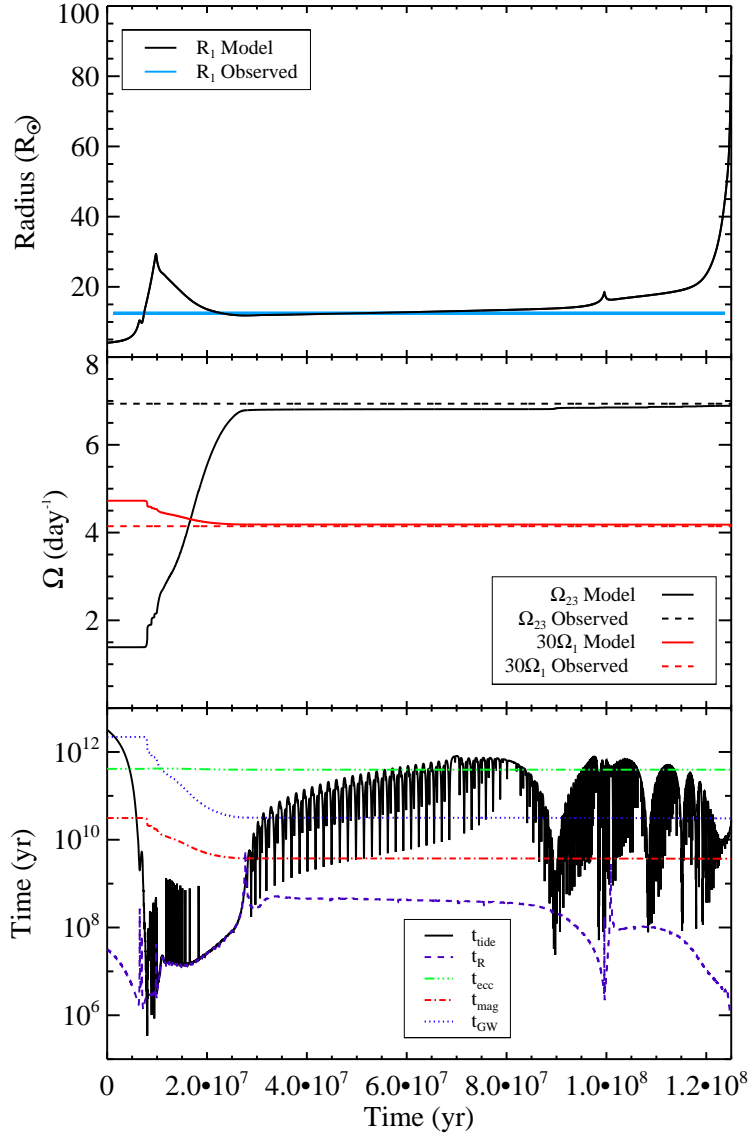


Figure 7.8: Top: Radius R_1 as a function of time since leaving the main sequence for an $M_1 = 3.0M_\odot$ stellar model. The horizontal blue strip is the measured radius of HD 181068, within the measurement uncertainty. Middle: Angular orbital frequencies Ω_{23} (solid black line) and $10\Omega_1$ (solid red line) as a function of time, including tidal dissipation. The horizontal lines are the values of Ω_{23} (dashed black) and $10\Omega_1$ (dashed red) for the HD 181068 system. Bottom: tidal dissipation timescale t_{tide} (solid black line), induced eccentricity orbital decay time scale t_{ecc} (triple dot dashed green line), gravitational wave decay timescale t_{GW} (dotted blue line), magnetic braking orbital decay time scale t_{mag} (dot dashed red line), and stellar evolution time scale t_R (dashed purple line) as a function of time.

resonance locking ends and tidal dissipation is drastically reduced.

The bottom panel of Figure 7.8 displays the relevant time scales of the evolution, including the stellar evolution time scale defined as

$$t_R = \frac{R_1}{|\dot{R}_1|}. \quad (7.52)$$

When Star 1 is on the main sequence, all the orbital time scales are longer than a Hubble time and can be ignored. As Star 1 moves up the red giant branch, the tidal dissipation time scale t_{tide} decreases by several orders of magnitude, as discussed above. When Star 1 is descending the red giant branch (at $t \approx 1.5 \times 10^7 \text{yr}$), we see that $t_{\text{tide}} \approx t_R$. This is a natural consequence of resonance locking, which we discuss in Section 7.7.2.

In contrast, the value of t_{tide} is generally much larger during the core helium burning phase, due to the decreased values of R_1 and a_{23} . While in the core helium burning phase, the value of t_{tide} has sharp dips due to resonance crossings with mixed modes. There are also deeper, broader dips due to resonance crossings with envelope p-modes, such as the resonance crossing that occurs at $t \approx 9 \times 10^7 \text{yr}$. However, these resonance crossing events are fairly brief and produce only small amounts of tidal dissipation. We are thus unlikely to observe any orbital decay in HD 181068, unless the system is in a resonance-locking state.

The initial orbital frequencies were chosen such that the final values of Ω_{23} and Ω_1 would be roughly equal to the observed orbital frequencies in HD 181068. This does not entail that our chosen values of $\Omega_{23,i}$ and $\Omega_{1,i}$ were the actual orbital frequencies of HD 181068 while Star 1 was on the main sequence. In reality, the initial orbital configuration of HD 181068 may have contained inclined or eccentric orbits for which the tidal dissipation rates may be substantially different. Nonetheless, the fact that a small value of $\Omega_{23,i}$ is required to match observations of HD 181068 indicates that the system may have experienced substantial orbital decay due to three-body tidal dissipation.

In the future, HD 181068 will likely enter a common envelope phase as Star 1 evolves up the asymptotic giant branch and envelops Stars 2 and 3. Additionally, it is possible that HD 181068 reached its compact configuration through a mass transfer phase while Star 1 was on the red giant branch. Our MESA-generated stellar models indicate that our $3M_{\odot}$ stellar model would not have overflowed its Roche lobe (assuming a_1 was equal to its current value) while Star 1 was on the red giant branch. However, a $4M_{\odot}$ star probably would have overflowed its Roche lobe while on the red giant branch, and it may be possible that this occurred in HD 181068. However, the outcome of stable mass transfer or common envelope evolution in triple systems is highly uncertain, and it warrants further study.

7.7.2 Resonance Locking

The orbital evolution discussed above contains periods of resonance locking in which a tidally excited mode is held near resonance for long periods of time, causing large amounts of tidal dissipation. Resonance locking involving tidally driven stellar oscillation modes was first investigated by Witte & Savonije (1999) and recently proposed by Fuller & Lai (2012) to explain the observed tidally driven oscillations in KOI-54. Resonance locking can occur when the frequency ω_{α} of a mode changes due to a stellar evolutionary process. As the mode approaches resonance with a tidal forcing frequency, enhanced tidal dissipation occurs. The dissipation feeds back on the process, changing the value of the forcing frequency ν_f by spinning up the star or causing orbital decay. Under the right circumstances, the system maintains the nearly resonant configuration such that $\dot{\omega}_{\alpha} \simeq \dot{\nu}_f$, i.e., the orbital evolution timescale is roughly equal to the stellar evolution time scale.

The resonance locking shown in Section 7.7 is qualitatively different from the locking investigated by Witte & Savonije (1999) and Fuller & Lai (2012), although the general principles described above are still true. In the case of a system like HD 181068, when Star 1 is descending the red giant branch, the frequencies of the stellar oscillation modes are increasing because the dynamical frequency of the star is increasing. When the value of ω_α of an envelope mode is nearly resonant with a forcing frequency ν_f , enhanced tidal dissipation occurs, causing the orbit of Stars 2 and 3 about one another to decay. Hence, the values of Ω_{23} and ν_f correspondingly increase, causing resonance locking.

When the system is resonantly locked, $\dot{\omega}_\alpha \simeq \dot{\nu}_f$. Assuming the star's oscillation frequencies change primarily due to the change in stellar radius, we have

$$\frac{\dot{\omega}_\alpha}{\omega_\alpha} \simeq -\frac{3}{2} \frac{\dot{R}_1}{R_1}. \quad (7.53)$$

Furthermore, the tidal forcing frequency changes primarily due to the increasing value of Ω_{23} , so that

$$\frac{\dot{\nu}_f}{\nu_f} \simeq -\frac{3}{2} \frac{\dot{a}_{23}}{a_{23}}. \quad (7.54)$$

Therefore, during resonance locking,

$$\frac{\dot{R}_1}{R_1} \simeq \frac{\dot{a}_{23}}{a_{23}}, \quad (7.55)$$

and thus $t_{\text{tide}} \simeq t_R$. This explains the near equality of t_{tide} and t_R during the descent of Star 1 from the red giant branch in Figure 7.8. It also suggests that compact triples may endure a period of rapid tidal dissipation, caused by resonance locking, as the primary descends from the red giant branch toward the horizontal branch. Such tidal dissipation may lie in the near future for other observed compact hierarchical triples, such as KOI-126 (see Carter et al. 2011) and KOI-928 (see Steffen et al. 2011).

7.8 Discussion

We have demonstrated that a new tidal dissipation mechanism exists for stars in compact hierarchical triple systems, even after the system has reached the quasi-equilibrium state of aligned and circular orbits with aligned and synchronous stellar spins. The three-body tidal forces produce forcing at frequencies of $\sigma = 2(\Omega_{23} - 2\Omega_1)$, $\sigma = 2(\Omega_{23} - \Omega_1)$, and $\sigma = 2\Omega_{23}$ (although more forcing frequencies will exist for non-coplanar and non-circular orbits). If the primary star is a red giant with a large radius and thick convective envelope, the three-body tidal potential can couple strongly with the envelope p-modes of the star, exciting modes to large amplitudes.

We compare our results to *Kepler* observations of HD 181068. The presence of oscillations in the lightcurve of HD 181068 at frequencies $\sigma = 2(\Omega_{23} - 2\Omega_1)$, $\sigma = 2(\Omega_{23} - \Omega_1)$, and $\sigma = 2\Omega_{23}$ indicates that the primary exhibits stellar oscillation modes excited by the three-body tidal forcing described in this paper. The large amplitude of the oscillations in HD 181068 are either due to large temperature variations produced by small amplitude, non-resonant modes, or they are due to geometric distortions produced by large amplitude, nearly resonant modes. In the latter case, the tidal dissipation rate is rapid, and the modes may be locked in resonance (see Section 7.7.2). However, the amplitudes and phases of the modes are best explained by the non-resonant scenario. Furthermore, since the lifetime of the resonance locking phase is brief compared to the lifetime of the star on the horizontal branch, we find the non-resonant scenario to be much more likely.

Because we have assumed adiabaticity when calculating stellar oscillation modes, there remains some uncertainty in the precise mode visibilities and damping rates. Fully non-adiabatic mode calculations can constrain the values of H_α and γ_α in future studies.

Furthermore, our calculations have been limited to the linear regime. As mentioned in Section 7.2, the three-body tidal forcing frequencies are nearly identical in the rotating frame of Star 1 if it is synchronized with the outer binary. This may allow for greatly enhanced non-linear mode coupling, affecting the mode amplitudes, damping rates, and visibilities.

The three-body tidal effects can also produce substantial orbital evolution among the stellar components, the main effect of which is the decay of the inner orbit of the compact binary. Our orbital evolution calculations for a system resembling HD 181068 reveal that, at most times, three-body tidal dissipation acts on long time scales and can be ignored. However, when the primary star is high on the red giant branch, three-body tidal dissipation may cause substantial orbital decay. Furthermore, stellar oscillation modes can become locked in resonance as the primary descends the red giant branch, resulting in greatly enhanced tidal dissipation. During resonance locking, tidal dissipation occurs on the same timescale as the stellar evolution, such that the orbital semi-major axis of Stars 2 and 3 decays as $\dot{a}_{23}/a_{23} \simeq \dot{R}_1/R_1$.

Future observations can detect and characterize tidally excited modes in compact triples. In non-eclipsing systems, the three-body nature of compact triples may not initially be detected from photometric and spectroscopic observations, especially if one star is much more luminous than its companions. The Kepler public red giant sample, consisting of more than 15,000 stars (Hekker et al. 2011), provides a unique resource that may contain several hidden clones of the Trinity system, which could be used to test our theory in a broader parameter space. The signature of three-body tidal forcing is a triplet of evenly spaced modes with frequencies $\sigma = 2(\Omega_{23} - 2\Omega_1)$, $\sigma = 2(\Omega_{23} - \Omega_1)$, and $\sigma = 2\Omega_{23}$, although the highest oscillation frequency may have a very small amplitude. The triplet could be mistaken for a rotationally split triplet of solar-like oscillations, but

the tidally excited modes can be distinguished by their indefinitely long lifetimes (and thus narrow Fourier peaks). In low inclination systems, the $\sigma = 2(\Omega_{23} - \Omega_1)$ oscillation will produce the largest luminosity fluctuations, while the $\sigma = 2(\Omega_{23} - 2\Omega_1)$ oscillation will be dominant in high-inclination systems like HD 181068.

CHAPTER 8

NON-RADIAL OSCILLATIONS IN ROTATING GIANT PLANETS WITH SOLID CORES: APPLICATION TO SATURN AND ITS RINGS

8.1 Introduction¹

Despite the abundance of planets in our galaxy, the internal structure of giant gaseous planets is largely unconstrained. Within our own solar system, the structures of Jupiter and Saturn remain enigmatic after centuries of observation. Most of the uncertainty stems from the lack of observational constraints on interior structure. Although it is possible to measure numerous global surface properties of gaseous giants (e.g., mass, radius, gravitational moments, magnetic field, spin rate, oblateness, luminosity, and surface composition), inferring the internal structure from these quantities is hampered by remaining uncertainties. In particular, the size of the planetary core and the stability of the surrounding envelope (i.e., an adiabatic and fully convective envelope or an envelope that contains regions of stable stratification as in Leconte & Chabrier 2012) remain unknown. Nevertheless, there is an abundance of theoretical work that has attempted to describe the formation and evolution of giant planet interiors (see reviews in Guillot 2005, Fortney et. al. 2011).

Global planetary seismology is a promising technique for probing the internal structures of planets. Indeed, the internal structure of the Earth, Moon, Sun, and numerous types of stars has been constrained primarily via measurements of seismic waves and global oscillations (see Dahlen & Tromp 1998, hereafter DT98, for a comprehensive description of the techniques of Earth seismology, and Chaplin & Miglio 2013 for a review of recent developments in asteroseismology). Unfortunately, direct detection of

¹This chapter is based on Fuller, Shabaltas, & Lai (2013), in press.

global oscillations in giant planets is extremely difficult because the oscillations produce negligible luminosity perturbations and have small surface displacements (radial surface displacements are likely on the order of centimeters). Recently, Gaulme et al. (2011) reported the detection of acoustic pressure modes (p-modes) in radial velocity data on Jupiter, although the quality of the data was insufficient to provide new constraints on Jupiter’s interior structure.

Saturn’s ring system offers a unique opportunity to perform planetary seismology, because even mild gravitational perturbations associated with the planet’s oscillation modes can generate density waves that propagate through the rings. Marley & Porco (1993) investigated this idea in detail, arguing that some of the unexplained wave features in Saturn’s C and D-rings were produced at Lindblad resonances with the gravitational perturbations associated with Saturn’s oscillation modes. However, existing *Voyager* data was insufficient to measure the properties of the waves, and so their seismic utility was limited.

Recently, Hedman & Nicholson (2013) (HN13 from here on) used *Cassini* occultation data to measure the radial location of Lindblad resonance (r_L), azimuthal pattern number (m), and angular pattern frequency (Ω_p) of several waves in Saturn’s C-ring. We retabulate the results of HN13 in Table 1. HN13 demonstrated that these waves were compatible with being excited by low degree prograde sectoral ($l = |m| = 2, 3, 4$) fundamental oscillation modes (f-modes) of Saturn (as predicted by Marley 1991 and Marley & Porco 1993), and incompatible with being excited by resonances with any of Saturn’s satellites. Moreover, HN13 found what appeared to be a “fine splitting” in the mode frequencies. Instead of one $m = -2$ wave excited by Saturn’s $l = 2$, $m = -2$ (prograde) f-mode, there were *two* discrete waves with a frequency difference of a few percent. Also, instead of one $m = -3$ wave excited by the $l = 3$, $m = -3$ f-mode, there

Table 8.1: Properties of the waves in Saturn’s rings measured by HN13. Resonant locations are measured from Saturn’s center, and are taken from Baillie et al. (2011). The value of $|\delta\tau|$ is the approximate maximum semi-amplitude of the optical depth variation associated with each wave.

Wave	Resonant location	m	Ω_p (deg/day)	$ \delta\tau $
W80.98	80988 km	-4	1660.3	0.09
W82.00	82010 km	-3	1736.6	0.07
W82.06	82061 km	-3	1735.0	0.21
W82.21	82209 km	-3	1730.3	0.15
W84.64	84644 km	-2	1860.8	0.09
W87.19	87189 km	-2	1779.5	0.14

were *three* waves with a frequency difference of less than a percent. Curiously, no fine splitting was observed for the $m = -4$ wave, and no waves with $m < -4$ have yet been observed.²

In this paper, we explore the properties of oscillation modes in giant planet interiors with the goal of explaining the observations of HN13. There have been many previous calculations of mode frequencies and eigenfunctions in giant planet models (e.g., Vorontsov & Zharkov 1981, Vorontsov 1981, Marley 1991, Wu 2005, Le Bihan & Burrows 2012), and several authors have investigated the effect of elasticity in the solid cores/crusts of white dwarfs/neutron stars (e.g., Hansen & Van Horn 1979, McDermott et al. 1988, Montgomery & Winget 1999). However, to our knowledge, no previous works have investigated the elastic response of a solid core in giant planets. The elasticity of a solid core adds entire new classes of modes that have previously been ignored, and which may have observable signatures. In particular, we examine the possibility of rotational mixing between elastic core modes and envelope f-modes, and whether such mixing can produce the observed fine splitting of the waves in Saturn’s rings.

Our paper is organized as follows. In Section 8.2, we generate toy giant planet

²Note that there are several other unidentified waves in the C-ring, mostly with shorter wavelengths, which may indicate they have larger $|m|$ values.

models that will serve as the basis of our oscillation mode calculations. Section 8.3 describes the characteristics of oscillations in non-rotating planets, while Section 8.4 investigates the process of mode mixing in rotating planets. In Section 8.5, we calculate the effects of oscillation modes on Saturn’s rings, and we compare our results to the observations of HN13. We discuss our results in Section 8.6.

8.2 Planetary Model

To understand the characteristics of elastic oscillations in rotating giant planets, we generate simple toy planet models composed of a one-component solid core surrounded by a neutrally stratified fluid envelope. These models allow us to capture the basic properties of giant planets without getting bogged down in uncertain details (e.g., helium rain out, liquid-metallic hydrogen phase transitions, core size and composition, etc.).

To generate our toy models, we first construct a polytropic model of index $n = 1$ (so that the pressure is related to density as $P \propto \rho^2$, which approximates the equation of state for gaseous giant planets). This model has a density profile $\rho_n(r)$. We then add a solid core by choosing a core radius, R_c , a dimensionless density enhancement D , and constant shear modulus μ (the shear modulus of the fluid above the core is zero). The density of material in the core is calculated by multiplying the density of material with $r < R_c$ in the polytropic model by D such that $\rho(r < R_c) = D\rho_n(r)$. We then normalize the density profile so that the total mass/radius equal the mass/radius of Saturn. With this density profile, we compute the gravitational acceleration via $g = GM(r)/r^2$, where $M(r) = \int_0^r 4\pi r'^2 \rho dr'$. We then assume the planet is neutrally stratified at all radii such that the Brunt-Vaisala frequency $N^2 = 0$. Under this assumption, the bulk modulus K is

given by

$$K = -\rho g \left(\frac{d \ln \rho}{dr} \right)^{-1} = \rho \frac{dP}{d\rho}. \quad (8.1)$$

The bulk modulus is related to the pressure P via $K = \Gamma_1 P$, with $\Gamma_1 = d \ln P / d \ln \rho$.

For the purposes of calculating adiabatic acoustic-elastic pulsations in non-rotating spherically symmetric planets, a planetary model is completely described by three quantities as a function of radius: the density ρ , adiabatic bulk modulus K , and the shear modulus μ (see elastic oscillation equations in Section 8.3). Integrating the hydrostatic equilibrium equation yields the pressure P , while the sound speed is $c_s = [(K + 4\mu/3)/\rho]^{1/2}$, and the shear speed is $v_s = (\mu/\rho)^{1/2}$.

Our models have only four free parameters (n , R_c , D , and μ), and are ideally suited for understanding the basic characteristics of elastic oscillations in giant planets. Although they are simplified, they exhibit all the basic features that will strongly affect the properties of elastic oscillations in giant planets. The $n = 1$ polytropic density profile will generate realistic estimates of frequencies of p-modes propagating in the fluid envelope of the planet. The values of R_c , D , and μ affect the spectrum of modes propagating in the solid core, therefore, observations of these modes could provide strong constraints on core properties.

Figure 8.1 displays the structure of our primary toy planet model discussed in this work. It was constructed using $n = 1$, $R_c = 0.25R$, and $D = 4$. It has a core mass $M_c = 16M_\oplus$, central density $\rho_c = 7.1 \text{ g/cm}^3$, and central pressure $P_c = 2.2 \times 10^{12} \text{ Pa}$. These values are consistent with the constraints provided by Guillot (2005).

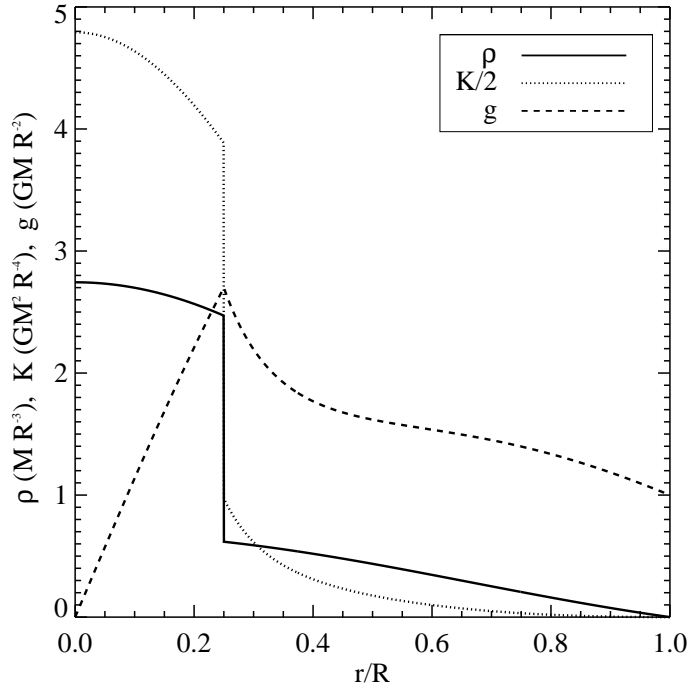


Figure 8.1: Toy planetary model of Saturn, with all quantities plotted in units with $G = M = R = 1$. This model has an envelope density profile of a polytrope of index $n = 1$, a core radius $R_c = 0.25R$ and a core density jump $D = 4$.

8.2.1 The Shear Modulus

As will be shown below, the value of the shear modulus in the solid core is pivotal in determining the characteristics of elastic oscillation modes within Saturn. The core of Saturn is likely composed of ices and rocks. Assuming the core is at least partially solid, its shear modulus may be determined by the properties of high pressure ices (of which water ice is the dominant component).

Unfortunately, the shear modulus of water ice is unknown at the pressures ($P \sim 10^{12}\text{Pa} \sim 10^7$ bars) and temperatures ($T \sim 8 \times 10^3\text{K}$, Guillot 2005) of Saturn's core. Asahara et al. (2010) found $\mu \approx 8 \times 10^{10}\text{Pa}$ for water ice at room temperature and pressures of 6×10^{10} Pa, well below the central pressure of Saturn. The measurements of

Asahara et al. (2010) show the shear modulus of ice increasing toward larger pressures, suggesting $\mu > 8 \times 10^{10} \text{Pa}$ in the core of Saturn. However, the shear modulus of many materials is also dependent on temperature. In the solid core of the Earth, the shear modulus of iron near its melting point is smaller than the shear modulus of iron at lower temperatures and pressures (Laio et al. 2000).

Recent molecular dynamics simulations (Cavazzoni 1999, French 2009, Militzer & Wilson 2010, Militzer 2012, Hermann et al. 2011, Wang et al. 2011) have predicted multiple new phases of ice at $P \gtrsim 10^{11} \text{Pa}$. In particular, ice is likely in either in a superionic or fluid phase at the core conditions of Saturn (French 2009, Wilson & Militzer 2012), depending on the core temperature. In the superionic phase, the oxygen atoms form an ordered lattice, while the hydrogen atoms diffuse freely through the lattice. It is possible that the shear modulus of this superionic state is smaller than lower temperature phases of ice in which the oxygen-hydrogen bonds contribute to the strength of the lattice structure.

With such uncertainty in the shear modulus of material in a solid core of Saturn, we take the shear modulus to be a free parameter. In this work, we consider shear moduli in the range $2 \times 10^8 \text{Pa} < \mu < 2 \times 10^{12} \text{Pa}$, which seems to be a reasonable range given the above considerations. For simplicity, we also assume the value of the shear modulus is constant throughout the core.

8.3 Oscillations of Non-rotating Planets

The presence of a solid core alters the form of planetary oscillations through the introduction of an elastic restoring force into the oscillation equations. The elastic forces act like a spring, with the spring constant governed by the value of the shear modulus μ ,

whereas the bulk modulus K characterizes the incompressibility of the material.

The introduction of elastic restoring forces allows for new types of modes to propagate in the solid regions of planets. In conventional asteroseismology, pressure is the dominant restoring force for p-modes, while gravity (buoyancy) is the dominant restoring force for g-modes. In terrestrial seismology, the elastic forces allow for the addition of two new classes of modes for whom the elasticity is the dominant restoring force. The first additional class are the spheroidal shear modes (we will refer to them as s-modes). Like p-modes and g-modes, the s-modes have poloidal displacement functions:

$$\boldsymbol{\xi}(\mathbf{r}) = U(r)Y_{lm}(\theta, \phi)\hat{\mathbf{r}} + V(r)\nabla_{\perp}Y_{lm}(\theta, \phi). \quad (8.2)$$

The second class are the toroidal shear modes (we will refer to them as t-modes), which have toroidal displacement functions

$$\boldsymbol{\xi}(\mathbf{r}) = W(r)\nabla \times [\hat{\mathbf{r}}Y_{lm}(\theta, \phi)]. \quad (8.3)$$

The t-modes exhibit no radial displacement, no gravitational perturbation, and are totally restricted to the solid regions of the planet. Each mode oscillates at its eigenfrequency ω such that

$$\boldsymbol{\xi}(\mathbf{r}, t) = \boldsymbol{\xi}(\mathbf{r})e^{i\omega t} \propto e^{i(m\phi + \omega t)}. \quad (8.4)$$

With this convention, prograde modes with positive frequency have $m < 0$, while retrograde modes with positive frequency have $m > 0$.

Introducing the elastic forces into the oscillation equations makes them considerably more complicated. In appendix F, we list the full oscillation equations (see also Dahlen & Tromp 1998, Hansen & Van Horn 1979, Montgomery & Winget 1999) and boundary conditions. The spheroidal oscillations are described by a system of six linear ordinary differential equations, while the toroidal oscillations are decoupled from the spheroidal oscillation equations and are described by two linear ordinary differential equations. We

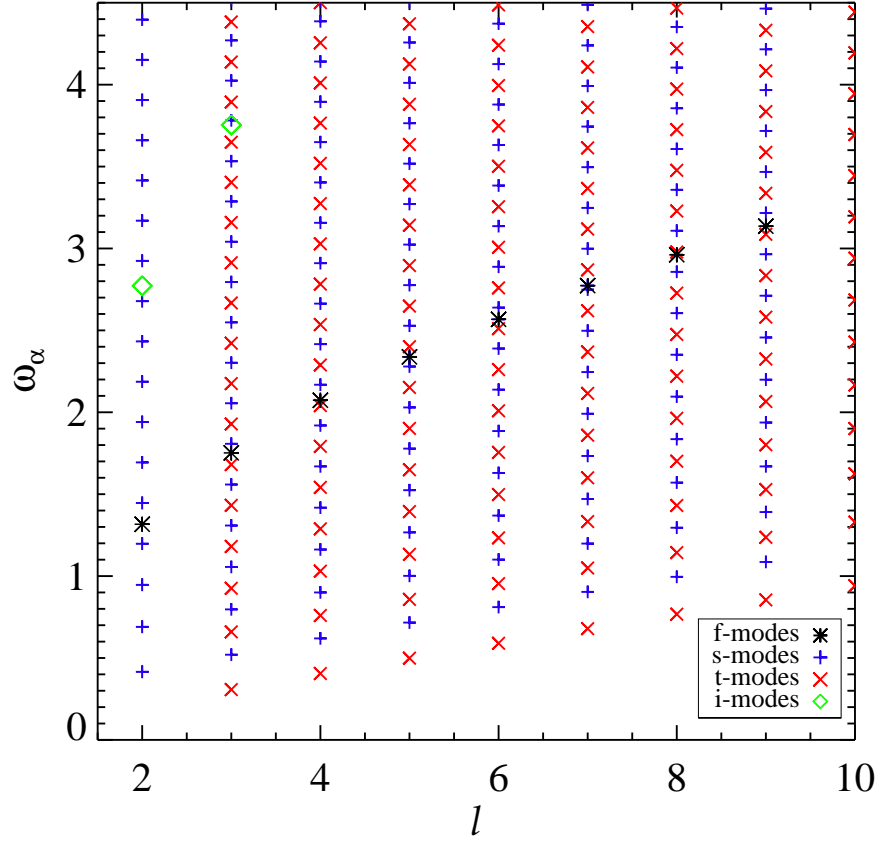


Figure 8.2: Oscillation mode spectrum of our planetary model with $n = 1$, $R_c = 0.25R$, $D = 4$, and $\mu = 1.6\text{GPa}$. The mode angular frequencies ω_α (in units of $\sqrt{GM/R^3} = 416\mu\text{Hz}$) are plotted as a function of the angular degree l . Envelope p-modes have been omitted for clarity. We have not included $l = 2$ t-modes because they cannot mix with modes with $|m| > 1$ (see Section 8.3.1). Note the nearly equal frequency spacing for both s-modes and t-modes at all values of l .

choose to normalize our mode eigenfunctions via their inertia such that for any mode (indexed by α),

$$\int dV \rho \boldsymbol{\xi}_\alpha \cdot \boldsymbol{\xi}_\alpha^* = 1, \quad (8.5)$$

with the integral extending over the volume of the planet.

We solve the adiabatic elastic oscillation equations (subject to the appropriate boundary conditions) for the spectrum of oscillation mode frequencies and eigenfunctions cor-

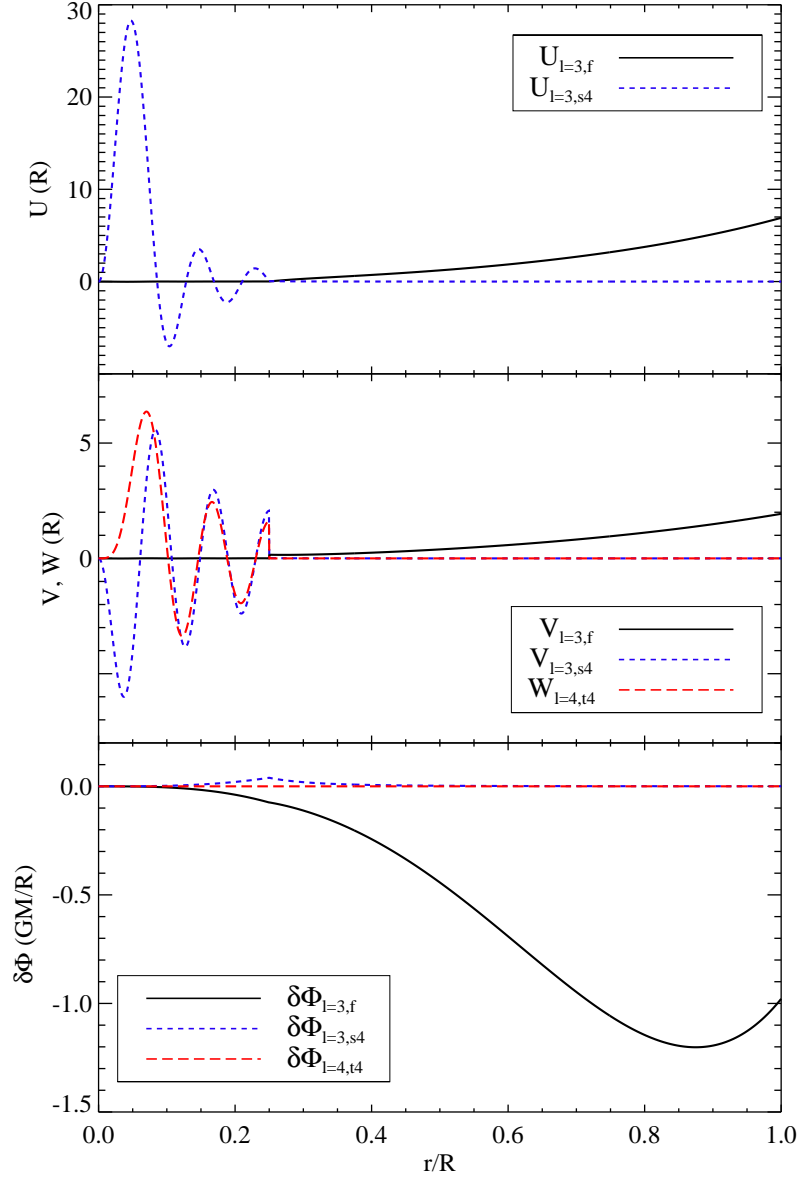


Figure 8.3: Oscillation mode displacement functions in our planetary model with $n = 1$, $R_c = 0.25R$, $D = 4$, and $\mu = 1.6\text{GPa}$. We plot the radial displacement $U_\alpha(r)$ (top panel), horizontal displacement $V_\alpha(r)$ or $W_\alpha(r)$ (middle panel), and gravitational potential perturbation $\delta\Phi_\alpha(r)$ (bottom panel). The different lines correspond to the $l = 3$ spheroidal f-mode (black line, $\omega_\alpha = 1.75$), a nearby $l = 3$ spheroidal mode ($s4$, blue short-dashed line, $\omega_\alpha = 1.55$), and an $l = 4$ toroidal mode ($t4$, red long-dashed line, $\omega_\alpha = 1.54$).

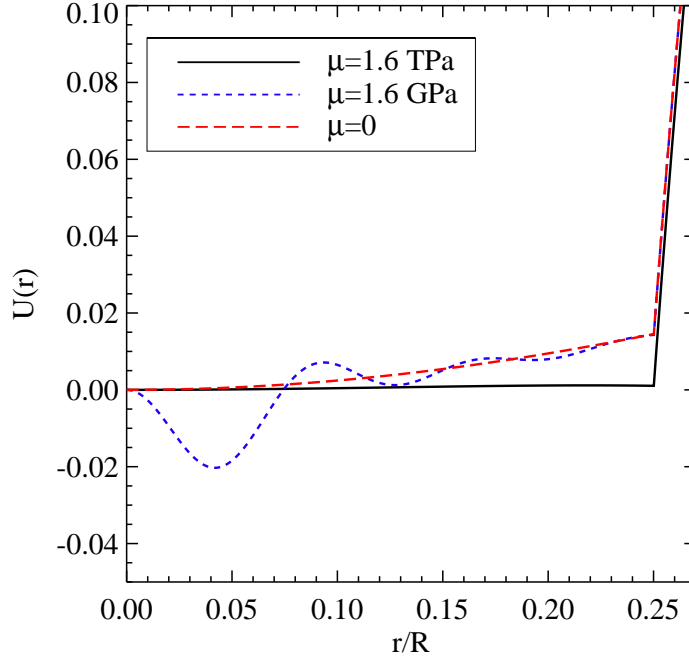


Figure 8.4: Radial displacements U of the $l = 3$ f-mode in the planetary model in Figure 8.1 for differing values of the core shear modulus μ . The f-mode wave function is nearly unaffected outside of the core.

responding to a chosen planetary model. Figure 8.2 shows a plot of mode frequencies as a function of l , while Figure 8.3 shows the displacement functions of some oscillation modes of different types. Gas giant planetary models with a solid core and fluid envelope support p-modes that are largely restricted to the fluid envelope, and s-modes that are largely restricted to the solid core. The p-modes typically have large surface displacements and gravitational potential perturbations, while the s-modes have very small surface displacements and potential perturbations. The t-modes are very similar to the core s-modes, except that their displacement and potential perturbations are exactly zero in the fluid envelope.

The dispersion relation for t-modes is

$$k_r^2 = \frac{\rho}{\mu} \omega^2 - \frac{l(l+1)}{r^2}. \quad (8.6)$$

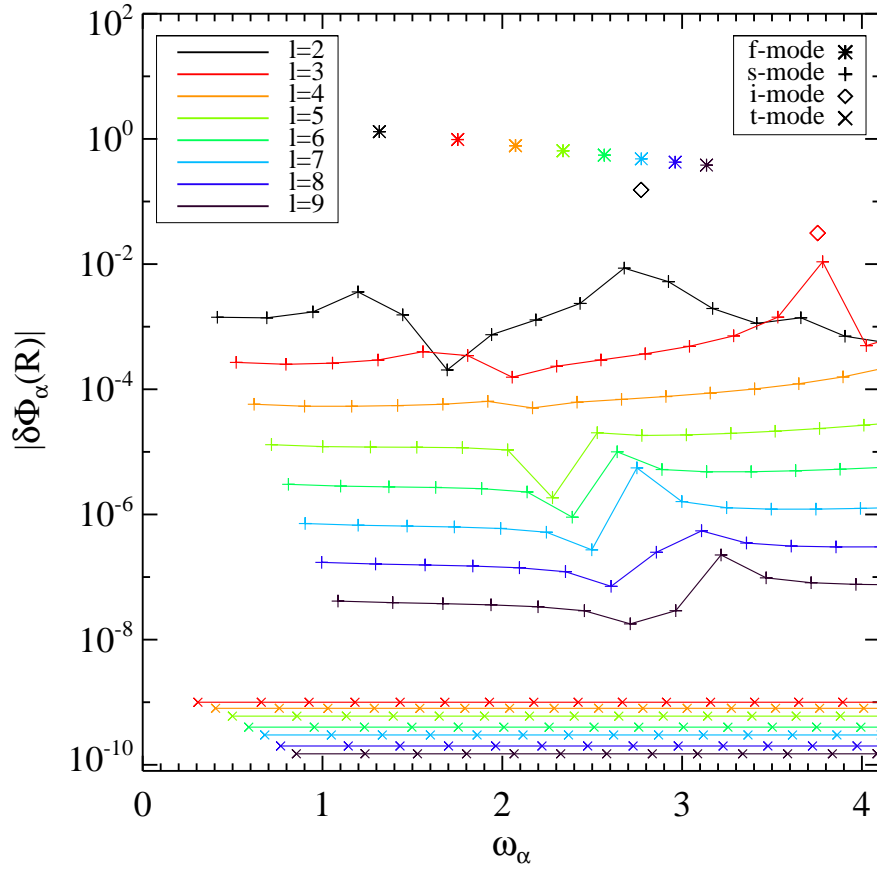


Figure 8.5: Surface gravitational potential perturbations, $\delta\Phi_\alpha(R)$, as a function of mode frequency ω_α in our planetary model with $n = 1$, $R_c = 0.25R$, $D = 4$, and $\mu = 1.6$ GPa. S-modes and t-modes of equal value of l have been connected by lines for clarity. The actual value of $\delta\Phi_\alpha(R)$ for the t-modes is exactly zero. The peaks in $\delta\Phi_\alpha(R)$ for s-modes are due to mixing with f-modes or i-modes.

This is also the approximate dispersion relation for s-modes. These modes propagate at the shear speed $v_s = \sqrt{\mu/\rho}$. A core with large density and small (but finite) shear modulus will support a dense spectrum of low frequency s-modes and t-modes. The frequency spacing of these modes is

$$\Delta\omega \simeq \frac{\pi}{R_c} \sqrt{\frac{\mu}{\rho_c}}, \quad (8.7)$$

where ρ_c is the central density of the planet. This frequency spacing is nearly independent of the mode index α (i.e., the values of l , m , and number of radial nodes), and is

dependent only upon the core radius, density, and shear modulus. In the asymptotic regime, s-modes and t-modes of the same l are offset from one another by $\sim \Delta\omega/2$ because of differing boundary conditions at the core-envelope boundary.³ Consequently, for s-modes of angular degree l , there exist t-modes of $l \pm 1$ with similar frequencies, and vice versa for t-modes.

The effect of a solid core on the properties of the f-mode and low order p-modes is miniscule. The main reason is that f-modes and low order p-modes have almost all of their inertia in the fluid envelope. Consequently, the value of the shear modulus has essentially no impact on the f-mode frequency (the f-modes shown in Figure 8.4 differ by less than one part in 10^5 in frequency), radial surface displacement, or potential perturbation.⁴ Nonetheless, the value of the shear modulus does effect the f-mode wave function in the core of the planet, as shown in Figure 8.4. For very rigid cores (large μ), incoming waves are reflected, and the f-mode is excluded from the core. For softer cores (small but finite μ), the f-mode may obtain a wave-like structure inside the core. Finally, for fluid cores, the f-mode penetrates into the core, but with a small amplitude, due to the jump in density.

In the absence of rotation, external gravitational perturbations will be produced almost exclusively by envelope f-modes and low order p-modes (see Figure 8.5).⁵ The incompressive nature of low order s-modes and t-modes creates very small density and gravity perturbations. Furthermore, because s-modes and t-modes are largely confined to the core, they produce very small fluid displacements at the surface. Thus, in the

³For modes completely confined to the solid core, the boundary conditions at the core-envelope boundary imply $U(r) \simeq 0$ for s-modes but imply $dW(r)/dr \simeq 0$ for t-modes. Therefore, the number of wavelengths differs by about 1/4 for s-modes and t-modes, accounting for the offset of $\sim \Delta\omega/2$ between s-modes and t-modes in Figure 8.2.

⁴An exception to this rule is at frequencies very near avoided crossings with s-modes or i-modes, see Section 8.3.1.

⁵Moreover, only relatively low-degree (low value of l) modes will produce significant external gravitational perturbations because the strength of the perturbation outside the planet falls off as $\delta\Phi(a) = \delta\Phi(R)(R/a)^{l+1}$, where a is the distance from the center of the planet.

absence of rotation, s-modes and t-modes should be nearly impossible to detect.

Because our planetary models are neutrally stratified, they do not support g-modes. However, a discontinuity in density at the core-envelope boundary is associated with a single interface mode for each value of l . The frequency of this i-mode is

$$\omega_i^2 \approx \frac{\sqrt{l(l+1)}g_c}{R_c} \frac{\rho_b - \rho_a}{\rho_b + \rho_a}, \quad (8.8)$$

where a and b indicate the quantity should be evaluated above and below the interface, respectively, and $g_c = g(R_c)$. For density jumps of $D \lesssim 2$ at the core-envelope boundary, the frequency of the interface mode may be comparable to that of the f-mode.⁶ The surface displacements and gravitational potential perturbations of the i-modes are typically greater than s-modes but less than f-modes for our planetary models.

8.3.1 Mode Mixing

The distinction between different types of modes (s-modes, t-modes, i-modes, and f-modes or p-modes) is not always clear. For a given planetary model, there may exist modes of nearly equal ω_α and identical l that will mix and obtain characteristics of two types of modes. This phenomenon is well known in Earth seismology (DT98), and is frequently observed in mixed modes in red giant stars (Chaplin & Miglio 2013).

Mode mixing may also occur in non-rotating, spherically symmetric giant planet models (we examine rotation-induced mode mixing in Section 8.4). To understand the process of mode mixing, we calculate the modes of the planetary model in Figure 8.1 for different values of the shear modulus μ . The frequencies ω_α and surface displacements $U_\alpha(R)$ of some selected modes are shown in Figure 8.6. At certain shear moduli

⁶Additional interface modes may also exist due to the presence of additional density discontinuities in the planet. This may occur at the molecular-metallic hydrogen phase transition, the metallic hydrogen-molecular helium composition gradient, or at discontinuities in a differentiated core.

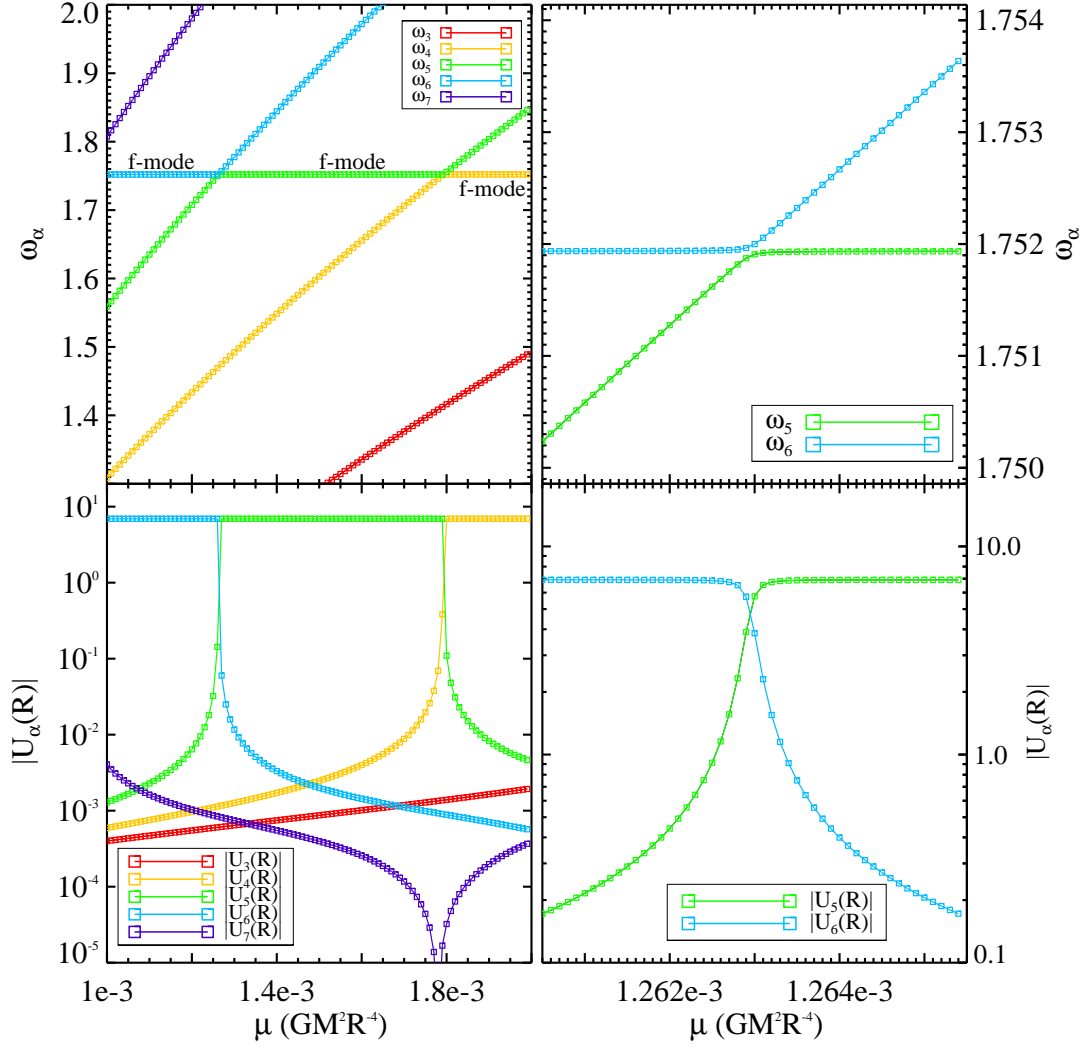


Figure 8.6: The frequencies ω_α (top two panels) and radial surface displacements $U_\alpha(R)$ (bottom two panels) of selected $l = 3$ modes from our model in Figure 8.1, plotted as a function of the value of the shear modulus μ . The shear modulus is plotted in units of $GM^2R^{-4} = 1.6\text{TPa}$. Away from avoided crossings, the f-mode corresponds to the mode lying along the nearly horizontal line at $\omega_\alpha \simeq 1.75$, while the other modes are core s-modes. The right two panels present a zoomed in view of an avoided crossing between an s-mode and the f-mode.

$\mu = \mu_c$, the f-mode and an s-mode have nearly identical frequencies. As the value of μ approaches μ_c , the modes begin to exchange character with one another, causing the f-mode to penetrate into the core and the s-mode to penetrate into the fluid envelope. At $\mu = \mu_c$, the modes reach a minimum frequency separation and are equal superpositions of one another. As μ increases away from μ_c , the mode frequencies diverge from one another (note the frequencies are never exactly equal, resulting in an “avoided” crossing), having smoothly exchanged mode character. If a planetary model happens to contain modes near these avoided crossings, core s-modes may obtain substantially larger surface displacements and gravitational potential perturbations.

However, we find that it is unlikely for an s-mode and an f-mode to be near an avoided crossing in our planetary models, as evidenced by the extremely narrow width of the avoided crossings in Figure 8.6. Avoided crossings between s-modes and i-modes have larger frequency widths, but will be difficult to observe due to the smaller surface displacements and potential perturbations of i-modes relative to f-modes. Finally, avoided crossings between i-modes and f-modes or p-modes have substantial frequency widths, but are unlikely to be observed because of the small number of i-modes (our models have only one i-mode for each value of l). We conclude that it is unlikely to see mode mixing phenomena (in the absence of rotation) in giant planets.

8.4 Rotational Mode Mixing

Thus far, we have considered the adiabatic acoustic-elastic oscillations of a spherically symmetric, non-rotating planet. However, the giant planets in our solar system spin rapidly, and the effects of rotation are quite important. For reference, Saturn’s rotation period of $\approx 10\text{h}39\text{m}$ corresponds to $\Omega_s \approx 0.39 \Omega_{\text{dyn}}$, while the frequencies of the

f-modes are typically $\omega_f \sim l^{1/2} \Omega_{\text{dyn}}$. Previous studies (e.g., Marley 1991 and Vorontsov & Zharkov 1981) have shown that including rotational forces is essential in predicting the frequencies of f-modes of giant planets. Most studies of modes in rotating planets utilize perturbation theory to obtain corrections to the frequencies and eigenfunctions of the modes, computed in powers of the small parameter $\epsilon = \Omega_s/\omega_0$, where ω_0 is the unperturbed mode frequency. To first order in ϵ , the only correction is the addition of the Coriolis force, which splits the $2l + 1$ degenerate eigenfrequencies (corresponding to the $2l + 1$ values of m for a given l) of the unperturbed planetary model. Second order rotational effects include the centrifugal force and the rotationally-induced planetary oblateness. In the absence of a solid core, the f-modes and p-modes are well separated in frequency, and non-degenerate perturbation methods suffice when calculating the influence of rotation.

However, in planetary models with a solid core, the addition of s-modes and t-modes may cause the spectrum of modes to become dense near the f-modes. In this case, the frequency spacing between modes may be smaller than the rotational corrections, and non-degenerate perturbation methods fail. The effect of rotation not only shifts the frequencies of oscillation modes, but it can also induce strong rotational mode mixing. The spheroidal modes acquire toroidal components, and vice versa. Both s-modes and t-modes may mix strongly with the f-mode, and a more accurate treatment of rotational mode mixing becomes necessary. In this paper, we consider only first order rotational effects (i.e., the Coriolis force), and consider uniform planetary rotation.

Mode mixing due to the Coriolis force is governed by some basic selection rules. First, only modes with $m = m'$ will mix. Second, spheroidal modes only couple to other spheroidal modes with $l = l'$, and likewise for toroidal modes. Finally, spheroidal and toroidal modes couple to one another only if $l = l' \pm 1$. Therefore, a spheroidal mode of

angular degree l does not couple directly to spheroidal modes of $l' = l \pm 2$,⁷ although they couple indirectly through intermediary toroidal modes. We do not consider rotational coupling with inertial modes (if they exist in Saturn's interior) because these modes have a maximum frequency of $\omega = 2\Omega_s$ in the rotating frame, and thus have smaller frequencies than any of Saturn's f-modes. Our method for calculating the effect of rotational mode mixing is outlined in Appendix G, here we describe only the basic ideas.

To understand the coupling effect of rotation, consider a simple two mode system. In the absence of rotation, the two eigenmodes have frequency ω_1 and ω_2 , with eigenvectors \mathbf{Z}_1 and \mathbf{Z}_2 . Including the Coriolis correction, we project the rotationally modified eigenmodes onto the original eigenmodes such that $\mathbf{Z} = a_1\mathbf{Z}_1 + a_2\mathbf{Z}_2$ (see Appendix G). The eigensystem (equation G.8) describing the coupled modes is

$$\begin{bmatrix} \bar{\omega}_1 - \omega & C_{12} \\ C_{12}^* & \bar{\omega}_2 - \omega \end{bmatrix} \begin{bmatrix} b_1 \\ b_2 \end{bmatrix} = 0 \quad (8.9)$$

where $b_1 = \omega_1 a_1$, $\bar{\omega}_1 = \omega_1 + C_{11}$, and likewise for mode 2. The Coriolis mixing coefficients $C_{\alpha\alpha'}$ are defined in equation G.20. We wish to solve for the eigenfrequencies ω and eigenvectors \mathbf{b} of this two mode system. Defining $\Delta_{12} = \bar{\omega}_1 - \bar{\omega}_2$, we have

$$\left(\begin{bmatrix} \bar{\omega}_1 + \bar{\omega}_2 - 2\omega & 0 \\ 0 & \bar{\omega}_1 + \bar{\omega}_2 - 2\omega \end{bmatrix} + \begin{bmatrix} \Delta_{12} & 2C_{12} \\ 2C_{12}^* & -\Delta_{12} \end{bmatrix} \right) \begin{bmatrix} b_1 \\ b_2 \end{bmatrix} = 0. \quad (8.10)$$

Then, defining the mode mixing angle

$$\tan 2\theta_{12} = \left| \frac{2C_{12}}{\Delta_{12}} \right|, \quad (8.11)$$

we have

$$\begin{bmatrix} \text{sgn}(\Delta_{12}) \cos(2\theta_{12}) & x_{12} \sin(2\theta_{12}) \\ x_{12}^* \sin(2\theta_{12}) & -\text{sgn}(\Delta_{12}) \cos(2\theta_{12}) \end{bmatrix} \begin{bmatrix} b_1 \\ b_2 \end{bmatrix} = \bar{\omega} \begin{bmatrix} b_1 \\ b_2 \end{bmatrix}, \quad (8.12)$$

⁷Second order rotational effects introduce coupling between modes with $l = l' \pm 2$, but we consider only Coriolis coupling in this work.

with the modified eigenvalue $\bar{\omega} = (2\omega - \bar{\omega}_1 - \bar{\omega}_2) / \sqrt{\Delta_{12}^2 + 4|C_{12}|^2}$, and $C_{12} = x_{12}|C_{12}|$.⁸

Equation 8.12 has eigenvalues $\bar{\omega} = \pm 1$ with corresponding eigenvectors

$$\mathbf{b}_+ = \begin{bmatrix} \cos \theta_{12} \\ x_{12}^* \sin \theta_{12} \end{bmatrix} \quad (8.13)$$

and

$$\mathbf{b}_- = \begin{bmatrix} \sin \theta_{12} \\ -x_{12}^* \cos \theta_{12} \end{bmatrix}. \quad (8.14)$$

The corresponding mode frequencies are

$$\omega = \frac{\bar{\omega}_1 + \bar{\omega}_2}{2} \pm \frac{1}{2} \sqrt{\Delta_{12}^2 + 4|C_{12}|^2}. \quad (8.15)$$

When mode mixing is weak, i.e., $2|C_{12}| \ll |\Delta_{12}|$, the mode frequencies and eigenfunctions are only slightly perturbed. When the mode mixing is strong, i.e., $2|C_{12}| \gg |\Delta_{12}|$, the modes are split in frequency by $\Delta\omega = 2|C_{12}|$. This represents the minimum splitting possible between two rotationally mixed modes.

For strongly mixed modes, the mixing angle θ_{12} increases above zero, approaching $\pi/4$ in the limit $\Delta_{12} \rightarrow 0$. In this limit, the modified mode eigenfunctions are an equal superposition of the original mode eigenfunctions. Hence, if a core mode is strongly mixed with the f-mode, it will obtain f-mode characteristics, including a much larger radial surface displacement $|\xi_\alpha(R)|$ and gravitational potential perturbation $|\delta\Phi_\alpha(R)|$. Modes not nearly degenerate with the f-mode may still have enhanced gravitational potential perturbations, with

$$\delta\Phi_\alpha \simeq \frac{C_{f\alpha}}{\Delta_{f\alpha}} \delta\Phi_f, \quad (8.16)$$

where $C_{f\alpha}$ and $\Delta_{f\alpha}$ are the coupling strength and frequency separation between the f-mode and a nearby mode. For models in which the mode spectrum is dense near the

⁸The value of C_{12} is real for spheroidal-spheroidal and toroidal-toroidal mode coupling (i.e., $x_{12} = \pm 1$ in this case), and is imaginary for spheroidal-toroidal mode coupling (i.e., $x_{12} = \pm i$ in this case).

f-mode, we should expect to see a peak in $\delta\Phi_\alpha$ centered on the f-mode, with a frequency width at its peak of $\sim 2|C_{f\alpha}|$.

8.4.1 Strength of Coriolis Mode Mixing

The importance of mode mixing due to the Coriolis force is determined by the value of $C_{\alpha\alpha'}$. For most modes, the value of $|C_{\alpha\alpha'}|$ is largest when $\alpha = \alpha'$, i.e., due to self-coupling. This self-coupling term is identical to the standard rotationally induced frequency perturbation. For s-modes and t-modes, the self-coupling coefficient has a value of $C_{\alpha\alpha} \approx m\Omega_s/[l(l+1)]$, while its value is typically of order $C_{ff} \approx m\Omega_s/l$ for f-modes in our models. Thus, low degree prograde sectoral ($m = -l$) modes near the f-mode are typically reduced in frequency by a few $\times 10\%$ in Saturn due to the effect of self-coupling.

In contrast to self-coupling, mixing between core modes and envelope modes is typically quite weak in our planetary models. The main reason is simply that s-modes and t-modes have nearly all their inertia in the core, while f-modes and p-modes have nearly all their inertia in the envelope, and so the mode eigenfunctions do not have a large overlap in any region of the planet. We find typical values $|C_{\alpha\alpha'}| \lesssim 10^{-3}|m|\Omega_s$ for mixing between core modes and f-modes of similar frequency in our planetary models. This value decreases with decreasing shear modulus μ because of the increasingly oscillatory wave functions of the s-modes and t-modes. The value of $|C_{\alpha\alpha'}|$ also decreases with increasing l because f-modes of larger angular degree are confined closer to the planetary surface and have less inertia in the core. Therefore, the detuning Δ_{12} between a core mode and an f-mode has to be very small for appreciable mixing to occur.

We also note that mixing between s-modes and t-modes can be large, with values

of $|C_{\alpha\alpha'}|$ rising as large as typical values for self-coupling. These large values of $|C_{\alpha\alpha'}|$ occur for s-modes of angular degree l and t-modes of angular degree $l \pm 1$ with the same number of nodes in their radial eigenfunctions. These mode pairs have similar frequencies in non-rotating models, however, their frequencies must be split by at least $\sim 2|C_{\alpha\alpha'}|$ in rotating planets. Such strong mixing implies that each low-frequency core mode is a strong superposition of both spheroidal and toroidal components in a rapidly rotating planet.

8.4.2 Two and Three-Mode Rotational Mixing

Figure 8.7 shows a plot of the results of mixing between two modes as a function of the spin frequency Ω_s . To make this figure, we consider mixing between the $l = 3, m = -3$ f-mode (Mode 1) and the $l = 4, m = -3$ t-mode (Mode 2) depicted in Figure 8.3. At most spin frequencies, the modes are well-separated, and the mixing angle is small because of the small value of $C_{f,\alpha}$. However, near a particular spin frequency the modes become nearly degenerate and mix strongly with one another, somewhat analogous to the mixing described in Section 8.3.1.

Three-mode mixing is more complex than two-mode mixing, and the general solution for a three mode eigensystem similar to equation 8.9 is sufficiently complicated that we do not attempt to analyze it here. Instead, we wish to understand the effect of rotational three-mode mixing between two core modes and an f-mode. For instance, there are many modes that do not couple directly to f-modes, but are coupled through an intermediary mode. One example is an $l = 5, m = -3$ s-mode mixed with an $l = 4, m = -3$ t-mode, which in turn is mixed with the $l = 3, m = -3$ f-mode. We detail a solution of such a three-mode system in Appendix I. The main result is that the $l = 5$ s-mode

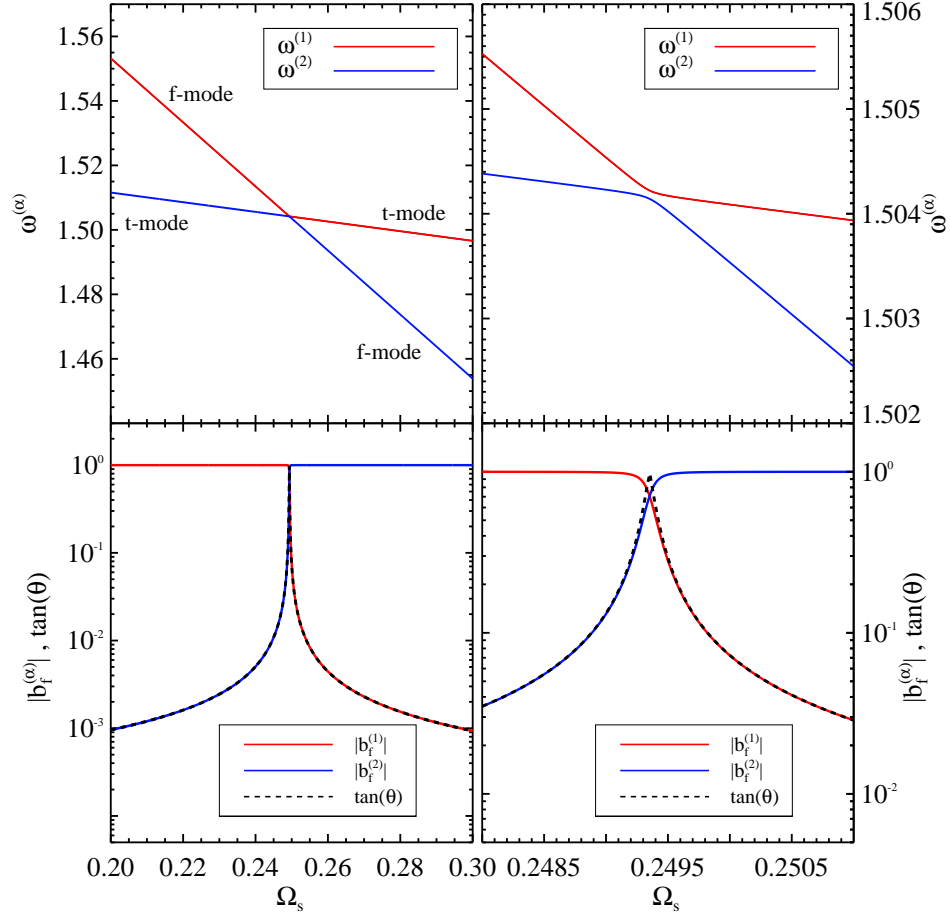


Figure 8.7: Top: the frequencies $\omega^{(\alpha)}$ of the rotationally mixed $l = 3$ f-mode and an $l = 4$ t-mode from our model from Figure 8.1, as a function of Saturn's spin frequency Ω_s (in units of $\sqrt{GM/R^3}$). Bottom: the projections $b_f^{(\alpha)}$ of each rotationally mixed mode onto the f-mode. We have also plotted the mode mixing angle $\tan(\theta)$. The modes have an avoided crossing at $\Omega_s \simeq 0.25$, where they are maximally mixed. The “f”-mode corresponds to ω_1 for $\Omega_s \lesssim 0.25$, and corresponds to ω_2 for $\Omega_s \gtrsim 0.25$. For clarity, the modes have been normalized via $\sum_{\beta} |b_{\beta}^{(\alpha)}|^2 = 1$.

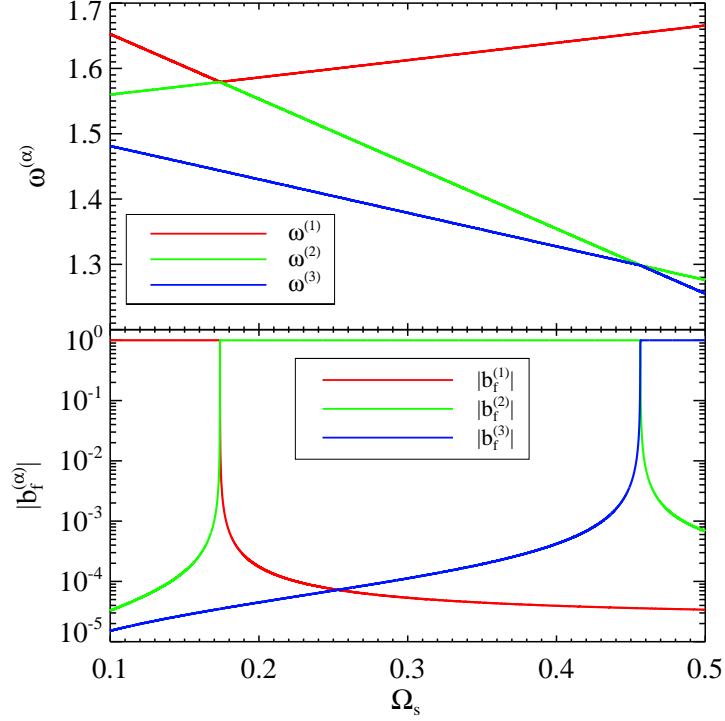


Figure 8.8: Same as Figure 8.7, but for a system of three mixed modes. Away from avoided crossings, the “f”-mode corresponds to the line with the steepest slope. The “s”-mode and “t”-mode are strongly mixed at all values of Ω_s , but only mix significantly with the “f”-mode near the avoided crossings.

can strongly mix with the f-mode even though it does not couple to it directly. Thus, we expect modes nearly degenerate with an f-mode will obtain substantial gravitational potential perturbations, even if they are not directly coupled with the f-mode.

We also calculate the exact numerical solution to the three-mode system described above, and we plot the results in Figure 8.8. As expected, both modes undergo avoided crossings with the f-mode in which they mix strongly with it. We also note that the strong mode mixing between the t-mode and s-mode causes their frequencies to diverge away from one another as the spin frequency is increased.⁹ This mode “repulsion”

⁹In a real system, these modes will also mix strongly with other s-modes and t-modes, which will mitigate this frequency divergence. Hence, it is important to extend mode mixing calculations to large values of l in order to capture the realistic mixing behavior.

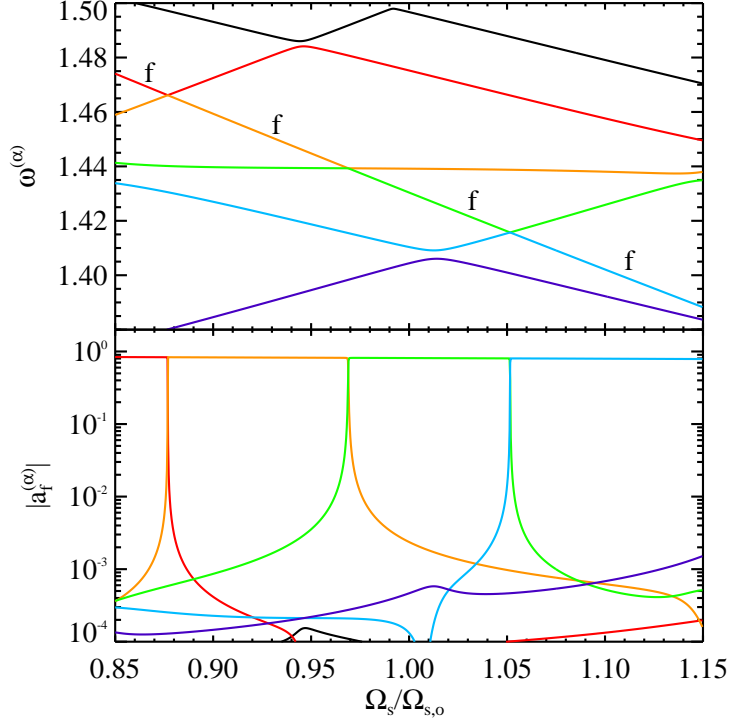


Figure 8.9: Same as Figure 8.8, but for a system containing 112 $m = -3$ modes (only the six modes with frequency nearest the f-mode are shown). Here we plot the projection onto the f-mode, $a_f^{(\alpha)} = b_f^{(\alpha)} / \omega^{(\alpha)}$, with the modes normalized via equation H.4. The spin frequency Ω_s is plotted in units of Saturn’s spin frequency. We incorporate modes up to $l = 18$, and have included all modes with frequency in the vicinity of the $l = 3$ f-mode. The “f”-mode is labeled away from avoided crossings.

affects the location of avoided crossings with the f-mode, causing them to occur at a spin frequency different than one would expect from a two mode analysis. Finally, note that even though the t-mode and s-mode are strongly mixed, only the mode nearly degenerate with the f-mode is affected by an avoided crossing with it. Therefore, modes that differ substantially in frequency from an f-mode will not strongly mix with it.

8.4.3 Multi-Mode Rotational Mixing

We now endeavor to understand the effects of mode mixing in more realistic systems, which may contain hundreds of coupled modes. To this end, we calculate the solution to equation G.19 for a system containing 112 modes from the planetary model in Figure 8.1 with $\mu = 1.6\text{GPa}$. We have included all the modes with frequency comparable to the $l = 3$ f-mode, which requires the inclusion of modes up to $l = 18$. The results, plotted as a function of spin frequency, are shown in Figure 8.9. The qualitative features of the mode mixing are similar to the two and three-mode mixing shown in Figures 8.7 and 8.8. Although many modes are capable of mixing with the f-mode, the small coupling coefficients $C_{\alpha\alpha'}$ ensure that the widths of the avoided crossings are small compared to the spacing between modes. We therefore determine that, for the toy planetary models considered in this paper, the chances of finding a core mode strongly mixed with the f-mode are very small.

8.5 Effect of Oscillation Modes on the Rings

Given a rotationally modified mode eigenfunction, we may calculate the gravitational potential perturbation it produces exterior to the planet. For a mode composed of a single spherical harmonic of angular degree l and azimuthal number m , the potential produced outside the planet is

$$\delta\Phi_\alpha(\mathbf{r}, t) = A_\alpha \delta\Phi_\alpha(R) \left(\frac{R}{r}\right)^{l+1} Y_{lm}(\theta, \phi) e^{i\sigma_\alpha t}, \quad (8.17)$$

where $\delta\Phi_\alpha(R)$ is the potential perturbation at the surface of the planet, calculated from our normalized mode eigenfunctions (equation 8.5), A_α is the (unspecified) amplitude

of the mode, and σ_α is the mode frequency in the inertial frame,

$$\sigma_\alpha = \omega_\alpha - m\Omega_s. \quad (8.18)$$

This compact expression is modified in the presence of rotational mixing because each mode acquires contributions from multiple angular degrees l (although m remains a good quantum number). The potential produced by a rotationally modified mode is then

$$\delta\Phi_\alpha(\mathbf{r}, t) = A_\alpha e^{i\sigma_\alpha t} \sum_\beta a_\beta^{(\alpha)} \delta\Phi_\beta(R) \left(\frac{R}{r}\right)^{l+1} Y_{lm}(\theta, \phi), \quad (8.19)$$

where $a_\beta^{(\alpha)}$ is the projection of the rotationally modified mode onto an original mode β (determined via the method in Appendix G), and the sum is over all original modes that contribute to the modified mode eigenfunction. Each rotationally modified mode will contain contributions from several types of modes (f-modes, t-modes, etc.) of many different values of l .

We are interested in the value of the potential $\delta\Phi_\alpha$ in the plane of the rings ($\theta = \pi/2$) at the location of the outer Lindblad resonance. The resonance occurs where the forcing frequency experienced by a particle is equal to the local epicyclic frequency κ , i.e., where

$$m(\Omega - \Omega_p) = \kappa, \quad (8.20)$$

Ω is the local orbital frequency, and $\Omega_p = -\sigma_\alpha/m$ is the mode pattern frequency. The orbital and epicyclic frequencies are not exactly equal because of the oblateness of Saturn, which causes the two frequencies to differ by a factor $\sim 10^{-2}$ in the C-ring. Here we set them equal because we are concerned primarily with the strength of the potential (but see Appendix J for a more accurate description). Then the resonant location is

$$r_L \simeq \left[\frac{(1-m)^2 GM}{\sigma_\alpha^2} \right]^{1/3}, \quad (8.21)$$

and the gravitational potential at the resonant location in the rings is

$$\delta\Phi_\alpha(r_L) \simeq A_\alpha e^{i\sigma_\alpha t + m\phi} \sum_\beta a_\beta^{(\alpha)} Y_{lm}(\pi/2, 0) \left[\frac{(1-m)^2 GM}{\sigma_\alpha^2} \frac{GM}{R^3} \right]^{-(l+1)/3} \delta\Phi_\beta(R). \quad (8.22)$$

In equation 8.22, we have used the fact that only modes of equal m couple to one another. The effective potential driving waves at the Lindblad resonance is (Goldreich & Tremaine 1979),

$$\begin{aligned}\Psi_\alpha(r_L) &= \left[\frac{d}{d \ln r} + \frac{2m\Omega}{\sigma_\alpha + m\Omega} \right] \delta\Phi_\alpha(r_L) \\ &\simeq A_\alpha e^{i\sigma_\alpha t + m\phi} \sum_\beta a_\beta^{(\alpha)} W_\beta \delta\Phi_\beta(R)\end{aligned}\tag{8.23}$$

with

$$W_\beta = (2m - l - 1) Y_{lm}(\pi/2, 0) \left[\frac{(1 - m)^2}{\sigma_\alpha^2} \frac{GM}{R^3} \right]^{-(l+1)/3}.\tag{8.24}$$

The surface density variation and associated optical depth variation produced near a Lindblad resonance is calculated in Appendix J.

The mode amplitudes A_α are unknown. To estimate them, we assume the most prominent $|m| = 3$ wave (labeled W82.06 in Table 1) is produced by an unmixed f-mode with frequency ω_3 , and we calculate the mode amplitude A_3 required to generate the observed optical depth variation in the rings (see Appendix J). We then assume the modes follow energy equipartition, such that their amplitudes are given by $\omega_\alpha^2 |A_\alpha|^2 = \omega_3^2 |A_3|^2$.¹⁰ The typical mode amplitudes required to produce the observed fluctuations are of order $|A| \sim 10^{-9}$, resulting in radial surface displacements of order $\xi_r(R) \sim 30\text{cm}$ for f-modes. These amplitudes are similar to those claimed to be observed by Gaulme et al. (2011) in Jupiter and approximately what we might expect if the modes are stochastically excited via convective turbulence, analogous to the excitation of solar p-modes (see discussion in Marley & Porco 1993). However, the detailed dynamics of mode excitation are beyond the scope of this paper.

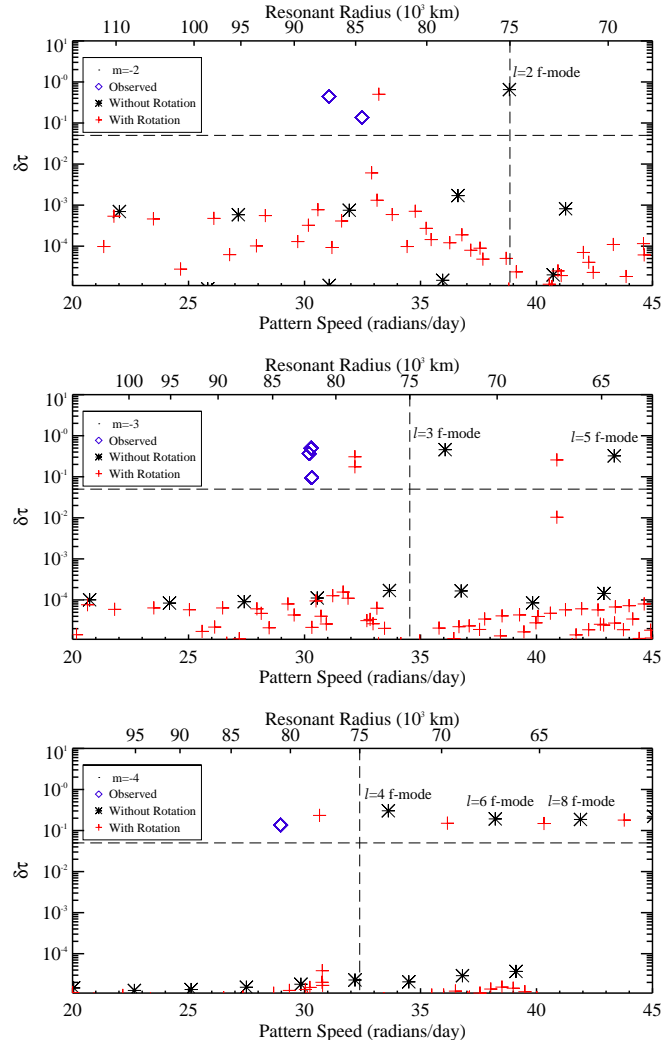


Figure 8.10: The predicted pattern frequencies $\sigma_\alpha/|m|$ and optical depth variations produced by waves at Lindblad resonances with oscillation modes of our Saturn models for $m = -2$ modes (top), $m = -3$ modes (middle), and $m = -4$ modes (bottom). We have plotted modes of non-rotating models (black asterisks), models rotating uniformly at Saturn's observed rotation frequency (red pluses), and the observed waves (blue diamonds) from HN13. These plots are made for the Saturn model in Figure 8.1 with $\mu = 1.6\text{GPa}$. The spin frequency has been slightly tuned ($\Omega_s/\Omega_{s,o} = 0.97$) to produce two strongly mixed modes near the f-mode in the middle panel. The vertical dashed line indicates the approximate inner edge of the C-ring, while the horizontal dashed line is an approximate minimum observable optical depth variation. Therefore, we should only expect to observe waves in the top-left corner of the figure. In the non-rotating models, the f-modes are the black asterisks in the top right, while the row of asterisks below them are the $l = |m|$ s-modes.

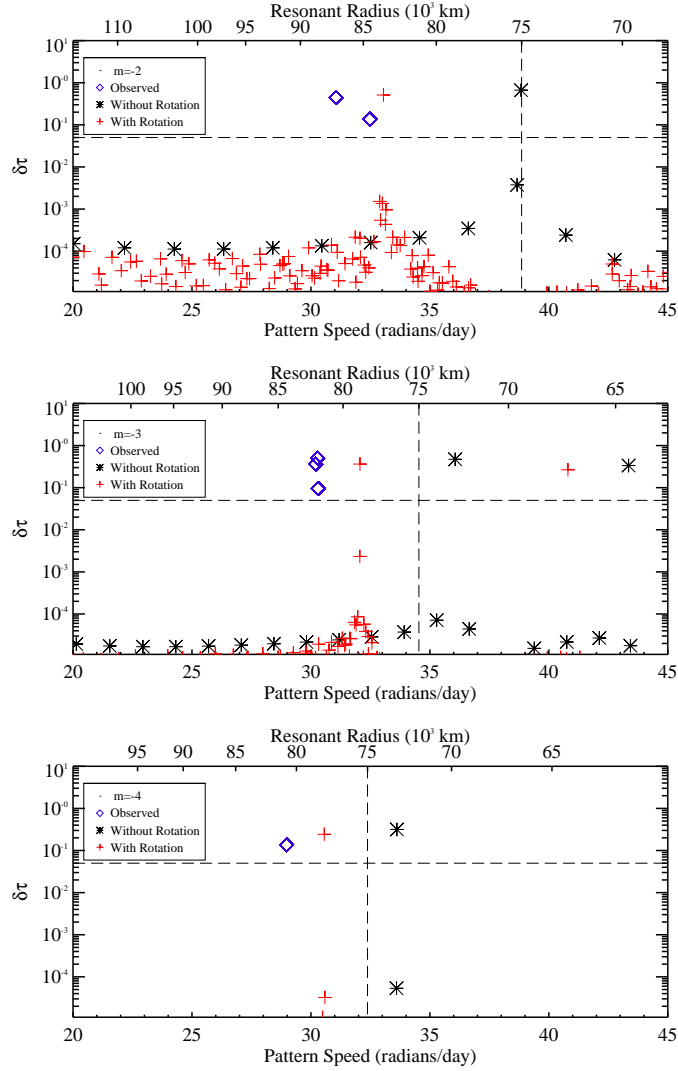


Figure 8.11: Same as Figure 8.10 but for a Saturn model with $\mu = 0.32\text{GPa}$.

8.5.1 Comparison with Observations

Figures 8.10-8.12 show the pattern frequencies Ω_p (and associated Lindblad radii r_L , calculated via equation J.3) and optical depth variations $\delta\tau$ (see equation J.6) produced by modes in our planetary models. We have also plotted the pattern frequencies, and optical depth variations of the observed waves in the C-ring as tabulated by HN13.

¹⁰Although energy equipartition may be unlikely to occur, it is a good place to begin since the modes of interest have similar frequencies ω_α and angular degrees l .

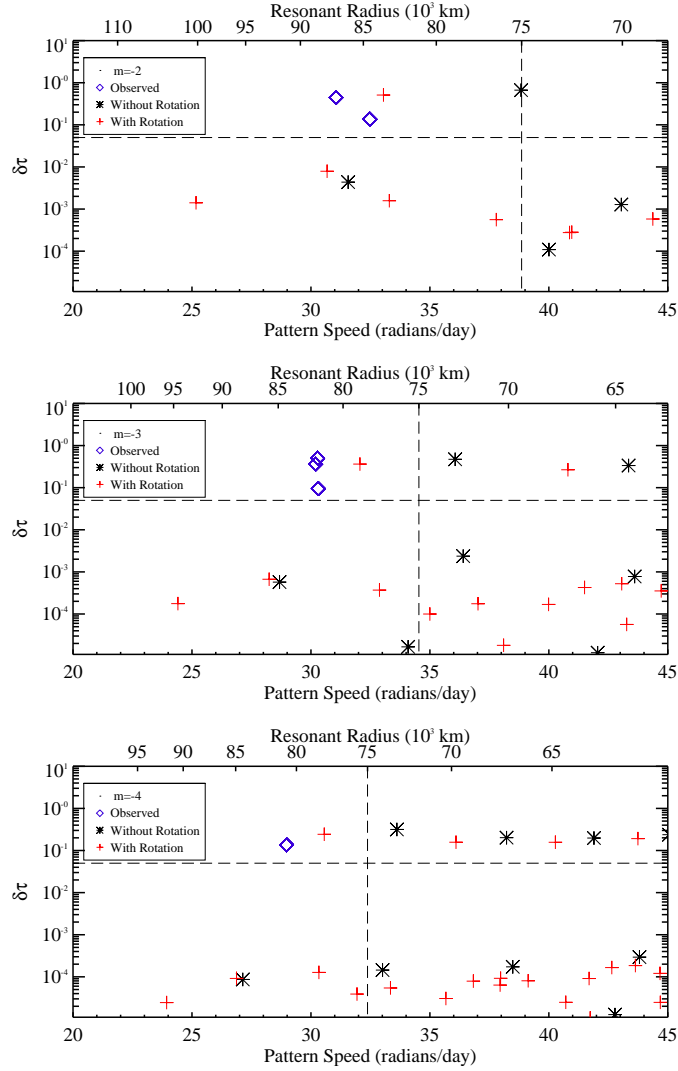


Figure 8.12: Same as Figure 8.10 but for a Saturn model $\mu = 8\text{GPa}$.

We begin by examining the mode pattern frequencies. In each model, the pattern speed of the $l = -m$ f-mode in the non-rotating models is consistently too large. Adding the Coriolis force lowers the pattern frequency of the modified “f”-mode (i.e., the lowest frequency mode with a large value of $\delta\Phi_\alpha$), moving it closer to the observed pattern frequencies, although the predicted frequencies remain too high. Adding second-order rotational effects will lower the predicted frequencies further, likely making them more consistent with observations. Moreover, with our simple planetary model, we should not

expect exact agreement. Nonetheless, the close proximity of the predicted and observed pattern frequencies of the “f”-modes is strong evidence that the observed waves are generated by Saturn’s “f”-modes. This is one of the key findings of this paper, and is consistent with the results of Marley & Porco (1993).

We can use Figures 8.10-8.12 to understand the qualitative effects of rotationally-induced mode mixing. In the absence of rotation, the spectrum of low frequency modes with significant gravitational perturbations is sparse, and is due almost entirely to f-modes. However, as the rotation rate increases, core modes with frequencies comparable to the f-mode obtain a potential perturbation

$$\delta\Phi_\alpha \approx \frac{|C_{f\alpha}|}{\omega_f - \omega_\alpha} \delta\Phi_f, \quad (8.25)$$

where ω_f and ω_α are the rotationally modified f-mode and core mode frequency, and $|C_{f\alpha}|$ is their coupling coefficient (equation G.20). Consequently, many modes that had miniscule potential perturbations in the non-rotating model (and thus fall below the plotted range of Figures 8.10-8.12) obtain larger potential perturbations in the presence of rotation (although typically still orders of magnitude smaller than the f-mode), causing the mode frequency spectrum for rotating models to appear much denser in Figures 8.10-8.12.

A mode nearly degenerate with the f-mode will obtain a potential perturbation $\delta\Phi_\alpha \simeq \delta\Phi_f / \sqrt{2}$, although in this case both modes are really hybrid f-modes. In this case, the modes are split in frequency by $\approx 2|C_{f\alpha}|$. Our results suggest that such exact degeneracies are rare in our models, as described in Section 8.4.3. To achieve significant mixing, the frequency separation between a core mode and f-mode, $|\Delta_{f\alpha}|$, must be of order $|C_{f\alpha}|$. However, in our models, the typical frequency separations $|\Delta_{\alpha\alpha'}|$ between core modes are much larger than typical values of $|C_{f\alpha}|$. It is thus unlikely that a core mode will fall close enough in frequency to the f-mode to strongly mix with it. Such

degeneracies are possible (see e.g., the middle panel of Figure 8.10), but usually require fine-tuning to obtain. Since frequency splitting is observed by HN13 for both $m = -2$ and $m = -3$ modes, we conclude that it is unlikely to be produced solely by Coriolis coupling between core modes and f-modes.

Finally, we examine the influence of the value of the shear modulus in the core. If Saturn’s core contains a shear modulus $\mu \gtrsim 8\text{GPa}$ (Figure 8.12), the core shear modes have frequencies that are typically larger than the f-mode. Moreover, the core mode spectrum is sparse, making it very unlikely for core modes to mix strongly with the f-mode. Therefore, if $\mu \gtrsim 8\text{GPa}$, the observed waves in Saturn’s rings cannot be generated due to the addition of elastic core oscillation modes for reasonable Saturnian models.

If the shear modulus is $\mu \lesssim 1.6\text{GPa}$ (Figure 8.10), there may exist many oscillation modes with frequencies in the vicinity of the f-mode, allowing for the possibility of strong mixing with it. However, a smaller shear modulus also decreases the coupling coefficients, requiring a higher degree of degeneracy (smaller $|\Delta_{f\alpha}|$) for efficient mode mixing to occur. Therefore, including only Coriolis mode mixing, we cannot identify a value of the shear modulus that is likely to produce a mode spectrum similar to that observed in Saturn’s rings.

8.6 Discussion and Conclusions

We have examined the influence of a solid core on the oscillation mode spectrum of giant planets. In our toy planetary models, the rigidity of the core has almost no effect on the frequencies of f-modes or low order p-modes (for the range of μ considered, they change by less than 0.2 percent). However, the addition of a solid core adds two new branches of oscillation modes: the spheroidal and toroidal core modes whose restoring

force is the elastic shear force of the solid material. The frequency spectrum of these modes is dependent primarily on the core radius R_c and shear modulus μ , with larger and less rigid (small μ) cores supporting dense spectra of low frequency shear modes. In the absence of rotation, these modes are almost completely confined to the core, and they produce negligible displacements or gravitational perturbations at the surface of the planet.

We have also examined the influence of the Coriolis force on the mode frequencies and eigenfunctions. In addition to decreasing the oscillation mode frequencies of prograde modes, the Coriolis force induces mixing between oscillation modes of equal azimuthal number m . Spheroidal modes (f-modes, s-modes, i-modes, and p-modes) of angular degree l mix with one another, as do toroidal modes. Furthermore, spheroidal modes of angular degree l mix with toroidal modes of angular degree $l \pm 1$, allowing for chains of mode mixing extending to arbitrary values of l . Mode mixing is strongest when the rotationally modified frequencies of two modes are nearly degenerate with one another. If value of the core shear modulus μ is small ($\mu \lesssim 3\text{GPa}$) but finite, the spectrum of core oscillation modes is dense near the f-mode. Therefore, one or multiple core modes may be nearly degenerate with the f-mode and mix strongly with it. These strongly mixed modes would manifest themselves as hybrid “f”-modes, with nearly equal frequencies and similar mode eigenfunctions.

The main objective of this investigation is to compare our planetary oscillation calculations with the results of HN13, who have measured the pattern numbers and frequencies of waves in Saturn’s rings that appear to be excited by Saturn’s oscillation modes. As speculated by HN13 and originally proposed by Marley & Porco (1993), we find the pattern frequencies and azimuthal numbers associated with individual waves in Saturn’s rings are consistent with being excited by Saturn’s prograde sectoral ($l = -m$)

f-modes. It is possible that with more realistic planetary models and including higher order spin affects, the measured frequencies of these modes can be used to constrain Saturn's interior structure.

HN13's observations of multiple wave trains (finely spaced in frequency but with identical m) seem to indicate the existence of multiple oscillation modes with frequencies near the frequencies of Saturn's f-modes. We have attempted to explain this observation through the rotational mixing between shear modes in Saturn's core and f-modes in Saturn's fluid envelope. This idea may be able to explain several features of HN13's observations, listed below.

1. Our theory would explain why the waves observed by HN13 all lie close to predicted locations of resonances with Saturn's f-modes. We have shown that only core modes very near in frequency to the f-mode will mix appreciably with it. Therefore, only these modes will obtain large enough gravitational potential perturbations to produce observable disturbances in Saturn's rings, and hence only modes with frequencies near the f-mode can be observed.

2. We can explain the relative magnitude of observed frequency splittings (largest frequency splittings for $|m| = 2$ modes, finer frequency splittings for $|m| = 3$ modes, and no observed frequency splitting for the $|m| = 4$ mode). Compared to higher degree modes, the $l = 2$, $|m| = 2$ f-mode penetrates deeper into the planet. It has more inertia in the core, and thus mixes more strongly with core modes, as evidenced by its larger rotational coupling coefficients $|C_{f\alpha}|$ with core modes. Therefore we should expect modes that mix strongly with the $l = 2$ f-mode to have larger frequency separations from it than the modes that mix with the $l = 3$, $|m| = 3$ f-mode. The $l = 4$, $|m| = 4$ mode may exhibit no splitting because it mixes so weakly with core modes that no modes are close enough in frequency to mix strongly with it.

3. Our theory can account for the unequal amplitudes of different waves. HN13's observations show that the finely spaced waves in Saturn's rings have very different optical depth variations, implying that they are excited by modes with different amplitudes and/or gravitational potential perturbations. According to our theory, modes nearly degenerate with the f-mode may obtain a potential perturbations comparable to (but less than) that of the unperturbed f-mode, with the precise value determined by the rotational coupling coefficient and degree of frequency detuning.

However, our theory cannot yet explain all the observations, and some remaining concerns are as follows:

1. Our calculations indicate that f-modes mix inefficiently with core shear modes, necessitating a very small frequency de-tuning for appreciable mixing to occur. Such small frequency de-tunings are unlikely to occur unless the model is fine-tuned to produce a mode nearly degenerate with an f-mode. Even with a finely tuned model, it is highly unlikely to simultaneously achieve the observed $|m| = 2$ and $|m| = 3$ frequency splittings. However, it remains possible that the inclusion of higher order rotational and non-spherical mixing terms may create larger mixing coefficients and alleviate this concern.

2. A very small value of the shear modulus ($\mu \lesssim 3$ GPa) is required for our mechanism to operate. In comparison, the shear modulus of Earth's core is $\mu \approx 100$ GPa. (Laio et al. 2000), and the pressure in Saturn's core is of order $P \approx 2$ TPa. Although such a small value of the shear modulus may seem unlikely, it may arise from the high pressure superionic phase of ice (see references in Section 8.2.1) likely to exist in Saturn's core.

3. We have essentially ignored the effects of inertial modes and gravity modes, and have only briefly considered interface modes. We have also ignored non-adiabatic and

anelastic damping effects. These effects should be more thoroughly quantified in the future.

APPENDIX A

CALCULATION WITH MASSIVE STAR MODEL

To test the accuracy of our numerical calculations and especially the importance of self-consistency in real stellar models, we compute the tidal response of several toy models. The first toy model we employ is shown in Figure A.1 and is meant to mimic a massive early-type star. The model contains an inner convection zone surrounded by a thick radiative envelope. The convection zone extends to $r = 0.25R$, beyond which the value of N^2 rises linearly to $N^2 \approx 8GM/R^3$. Dynamical tides in such massive stars have been studied by Zahn (1975, 1977) and Goldreich & Nicholson (1989), who showed that the dominant effect arises from the gravity waves launched at the core-envelope boundary, which then propagate outwards and eventually dissipate near the stellar surface. Zahn (1975) derived an analytic solution for the wave amplitude and the corresponding tidal torque. Although our model does not contain some of the details exhibited by realistic massive star models, it does capture the most important features. We can compare our result with Zahn's to calibrate our numerical method and to assess the degree of self-consistency required to produce reliable results for the tidal torque.

Figure A.2 shows an example of our numerical results for the dynamical tides generated in a massive star by a companion, for a given tidal frequency $\omega = 2\Omega = 2.3 \times 10^{-2}$ (in units where $G = M = R$). We see that gravity waves are excited at the base of the radiative zone where N^2 begins to rise above zero. A net energy flux $\dot{E} = \Omega \dot{J}_z = \Omega(GM'^2R^5/a^6)F(\omega)$ flows outwards toward the stellar surface. Figure A.3 shows our numerical result of the dimensionless function $F(\omega) \equiv \dot{J}_z/T_o$ [see equation (3.42)], evaluated at the outer boundary, as a function of the tidal frequency ω . The result can be fitted by $F(\omega) \propto \omega^{8/3}$, in agreement with the scaling found by Zahn (1975).

The power-law scaling of the energy flux can be derived using the method of Goldreich-

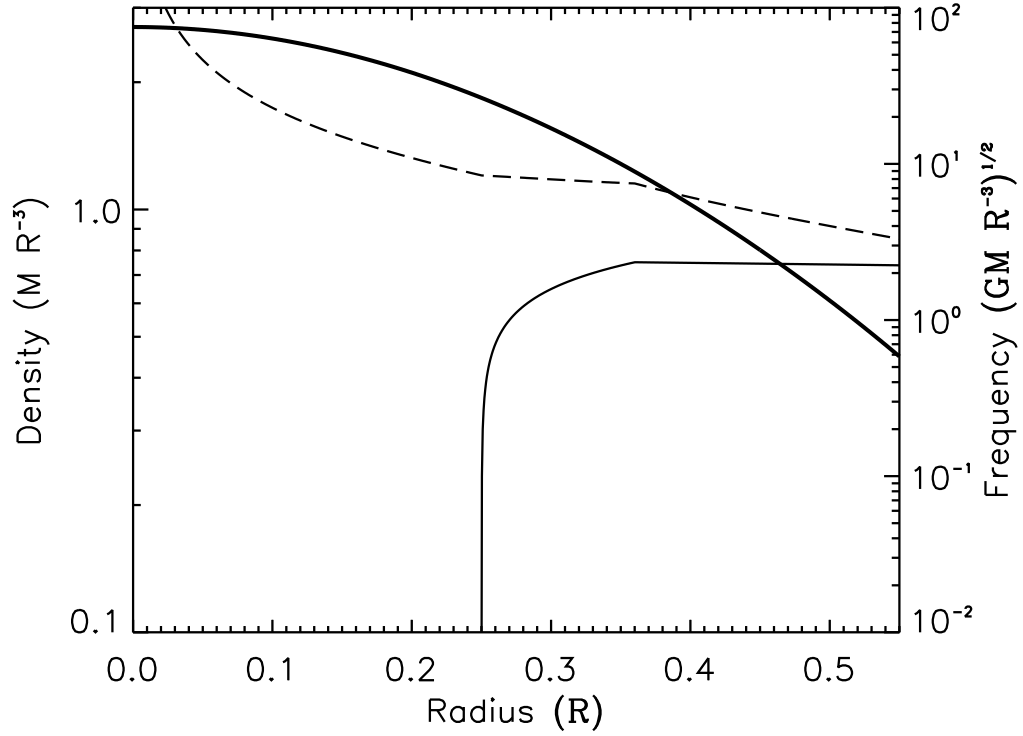


Figure A.1: The square of the Brünt-Vaisälä (thin solid line) and Lamb (dashed line) frequencies (for $l = 2$), in units of GM/R^3 , as a function of the normalized radius in a simple massive star model. Also plotted is the stellar density profile (thick solid line) in units of M/R^3 . The model has an inner convection zone extending to $r = 0.25R$. The stellar properties are only plotted out to $r = 0.6R$, where an outgoing wave boundary condition is adopted in our calculation of the tidal excitation.

ich & Nicholson (1989). Assume $|\xi_{\perp}^{\text{dyn}}| \approx \xi_{\perp}^{\text{eq}}$ at $r = r_{c+}$, which is located one wavelength above the convective boundary ($r = r_c$). From the dispersion relation (3.27), we find that the Brünt-Vaisälä frequency at r_{c+} is given by (for $l = 2$)

$$N(r_{c+}) \approx \left(\frac{dN^2}{dr} r_c \right)^{1/3} \omega^{1/3}. \quad (\text{A.1})$$

Using $\xi_{\perp}^{\text{eq}} \simeq -[1/(6r)](Ur^2/g)' \simeq -U/(2g)$, we evaluate equation (3.41) to find

$$\dot{E} \approx \frac{3\pi\sqrt{6}}{10} \left(\frac{M'}{M_t} \right)^2 \frac{\rho r^7 \Omega^5 \omega^{8/3}}{g^2 (dN^2/d \ln r)^{1/3}}. \quad (\text{A.2})$$

where $M_t = M + M'$, and all the quantities (ρ , r , g , and dN^2/dr) are evaluated at $r = r_{c+} \simeq r_c$. The scaling of this estimate nearly agrees Goldreich & Nicholson (1989), who

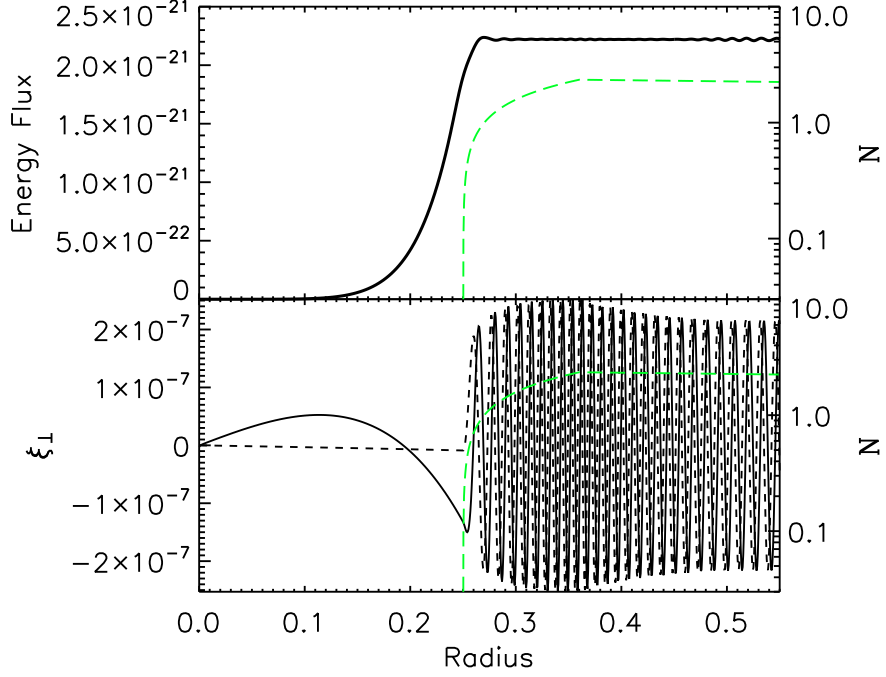


Figure A.2: Dynamical tide in a massive star (based on the toy model depicted in Figure A.1) driven by a companion of mass $M' = M$, with the tidal frequency $\omega = 2.3 \times 10^{-2}$. Top: The energy flux (dark solid line) $\dot{E} = \Omega \dot{J}_z$ as a function of radius, with \dot{J}_z calculated from equation (3.39). All values are plotted in units of $G = M = R = 1$. Bottom: The real part of ξ_{\perp}^{dyn} (dark solid line) and imaginary part of ξ_{\perp}^{dyn} (dashed line) as a function of stellar radius. The value of N has been plotted in green (light solid line) in both panels. In this model, the energy flux rises to its final value just outside of the convective zone, showing that the wave is excited at this location.

obtained $\dot{E}_r \propto \Omega^4 \omega^{11/3}$, where \dot{E}_r is the energy flux carried by outgoing gravity waves in the rotating frame of the star, not the total energy transfer rate from the orbit. These two energy transfer rates are related by $\dot{E} = \Omega \dot{J}_z = 2\Omega \dot{E}_r / \omega$. Goldreich & Nicholson (1989) estimates $dN^2/dr \approx g/H \approx g/r$, and with $g \approx 4\pi G \bar{\rho} r/3$ ($\bar{\rho}$ is the mean density interior to r_c), equation (A.2) becomes

$$\dot{E} \approx 0.08 \left(\frac{M'}{M_t} \right)^2 \frac{\rho r^5 \Omega^5 \omega^{8/3}}{(G \bar{\rho})^{7/3}}. \quad (\text{A.3})$$

The value of $F(\omega)$ based on equation (A.2) is plotted in Figure A.3. Compared to our numerical results, we see that equation (A.2) overestimates $F(\omega)$ by an order of magnitude [by contrast, equation (A.3) would overestimate $F(\omega)$ by more, since for our toy

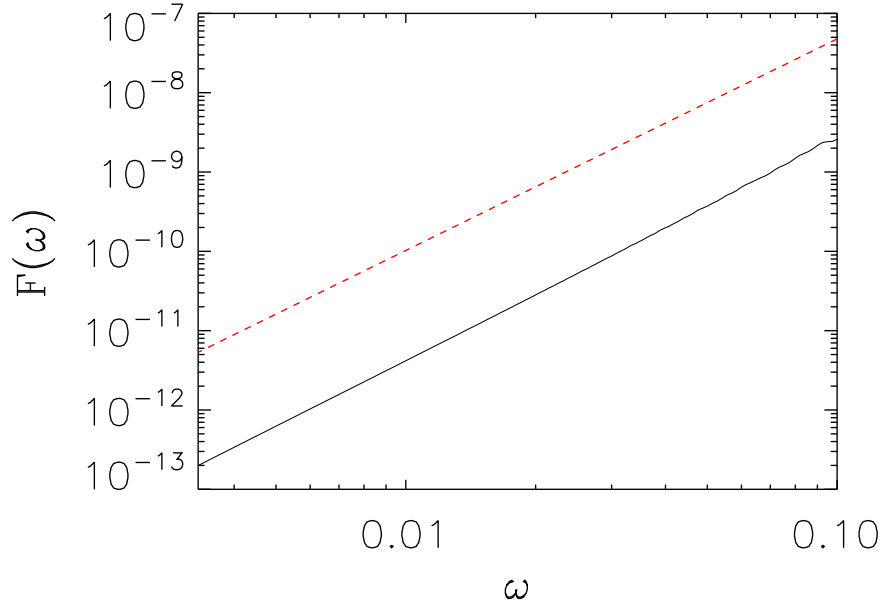


Figure A.3: The dimensionless tidal torque $F(\omega) = \dot{J}_z/T_o$ [see equation (3.42)] carried by the outgoing gravity wave as a function of the tidal frequency ω (solid line). The analytical estimate from equation (A.2) is also plotted (dashed line). The frequency is in units of $G = M = R = 1$. The small wiggles at high frequencies are likely due to the slight inaccuracy of our implementation of the outer boundary condition due to the neglected terms which become non-negligible at higher tidal frequencies.

stellar model $dN^2/d\ln r \gg g/r$]. From our numerical results, we find that the dynamical part of the tide only reaches an amplitude of $\xi_{\perp}^{\text{dyn}} \approx \xi_{\perp}^{\text{eq}}/4$. If we had used this wave amplitude in our estimate, equation (A.2) would be a factor of 16 smaller and would provide an accurate approximation to $F(\omega)$ at all frequencies considered.

APPENDIX B

CALCULATION OF EQUILIBRIUM TIDE

In this appendix we present our improved method for isolating the dynamical and equilibrium components of the tidal perturbation. Using the Cowling approximation, the oscillation equations are

$$\frac{1}{r^2}(r^2\xi_r)' - \frac{g}{c_s^2}\xi_r + \frac{1}{\rho c_s^2}\left(1 - \frac{L_l^2}{\omega^2}\right)\delta P - \frac{l(l+1)U}{\omega^2 r^2} = 0, \quad (\text{B.1})$$

and

$$\delta P' + \frac{g}{c_s^2}\delta P + \rho(N^2 - \omega^2)\xi_r + \rho U' = 0, \quad (\text{B.2})$$

where U is the tidal potential produced by the companion, the $'$ denotes d/dr , and g is the gravitational acceleration. The other perturbation variables are related to δP and ξ_r by

$$\xi_\perp = \frac{1}{r\omega^2}\left(\frac{\delta P}{\rho} + U\right), \quad (\text{B.3})$$

$$\delta\rho = \frac{1}{c_s^2}\delta P + \frac{\rho N^2}{g}\xi_r. \quad (\text{B.4})$$

Using equation (B.3), equations (B.1) and (B.2) may be rewritten

$$\frac{1}{r^2}(r^2\xi_r)' - \frac{g}{c_s^2}\xi_r + \left(\frac{r\omega^2}{c_s^2} - \frac{l(l+1)}{r}\right)\xi_\perp - \frac{U}{c_s^2} = 0, \quad (\text{B.5})$$

$$\xi_\perp' + \left(\frac{1}{r} - \frac{N^2}{g}\right)\xi_\perp + \frac{N^2 - \omega^2}{r\omega^2}\xi_r + \frac{N^2}{rg\omega^2}U = 0. \quad (\text{B.6})$$

The zeroth order solution to the equilibrium tide can be found by taking the limit $\omega = 0$ in equations (B.5) and (B.6), yielding (see also Goldreich & Nicholson 1979)

$$\xi_r^{\text{eq},0} = -U/g \quad (\text{B.7})$$

and

$$\xi_\perp^{\text{eq},0} = -(Ur^2/g)'/[l(l+1)r]. \quad (\text{B.8})$$

Defining $\xi_r = \xi_r^{\text{eq},0} + \bar{\xi}_r$ and likewise for ξ_\perp , we substitute into equations (B.5) and (B.6) to find

$$\frac{1}{r^2}(r^2\bar{\xi}_r)' - \frac{g}{c_s^2}\bar{\xi}_r + \left(\frac{r\omega^2}{c_s^2} - \frac{l(l+1)}{r}\right)\bar{\xi}_\perp + \frac{r\omega^2}{c_s^2}\xi_\perp^{\text{eq},0} = 0, \quad (\text{B.9})$$

and

$$\bar{\xi}_\perp' + \left(\frac{1}{r} - \frac{N^2}{g}\right)\bar{\xi}_\perp + \frac{N^2 - \omega^2}{r\omega^2}\bar{\xi}_r + \left[\xi_\perp^{\text{eq},0'} + \left(\frac{1}{r} - \frac{N^2}{g}\right)\xi_\perp^{\text{eq},0} - \frac{1}{r}\xi_r^{\text{eq},0}\right]. \quad (\text{B.10})$$

To find the first order term of the equilibrium tide, we again take the limit of $\omega = 0$ in equations (B.9-B.10) to find

$$\xi_r^{\text{eq},1} = \frac{r\omega^2}{N^2 - \omega^2} \left[\left(\frac{N^2}{g} - \frac{1}{r}\right)\xi_\perp^{\text{eq},0} + \frac{1}{r}\xi_r^{\text{eq},0} - \xi_\perp^{\text{eq},0'} \right], \quad (\text{B.11})$$

and

$$\xi_\perp^{\text{eq},1} = \frac{1}{l(l+1)} \left[\left(2 - \frac{gr}{c_s^2}\right)\xi_r^{\text{eq},1} + r\xi_r^{\text{eq},1'} + \frac{r^2\omega^2}{c_s^2}\xi_\perp^{\text{eq},0} \right]. \quad (\text{B.12})$$

We find that higher order terms are not essential for our purposes. Moreover, these terms typically involve multiple derivatives of stellar properties that are difficult to compute from a grid of stellar quantities. The total equilibrium tide is $\xi^{\text{eq}} = \xi^{\text{eq},0} + \xi^{\text{eq},1} + O(\omega^4)$. At our outer boundary, the dynamical tide is computed using $\xi^{\text{dyn}} = \xi - \xi^{\text{eq}}$.

APPENDIX C

GENERAL SCALING FOR SPIN-ORBIT SYNCHRONIZATION AND TIDAL HEATING

In Section 5.2, we showed that the averaged dimensionless tidal torque on a He WD scales with the tidal forcing frequency as $F \propto \omega^6$. For a CO WD, the scaling is $F \propto \omega^5$ (see Paper II). In general, we may parameterize the tidal torque by

$$T_{\text{tide}} = \dot{J}_z = T_0 \hat{f} \hat{\omega}^n \quad (\text{C.1})$$

with the dimensionless values \hat{f} and n determined from the dynamics of gravity wave excitation and dissipation within the WD. Using equation (C.1), we can examine the general behaviors of spin-orbit synchronization and tidal heating in a compact binary undergoing gravitational radiation-driven orbital decay (see also Section 8.1 of Paper II).

Combining equations (5.6) and (5.12) as we did in Section 5.3, we find that tides begin to synchronize the star at a critical orbital frequency

$$\Omega_c = \left[\frac{2.4}{2^{n+1/2}} \frac{\kappa}{\hat{f}} \left(\frac{R_s}{R} \right)^{5/2} q_M \right]^{\frac{3}{3n+1}} \Omega_{\text{dyn}}. \quad (\text{C.2})$$

Here, $R_s = 2GM/c^2$, $q_M = (M + M')^{5/3}/(M^{2/3}M')$, and $\Omega_{\text{dyn}} = \sqrt{GM/R^3}$. Thus, less compact stars (with larger R/R_s) begin synchronization at larger orbital periods. Note that if $n \gtrsim 3$ as for WDs, the critical frequency Ω_c does not depend sensitively on \hat{f} or $\hat{\kappa}$, and only a very rough estimate of these quantities is necessary.

The tidal heating rate is given by equation (5.15). For $\Omega > \Omega_c$ (see Paper II),

$$\Omega_s \simeq \Omega - \Omega_c \left(\frac{\Omega_c}{\Omega} \right)^{1/(3n)}, \quad (\text{C.3})$$

and combining equations (5.15), (C.2), and (C.3) yields

$$\dot{E}_{\text{heat}} = \left[\frac{2.4}{2^n \sqrt{2}} \frac{\kappa^{n+1}}{\hat{f}} \left(\frac{R_s}{R} \right)^{5/2} q_{M2} \right]^{\frac{1}{n}} \left(\frac{\Omega}{\Omega_{\text{dyn}}} \right)^{\frac{n-1}{3n}} \dot{E}_{\text{GW}}, \quad (\text{C.4})$$

where $q_{M2} = (M+M')^{(5+n)/3} M^{2(n-1)/3} / M'^{n+1}$. Note that for $n \gtrsim 3$ as it is for WDs, the tidal heating rate is very insensitive to the value of \hat{f} . At typical orbital periods ($\Omega \ll \Omega_{\text{dyn}}$), the tidal heating rate is a small fraction of the energy loss rate due to gravitational waves (especially for non-compact stars), but it becomes more significant at shorter orbital periods.

APPENDIX D

ESTIMATING THE CORE-ENVELOPE COUPLING TIME SCALE

In the two zone model (see Section 5.4.2), the thickness of the synchronized envelope is dependent on the parameter t_{coup} . In stably stratified stars like WDs, angular momentum can be transported by magnetic fields. In the presence of a poloidal field B connecting the core and envelope, t_{coup} can be estimated from the Alfven wave crossing time,

$$t_A = \int_0^R dr \frac{\sqrt{4\pi\rho}}{B}. \quad (\text{D.1})$$

We find $t_A \approx 10^2 \text{ yr}(10^3\text{G}/B)$ for our CO WD model, and $t_A \approx 50 \text{ yr}(10^3\text{G}/B)$ for our He WD model.

For WDs without an intrinsic magnetic field, angular momentum may be transported via the Tayler-Spruit dynamo (Spruit 2002). To estimate t_{coup} , we calculate the effective viscosity ν_{TS} for angular momentum transport using the the method outlined in Spruit (2002). For simplicity, we calculate ν_{TS} without including the effects of composition gradients in the WD to find

$$\nu_{TS} = r^2 \Omega_s \left(\frac{\Omega_s}{N} \right)^{1/2} \left(\frac{\kappa_T}{r^2 N} \right)^{1/2}, \quad (\text{D.2})$$

where κ_T is the heat diffusivity. This viscosity does not depend on the local shear, and is thus independent of the precise rotation profile of the star.¹

We then estimate the coupling time from the Tayler-Spruit dynamo to be

$$t_{TS} = \int_0^R dr \frac{R-r}{\nu_{TS}}. \quad (\text{D.3})$$

We find $t_{TS} \approx 2 \times 10^3 \text{ yr} (P/30\text{min})^{3/2}$ for both $0.3M_\odot$ He and $0.6M_\odot$ CO WDs. The values of t_A and t_{TS} convince us that $t_{\text{coup}} \lesssim 10^3 \text{ yr}$ for the short orbital periods of interest.

¹The Tayler-Spruit dynamo requires a minimum local shear to operate (see Spruit 2002), causing significant shear to persist if the dynamo dominates angular momentum transport. This shear may significantly impact wave dynamics, in addition to causing viscous heating and mixing.

APPENDIX E

NON-TIDAL ORBITAL EVOLUTION

We wish to compare the effects of three-body tides to other physical mechanisms that may produce orbital evolution in triple-star systems. One such mechanism is tidal orbital decay due to the induced eccentricity of the inner binary (Stars 2 and 3) due to the perturbing gravitational influence of Star 1. This effect has been studied in detail by, e.g., Ford et al. 2000. In this mechanism, the eccentricity of the orbit of Stars 2 and 3 about one another oscillates around a small, non-zero value due to the presence of Star 1. Tidal interactions between Stars 2 and 3 act to re-circularize the orbit, dissipating energy and causing the orbit of Stars 2 and 3 about one another to decay. The orbital decay time scale due to dissipation in Star 2 is (Lithwick & Wu 2012)

$$t_{\text{ecc}} = \frac{a_{23}}{\dot{a}_{23}} = \frac{1}{18\pi} \frac{Q}{k_2} \frac{\Omega_{23} R_2^3}{GM_2} \frac{1}{q(1+q)} \left(\frac{a_{23}}{R_2} \right)^8 \frac{1}{\langle e^2 \rangle}, \quad (\text{E.1})$$

where Q is the tidal quality factor, k_2 is the constant of apsidal motion, $q = M_2/M_3$, and $\langle e^2 \rangle$ is the mean square eccentricity of the orbit of Stars 2 and 3 about one another. We have divided by an extra factor of two to account for tidal dissipation in both stars. According to Georgakarakos (2002), the mean square eccentricity for a nearly equal mass binary ($M_2 \simeq M_3$) is

$$\langle e^2 \rangle \simeq \frac{43}{4} \left(\frac{M_1}{M_1 + M_2 + M_3} \right)^2 \left(\frac{\Omega_1}{\Omega_{23}} \right)^4. \quad (\text{E.2})$$

However, for unequal mass inner binaries ($M_2 \neq M_3$) or systems near an orbital resonance, the mean square eccentricity may be significantly larger. In our calculations, we use $k_2 = 0.02$ (appropriate for low mass dwarf stars), and $Q = 10^5$.

Another effect that can cause orbital decay in a compact triple system is magnetic braking. Magnetic braking is likely to act on short time scales in systems like HD

181068 because Stars 2 and 3 are rapidly rotating, low mass stars with convective envelopes that likely have strong magnetic dynamos. We estimate the torque due to magnetic braking according to the prescription of Krishnamurthi et al. 1997, yielding a magnetic braking timescale of

$$t_{\text{mag}} = \frac{a_{23}}{\dot{a}_{23}} = \frac{\mu_{23} a_{23}^2}{4K_{MB}\Omega_{s,c}^2} \left(\frac{M_2}{M_\odot} \right)^{1/2} \left(\frac{R_2}{R_\odot} \right)^{-1/2}, \quad (\text{E.3})$$

where $\Omega_{s,c}$ is a critical rotation rate of $\Omega_c \sim 10\Omega_{s,\odot}$, and K_{MB} is a calibrated constant of $K_{MB} \approx 2.6 \times 10^{47} \text{ g s cm}^2$. Once again, we have divided by an extra factor of two to account for magnetic braking produced by Stars 2 and 3, assuming they are nearly identical. Star 1 may produce additional magnetic braking, but because $a_1 \gg a_{23}$ in hierarchical triples, the time scale of tidal orbital decay associated with this process is long, and can be ignored.

Finally, the orbit of Stars 2 and 3 may decay due to the emission of gravitational waves. The orbital decay time scale due to gravitational waves is

$$t_{\text{GW}} = \frac{a_{23}}{\dot{a}_{23}} = \frac{5c^5}{64G^3} \frac{a_{23}^4}{M_2 M_3 (M_2 + M_3)}. \quad (\text{E.4})$$

APPENDIX F

ELASTIC OSCILLATION EQUATIONS

In this work we consider purely adiabatic and elastic oscillations, i.e., we neglect damping produced by non-adiabaticity and anelasticity. Under these approximations, the elastic forces act like a spring, which is characterized by the stress tensor

$$\boldsymbol{\sigma} = K(\boldsymbol{\nabla} \cdot \boldsymbol{\xi})\mathbf{I} + 2\mu\mathbf{s}. \quad (\text{F.1})$$

Here, K is the adiabatic bulk modulus, related to the pressure P via $K = \Gamma_1 P$, with Γ_1 the adiabatic index of the material. Also, μ is the shear modulus, $\boldsymbol{\xi}$ is the vector displacement, \mathbf{I} is the identity matrix, and the deviatoric strain tensor \mathbf{s} is defined

$$\mathbf{s} \equiv \frac{1}{2}[\boldsymbol{\nabla}\boldsymbol{\xi} + (\boldsymbol{\nabla}\boldsymbol{\xi})^T] - \frac{1}{3}(\boldsymbol{\nabla} \cdot \boldsymbol{\xi})\mathbf{I} \quad (\text{F.2})$$

The perturbed hydroelastic oscillation equations read

$$\frac{\partial^2 \boldsymbol{\xi}}{\partial t^2} = \frac{\delta\rho}{\rho^2} \boldsymbol{\nabla} P - \frac{1}{\rho} \boldsymbol{\nabla} \delta P - \boldsymbol{\nabla} \delta\Phi + \delta\mathbf{f}_e, \quad (\text{F.3})$$

where the elastic force \mathbf{f}_e is

$$\begin{aligned} \delta\mathbf{f}_e &= \frac{2}{\rho} \boldsymbol{\nabla} \cdot (\mu\mathbf{s}) \\ &= \frac{2}{\rho} \boldsymbol{\nabla} \mu \cdot \mathbf{s} + \frac{\mu}{\rho} \left(\nabla^2 \boldsymbol{\xi} + \frac{1}{3} \boldsymbol{\nabla}(\boldsymbol{\nabla} \cdot \boldsymbol{\xi}) \right) \end{aligned} \quad (\text{F.4})$$

We decompose all variables into spherical harmonics, or spherical vector harmonics where appropriate:

$$\begin{aligned} \boldsymbol{\xi}(\mathbf{r}, t) &= \sum_{l,m} [U_l(r)Y_{lm}\hat{\mathbf{r}} + V_l(r)r\boldsymbol{\nabla}Y_{lm} + W_l(r)\boldsymbol{\nabla} \times (\mathbf{r}Y_{lm})] e^{i\omega t} \\ \delta\Phi &= \sum_{l,m} [\delta\Phi_l(r)Y_{lm}] e^{i\omega t} \end{aligned} \quad (\text{F.5})$$

Then the equations become separated such that only r -dependence is left, and the equations for different harmonics are self-contained. From now on we will drop the subscript l and consider the equations for a single harmonic. Explicitly, the displacement vector becomes:

$$\begin{aligned}\xi_r &= U(r)Y_{lm} \\ \xi_\theta &= V(r)\frac{\partial Y_{lm}}{\partial \theta} + \frac{W(r)}{\sin \theta} \frac{\partial Y_{lm}}{\partial \phi} \\ \xi_\phi &= \frac{V(r)}{\sin \theta} \frac{\partial Y_{lm}}{\partial \phi} - W(r) \frac{\partial Y_{lm}}{\partial \theta}.\end{aligned}\tag{F.6}$$

In addition, there is also the Poisson equation for $\delta\Phi$:

$$\nabla^2 \delta\Phi = 4\pi G \delta\rho.\tag{F.7}$$

We also define

$$\alpha Y_{lm} = \nabla \cdot \xi = \left[\dot{U} + \frac{2}{r}U - \frac{l(l+1)}{r}V \right] Y_{lm},\tag{F.8}$$

where the dot denotes a radial derivative, and we have dropped the radial functionality for simplicity. The continuity equation gives

$$\begin{aligned}\delta\rho &= -\xi \cdot \nabla \rho - \rho \nabla \cdot \xi \\ &= -(U\dot{\rho} + \rho\alpha) Y_{lm}\end{aligned}\tag{F.9}$$

Equation F.3 represents three 2nd-order ordinary differential equations for U , V , W , while equation F.7 is a 2nd order ODE for $\delta\Phi$. We wish to transform these four second-order ODEs into eight first-order ODEs. First we define a new quantity, the Lagrangian

traction $\mathbf{T} \equiv \hat{\mathbf{r}} \cdot \Delta\boldsymbol{\sigma}$, where $\Delta\sigma_{ij} = K\alpha\delta_{ij} + 2\mu s_{ij}$. Then we have

$$\begin{aligned}
\mathbf{T} &= \hat{\mathbf{r}} \cdot \Delta\boldsymbol{\sigma} \\
&= T_r(r)Y_{lm}\hat{\mathbf{r}} + T_\perp(r)r\nabla Y_{lm} + T_t(r)\nabla \times (\mathbf{r}Y_{lm}) \\
&= \left(\left[K - \frac{2}{3}\mu \right] \alpha + 2\mu\dot{U} \right) Y_{lm}\hat{\mathbf{r}} \\
&\quad + \mu \left\{ \left(\frac{U}{r} + \dot{V} - \frac{V}{r} \right) \frac{\partial Y_{lm}}{\partial \theta} + \left(\dot{W} - \frac{W}{r} \right) \frac{1}{\sin \theta} \frac{\partial Y_{lm}}{\partial \phi} \right\} \hat{\theta} \\
&\quad + \mu \left\{ \left(\frac{U}{r} + \dot{V} - \frac{V}{r} \right) \frac{1}{\sin \theta} \frac{\partial Y_{lm}}{\partial \phi} - \left(\dot{W} - \frac{W}{r} \right) \frac{\partial Y_{lm}}{\partial \theta} \right\} \hat{\phi}. \tag{F.10}
\end{aligned}$$

We now define 8 new variables as follows:

$$y_1 = U, \tag{F.11}$$

$$y_2 \equiv T_r = \left(K - \frac{2}{3}\mu \right) \alpha + 2\mu\dot{U}, \tag{F.12}$$

$$y_3 = V, \tag{F.13}$$

$$y_4 \equiv T_\perp = \mu \left(\frac{U}{r} + \dot{V} - \frac{V}{r} \right), \tag{F.14}$$

$$y_5 = \delta\Phi, \tag{F.15}$$

$$y_6 = \dot{y}_5 + 4\pi G\rho y_1, \tag{F.16}$$

$$y_7 = W, \tag{F.17}$$

$$y_8 \equiv T_t = \mu \left(\dot{W} - \frac{W}{r} \right). \tag{F.18}$$

Note that y_1, y_3, y_7 are the displacement components, while y_2, y_4, y_8 are the Lagrangian tractions. y_6 is the Lagrangian gravitational attraction, chosen as a variable for convenience when applying boundary conditions (see section F.0.1). Then the final

equations are:

$$\dot{y}_1 = -\frac{2(K - \frac{2}{3}\mu)}{(K + \frac{4}{3}\mu)} \frac{y_1}{r} + \frac{1}{(K + \frac{4}{3}\mu)} y_2 + \frac{l(l+1)(K - \frac{2}{3}\mu)}{(K + \frac{4}{3}\mu)} \frac{y_3}{r}, \quad (\text{F.19})$$

$$\begin{aligned} \dot{y}_2 = & \left[-4\rho g - \omega^2 \rho r + \frac{12\mu K}{(K + \frac{4}{3}\mu)r} \right] \frac{y_1}{r} - \frac{4\mu}{(K + \frac{4}{3}\mu)} \frac{y_2}{r} \\ & + l(l+1) \left[\rho g - \frac{6\mu K}{(K + \frac{4}{3}\mu)r} \right] \frac{y_3}{r} + l(l+1) \frac{y_4}{r} + \rho y_6, \end{aligned} \quad (\text{F.20})$$

$$\dot{y}_3 = -\frac{y_1}{r} + \frac{y_3}{r} + \frac{y_4}{\mu}, \quad (\text{F.21})$$

$$\begin{aligned} \dot{y}_4 = & \left[\rho g - \frac{6\mu K}{(K + \frac{4}{3}\mu)r} \right] \frac{y_1}{r} - \frac{(K - \frac{2}{3}\mu)}{(K + \frac{4}{3}\mu)} \frac{y_2}{r} \\ & + \left\{ -\omega^2 \rho r + \frac{2\mu[(K - \frac{2}{3}\mu)(2l^2 + 2l - 1) + 2\mu(l^2 + l - 1)]}{(K + \frac{4}{3}\mu)r} \right\} \frac{y_3}{r} \\ & - 3 \frac{y_4}{r} + \rho \frac{y_5}{r}, \end{aligned} \quad (\text{F.22})$$

$$\dot{y}_5 = -4\pi G \rho y_1 + y_6, \quad (\text{F.23})$$

$$\dot{y}_6 = 4\pi G \rho l(l+1) \frac{y_3}{r} + \frac{l(l+1)}{r} \frac{y_5}{r} - \frac{2}{r} y_6, \quad (\text{F.24})$$

$$\dot{y}_7 = \frac{y_7}{r} + \frac{y_8}{\mu}, \quad (\text{F.25})$$

$$\dot{y}_8 = \left[-\omega^2 \rho r + \frac{\mu(l^2 + l - 2)}{r} \right] \frac{y_7}{r} - \frac{3}{r} y_8. \quad (\text{F.26})$$

Note that y_7 and y_8 completely decouple from the other equations. The first six equations are integrated to obtain the spheroidal modes, while the last two are integrated to obtain the toroidal modes.

In fluid regions where $\mu \rightarrow 0$, $y_4 \rightarrow 0$ and y_3 is found from the algebraic relation

$$y_3 = \frac{1}{r\omega^2} \left(g y_1 - \frac{1}{\rho} y_2 + y_5 \right). \quad (\text{F.27})$$

F.0.1 Boundary Conditions

The boundary conditions (BCs) for elastic oscillations can be found in Dahlen and Tromp (1998) and in Crossley (1975). For the spheroidal oscillations, the BCs at $r = 0$

are, to lowest order in r ,

$$y_1 = Ar^{l-1}, \quad (\text{F.28})$$

$$y_2 = 2(l-1)\mu Ar^{l-2}, \quad (\text{F.29})$$

$$y_3 = \frac{A}{l}r^{l-1}, \quad (\text{F.30})$$

$$y_4 = \frac{2(l-1)\mu A}{l}r^{l-2}, \quad (\text{F.31})$$

$$y_5 = \left[-\frac{4\pi G\rho A}{l} + \frac{B}{l} \right] r^l, \quad (\text{F.32})$$

$$y_6 = Br^{l-1}. \quad (\text{F.33})$$

$$(\text{F.34})$$

For $l = 0$, $A = 0$ and higher order terms in r are needed to establish the BCs (see Crossley 1975). When $l = 1$, the displacements are finite at the center of the planet. Note that for $l = 2$, the value of the tractions T_r and T_\perp are finite, i.e., the core is undisplaced but is under stress. For $l > 2$, the values of all perturbation variables are zero at the center of the planet. Equations (F.28) comprise only two independent BCs (corresponding to the undetermined constants A and B), and additional inner BCs are trivially satisfied due to the form of the oscillation equations. In practice, for $l \geq 2$, we use the four inner BCs

$$y_1 = 0, \quad (\text{F.35})$$

$$y_2 = ly_4, \quad (\text{F.36})$$

$$y_4 = 0, \quad (\text{F.37})$$

$$y_6 = 0, \quad (\text{F.38})$$

$$(\text{F.39})$$

although other choices are possible.

The three independent boundary conditions at the surface of the planet are

$$y_2 = 0, \tag{F.40}$$

$$y_4 = 0, \tag{F.41}$$

$$y_6 = -\frac{l+1}{R}y_5. \tag{F.42}$$

$$\tag{F.43}$$

Note that in a fluid envelope, the first of these conditions is equivalent to the boundary condition $\Delta P = 0$ commonly used in asteroseismology. The condition on y_4 is trivially satisfied in a planetary model with a fluid envelope, since $y_4 = 0$ in fluid regions. In our calculations, we instead use the outer BCs involving y_2 and y_6 , the four inner BCs listed above, and the jump conditions at internal discontinuities described below.

At an internal fluid-solid interface, the values of y_1 , y_2 , y_4 , y_5 , and y_6 must be continuous. There is no relation to determine the change in y_3 across a fluid-solid interface, and in general y_3 is discontinuous at these interfaces. At a solid-solid interface, however, y_3 must also be continuous. Note that the continuity of y_6 across an interface implies a discontinuity in the gravitational perturbation, $\delta d\Phi/dr$. Also note that the continuity of y_4 implies that it is zero at a fluid-solid interface.

For torsional oscillations of $l \geq 2$, the BCs are $y_7 = 0$ at $r = 0$ and $y_8 = 0$ at $r = R$. At a fluid-solid interface, y_8 is continuous but y_7 is generally discontinuous. At solid-solid interfaces, both y_7 and y_8 are continuous.

Solving the eigensystem F.26 for an eigenvalue ω also requires a normalization boundary condition. Typically, the normalization

$$y_1(R) = 1 \tag{F.44}$$

is used to solve for the oscillation modes, although the choice of normalization is entirely arbitrary. For oscillation modes in planets with a solid core and a fluid envelope,

the condition of equation F.44 is poorly suited for numerical computation. The reason is that p-modes confined to the fluid envelope have very large relative surface displacements, while shear modes confined to the solid core have very small relative surface displacements. It is very difficult for numerical routines to converge to both types of modes, as their scales using equation F.44 may be different by many orders of magnitude. For our models, we find the normalization condition $y_3 = 1$ just below the core-envelope boundary allows our code to quickly converge to both p-modes and shear modes. The modes are then renormalized via equation 8.5.

APPENDIX G

SOLVING FOR ROTATIONALLY MIXED MODES

In the absence of rotation, the perturbed momentum equations take the form

$$\frac{\partial^2 \xi}{\partial t^2} + \mathcal{H}\xi = 0, \quad (\text{G.1})$$

where $\mathcal{H}\xi$ is given by the negative of the right hand side of equation F.3. An eigenfunction ξ_α and its associated eigenvalue ω_α^2 satisfy $\mathcal{H}\xi_\alpha = \omega_\alpha^2 \xi_\alpha$. The eigenfunctions are orthonormal such that the inner product between two eigenfunctions is

$$\langle \xi_\alpha | \xi_\beta \rangle = \int dV \rho \xi_\alpha^* \cdot \xi_\beta = \delta_{\alpha\beta}. \quad (\text{G.2})$$

and the integral extends over the volume of the planet.

We now consider the effect of rotation, in the rotating frame of the planet. First order rotational effects result in the addition of the Coriolis force to the momentum equation such that equation G.1 becomes

$$\frac{\partial^2 \xi}{\partial t^2} + C\xi + \mathcal{H}\xi = 0, \quad (\text{G.3})$$

where the Coriolis force is given by

$$C\xi_\alpha = 2i\omega_\alpha(\mathbf{\Omega}_s \times \xi_\alpha), \quad (\text{G.4})$$

and $\mathbf{\Omega}_s$ is the spin vector. In this paper, we consider uniform rotation about the z -axis such that $\mathbf{\Omega}_s = \Omega_s \hat{\mathbf{z}}$.

The original eigenfunctions and eigenfrequencies are no longer solutions to the eigensystem of equation G.3. Instead, we look for solutions using the original eigenfunctions as basis functions such that

$$(\mathcal{H} + C)\left(\sum_\beta a_\beta \xi_\beta\right) = \omega^2 \left(\sum_\beta a_\beta \xi_\beta\right), \quad (\text{G.5})$$

where a_β are undetermined complex constants. In equation G.5, the sum runs over all eigensolutions of equation G.1 such that there are N terms, where N is the dimension of \mathcal{H} . In practice, this sum will need to be truncated, as we will describe below. In Dirac notation, equation G.5 is

$$(\mathcal{H} + C) \sum_{\alpha} a_{\beta} |\xi_{\beta}\rangle = \omega^2 \sum_{\alpha} a_{\beta} |\xi_{\beta}\rangle. \quad (\text{G.6})$$

To solve for the constants a_β , we operate on each side of equation G.6 by an arbitrary eigenvector $\langle \xi_{\alpha} |$ to obtain

$$\omega_{\alpha}^2 a_{\alpha} + \sum_{\beta} \langle \xi_{\alpha} | C | \xi_{\beta} \rangle a_{\beta} = \omega^2 a_{\alpha}. \quad (\text{G.7})$$

Using equation G.4, we obtain

$$\omega_{\alpha}^2 a_{\alpha} + 2\omega \sum_{\beta} C_{\alpha\beta} a_{\beta} = \omega^2 a_{\alpha}. \quad (\text{G.8})$$

where $C_{\alpha\beta}$ is a complex coupling coefficient that describes the strength of coupling due to the Coriolis force between two original oscillation modes. Explicit expressions for $C_{\alpha\beta}$ are given in Appendix G.0.3.

Equation G.8 represents an eigensystem for the modified eigenvalues ω , with each row in the matrix equation indexed by α and each column indexed by β . For each eigenvalue ω^2 , the complex components of the eigenvector $\mathbf{a} = \{a_1, \dots, a_N\}$ represent the projection of the new eigenmode onto each original mode β . In matrix form, equation G.8 is a quadratic eigenvalue problem:

$$(\mathbf{\Omega} + 2\omega\mathbf{C})\mathbf{a} = \omega^2\mathbf{I}\mathbf{a}, \quad (\text{G.9})$$

with $\mathbf{\Omega} = \text{diag}\{\omega_1^2, \dots, \omega_N^2\}$, \mathbf{I} is the identity matrix, and

$$\mathbf{C} = \begin{bmatrix} C_{11} & \cdots & C_{1N} \\ \vdots & \ddots & \vdots \\ C_{N1} & \cdots & C_{NN} \end{bmatrix} \quad (\text{G.10})$$

The $N \times N$ eigenvalue problem of equation G.9 is equivalent to the $2N \times 2N$ eigenvalue problem

$$\begin{bmatrix} 0 & \mathbf{I} \\ \boldsymbol{\Omega} & 2\mathbf{C} \end{bmatrix} \begin{bmatrix} \mathbf{a} \\ \mathbf{b} \end{bmatrix} = \omega \begin{bmatrix} \mathbf{a} \\ \mathbf{b} \end{bmatrix}, \quad (\text{G.11})$$

where $\mathbf{b} = \omega \mathbf{a}$. Equation G.11 is equivalent to the phase space mode expansion, where a mode \mathbf{Z} of eigenvalue ω is defined by both its displacement and velocity vectors such that $\mathbf{Z} = [\mathbf{a}, \mathbf{b}] = [\mathbf{a}, \omega \mathbf{a}]$. Solving the eigensystem of equation G.11 yields $2N$ eigenvalues ω . In the limit $\Omega_s \rightarrow 0$, the solutions come in pairs ω_α and $-\omega_\alpha$, representing the prograde and retrograde modes. Note that in this form, the matrix on the left hand side of equation G.11 is not explicitly Hermitian, however, we show below that the system can be written in a Hermitian form.

We solve the eigensystem G.11 for the eigenvalues ω and the associated eigenfunctions \mathbf{a} . Because only modes of the same m are coupled (see Section G.0.3), we may solve equation G.11 separately for each value of m we wish to consider. For negative m , the positive values of ω represent prograde modes, and the negative values of ω represent retrograde modes. In principle, we must include every oscillation mode (i.e., for a given m we must include modes of all l and n) in the eigensystem. In practice, we must truncate the eigensystem at finite values of l and n . To determine which modes to include, we can solve equation G.11 for a limited set of modes near the $l = m$ f-modes, and then extend our calculations to larger values of l and larger frequency ranges to see if the results change. For the planetary models, spin frequencies, and mode frequencies considered in this paper, we find that including only modes with $l \lesssim 14$ and $\omega_{l,n}/3 \lesssim \omega_f \lesssim 3\omega_{l,n}$ yields a good approximation.

G.0.2 Alternative Formalism

The eigensystem equation G.11 can be solved more elegantly, as shown in Dyson & Schutz (1979) and DT98. We seek to solve the eigenvalue problem

$$[\mathcal{H} + \omega \bar{C}] \xi = \omega^2 \xi, \quad (\text{G.12})$$

where \mathcal{H} has the same definitions as above, and $\bar{C} = 2i\Omega_s \times$. Defining each eigenvector via its six-dimensional eigenfunction

$$\mathbf{Z} = \begin{bmatrix} \xi \\ \omega \xi \end{bmatrix}. \quad (\text{G.13})$$

We rewrite equation G.12 as

$$\left(\begin{bmatrix} 0 & I \\ \mathcal{H} & 0 \end{bmatrix} + \begin{bmatrix} 0 & 0 \\ 0 & \bar{C} \end{bmatrix} \right) \mathbf{Z} = \omega \mathbf{Z}, \quad (\text{G.14})$$

where I is the identity matrix. We decompose \mathbf{Z} in terms of original eigenvectors,

$$\mathbf{Z} = \sum_{\beta} a_{\beta} \mathbf{Z}_{\beta}, \quad (\text{G.15})$$

where here the sum runs over the $2N$ components β (accounting for both negative and positive eigenfrequencies) because we have employed the phase space mode expansion, in contrast to the configuration space expansion used in equation G.5. Recalling that $\mathcal{H}\xi_{\beta} = \omega_{\beta}^2 \xi_{\beta}$, equation G.14 becomes

$$\sum_{\beta} \omega_{\beta} a_{\beta} \mathbf{Z}_{\beta} + \sum_{\beta} \begin{bmatrix} 0 & 0 \\ 0 & \bar{C} \end{bmatrix} a_{\beta} \mathbf{Z}_{\beta} = \sum_{\beta} \omega a_{\beta} \mathbf{Z}_{\beta}. \quad (\text{G.16})$$

We now multiply by the auxiliary operator

$$\mathcal{P} = \begin{bmatrix} \mathcal{H} & 0 \\ 0 & I \end{bmatrix}, \quad (\text{G.17})$$

and take the inner product with \mathbf{Z}_α to obtain

$$2\omega_\alpha^3 a_\alpha + 2\omega_\alpha \sum_\beta \omega_\beta a_\beta C_{\alpha\beta} = 2\omega_\alpha^2 \omega a_\alpha, \quad (\text{G.18})$$

where $C_{\alpha\beta}$ has the same definition as above. Defining $b_\alpha = \omega_\alpha a_\alpha$, we have

$$\omega_\alpha b_\alpha + \sum_\beta C_{\alpha\beta} b_\beta = \omega b_\beta. \quad (\text{G.19})$$

Equation G.19 represents a Hermitian eigensystem because $C_{\alpha\beta} = C_{\beta\alpha}^*$, therefore it is amenable to numerical matrix solving techniques. Once the eigenvectors \mathbf{b} are determined, components of the desired eigenvector \mathbf{a} are given by $a_\beta = b_\beta/\omega_\beta$.

G.0.3 Rotational Coupling Coefficients

The elements $C_{\alpha\alpha'}$ of the rotational coupling matrix are defined as

$$C_{\alpha\alpha'} = i\Omega_s \int dV \rho \xi_\alpha^* \cdot (\hat{\mathbf{z}} \times \xi_{\alpha'}), \quad (\text{G.20})$$

where $\hat{\mathbf{z}}$ is the unit vector in the z direction. Explicitly, the value of $C_{\alpha\alpha'}$ is (see also Dahlen & Tromp 1998)

$$\begin{aligned} C_{\alpha\alpha'} = & m\Omega_s \delta_{ll'} \delta_{mm'} \int_0^R dr \rho r^2 (UV' + VU' + VV' + WW') \\ & - \frac{i\Omega_s}{2} (S_{lm} \delta_{ll'+1} + S_{l'm} \delta_{ll'-1}) \delta_{mm'} \\ & \times \int_0^R dr \rho r^2 \left[(k_l^2 - k_{l'}^2 - 2) U W' + (k_l^2 - k_{l'}^2 + 2) U' W + (k_l^2 + k_{l'}^2 - 2) (V W' - V' W) \right], \end{aligned} \quad (\text{G.21})$$

with $k_l^2 = l(l+1)$ and

$$S_{lm} = \left[\frac{(l+m)(l-m)}{(2l+1)(2l-1)} \right]^{1/2}. \quad (\text{G.22})$$

For compactness, we have dropped the α subscript on the right hand side of equation G.21. The displacement functions U , V , and W are defined in equation F.6. The

first integral in equation G.21 accounts for spheroidal-spheroidal coupling and toroidal-toroidal mode coupling. For $\alpha = \alpha'$, it reduces to the conventional rotational splitting parameter. The second integral in equation G.21 accounts for spheroidal-toroidal mode coupling. Note the Hermitian nature of $C_{\alpha\alpha'}$, i.e., $C_{\alpha\alpha'} = C_{\alpha'\alpha}^*$.

The value of $C_{\alpha\alpha'}$ is zero unless the modes satisfy certain angular selection rules. In particular, only modes of equal azimuthal number $m = m'$ can couple since the introduction of rotation does not break the axial symmetry of the problem. Similarly, spheroidal modes couple only to other spheroidal modes of equal angular degree such that $l = l'$. The same is true for toroidal modes. However, spheroidal modes of degree l may couple to toroidal modes of degree $l' = l \pm 1$, and vice versa. Therefore, spheroidal modes of $Y_{l,m}$ are coupled to toroidal modes of $Y_{l+1,m}$, which in turn are coupled to spheroidal modes of $Y_{l+2,m}$, etc. Thus, the inclusion of the Coriolis forces introduces an infinite chain of coupling with modes of higher angular degree l .

APPENDIX H

MODE NORMALIZATION

The modes obtained by solving the eigensystem G.11 or G.19 must be appropriately normalized, because they are no longer orthonormal under expression G.2. Instead, the modes satisfy the modified orthonormality condition

$$\langle\langle \mathbf{Z}_\alpha | \mathbf{Z}_{\alpha'} \rangle\rangle \equiv \langle \mathbf{Z}_\alpha | \mathcal{P} | \mathbf{Z}_{\alpha'} \rangle = 2\omega_\alpha^2 \delta_{\alpha, \alpha'}, \quad (\text{H.1})$$

with \mathcal{P} defined by equation G.17. Explicitly, equation H.1 is

$$\left\langle \left[\sum_{\beta} a_{\alpha, \beta}^* \xi_{\alpha}^*, \quad \omega_{\alpha} \sum_{\beta} a_{\alpha, \beta}^* \xi_{\beta}^* \right] \left[\sum_{\beta'} a_{\alpha', \beta'} \omega_{\beta'}^2 \xi_{\alpha'}^*, \quad \omega_{\alpha'} \sum_{\beta} a_{\alpha', \beta'} \xi_{\beta'} \right]^T \right\rangle = 2\omega_{\alpha}^2 \delta_{\alpha, \alpha'}. \quad (\text{H.2})$$

Recall that these sums include the $2N$ original modes, with each of the N eigenfunctions ξ_{β} corresponding to the modes of frequency ω_{β} and $-\omega_{\beta}$. Therefore, for identical modes $\alpha = \alpha'$, each value of β on the left hand vector of equation H.2 will have a finite overlap with two terms in the sum in the right hand vector (corresponding to both the $\omega_{\beta} = \omega_{\beta'}$ term and the $\omega_{\beta} = -\omega_{\beta'}$ term). So for modes with $\alpha = \alpha'$ the normalization condition becomes

$$\sum_{\beta} \left(|a_{\alpha, \beta}|^2 \omega_{\beta}^2 + a_{\alpha, \beta}^* a_{\alpha, -\beta} \omega_{-\beta}^2 \right) + \omega_{\alpha}^2 \sum_{\beta} \left(|a_{\alpha, \beta}|^2 + a_{\alpha, \beta}^* a_{\alpha, -\beta} \right) = 2\omega_{\alpha}^2, \quad (\text{H.3})$$

where the subscript $-\beta$ refer to the original mode with eigenfrequency of opposite sign, respectively. The sum in equation H.3 over the $2N$ modes β can be written more simply as a sum over the N modes with $\omega_{\beta} > 0$:

$$\sum_{\omega_{\beta} > 0} \frac{1}{2} \left(1 + \frac{\omega_{\beta}^2}{\omega_{\alpha}^2} \right) \left(|a_{\alpha, \beta}|^2 + |a_{\alpha, -\beta}|^2 + 2\text{Re}[a_{\alpha, \beta}^* a_{\alpha, -\beta}] \right) = 1. \quad (\text{H.4})$$

In the limit $\Omega_s \rightarrow 0$, equation H.4 reduces to $|a_{\alpha, \beta}|^2 \delta_{\alpha, \beta} = 1$, equivalent to equation G.2.

APPENDIX I

THREE-MODE MIXING

In this section we solve for the eigenvalues and eigenvectors of a three mode system coupled through the Coriolis force. We consider Mode 1 to be an f-mode, Mode 2 to be an arbitrary mode mixed with the f-mode, and Mode 3 to be an arbitrary mode that does not mix directly with Mode 1 but does mix with Mode 2. The eigensystem describing these three modes is

$$\begin{bmatrix} 2(\bar{\omega}_1 - \omega) & 2C_{12} & 0 \\ 2C_{12}^* & 2(\bar{\omega}_2 - \omega) & 2C_{23} \\ 0 & 2C_{23}^* & 2(\bar{\omega}_3 - \omega) \end{bmatrix} \begin{bmatrix} b_1 \\ b_2 \\ b_3 \end{bmatrix} = 0, \quad (\text{I.1})$$

with $\bar{\omega}_1 = \omega_1 + C_{11}$ and likewise for modes 2 and 3. This eigensystem is equivalent to

$$\begin{bmatrix} \Delta_{13} - \Delta & 2C_{12} & 0 \\ 2C_{12}^* & \Delta_2 - \Delta & 2C_{23} \\ 0 & 2C_{23}^* & -\Delta_{13} - \Delta \end{bmatrix} \begin{bmatrix} b_1 \\ b_2 \\ b_3 \end{bmatrix} = 0, \quad (\text{I.2})$$

where $\Delta_{13} = \bar{\omega}_1 - \bar{\omega}_3$, $\Delta_2 = 2\bar{\omega}_2 - \bar{\omega}_1 - \bar{\omega}_3$, and $\Delta = 2\omega - \bar{\omega}_1 - \bar{\omega}_3$.

We now examine the specific case where modes 1 and 3 are degenerate, i.e., $\Delta_{13} = 0$. The characteristic equation for this case is

$$\Delta \left[\Delta^2 - \Delta_2 \Delta - 4(|C_{12}|^2 + |C_{23}|^2) \right] = 0. \quad (\text{I.3})$$

The eigenvalues are $\Delta_0 = 0$ and $\Delta_{\pm} = \frac{1}{2} \left[\Delta_2 \pm \sqrt{\Delta_2^2 + 16(|C_{12}|^2 + |C_{23}|^2)} \right]$. These frequencies correspond to $\omega_0 = \bar{\omega}_1 = \bar{\omega}_3$ and

$$\omega_{\pm} = \frac{2\bar{\omega}_2 + \bar{\omega}_1 + \bar{\omega}_3}{4} \pm \frac{1}{4} \left[\Delta_2^2 + 16(|C_{12}|^2 + |C_{23}|^2) \right]^{1/2}. \quad (\text{I.4})$$

The associated (unnormalized) eigenvectors are

$$\mathbf{b}_0 = \begin{bmatrix} C_{23} \\ 0 \\ -C_{12}^* \end{bmatrix} \quad (\text{I.5})$$

and

$$\mathbf{b}_{\pm} = \begin{bmatrix} 2C_{12} \\ \Delta_{\pm} \\ 2C_{23}^* \end{bmatrix}. \quad (\text{I.6})$$

In all cases, the mode with frequency ω_0 is a superposition of Modes 1 and 3, with the relative weights determined by the relative values of $|C_{12}|$ and $|C_{23}|$. If $|C_{12}| \ll |C_{23}|$, i.e., Mode 1 is essentially decoupled from the system, then this mode is a slightly perturbed version of Mode 1. If $|C_{12}| \gg |C_{23}|$, i.e., Mode 3 is essentially decoupled from the system, then this mode is a slightly perturbed version of Mode 3.

If the modes are minimally mixed, [$16(|C_{12}| + |C_{23}|) \ll |\Delta_2|$], two modes have frequency $\omega \simeq \bar{\omega}_1 = \bar{\omega}_3$ and one has $\omega \simeq \bar{\omega}_2$, as we would expect for non-mixed modes. However, the two modes with $\omega \simeq \bar{\omega}_1 = \bar{\omega}_3$ may still be strongly mixed. In the nearly degenerate limit [$16(|C_{12}| + |C_{23}|) \gg |\Delta_2|$], all three modes are mixed with one another, with the weights determined by the relative coupling coefficients.

It is important to note that if $|C_{12}|$ and $|C_{23}|$, have similar magnitudes, there will always exist at least two modes that are strong superpositions of Modes 1 and 3, regardless of the value of Δ_2 . This entails that if a mode (in our example Mode 3) is nearly degenerate with the f-mode, it can mix strongly with it (through another mode, in our example Mode 2) even if it does not mix directly with the f-mode. The mode that serves as intermediary (Mode 2) need not be similar in frequency to Mode 1 and 3. Furthermore, in Section 8.4.2, we show that systems in which $|C_{12}|$ and $|C_{23}|$ have very different magnitudes can still exhibit strong mixing between Modes 1 and 3. In this case, the strong mixing does not occur when $\bar{\omega}_1 \simeq \bar{\omega}_3$, although it does occur when there are two eigenfrequencies with $\omega \simeq \bar{\omega}_1$. We should therefore expect that modes very near in frequency to the f-mode will mix strongly with it, regardless of their original characteristics.

APPENDIX J

EFFECT OF MODES ON THE RINGS

The characteristics of density waves launched at Lindblad resonances are elegantly characterized in Goldreich & Tremaine (1979) and in Greenberg & Brahic (1984). Here we summarize the relevant results and apply them to the Saturnian ring system. The wave-like response of the disk near (but not exactly at) the Lindblad resonance is a traveling wave of form

$$\delta\Phi \simeq -\Psi \sqrt{2\pi|z|} \exp\left[ix^2/(2z)\right]. \quad (\text{J.1})$$

Here, $\delta\Phi$ is the wave-like gravitational perturbation induced in the rings, not to be confused with the value of the $\delta\Phi_\alpha$ associated with a given oscillation mode. Ψ is the effective perturbing potential (see equation J.4), $x = (r - r_L)/r_L$ is the fractional distance away from the Lindblad resonance, and

$$z = \frac{2\pi G\Sigma}{r\mathcal{D}}, \quad (\text{J.2})$$

is approximately the square of the radial wavelength. Here, Σ is the unperturbed ring surface density, and $\mathcal{D} \simeq 3(m-1)\Omega^2$ near Lindblad resonances in Saturn's rings. The value of z is of order $z \sim M_{\text{rings}}/M \sim 10^{-9}$, where M_{rings} is the mass of the C-ring. The wavelength of the waves is very short compared to the Lindblad radius, thus, the waves are very tightly wound. The wavelength decreases away from the Lindblad radius, although the waves typically damp out after ~ 10 wavelengths. This form of the response is accurate for $c_s/(\Omega r) \ll 1$, $G\Sigma/(\Omega^2 r) \ll 1$, $c_s^2/(G\Sigma r) \ll 1$, where c_s is the typical random velocity of ring particles. These are all excellent approximations for Saturn's rings.

A fairly accurate location of the resonant location of a mode is obtained by solving equation 8.20, including corrections due to the gravitational moments of Saturn. The

solution is

$$r_L \simeq r_{L0} \left[1 - \frac{1+m}{2(1-m)} J_2 \left(\frac{R}{r_0} \right)^2 + \frac{5(3+m)}{8(1-m)} J_4 \left(\frac{R}{r_0} \right)^4 \right] + O(J_6, J_2^2), \quad (\text{J.3})$$

where r_{L0} is given by equation 8.21, and for Saturn $J_2 = 1.633 \times 10^{-2}$ and $J_4 = -9.2 \times 10^{-4}$ (Guillot 2005). The effective forcing potential is

$$\Psi = A \left[\frac{d}{d \ln r} + \frac{2m\Omega}{m\Omega + \sigma_\alpha} \right] \delta\Phi_\alpha(r_L), \quad (\text{J.4})$$

where A is the mode amplitude. Each component l' of the potential has the form $\delta\Phi_{\alpha,l'} \propto r^{-(l'+1)}$, resulting in $\Psi_{\alpha,l'} = (2m' - l' - 1)\delta\Phi_{\alpha,l'}$ (see also equation 8.23).

The associated density perturbation is

$$\begin{aligned} \delta\Sigma &\simeq \frac{i}{2\pi G r^{1/2}} \frac{d}{dr} \left(r^{1/2} \delta\Phi \right) \\ &\simeq \left| \frac{3(1-m)\Omega^2 |\Psi|^2}{4\pi^2 G^3 \Sigma r_L} \right|^{1/2} x \exp \left(i \left[x^2 / (2z) + m\phi + \sigma t \right] \right). \end{aligned} \quad (\text{J.5})$$

This equation applies in the inviscid limit and predicts the density perturbation to become larger with increasing distance away from resonance. In reality, the waves damp out and (in Saturn's rings) the density perturbations typically decrease after one or two wavelengths away from resonance.¹ The associated perturbation in optical depth is $\delta\tau = \kappa_m \delta\Sigma$, where κ_m is the local mass extinction coefficient (opacity) of the rings, and we have assumed that it is independent of Σ .

We would like to use the observed variation in optical depth to estimate the amplitudes of the modes driving the waves. Since the wave amplitude is damped by viscous effects, we must judiciously choose a location x at which to evaluate equation J.5. This location must be far enough from the resonance such that equation J.1 is applicable, but

¹Equation J.5 applies in the linear regime. Detectable waves in Saturn's rings often have density perturbations of order unity and are relatively non-linear, causing their optical depth variations to be cuspy. We ignore this issue in this work, although it may affect estimates of mode amplitude.

close enough so that the wave has not been significantly damped. Evaluating equation J.5 at $x = \Delta r/r_L$, we have

$$|\delta\tau| \approx \left| \frac{3(1-m)\kappa_m^2\Omega^2|\Psi|^2}{4\pi^2 G^3 \Sigma r_L} \right|^{1/2} \left| \frac{\Delta r}{r_L} \right|, \quad (\text{J.6})$$

Thus, the amplitude of the mode is

$$|A| \approx \left| \frac{3(1-m)\kappa_m^2\Omega^2|\bar{\Psi}|^2}{4\pi^2 G^3 \Sigma r_L} \right|^{-1/2} \left| \frac{r_L}{\Delta r} \right| |\delta\tau|, \quad (\text{J.7})$$

with

$$\bar{\Psi} = \sum_{\beta} a_{\beta} W_{\beta} \delta\Phi_{\beta}(R). \quad (\text{J.8})$$

To estimate mode amplitudes from HN13, we typically evaluate $\delta\tau$ near its maximum, about one wavelength away from the resonant radius, where $\Delta r \sim 5\text{km}$. This procedure assumes that damping has had a negligible effect on wave amplitude within the first wavelength.

Finally, to calculate optical depth fluctuations produced by modes in our toy Saturn models, we first calculate the amplitude of a mode required to produce the largest observed $m = -3$ wave in Saturn's rings. We use the observed values of κ_m and σ_m from HN13, and we assume the wave is generated by an unmixed $l = 3$, $m = -3$ f-mode with $\delta\Phi_{\alpha}(R) \simeq 1$, determined from our mode calculations. This procedure typically results in a dimensionless amplitude $|A_3| \simeq 10^{-9}$. We then assume energy equipartition amongst the oscillation modes, such that the amplitudes of modes in our model are determined by $\omega_{\alpha}^2 |A_{\alpha}|^2 = \omega_3^2 |A_3|^2$. The optical depth variation is then calculated according to equation J.6, and is evaluated where $\Delta r \sim 5\text{km}$.

BIBLIOGRAPHY

- [1] Abt, H., Boonyarak, C., 2004, ApJ, 616, 562
- [2] Abt, H., 2005, ApJ, 629, 507
- [3] Abt, H., 2006, ApJ, 651, 1151
- [4] Alexander, M.E. 1973, Astrophys. Space Sci., 23, 459
- [5] Asahara, Y., Hirose, K., Ohishi, Y., Hirao, N., Murakami, M., 2010, Earth and Plan. Sci. Let., 299, 474
- [6] Badenes, C., et al. 2009, ApJ, 707, 971
- [7] Baillie, K., Colwell, J., Lissauer, J., Esposito, L., Sremcevic, M., 2011, Icarus, 216, 292
- [8] Baker, N., Kippenhahn, R. 1965, ApJ, 142, 868
- [9] Barker, A., Ogilvie, G. 2010, MNRAS, 404, 1849
- [10] Barker, A., Ogilvie, G. 2011, MNRAS, 417, 745
- [11] Beck, P., et al., 2012, Nature, 481, 55
- [12] Bedding, T., et al., 2011, Nature, 471, 608
- [13] Benacquista, M. 2011, ApJL, 740, 54
- [14] Bloom, J., et al., 2012, ApJL, 744, 17
- [15] Borkovits, T., et al., 2012, MNRAS, 428, 1656
- [16] Brassard, P., Fontaine, G., Wesemael, F., Kawaler, S.D., Tassoul M. 1991, ApJ, 367, 601
- [17] Brassard, P., et al. 1992, ApJ Supplement Series, 80, 369
- [18] Breger, M., et al., 1993, A&A, 271, 482

- [19] Brickhill, A.J., 1983, MNRAS, 204, 537
- [20] Brown, T., Gilliland, R., Noyes, R., Ramsey, L., 1991, ApJ, 368, 599
- [21] Brown, W., Kilic, M., Hermes, J.J., Allende Prieto, C., Kenyon, S.J., Winget, D.E. 2011, ApJL, 737, 23
- [22] Burkart, J., Quataert, E., Arras, P., Weinberg, N. 2011, MNRAS, 421, 983
- [23] Buta, R.J. & Smith, M.A. 1979, ApJ, 232, 213
- [24] Carter, J., et al. 2011, Science, 331, 562
- [25] Cavazzoni, C., Chiarotti, G., Scandalo, S., Tosatti, E., Bernasconi, M., Parrinello, M., 1999, Science, 283, 44
- [26] Chaplin, W., et al., 2011, Science, 332, 213
- [27] Chaplin, W., et al. 2011, ApJL, 732, 5
- [28] Chaplin, W., Miglio, A., 2013, Ann. Rev. Ast. Astro, 51
- [29] Correia, A., Laskar, J., Farago, F., Bou, G. 2011, CeMDA, 111, 105
- [30] Crossley, D., 1975, Geophys. J. R. Astr. Soc., 41, 153
- [31] Dahlen, F., Tromp, J., 1998, Theoretical Global Seismology, Princeton University Press
- [32] Dan, M., Rosswog, S., Guillochon, J., Ramirez-Ruiz, E. 2012, MNRAS, 422, 2417
- [33] Darwin, G., 1879, The Observatory, 3, 79
- [34] Derekas, A., et al., 2011, Science, 332, 216
- [35] De Ridder, J., et al., 2009, Nature, 459, 398
- [36] Di Stefano, R. 2010, ApJ, 719, 474
- [37] Dobbs-Dixon, I., Lin, D.N.C., Mardling, R. 2004, ApJ, 610, 464

- [38] Dyson, J., Schutz, B., 1979, Roy Soc. Proc. Series A, 368, 389
- [39] Dziembowski, W. 1971, Acta Astronomica, 21, 3
- [40] Dziembowski, W. & Krolikowska, M. 1984, Acta Astronomica, 35, 5
- [41] Eggleton, P., Kisleva-Eggleton, L., 2001, ApJ, 562, 1012
- [42] Fabrycky, D., Tremaine, S., 2007, ApJ, 669, 1298
- [43] Flanagan, E., Racine, E. 2007, Phys. Rev. D75, 044001
- [44] Ford, E., Kozinsky, B., Rasio, F., 2000, ApJ, 535, 385
- [45] Fortney, J., Baraffe, I., Militzer, B., 2009, arXiv:0911.3154v1
- [46] French, M., Mattsson, T., Nettelmann, N., Redmer, R., 2009, Phys. Rev. B., 79, 054107
- [47] Friedman, J. L. & Schutz, B. F. 1978, ApJ, 221, 937
- [48] Fuller, J., Lai, D. 2011, MNRAS, 412, 1331
- [49] Fuller, J., Lai, D. 2012, MNRAS, 420, 3126
- [50] Fuller, J., Lai, D., 2012, MNRAS, 421, 426
- [51] Fuller, J., Lai, D., 2012, ApJL, 756, 17
- [52] Fuller, J., Derekas, A., Borkovits, T., Huber, D., Bedding, T., Kiss, L., 2013, MNRAS, 429, 2425
- [53] Fuller, J., Lai, D., 2013, MNRAS, 430, 274
- [54] Gaulme, P, Schmider, F., Gay, J., Guillot, T., Jacob, C., 2011 A&A, 531, 104
- [55] Georgakarakos, N., 2002, MNRAS, 337, 559
- [56] Gilfanov, M., Bogdan, A., 2010, Nature, 463, 924
- [57] Goldreich, P., Soter, S. 1966, Icarus, 5, 375

- [58] Goldreich, P., Nicholson, P., 1977, *Icarus*, 30, 301
- [59] Goldreich, P., Nicholson, P., 1989, *ApJ*, 342, 1079
- [60] Goldreich, P., Wu, Y. 1999, *ApJ*, 511, 904
- [61] Goldman, J., Lackner, C. 2009, *ApJ*, 296, 2054
- [62] Gonzalez Hernandez, J., et al. 2012, *Nature*, 489, 533
- [63] Goodman, J., Dickson, E.S., 1998, *ApJ*, 507, 938
- [64] Goodman, J., Oh, S.P. 1997, *ApJ*, 486, 403
- [65] Gouttebroze, P., Toutain, T., 1994, *A&A*, 287, 535
- [66] Greenberg, R., Brahic, A., 1984, *Planetary Rings*, University of Arizona Press
- [67] Guillot, T., 2005, *Annu. Rev. Earth Planet. Sci.*, 33, 493
- [68] Hansen, C., Van Horn, H., 1979, *ApJ*, 233, 253
- [69] Hedman, M., Nicholson, P., 2013, *arXiv:1304.3735*
- [70] Hekker, S., et al., 2011, *MNRAS*, 414, 2594
- [71] Hermann, A., Ashcroft, N., Hoffmann, R., *Proc. of the Nat. Acad. of Sci.*, 2012, 109, 745
- [72] Hermes, J.J., Kilic, M., Brown, W., Winget, D., Allende Prieto, C., Gianninas, A., Mukadam, A., Cabrera-Lavers, S., Kenyon, S., 2012, *ApJL*, 757, 21
- [73] Hinderer, T., Lackey, B.D., Lang, R.N., Read, J.S. 2010, *Phys. Rev. D* 81, 123016
- [74] Ho, W.C.G., Lai, D. 1999, *MNRAS*, 308, 153
- [75] Houdek, G., Balmforth, N. J., Christensen-Dalsgaard, J., Gough, D. O., 1999, *A&A*, 351, 582
- [76] Huber, D., et al., 2010, *ApJ*, 723, 1607

- [77] Huber, D., et al., 2011, ApJ, 743, 143
- [78] Hut, P. 1981, A&A, 99, 126
- [79] Iben, I., Tutukov, A. 1984, ApJS, 54, 335
- [80] Iben, I., Tutukov, A., Fedorova, A. 1998, ApJ, 503, 344
- [81] Ivanov, P.B., & Papaloizou, J.C.B. 2004, MNRAS, 347, 437
- [82] Ivanov, P.B., Papaloizou J.C.B. 2007, A&A, 476, 121
- [83] Kallinger, T., et al., 2010, A&A, 522, A1
- [84] Kilic, M., et al. 2009, ApJ, 695, L92
- [85] Kilic, M., Brown, W.R., Kenyon, S.J., Allende Prieto, C., Andrews, J., Kleinman, S.J., Winget, K.I., Winget, D.E., Hermes, J.J. 2011, MNRASL, 413, 101
- [86] Kilic, M., Brown, W.R., Hermes, J.J., Allende Prieto, C., Kenyon, S.J., Winget, D.E., Winget, K.I., 2011, MNRASL, 418, 157
- [87] Kilic, M. Brown, W., Allende Prieto, C., Kenyon, S., Heinke, C., Ageros, M., Kleinman, S., 2012, ApJ, 751, 141
- [88] Kulkarni, S.R., van Kerkwijk, M.H., 2010, ApJ, 719, 1123
- [89] Kumar, P., Goodman, J. 1996, ApJ, 466, 946
- [90] Kumar, P., Quataert, E.J. 1998, ApJ 493, 412
- [91] Lai, D. 1994, MNRAS, 270, 611
- [92] Lai, D., Rasio, F.A., Shapiro, S.L., 1994, ApJ, 420, 811
- [93] Lai, D., Wiseman, A.G. 1996, Phys. Rev. D54, 3958
- [94] Lai, D. 1996, ApJL, 466, 35
- [95] Lai, D. 1997, ApJ, 490, 847

- [96] Lai, D., Wu, Y. 2006, Phys. Rev. D74, 024007
- [97] Laio, A., Bernard, S., Chiarotti, G., Scandolo, S., Tosatti, E., 2000, Science, 287, 1027
- [98] Le Bihan, B., Burrows, A., ApJ, 764, 18
- [99] Leconte, J., Chabrier, G., 2012, A&A 540, A20
- [100] Lenz, P., & Breger, M., 2005, Comm. Asteroseis., 146, 53
- [101] Li, W., et al. 2011, Nature, 480, 348
- [102] Lithwick, Y. & Wu, Y., 2012, ApJL, 756, 11
- [103] Loren-Aguilar, P., Isern, J., Garcia-Berro, E. 2009, AA, 500, 1193
- [104] Maoz, D., Sharon, K., Gal-Yam, A. 2010, ApJ, 722, 1979
- [105] Marley, M., 1991, Icarus, 94, 420
- [106] Marley, M., Porco, C., 1993, Icarus, 106, 508
- [107] Marsh, T., Gansicke, B., Steeghs, D., Southworth, J., Koester, D., Harris, V., Merry, L., 2011, ApJ, 736, 95
- [108] Marsh, T., 2011, CQGra, 28, 094019
- [109] Mathur, S., et al., 2011, ApJ, 741, 119
- [110] Mazeh, T., Shaham, J., 1979, A&A, 77, 145
- [111] McDermott, P., Van Horn, H., Hansen, C., 1988, 325, 725
- [112] de Medeiros, J.R., Da Rocha, C., Mayor, M., 1996, A&A 314, 499
- [113] Militzer, B., Wilson, H., 2010, PRL 105, 195701
- [114] Militzer, B., 2012, Int. Jour. of Quant. Chem., 112, 314
- [115] Mochkovitch, R., Livio, M. 1989, Astr. Astr., 209, 111

- [116] Montgomery, M., Winget, D., 1999, *ApJ*, 526, 976
- [117] Mosser, B., et al., 2012, [arXiv:1209.3336](#)
- [118] Mullally, F., Badenes, C., Thompson, S.E., Lupton, R. 2009, *ApJ*, 707, L51
- [119] Nelemans, G. 2009, *CQGra*, 26, 094030
- [120] Nelemans, G., et al. 2001, *AA*, 365, 491
- [121] Nowak, M. A. & Wagoner, R. V., 1991, *ApJ*, 378, 656
- [122] Ogilvie, G.I., Lin, D.N.C. 2004, *ApJ*, 610, 477
- [123] Ogilvie, G.I., Lin, D.N.C. 2007, *ApJ*, 661, 1180
- [124] Pakmor, R., Kromer, M., Ropke, F.K., Sim, S.A., Rüter, A.J., Hillebrandt, W. 2010, *Nature*, 463, 61
- [125] Pakmor, R., Hachinger, S., Ropke, F.K., Hillebrandt, W., 2011, *AA*, 528, A117
- [126] Papaloizou, J.C.B., & Ivanov, P.B. 2010, *MNRAS*, 407, 1631
- [127] Paxton, B., Bildsten, L., Dotter, A., Herwig, F., Lasaffre, P. Timmes, F. 2011, *ApJS*, 192, 3
- [128] Peters, P.C. 1964, *Phys. Rev.*, 136, B1224
- [129] Piro, T. 2011, *ApJ*, 740, L53
- [130] Press, W.H., Teukolsky, T.A. 1977, *ApJ*, 213, 183
- [131] Press, W.H., Teukolsky, S.A., Vetterling, W.T., Flannery, B.P. 1998, *Numerical Recipes* (Cambridge Univ. Press)
- [132] Ramsay, G. et al. 2005, *MNRAS*, 357, 49
- [133] Raskin, C., Scannapieco, E., Fryer, C., Rockefeller, G., Timmes, F. 2012, *ApJ*, 746, 62
- [134] Reisenegger, A. 1994, *ApJ*, 432, 296

- [135] Reisenegger, A., Goldreich, P. 1994, *ApJ*, 426, 688
- [136] Robinson, E., Kepler, S., Nather, R. 1982, *ApJ*, 259, 219
- [137] Samadi, et al., 2007, *A&A*, 463, 297
- [138] Savitzky, A., Golay, M., 1964, *Analytical Chemistry*, 36, 1627
- [139] Schaefer, B., Pagnotta, A., 2012, *Nature*, 481, 164
- [140] Schenck, A. K., Arras, P., Flanagan, E. E., Teukolsky, S. A., Wasserman, I. 2001, *Phys Rev D*, 65, 024001
- [141] Segretain, L., Chabrier, G., Mochkovitch, R. 1997, *ApJ*, 481, 355
- [142] Shibata, M. 1994, *Prog. Theo. Phys.*, 91, 871
- [143] Spruit, H.C. 2002, *A&A*, 381, 923
- [144] Steffen, J., et al. 2011, *MNRAS*, 417L, 31
- [145] Steinfadt, J., Kaplan, D.L., Shporer, A., Bildsten, L., Howell, S.B. 2010, *ApJ*, 716, L146
- [146] Steinfadt, J., Bildsten, L., Arras, P. 2010, *ApJ*, 718, 441
- [147] Strohmayer, T.E. 2005, *ApJ*, 627, 920
- [148] Thompson, S., et al. 2012, *ApJ*, 753, 86
- [149] Truran, J.W., 2002, *Publ. Astr. Soc. Pacific*, 261, 576
- [150] Unno, W., Osaki, Y., Ando, H., Saio, H., Shibahashi, H. 1989, *Nonradial Oscillations of Stars* (University of Tokyo Press)
- [151] Valsecchi, F., Farr, W., Willems, B., Kalogera, V., 2012, arXiv:1210.5023
- [152] Van Kerkwijk, M.H., Chang, P., Justham, S. 2010, *ApJL*, 722, 157
- [153] Vorontsov, S., Zharkov, V., 1981, *Astron. Zh.*, 58, 1101

- [154] Vorontsov, S., 1981, *Astron. Zh.*, 58, 1275
- [155] Wang, Y., Liu, H., Lv, J., Zhu, L., Wang, H., Ma, Y., 2011, *Nature Comm.*, 2, 563
- [156] Webbink, R.F. 1984, *ApJ*, 277, 355
- [157] Weinberg, N., Arras, P., Quataert, E., Burkart, J., 2012, *ApJ*, 751, 136
- [158] Welsh, W. F., et al. 2011, *ApJS*, 197, 4
- [159] Willems, B., van Hoolst, T., & Smeyers, P. 2003, *A&A*, 397, 974
- [160] Willems, B., Deloye, C.J., Kalogera, V. 2010, *ApJ*, 713, 239
- [161] Wilson, H., Militzer, 2012, *ApJ*, 745, 54
- [162] Witte, M. G. & Savonije, G.J. 1999, *ApJ*, 350, 129
- [163] Witte, M.G., & Savonije, G.J. 2001, *A&A*, 366, 840
- [164] Wu, Y. 1998, PhD Thesis, CalTech
- [165] Wu, Y., Goldreich, P. 1999, *ApJ*, 519, 783
- [166] Wu, Y. & Goldreich, P. 2001, *ApJ*, 546, 469
- [167] Wu, Y., 2005, *ApJ*, 635, 674
- [168] Wu, Y. 2005, *ApJ*, 635, 688
- [169] Yoon, S.-C., Podsiadlowski, Ph., Rosswog, S., 2007, *MNRAS*, 380, 933
- [170] Zahn, J.P. 1970, *AA*, 4, 452
- [171] Zahn, J.P. 1975, *AA*, 41, 329
- [172] Zahn, J.P. 1977, *AA*, 57, 383
- [173] Zahn, J.P. 1989, *AA*, 220, 112
- [174] Zahn, J.-P., 2008, *EAS*, 29, 67